THE UNIVERSITY *of* EDINBURGH

Advancements and Understanding of Blister-Based Laser-Induced Forward-Transfer

Nathan Goodfriend

Degree of Doctor of Philosophy

The University of Edinburgh

2017

Abstract

Blister-Based Laser-Induced Forward-Transfer (BB LIFT) is a new method of particle transfer, capable of projecting complex and fragile particles into the gas phase. The technique uses a laser pulse to deform a metal or polymer film on a transparent substrate. The deformation of the film creates a blister which can mechanically desorb particles adhered to the surface. This thesis covers the study of the underlying mechanisms of blister formation in relation to laser pulse duration and film properties, whilst also advancing upon the technique by developing new methods for particle transfer of 0-dimensional point particles, 1-dimensional nanotubes, and 2-dimensional crystals.

Study of the blister formation was carried out on uncoated 200-400 nm Titanium films, using 120 fs and 7 ns laser pulses. The blisters were studied by Atomic Force Microscopy and optical analysis. Furthermore a theoretical model for the blister formation using ns laser pulses was developed using a linear heat transfer model, showing a good agreement between experiment and theory. From this,, model mechanisms for blister formation under both of these pulse durations were developed. It was concluded that ns laser pulses heat the thin film causing it to undergo thermal expansion where the temperature and thermal expansion properties of the film define the blister. Femtosecond pulses form blisters due to confined ablation of the film at the interface of the transparent substrate and the film. The expanding gas forces the metal to stretch, where the deformation is dictated by the Young's modulus of the material with the major factor being the thickness of the titanium film.

The velocity distribution of the desorbed material was studied by means of mass spectroscopy. An ionising laser pulse was focused a known distance from the donor film. The ejected particles crossed the laser beam, and with a controlled delay of the time between the blister pulse and ionisation pulse the velocities could be determined for fullerenes (C_{60}) and gold coated silicon nanoparticles (Auroshells). Utilising C_{60} as the desorbed material we could identify that for ns BB-LIFT the C_{60} was emitted at a velocity mostly dependent upon the heat expansion coefficient for the titanium film, resulting in a velocity approximating 100 ms^{-1} with a secondary emission of fullerenes due to evaporation from the hot surface. However, for fs BB-LIFT this evaporated emission was not present and the velocities could be adjusted from 7-70 ms^{-1} by varying the Ti film thickness from 360 nm to 210 nm respectively. These results are consistent with the mechanisms proposed earlier.

The spread of the desorbed particle beam was also studied for nanosecond and femtosecond laser-induced blisters utilising auroshells and C_{60}. This was accomplished by placing a receiver platform at a known distance in front of the donor film in order to collect the desorbed particles. The radial spread was then analysed indicating a flat deposit approximately the size of the initial blister with a 5 degree spread from that point. This indicates that the desorbed beam is highly directional. From this it could be ascertained that the blisters do not form from a single point position on the film but expand uniformly with the area of laser irradiation defining the growth point of the blister.

A problem with many molecular beam techniques is that large fragile molecules or nanoparticles cannot be introduced to the gas phase without causing damage to the particles. Studies into the desorption of Auroshells (150 nm diameter), C_{60} (1 nm), PCBM (a fragile exohedral fullerene), carbon nanotubes (1x1000 nm), and 2D films (1x10000x10000 nm) showed that these materials were successfully transferred from the donor film to a receiver plate without causing damage to the particles. This was determined via Raman, NMR, AFM, and SEM measurements.

Lastly a technique that allowed the growth of carbon nanotubes directly on the donor film utilising a a multi-layered substrate was developed, enabling the removal and deposition of the nanotubes, without exposing them to any chemical treatment.

Lay Summary

Have you ever thought about how you would move a material, which is so fragile, touching it would damage it, and it's so thin (1 atom thick) that it could break or crease with absolute ease?
How about placing molecules into a beam? There are many ways we can already place some particles into a beam. For example, place a lid with a hole over a pot of boiling water, congratulations, you have made a rudimentary beam of water molecules. However, as the objects become more complex the techniques we have stop working. Let's try this example again, this time with a more complex objects, apples. If we wanted to make a beam of apples, it wouldn't be so simple as boiling a lot of them together in a pot. The apples would begin to break down physically, long before a beam of anything would be produced. These are some of the problems presenting fundamental and applied research of nanomaterials and molecular systems today. We have difficulty manipulating these objects and therefore cannot study and build with them as effectively as we can other, more robust, materials.

We have successfully developed a method which allows us to the move and position particles which can be from the molecular scale to the nanoscale, and even mixed objects which are as thin as an atom yet as wide as a human hair. This opens up possibilities in nanofabrication of transistors, solar cells, diodes, batteries, and capacitors. It also could help us study materials which previously have been too difficult to look at with our special types of microscope which require them to be in a beam. Think back to our beam of apples problem. We have even rudimentarily tested whether it is possible growing these complex objects to a surface, followed by directly placing the objects into a beam, without needing to go through a potentially damaging process of growing them elsewhere. This would then have to be followed by removing them from this "elsewhere" and then placing them into our system and transferring them.

So, how would we make a beam of complex and fragile objects such as apples? We do this with lasers. Specifically, very special lasers which can send highly dense packages of light instead of a continual stream of relatively disperse light. Firstly though, we need to prepare the system for the specific particles we want to transfer. We do this by coating a piece of glass, or something that allows the laser light through, with a thin film of metal which will block the laser light. So, let's imagine we have a pool of water, something which an object can easily flow through. We then place a sheet or tarpauline over this pool of water, as something that will block the object which is flowing through the water. Ontop of this tarpauline we place our apples, or complex objects. We then send something (our laser pulse) through the water which hits the tarpauline, this causes the tarpauline and apples to move upwards, away from the pool of water. Whilst the tarpauline will eventually stop moving, the apples will continue to travel upwards, and be transferred to the gas phase. Now imagine all of this to be taking place inside a building, then the apples will eventually hit the ceiling and, presuming no gravity, be deposited there. Thus transferring them from one place to a specific location elsewhere, without breaking them. This is the basis for our technique called Blister-Based Laser-Induced Forward-Transfer, or BB LIFT. So, we use a laser pulse to cause a blister, or deformation on our tarpaulin/metal film, this ejects/transfers our apples/particles from one place, through the gas phase, to a separate location/the ceiling.

The research was done through experimentation, computational modeling and theoretical calculations. We have managed to find ways to remove gold coated silicon nanoparticles, 150 nm in diameter, fullerenes, like C_{60} and PCBM, as well as quasi one dimensional materials like Carbon nanotubes, and finally quasi two dimensional materials such as $MoSe_2$ and MoS_2. As said above, we have even managed

to grow materials like carbon nanotubes directly to the metal film/tarpaulin and successfully transferred them. We have found how much the particles spread out when emitted and we have looked at the underlying mechanisms behind BB LIFT and how the blisters grow under different laser conditions, and from this we have been able to find ways to control the speed of the emitted particles. We've also used multiple different analysis tools on each of the removed particles to make sure that they are the same type of molecule or nanostructure as before, in order to show that the transfer process hasn't harmed them. It's hoped that with this research we will be able to use this technique in both fundamental and applied sciences.

Acknowledgements

I would like to first thank Professor Eleanor Campbell, my thesis supervisor. She gave me the opportunity to do this PhD, which I hope will lead to further advancements in science. I'm also grateful for the opportunities she has provided for me throughout this project which have given me a wide array of experiences.

Dr. Alexander Bulgakov helped start this project and gave me direct guidance for the first year of my PhD, and even after returning to Novosibirsk, he continued to provide me with opportunities, even helping me find my next adventure.

I'm thankful to Dr. Olof Johansson for his knowledge and experience of working within the laser lab.

I'm not entirely sure how to thank Dr. Oleg Nerushev who has been a guide to me since the 4th year of my undergraduate degree. It was working with Oleg 6 years ago which helped me get a summer job in his lab the following summer, which then helped me get this PhD opportunity.

I would like to thank Dr. Andrei Gromov for his jolly humor and ever ready smile and suggestion of coffee.

I would especially like to thank all the other PhD students who I have shared my office and research with. Kirsten, Elvira and Arran you get a special thank you for the initial warm welcome you gave me. Since that point it has been great to spend time with all of you, whether it be in the lab office or socially. Luke, I'd like to think that I helped get you this PhD by first directing you to Olof on your first visit. I hope that it makes you proud. Thank you, Florian and Minas for joining the office and bringing with you a new energy.

I'd like to thank all of the research students who have helped me with the research for this PhD, Max, Shu, Briony and Jan. Their time and enthusiasm has made great contributions to this thesis.

I would also like to acknowledge all of those in the Physchem group for building a small and close community outside of our research groups. But, I'm also grateful to the rest of the community within the School of Chemistry and throughout.

I'd like to thank my Parents for their support no matter what. I'd also like to thank the rest of my friends and family for their company and companionship.

I'd also like to specially thank Toni. I'm not sure I could have finished without you.

Contents

Acronym definitions

AFM	Atomic Force Microscopy
CVD	Chemical Vapour Deposition
LIFT	Laser Induced Forward Transfer
QCB	Quartz Crystal Balance
BB LIFT	Blister Based LIFT
TOF MS	Time of Flight Mass Spectrometer
UV	Ultraviolet
LIAD	Laser Induced Acoustic Desorption
LITD	Laser Induced Thermal Desorption
MALDI	Matrix Assisted Laser Desorption and Ionisation
IR	Infrared
PMMA	Polyimide
fs	Femtosecond
ns	Nanosecond
ps	Picosecond
SEM	Scanning Electron Microscopy
PCBM	Phenyl-C_{61}-Butyric acid Methyl ester
MCP	MicroChannel Plate
EBE	Electron Beam Evaporator
SWCNT	Single Walled Carbon Nanotube
MWCNT	Multi Walled Carbon Nanotube
NMP	N-Methyl-2-Pyrrolidone
DMF	DiMethylFormamide
RBM	Radial Breathing Mode
XRD	X-Ray powder Diffraction

1. Introduction

The aim of this thesis was to develop a technique for producing a sufficiently high density target of particles in the gas phase to enable fs laser ionisation studies. For the initial characterisation of the technique, the particle source was combined with a fs laser ablation/ionisation time-of-flight mass spectrometer. Once sufficiently characterised and developed, the method may be used to enable fs laser photoionisation studies of complex molecules, with a low vapour pressure, that cannot easily be introduced to the gas phase by other means without inducing extensive fragmentation. In addition, this technique's potential to cleanly 'print' nanomaterials, such as quasi 2D and 1D materials, or complex molecules, which can prove difficult to spatially position without introducing contaminants, was also explored. This "clean printing" capability could then be applied to further fundamental research into these novel nanomaterials as well as to assess its applicability in the fabrication of functional devices. The method chosen was Blister-Based Laser-Induced Forward Transfer (BB-LIFT), an extension of LIFT that allows for low temperature transferal of particles.

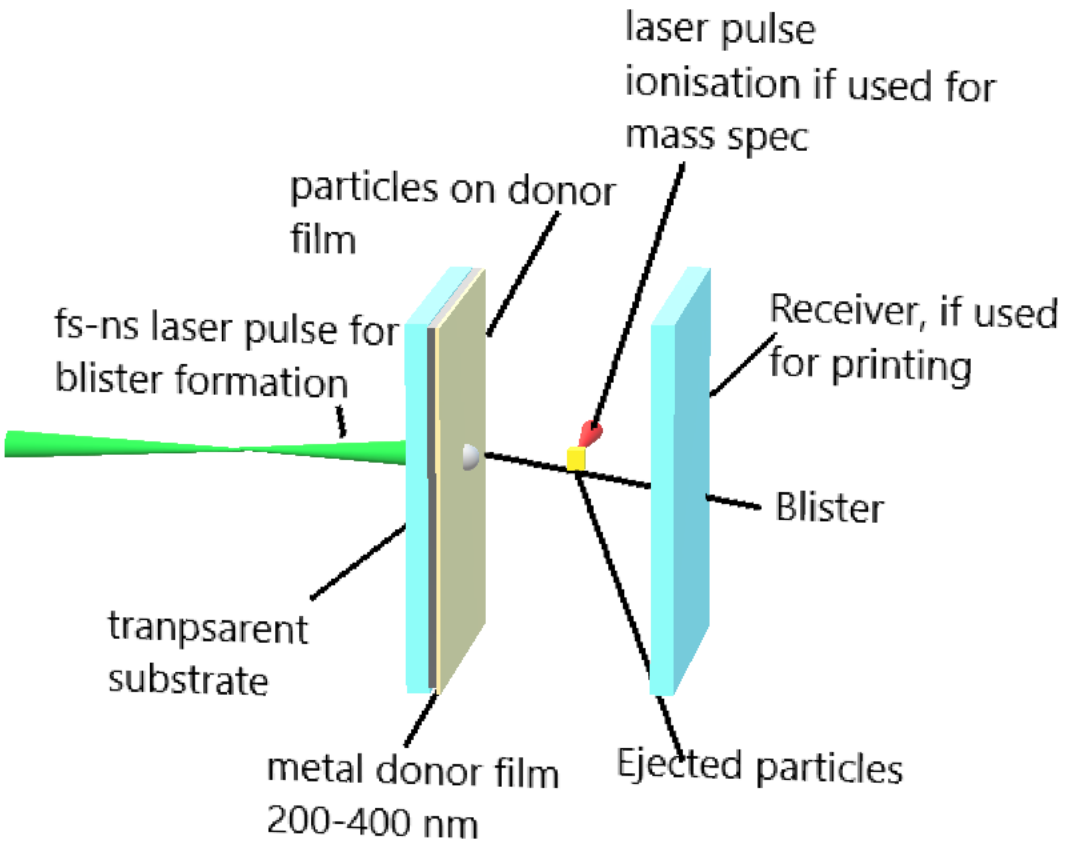

FIGURE 1-1: SCHEMATIC FOR BB-LIFT. A FS OR NS LASER PULSE INDUCES A BLISTER AT THE INTERFACE OF A TRANSPARENT SUBSTRATE AND A METAL FILM ~200-400 NM. THE BLISTER EJECTS MOLECULES OR NANOPARTICLES ON THE SURFACE OF THE METAL FILM. THESE PARTICLES CAN THEN BE PRINTED TO A RECIEVER PLATE OR IONISED BY ANOTHER FS OR NS LASER PULSE, IF USED FOR SPECTROSCOPY.

1.1 Motivation

1.1.2 Improvement upon alternative gas phase sources.

Within this thesis, the mechanism behind BB LIFT is investigated and the technique is tested as a means to gently desorb large complex molecules and nanoparticles. Therefore it should be considered alongside other techniques for introducing species into the gas phase, such as thermal ovens, electrospray[1,2,3], matrix-assisted laser desorption/ionisation (MALDI)[1,4], and laser-induced thermal desorption (LITD) (formerly known as laser induced acoustic desorption (LIAD)).[5,6] The advantages and disadvantages of these other methods are outlined below

Introducing the constituents of solid material into the gas phase, and forming them into a directed beam, was first done through heating. The first atomic beam, created by Otto Stern, was vaporised silver.[7] This method shifts the particles from the solid phase, or potentially the liquid phase, into the gas phase. From this point, the particles pass through small apertures which limit the particles' movement to only one direction. Whilst this technique is simple, it can only be applied to molecules which have a significant vapour pressure at temperatures lower than the temperature at which they become unstable and will not break down during this vaporisation process. The molecules must also be heated within a non-reactive vessel, lest they react with the crucible walls rather than evaporate.

Electrospray ionisation is a technique often used in conjunction with mass spectroscopy of large biological molecules.[1,2] It was first suggested by Dole et al. in 1968 but it was Fenn et al. who successfully demonstrated the technique in 1988[8,2] Fenn and Koichi Tanaka (the developer of MALDI) were awarded the Nobel Prize in 2002[3] for their work in mass spectrometry. Using the electrospray ionisation technique, the molecules or particles of interest must first be dissolved in a relatively volatile solvent. The solvent is then pressed through a highly charged needle inside a vacuum chamber into an extraction region. The high potential from the needle to another position within the grounded vacuum chamber will attract the charged droplets containing the volatile solvent and particle of interest. The solvent will evaporate quickly, leaving smaller charged droplets behind. As the droplets shrink further, the amount of charge per droplet volume becomes unstable, which results in a coulomb explosion. This creates many smaller droplets of solvent and particles of interest. Eventually all of the solvent will evaporate, leaving only the particles of interest and whatever charges remain upon them. Whilst this technique is powerful, it often causes fragmentation; and, by its nature, the chosen particles must be soluble in a volatile substance. The particles will also become highly charged in the process.

MALDI is another soft ionisation technique.[9,1] The layout of MALDI is similar to that of a laser ablation system. However, the wavelength of the laser must be set so as not to interact strongly with the particles of interest. The particles are combined with a solution/matrix deposited on a substrate. An individual laser pulse focused on the deposited droplet, is strongly absorbed by the pulse and vaporises the matrix, removing the particles of interest inside a plume of positively and negatively charged ions, alongside some neutral particles. This technique is very powerful; however, it still causes fragmentation and heating of the particles. There is also a background of the original matrix inside the desorbed plume and it is not always possible to find a suitable matrix for a given class of molecules.

Laser induced acoustic desorption/laser induced thermal desorption (LIAD/LITD), is a technique that has been in development since the 1980s.[10] However, in 2016, the name LITD began to be used more, since desorption can no longer be attributed to acoustic waves.[11] Of the various techniques, LITD is the most similar to LIFT. Particles are deposited on a metal foil, the rear side of the metal foil, which does not have any particles adsorbed, is then impacted by a laser pulse with a nanosecond or smaller pulse duration. It is now believed that this gently thermally desorbs the molecules from the surface. This technique has shown promise for small molecules[10,12–14]; however, it is yet to be seen if it can desorb larger and more fragile systems. It does have the advantage of not requiring a solution base and also removes neutral particles. Despite being a technique which involves heating, it does seem capable of removing the particles more gently than in classic oven systems.

We believe that BB LIFT can fill a niche left by these techniques. It projects the molecules in a pulse fashion, allowing easy application to printing. The desorbed materials are neutral, and, in most cases, not thermally desorbed (discussed later in ns BB LIFT). The particles don't need to be soluble, and no other particles from a solvent or matrix travel with the beam.

1.1.2 Materials of interest that BB LIFT may transfer

The BB LIFT technique uses an innovative transfer mechanism, which increases its potential to transfer a variety of materials, filling a niche left open by the previously discussed methods. The wide range of materials BB LIFT is capable of transferring, which cannot be effectively transferred via LIAD, MALDI, Electrospray or thermal desorption, gives it the potential to have a large variety of potential applications.

1.1.2.1 Nanoparticles of diameter 20-300 nm

Initial development revolved around nanoparticles that are typically too large for conventional mass spectrometry, but on the limit for detection by other means such as light scattering. The idea was to use fs laser pulses to ablate the particles once they were introduced to the gas phase to obtain information on their content. As test materials, Auroshells (gold coated silicon nanoparticles of 150 nm in diameter) were chosen. Materials of this size are often placed or formed in the gas phase and directed into a beam via aerodynamic lenses. Typically aerodynamic lenses propel particles that are 20-300 nm in diameter

before entering the aerodynamic lens, which, through a series of pumping stages, will collimate the previously generated particles.[15,16] BB LIFT was successfully tested as an alternative for transferring particles of this size, without the necessity of generating them immediately before analysis, thus, potentially allowing a greater variety of nanoparticles to be analysed.

Relatively Large particles on this scale are of great interest, with a main focus revolving around pollution.[1517] They are often generated around population centres; and, their impact on public health can be drastic.[18] Understanding of the structure and makeup of these particles can help in understanding their impact on the human body, as well as enabling research into limiting their generation and reducing their prevalence in the atmosphere.

1.2.2.2 Fragile molecules

Molecules are often transferred utilising the previously mentioned techniques. However, as stated above, they are often subjected to a wide variety of forces which can cause damage or alter their state to one incompatible with their intended usage.[19] As part of the research and experimentation which underlies this thesis, we have successfully transferred phenyl-C_{61}-butyric acid methyl ester (PCBM) shown on the top left of Figure 0-1 using the BB LIFT technique. This molecule, like the others shown in Figure 0-1, is one of the most viable for usage within development of organic solar cells.[20] These molecules can be very complex or fragile, which limits the ability to study them in vacuum, thus reducing researchers ability to understand the complex electronic capabilities within the molecules. As such, further development of them from a fundamental understanding of their chemistry and physics remains arduous. However, investigation into transfer to the gas phase and printing of these molecules via BB LIFT can help fill this void.

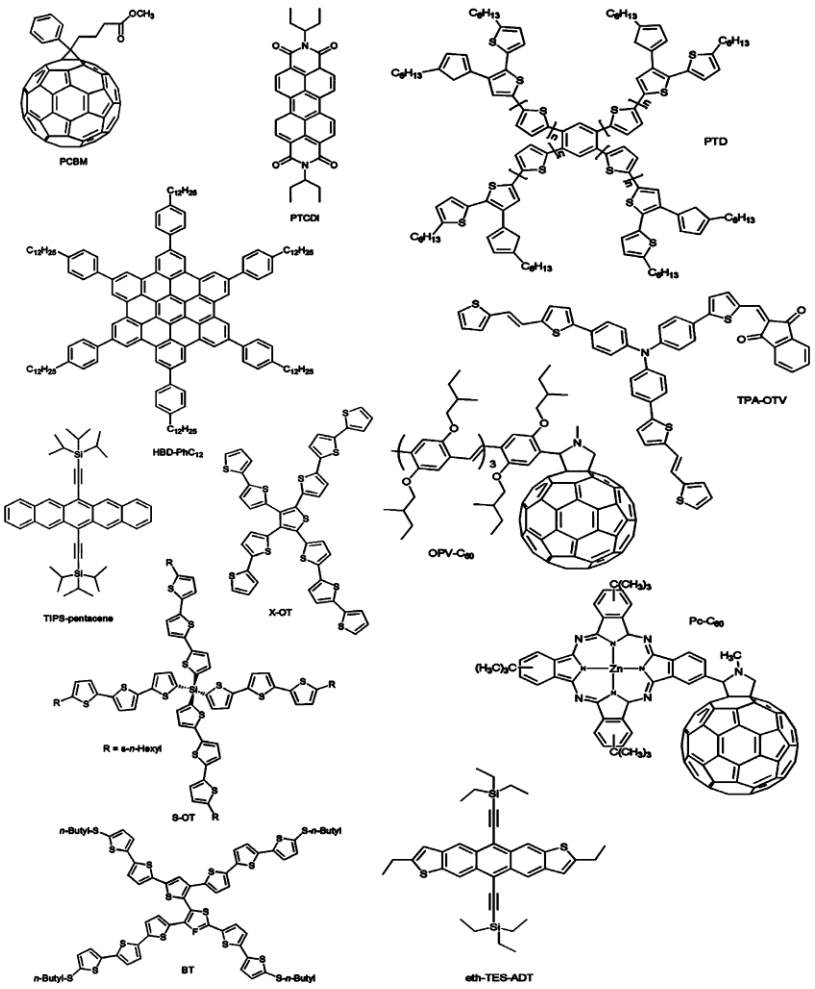

FIGURE 1-2: SOLUBLE DONOR AND ACCEPTOR MOLECULES WHICH SHOW THE HIGHEST AFFINITY FOR ORGANIC SOLAR CELLS. [20] **PCBM BEING (TOP LEFT) BEING ONE SUCCESSFULLY TRANSFERRED BY BB-LIFT WITHIN THIS THESIS. THESE OTHER FRAGILE YET USEFUL MOLECULES SHOULD THEN BE VIEWED AS POTENTIAL OPTIONS FOR ADVANCING BB-LIFT WHILST PROVIDING USE TO OTHER FIELDS OF SCIENCE.**

1.1.2.3 Quasi 1D and 2D materials

Quasi 1D and 2D materials such as carbon nanotubes (1D) and graphene (2D) are subjects of keen interest.[21,22] Alongside quasi-2D materials such as graphene, are transition metal dichalcogenides. These 2D materials have various optical and electrical properties which make them good subjects for use in solar cells[23], transistors[24], quantum dot studies,[21] batteries[25,26], and novel forms of mass spectrometry.[27] The transfer of these materials to form nanoscale devices that will take full advantage of their intrinsic

properties is, however, extremely time consuming and difficult. So, developments, such as the 1 nm gate MoS_2 transistor by Desai et al.[24], which can work below the 5 nm limit for silicon transistors, are difficult to develop. The process, described in Figure 0-2, illustrates the 13-step process (not including the initial growth of the carbon nanotubes and $MoS_{2)}$ in order to successfully create one transistor in which the gates, sources, and drain electrodes must all be etched to the location, after finding the position of the carbon nanotube. The work done in this thesis has shown the potential for reducing the difficulty drastically, by developing a technique for growing carbon nanotubes directly to a transfer system, and successfully transferring quasi 2D materials to a target location, with the potential to expand into direct growth of the quasi 2D material to the transfer system, thus, potentially leading towards better development of these technologies. The current transfer processes also involve potentially corrosive chemicals and introduce contamination to these nanomaterials, which affects their properties. BB LIFT can achieve a contamination-free method of transfer, thus allowing improved and more efficient studies and production of each of the earlier listed subjects of study.

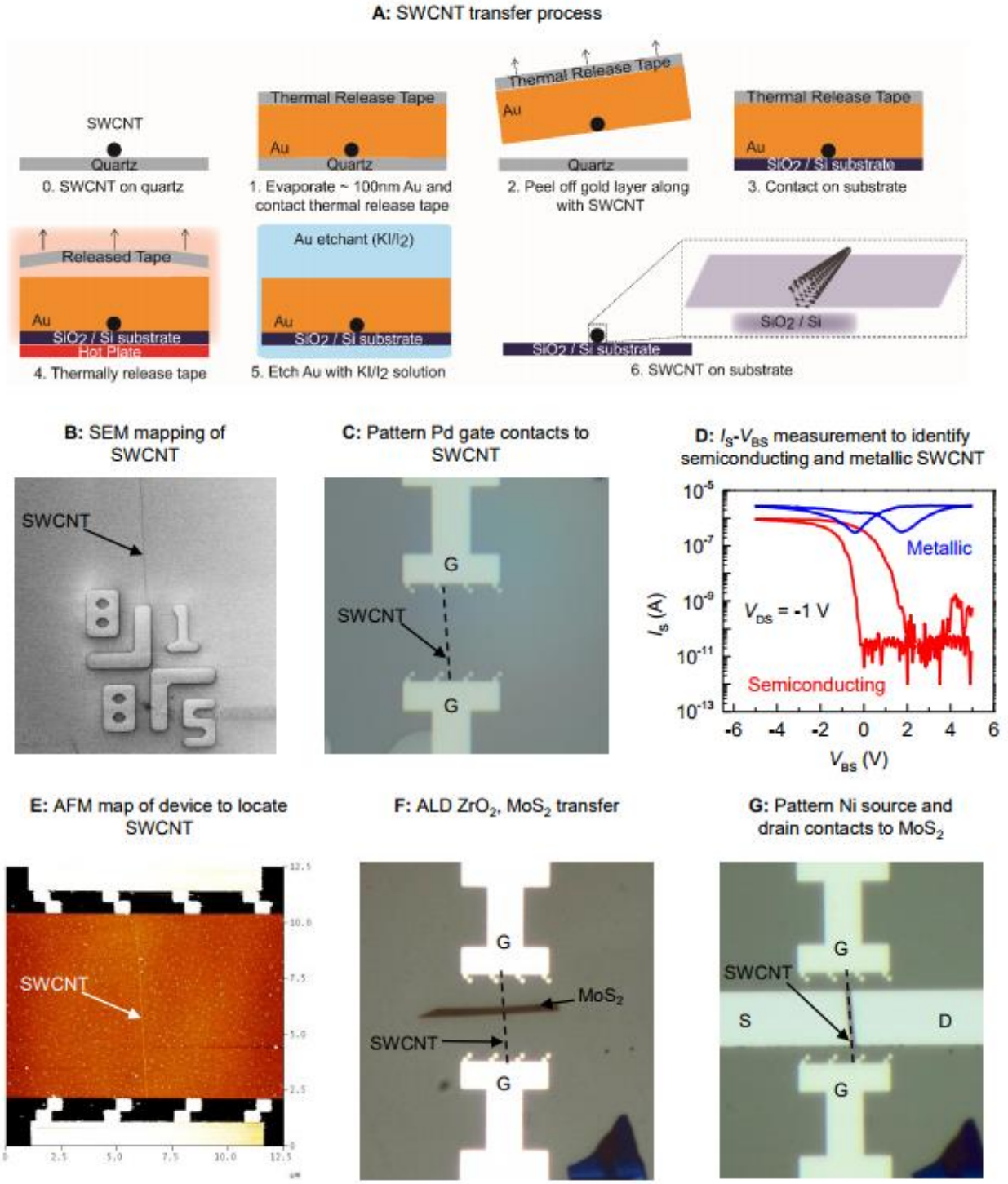

FIGURE 1-3: METHODOLOGY FOR CREATING A 1 NM GATE TRANSISTOR WITH A CARBON NANOTUBE AND MoS_2.[28]

A) TRANSFER OF GROWN SWCNT FROM QUARTZ GROWTH SUBSTRATE. TO TARGET SiO_2 SUBSTRATE COATING THE SYSTEM IN GOLD WITH AND THERMAL RELEASE TAPE. ONCE TRANSFERRED TO THE SiO_2 THE SYSTEM IS HEATED THUS REMOVING THE TAPE AND THE GOLD IS ETCHED AWAY WITH KI/I_2 LEAVING THE SWCNT UPON THE SiO_2. B) THE SiO_2 IS

PREPATTERNED WITH ALIGNMENT MARKERS TO HELP FIND THE SWCNT WITH SEM ONCE TRANSFERRED. DURING THE PROCESS ITS POSSIBLE TO DAMAGE THE SWCNT WITH THE SEM AND EXPOSURE TIME MUST BE LIMITED. C) USING ELECTRON LITHOGRAPHY FOLLOWED BY PD EVAPORATION AND LIFT OF GATE ELECTRODES ARE FORMED. D) THE GATE ELECTRODES ARE USED TO IDENTIFY IF THE SWCNT IS SEMICONDUCTING OR METALLIC. E) THE SYSTEM IS THEN MAPPED AGAIN WITH AFM. F) A ZrO_2 LAYER IS DEPOSITED USING ATOMIC LAYER DEPOSITION AS A GATE DIELECTRIC AND A FLAKE OF MoS_2 IS THEN DEPOSITED USING PMMA AS A TRANSFER MEDIUM. G) USING THE AFM IMAGE AS A MAP TAKEN PRIOR TO THE ATOMIC LAYER DEPOSITION OS ZrO_2 THE FURTHER ELECTRON LITHOGRAPHY IS CONDUCTED TO NI SOURCE DRAIN ELECTRODES

1.2 Laser- Induced Forward Transfer

Laser-Induced Forward Transfer (LIFT) is an established technique for high resolution printing of nanodroplets from a thin donor film of metal.[29] A transparent donor substrate is coated with a thin film of metal which will produce the desired nanoparticles. The film is then struck by a pulsed laser of a high enough intensity to melt the thin film locally, as illustrated in Figure 1-1 and Figure 1-4.

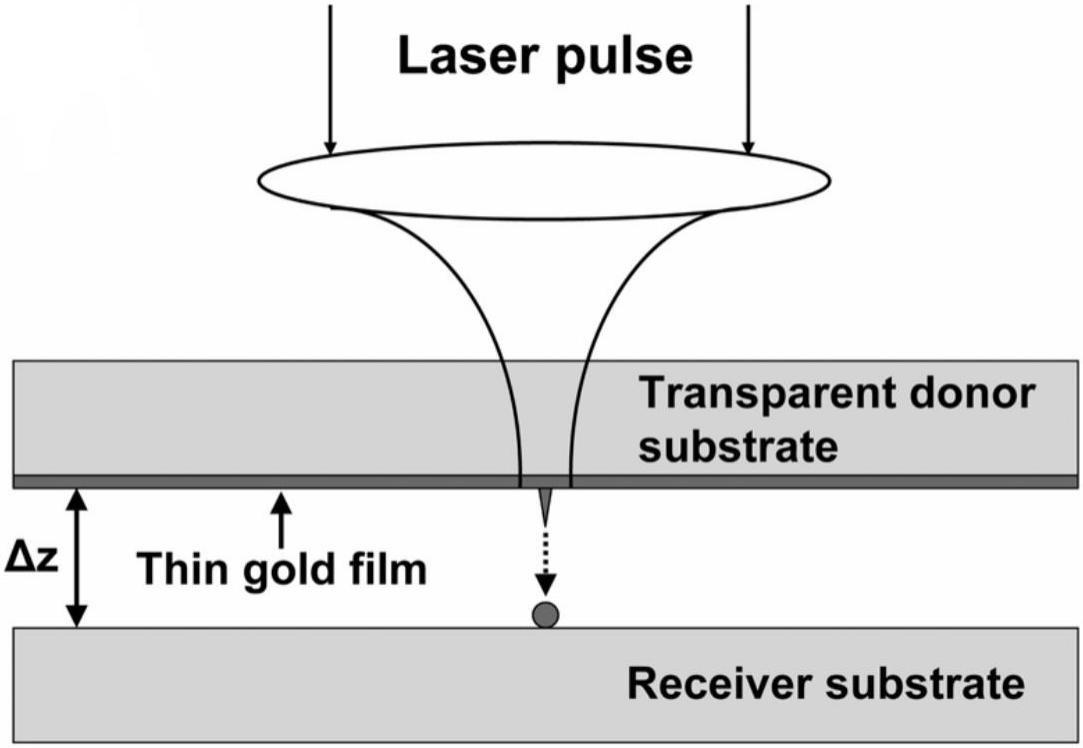

FIGURE 1-4: DIAGRAM ILLUSTRATING THE IMPACT OF A LASER PULSE THROUGH A TRANSPARENT SUBSTRATE TO A THIN METAL (AU) FILM. THIS INDUCES THE FORMATION OF A DROPLET PICTURED IN FIGURE 1-5, WHICH CAN BE FINELY PRINTED ONTO A RECEIVER PLATE, AS SHOWN IN FIGURE 1-6.[30]

The laser pulse induces the creation of a molten microdroplet, as shown in Figure 1-5. As can be seen from Figure 1-5(d), at a high enough intensity, the droplet is ejected forward towards the receiver substrate.

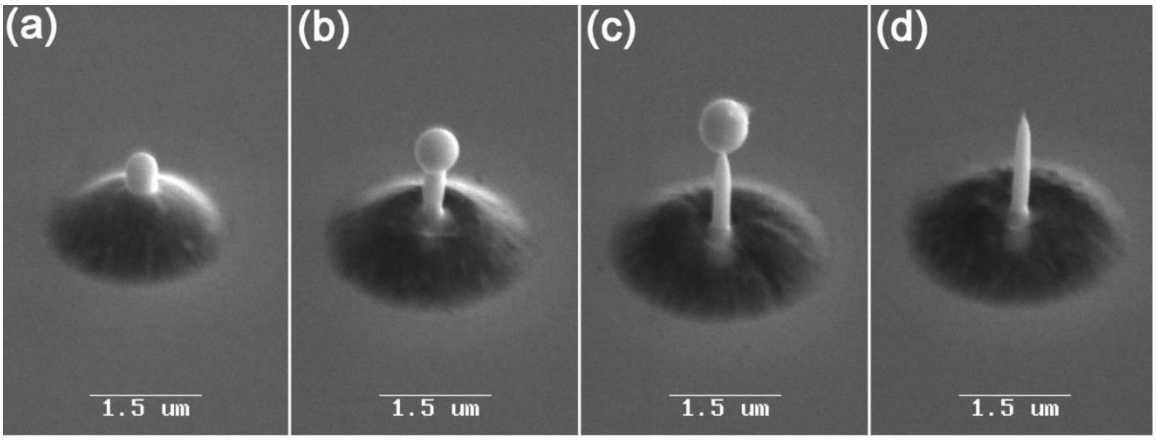

FIGURE 1-5: PATTERNED STRUCTURES ON 60 NM GOLD FILM CREATED BY 30 FS GAUSSIAN PROFILE LASER PULSE. THE SEM IMAGES ARE TAKEN AT A 45 DEGREES. LASER PULSE ENERGY IS 60 NJCM^{-2} (A), 65 NJCM^{-2} (B), 70 NJCM^{-2} (C), AND 75 NJCM^{-2} (D) [30]

The receiver plate of chosen material can then be successfully printed to a very fine resolution as shown in Figure 1-6.

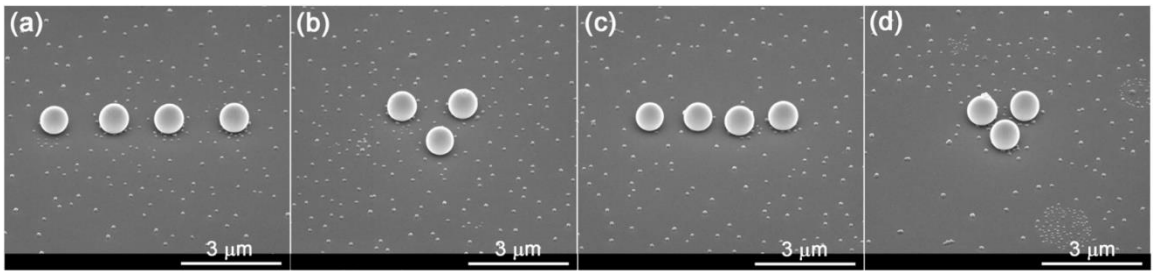

FIGURE 1-6: THE GOLD NANOPARTICLES EACH OF 500 NM IN DIAMETER CAN BE PRINTED TO A RESOLUTION OF ≈ 1 μM [30]. EACH SEM IMAGE IS TAKEN AT 45° ANGLE. THE INTERPARTICLE DISTANCE IS 1.5 μM (A)(B) AND 1 μM (C)(D). THE LASER BEAM WITH A DIAMETER OF 8 MM WITH PULSE ENERGY 50 NJ WAS FOCUSED VIA A 20 MM FOCUS LENS.

Whilst a very powerful tool for nanofabrication, this method was developed to transfer the metal film, which limits it to materials with the right melting conditions as well as the ability to deposit a uniform film onto the transparent substrate. A variety of nanoparticles such as nickel [31], chromium [32], copper [33]

and $FeSi_2$[34] were initially tested. Recently the technique has advanced further and can now be used to transfer gelatinous materials as well such as silver paste, thus allowing advancements upon technologies such as photovoltaic solar cells.[35] Further advances have also shown use in formation of micro-electronics such as organic thin film transistors.[36]

LIFT has also been expanded to incorporate vaporisable sacrificial donor layer such as a triazine polymer.[37] This has advantages over other LIFT transfer techniques, which often involve imbedding the material within a polymer paste, which can be used to transfer an array of electronically applicable materials.[38,39] Whilst utilising sacrificial layers has the advantages of transferring only the particle of interest, without an encompassing substrate, the sample preparation still has its drawbacks. As the triazine polymer is soluble in chlorobenzene or cyclohexanone, the materials which can be transferred from this technique must use a different solvent to apply them to the sacrificial layer. Furthermore, the transferred particles are then transferred within a plume of plasma and ions, which can damage the particles as well as influence the ability for the technique to be applied to gas phase spectroscopy.[40]

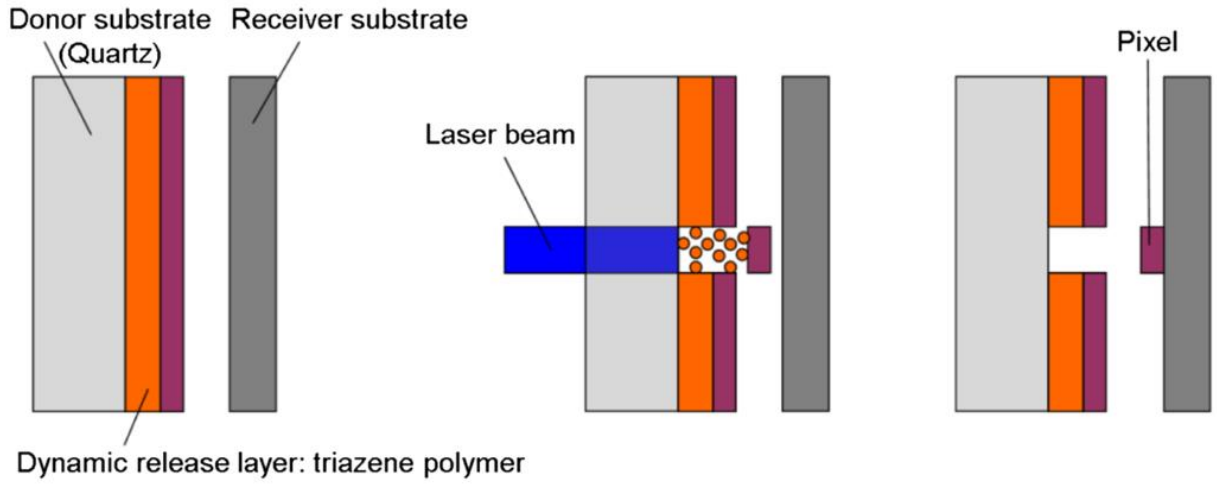

FIGURE 1-7: SCHEMATIC OF SACRIFICIAL LIFT TECHNIQUE. USING A TRANSPARENT QUARTZ SUBSTRATE COATED IN TRIAZENE FOLLOWED BY THE OBJECT TO BE TRANSFERRED. A SET DISTANCE AWAY IS THE RECEIVER SUBSTRATE, WHICH ACCEPTS THE LASER PULSE EJECTED MATERIAL. [40] THE TRIAZENE IS A SACRIFICIAL LAYER AND VAPORISED DURING THE TRANSFER PROCESS.

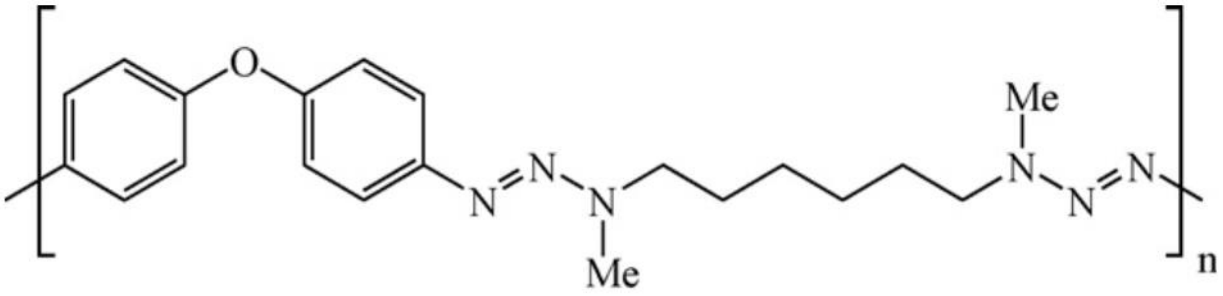

FIGURE 1-8: FORMULA FOR THE TRIAZINE POLYMER.[37] A COMMON POLYMER USED IN A VARIATION OF LIFT IN WHICH THE TRIAZINE ACTS AS A SACRIFICIAL LAYER. IT'S STRUCTURE ABSORBS THE MAJORITY OF THE LASER PULSE CAUSING VAPORISATION.

Blister-Based Laser-Induced Forward Transfer (BB-LIFT) advances upon the methods of LIFT and instead utilises a thicker-film/less-intense pulse so as to only create a blister on the surface. This obviously does not transfer the metal film, which instead deforms. This deformation opens up the possibility of mechanically ejecting a second layer of pre-made nanoparticles/molecules. The particles can be in the form of a thin film, a powder [41], a liquid [42] or even a gel [43].

1.3 Laser-induced acoustic-desorption (LIAD)

Laser induced acoustic desorption (LIAD) is another technique for projecting particles into the gas phase at low temperatures. It was first reported in 1985, and demonstrated the projection of negatively charged hydrogen ions.[5] However, it has been shown that the majority of the particles which it emits are neutral.[12] As LIAD gently emits molecules from the surface, it is often combined with mass spectrometry techniques in order to analyse complex and fragile molecules.[10,12] However, over the approximate 30 years of its existence, it has not yet become a mainstream technique. This is likely due to the difficulty in understanding and controlling the process by which it emits the molecules. This has made it difficult to enhance the technique and correct some of its failings.

The technique itself is similar to LIFT, a nanosecond pulse laser is fired at the back of a metal substrate. This has since been shown to also work with a continuous laser.[11] The molecules to be emitted are deposited upon the front side of the metal substrate. Through some mechanism, the molecules on the

front of the metal substrate are desorbed. What differentiates this technique from LIFT, is that there is no glass substrate behind the metal. Therefore, no blister is formed. Instead the impact of the pulse on the metal film was thought to create an acoustic vibration in the metal which desorbs the surface molecules.

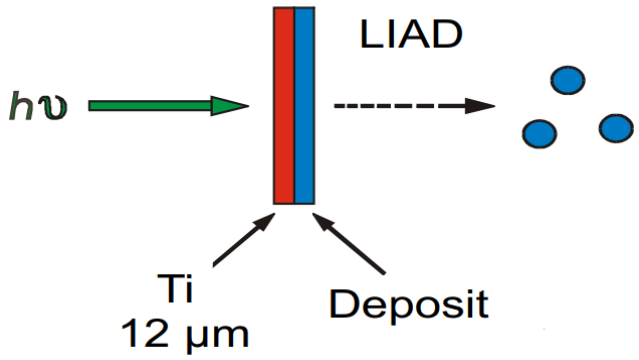

FIGURE 1-9: LIAD/LITD SCHEMATIC FOR DESORPTION. A FOIL OF TI IS COATED (OFTEN BY DIRECT DRY PLACEMENT OF THE MATERIAL) OF THE MATERIAL OF INTEREST.[44] LIAD TYPICALLY IS NOT USED AS A PRINTING METHOD, BUT INSTEAD THE EJECTED MATERIAL IS SENT TO A SPECTROMETER OF CHOICE.

Initially it was believed that the molecules were emitted by a 'shake off' process. This insinuated that the impact of the laser would vibrate the metal to the extent that the molecules would simply fly off when the metal retracted from a vibration-induced, forward movement. However, research conducted in 2007 established that this was not the case and instead, two non-mutually exclusive mechanisms were proposed.[45] One possibility is that the laser will create non-equilibrium electronic states on the substrate surface followed by electron-phonon coupling. This could provide a repulsive force necessary to desorb the molecules. Another possibility is that the acoustic waves provide enough energy to break the molecular crystals of the deposits.[12] The crystal fracturing is what provides the energy, allowing the particles to leave the surface. In 2012, Greenwood Calvert discovered that they observe the strongest signal if the ionizing pulse has a delay of 10-15 microseconds between the pump and probe.[10] This implies that the crystal fracturing is likely to be the dominant removal force. However, they do admit that, whilst they could model the phonon coupling of the first proposed mechanism, modelling the crystal fracturing is not possible with their current simulations.

Whilst LIAD/LITD has yet to truly show its full potential, work is still being done to improve the technique. Despite these difficulties in formulating a mechanism for molecular removal, the technique does work. [46] The molecules emitted are estimated to have an internal temperature of approximately 200°C.[10] The velocities of the molecules are dependent upon their respective mass and have an associated kinetic energy approximating 700 K.[10,12] The density of the molecules is approximately 10^9-10^{10} molecules per cm^3.[10] This concentration is less than that of other techniques such as MALDI; however, it has been demonstrated that analytical measurements are possible. That being said, this density is not consistent, and the shot to shot variation is quite variable. Figure 1-10 shows the signal of Phenylalanine detected by the mass spectrometer over 2500 emissions. Each of these emissions was created by firing a nanosecond laser at the same position on the film. However, it can clearly be seen that the emission is rather erratic. Furthermore, it has been shown that, despite its advances, LIAD/LITD may be approaching a barrier, as shown recently by Arndt et al. [47] which demonstrated its inability to remove the biochromophore chlorophyll.

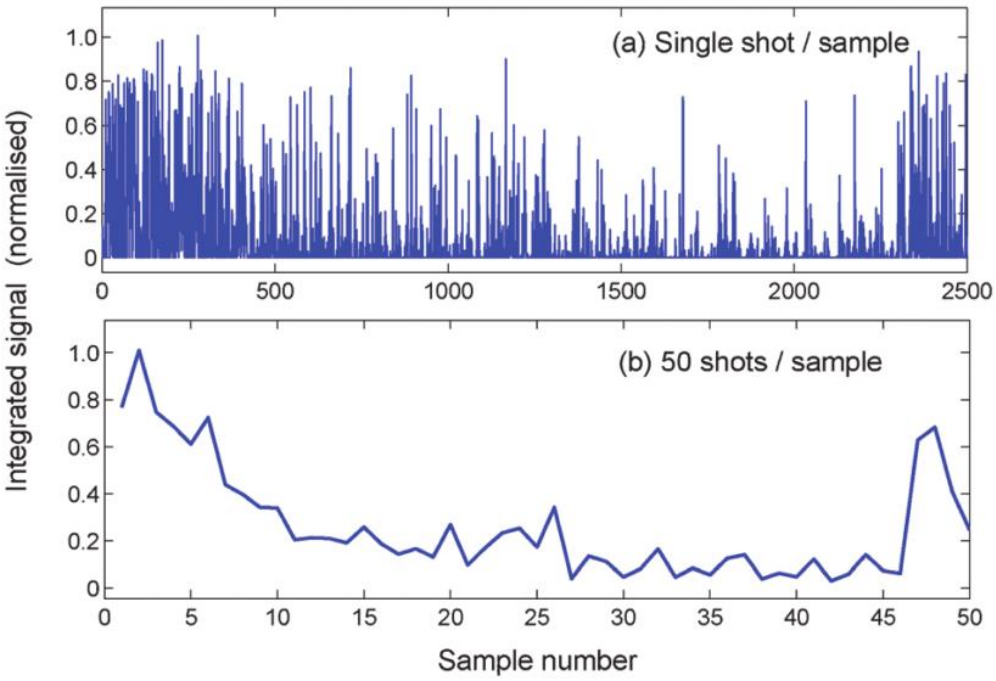

FIGURE 1-10: SHOT-TO-SHOT SIGNAL OF PHENYLALANINE IONS DETECTED BY THE MASS SPECTROMETER COMBINED WITH THE LIAD -TECHNIQUE. THE TOP CHART SHOWS THE INTEGRATED YIELD OF MASS PEAKS AT 74 AU CORRESPONDING WITH PHENYLALANINE, OVER 2500 INDIVIDUAL PULSES. THIS SHOWS A CONTINUOUS FLUCTUATION IN AMPLITUDE IRRESPECTIVE OF THE CONSTANT EXTERNAL PARAMETERS. THE BOTTOM CHART BINS EACH OF THESE INTO A SUMMATION OVER 50 SHOTS. THIS GIVES A BROADER INSIGHT INTO THE CHANGE IN PARTICLE CONCENTRATION OVER THE CONTINUED SERIES OF PULSES. EACH OF THESE EMISSIONS WAS FROM THE SAME POSITION ON THE METAL FILM.[10]

1.4 Blister-Based Laser-Induced Forward Transfer (BB LIFT)

1.4.1 State-of-the-Art

The first group to publish results on the BB LIFT technique was the Kononenko group, based at the Prokhorov General Physics institute, in Moscow, Russia [41]. This group used titanium films, with thickness varying from 50-2000nm. Since showing an initial capability with dried diamond nanoparticles, they have since studied the speed of blister formation[48] and printing of various other substances, in order to establish BB-LIFT as a useful technique.

The Arnold group, at Princeton University, published a year later with a novel take on BB-LIFT, which they renamed blister-actuated (BA) LIFT[49]. Their technique uses the same blister formation principle to induce the removal of a surface coating; however, they replaced the thin titanium film with a 3-6 µm polyimide coating, so as to fully absorb their UV laser pulse. Furthermore, they projected micro-jets of liquid ink to the receiver, rather than solid nanoparticles. Since their initial publication, in which they began to incorporate blister formation to their previous research of LIFT, they have utilised strobe-based photography to study the growth of the blisters and the formed micro-jets, as-well as computational models to help interpret the experimental results.[42,50]

Despite the differences in material, both groups use Gaussian-profiled laser pulses between 0.7 - 40 ns, with the exception of the initial paper by Kononenko[41], which used a 50ps pulse duration. The Arnold group used pulses of enough energy to ablate the film used, and through a high-speed imaging technique, they showed that plasma was formed at the interface[50]. This implies, that the dominating mechanism for blister formation is through formation of a pressurised gas at the interface, which provides the force for blister formation. The Kononenko group also claim their blisters are formed via this method, as they have observed damage of the transparent substrate at the interface[41].

1.4.2 Blister formation

Blisters can be formed using a variety of laser sources, which vary in pulse duration, wavelengths and beam profile. As only a few groups currently work with this technique only a limited range of laser parameters has been explored so far.

The blisters presented above is believed to be caused by ablation of the thin film at the confined, glass, thin film, interface. This ablation creates a fluence-dependent plume of confined plasma, which provides the pressure necessary to delaminate and expand the thin film[42,50]. There is another competing interpretation, which suggests that it is the non-vaporising heating of the film itself which induces thermal expansion of the thin film. As the film cannot expand into the glass substrate; and, its lateral expansion is confined by the temperature gradient, it balloons normal to the glass forming a blister. The basis for contention of these mechanisms is whether the low energy of the laser can provide enough energy to ablate enough material at the interface if any. The main difference between the mechanisms is that there would be a near vacuum within the blister for the thermal expansion method, as opposed to the high pressure of the ablation interpretation. Due to the high pressure of the ablation mechanism, the ductility of the material will be the most important parameter, along with the ablation threshold. Within the thermal expansion interpretation, the malleability and thermal expansion coefficient play the largest role in blister formation. As of yet, there has been no study which has unambiguously determined the blister formation mechanism.

1.4.2 Blister formation through expanding gas

The Arnold group have conducted experimental and computational studies on the dynamics of blister formation.[50,51] Like their other work, they focus on 3-6 µm of spin-coated polyimide film, which absorbs in the UV region. Both experimental and computational studies were conducted/modelled with top-hat 40 ns laser pulses with a fluence of approximately 120 mJ cm^{-2} and a wavelength of 355 nm. The computational finite element analysis was tuned via adjusting a computational pre-factor for material strain-rate (η) at varying laser fluences on a 7 µm film. It was then tested on a 3µm film, as shown in Figure 1-11.

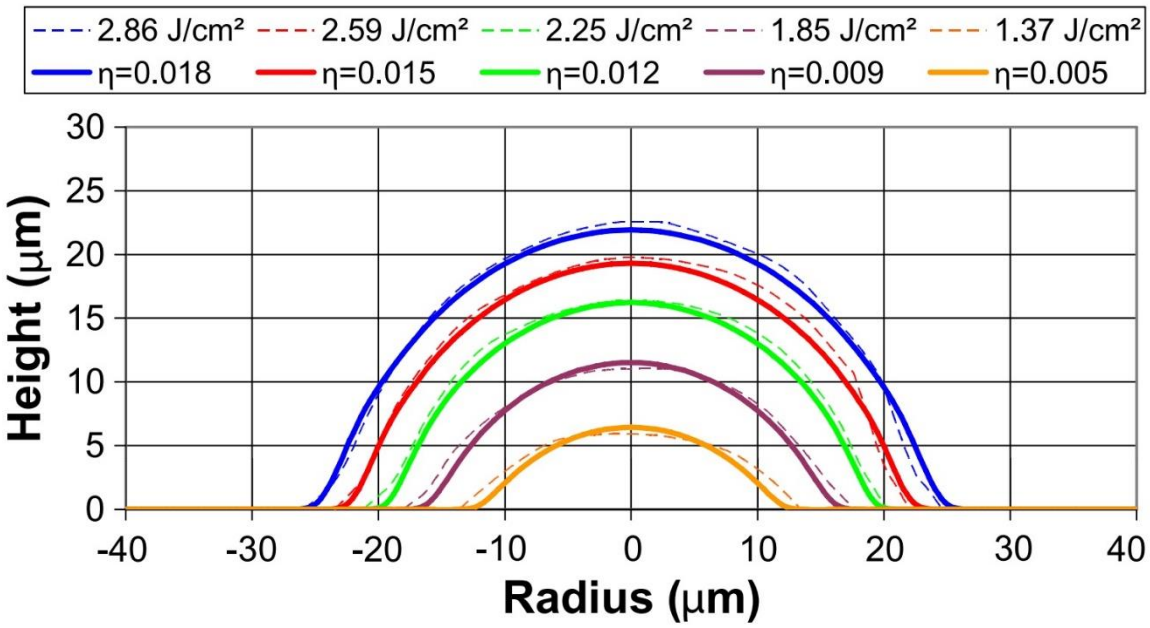

FIGURE 1-11: EXPERIMENTAL AND COMPUTATIONAL RESULTS FOR THE CROSS SECTION OF BLISTERS FORMED BY 40 NS, 355 NM LASER PULSES ON A POLYIMIDE SUBSTRATE. THIS PLOT DEMONSTRATES THE CHANGE IN EMPIRCAL (STRAIN-RATE, η) COMPUTATIONAL RESULTS (BOLD) WITH CORRESPONDING EXPERIMENTAL RESULTS (DASHED) FOR THE CHANGING LASER FLUENCE.[51]

From this it can be seen there is good agreement. Compellingly, a time dynamic model of the blister formation shows an oscillation of the blister after formation which, whilst it cannot be ruled out, was not clearly visible in the experimental results shown in Figure 1-12.

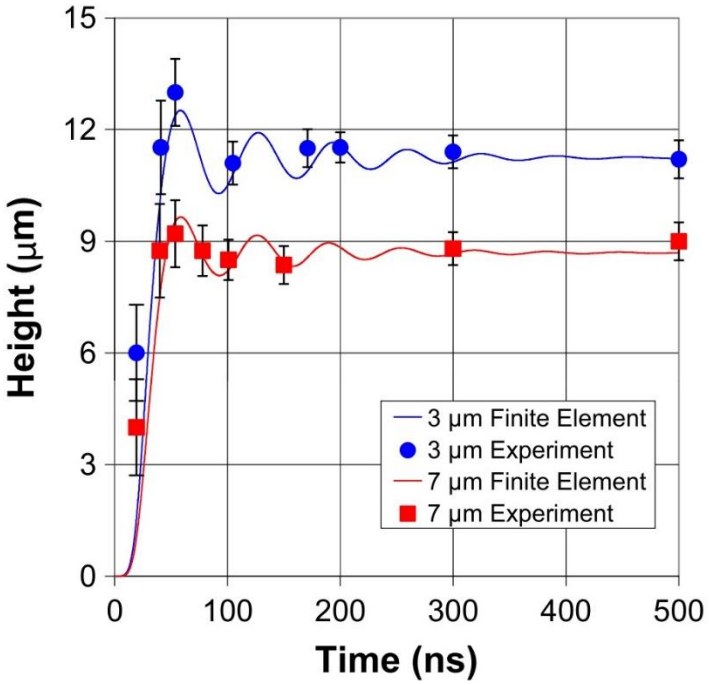

FIGURE 1-12: PLOT COMPARING COMPUTATIONAL RESULTS (FULL LINE) AND EXPERIMENTAL RESULTS (SYMBOLS) FOR BLISTER FORMATION IN POLYIMIDE FILMS, USING 40 NS, 355 NM LASER PULSES, OVER TIME. THUS FORMING A MODEL WHICH SHOWS THE POTENTIAL FOR SURFACE OSCILLATION OF THE FORMED BLISTERS OVER A TIME OF 70 NS PER OSCILATION. [51]

Whilst the Arnold group were unable to effectively provide evidence for this blister oscillation, the Kononenko group have observed oscillations in 1.6 µm-thin titanium films[48]. Time-dependent height measurements for titanium in Figure 1-13 indicate surface annular waves, capable of travelling from the edge to the center in approximately two nanoseconds. This is contrary to Figure 1-12, which shows a period of gradual oscillation over 70 ns. This discrepancy can be attributed to the varying thickness, material, pulse width, laser fluence and profile in the two experiments. The origin of these surface annular waves was not explained and the Arnold group, whose programme predicts a height oscillation, does not relate this to transverse annular waves.

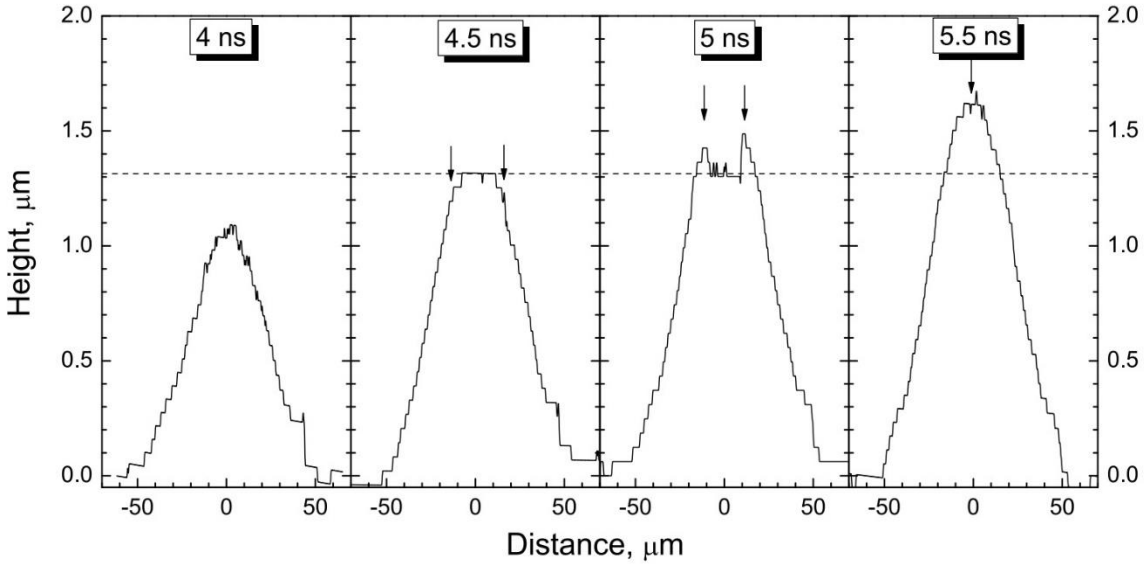

FIGURE 1-13: TRANSVERSE ANNULAR WAVES TRAVELING ALONG A BLISTER. THE ARROWS STARTING AT 4.5 NS INDICATE THE LOCATION OF THE WAVE. THIS DATA WAS GATHERED FROM INTERFERENCE PATTERNS, AT DIFFERENT TIMEFRAMES, FORMED BY AN INTERFEROMETER MEASURING VERTICAL EXPANSION OF THE BLISTER. THESE ANNULAR COULD ALSO BE AN EXPLANATION FOR THE HEIGHT PREDICTED HEIGHT OSCILLATION IN THE POLYIMIDE DESCRIBED IN FIGURE 1-11. HOWEVER, THE TIME FRAME IS AN ORDER OF MAGNITUDE QUICKER FOR THESE EXPERIMENTALLY GATHERED RESULTS ON A TITANIUM FILM IRRADIATED WITH A 0.7 NS 1078 NM LASER PULSE OF FLUENCE 1 JCM^{-2} [48]

1.4.3 Effect of Fluence on Blister

Within either model of blister formation, laser fluence is expected to be a key variable involved in the blister mechanism. The greater the fluence, the more plasma will be created, or the more heat will be transferred. However, there are thresholds which confine the fluence to a region in which blister formation can occur. Figure 1-14 indicates four different regimes relating to the interaction of the laser with a Ti thin film. The regimes are, in general, expanded by increasing the thickness of the film. The regime of lowest fluence is where no delamination of the film from the substrate occurs. It can be seen that this curve reaches a plateau, which is to be expected if the energy of delamination is the main

factor, as this would not change with film thickness. However, there is a slight curve clearly visible at low thickness, which could indicate dependence upon the plasticity/flexibility of the material. Between this solid line and the dashed curve there is another region in which a blister is formed, material can be transferred and a smooth, undamaged blister is created. Above this curve, the blisters often show cracks. In the ablative mechanism, these cracks are caused by the expansion and escape of the pressurised plasma. In the thermal expansion mechanism, they are caused by the contraction of the film. Above this region of blister formation, the laser forms a hole within the thin film.

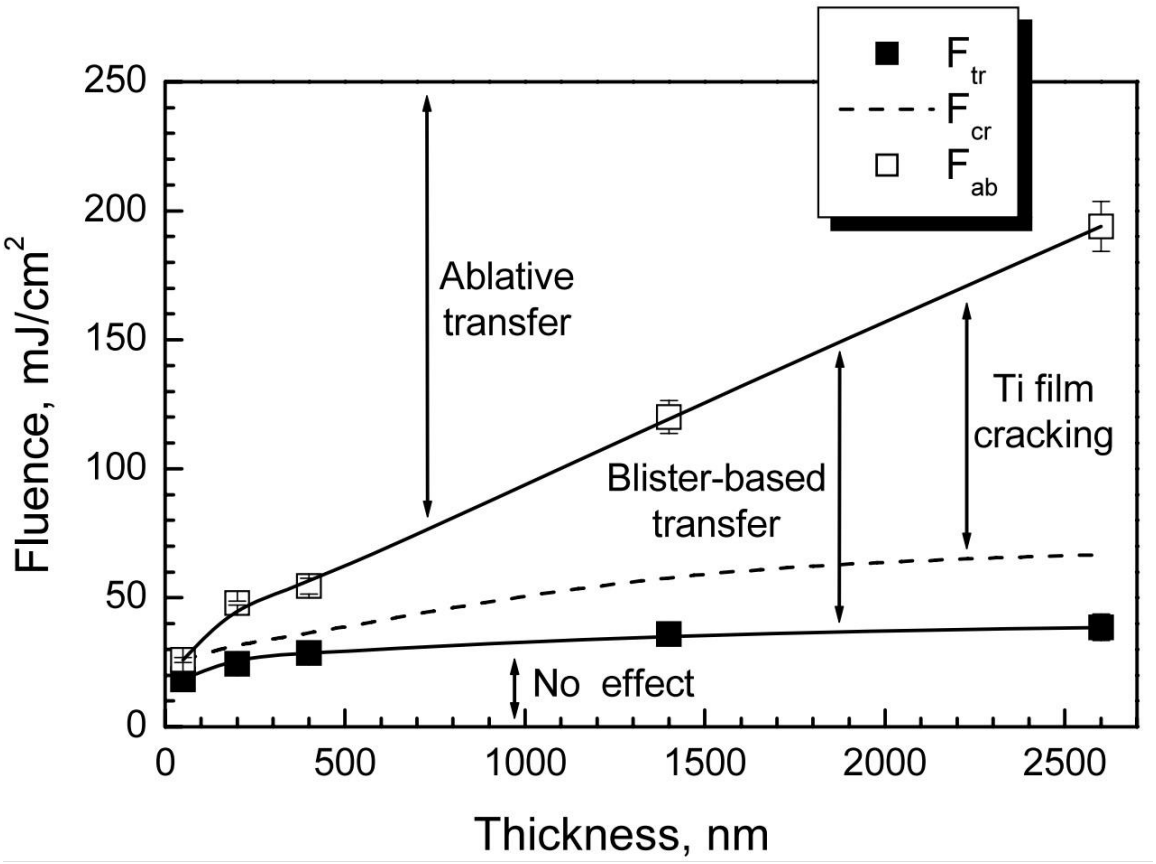

FIGURE 1-14: PLOT DESCRIBING HOW A THIN FILM OF TITANIUM USED IN BB-LIFT IS AFFECTED BY THE LASER INTENSITY DEPENDENT UPON ITS THICKNESS. THE REGION WITHIN THE TWO SOLID LINES SHOWS THE PRESENCE OF BLISTERS WHICH ARE CAPABLE OF EJECTING NANOPARTICLES WITHOUT CONTAMINATION FROM THE FILM ITSELF. THE REGION ABOVE THE DASHED LINE INDICATES WHERE THE FORMED BLISTER IS LIKELY TO HAVE CRACKED DUE TO EITHER THE FORCES OF EXPANSION OR CONTRACTION. THE PULSE WIDTH WAS 50 PS, WITH A WAVELENGTH OF 530 NM. HOWEVER, AT THE

SAMPLE FLUENCE OF 100 MJCM^{-2}, THE MAX SURFACE TEMPERATURE SHOULD BE APPROXIMATELY 2000 K, 1000 K BELOW THE BOILING POINT OF TITANIUM. [41]

Figure 1-15 and Figure 1-16 show how the shape of the blister changes for a polyimide film, Figure 1-15 plots the highest point of the blister, and Figure 1-16 indicates the width of the blister each with respect to the fluence, and for two varying thicknesses of polyimide film and one of smaller beam width. From these figures, it can again be seen there is a fully ablative regime in which the fluence above a certain point will destroy the film. The Arnold group also show that thinner films form larger blisters, likely due to the increased flexibility of the film. This allows for faster emitted particles from thinner films with a velocity from 30-100 ms^{-1}.[50,52,53] However, as the fluence also increases the blister size, and with thicker films one can achieve higher fluences before rupturing, it cannot be said that thin films will always produce faster particles. From the plots, it can be seen that both height and width increase roughly linearly with laser fluence. Also, clear and expected is that the rate of blister-width expansion increases faster and to a greater extent than the blister-height expansion rate.

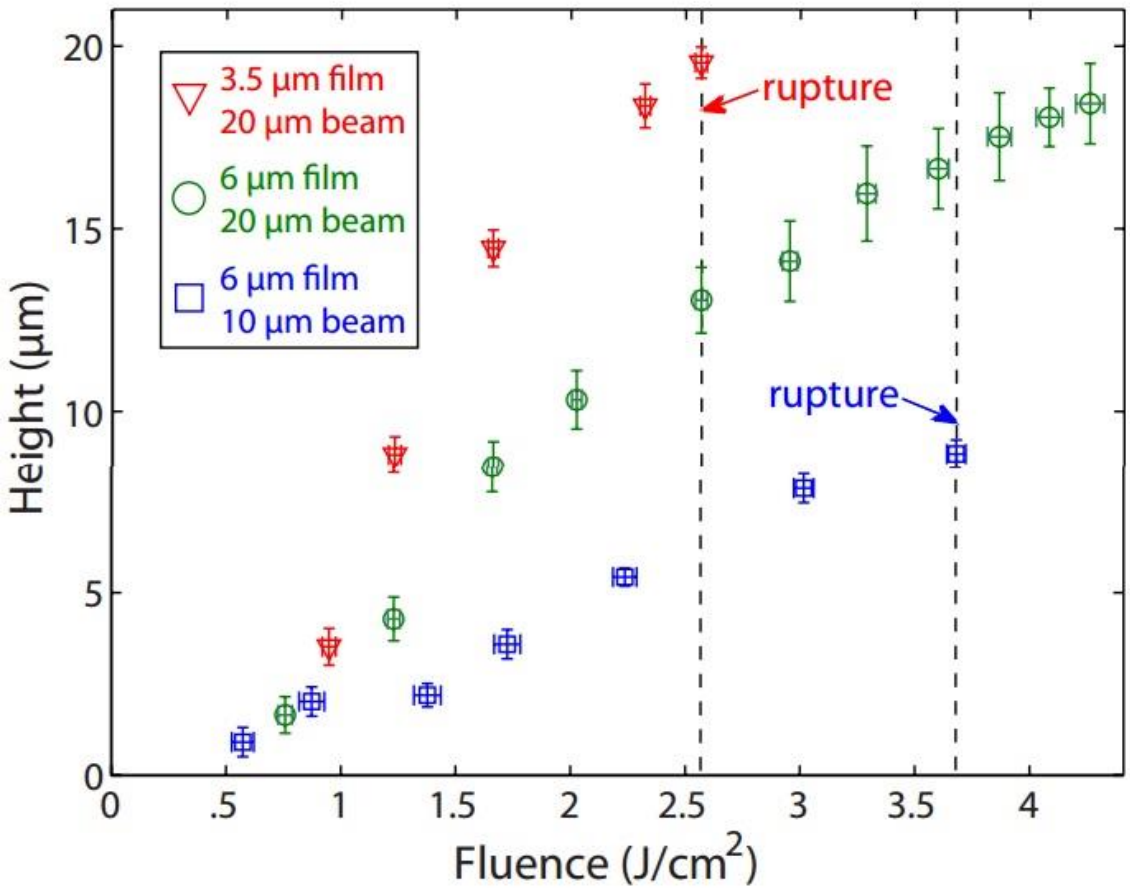

FIGURE 1-15: PLOT ILLUSTRATING HOW THE HEIGHT OF THE BLISTERS FORMED ON A THIN FILM OF POLYIMIDE INCREASES WHEN THE FILM IS THINNER (RED COMPARISON TO GREEN), AND THE BEAM PROFILE IS WIDER (GREEN COMPARISON TO BLUE). EACH OF THESE ARE RECORDED AT DIFFERENT FLUENCES DEMONSTRATING THE INCREASING SHIFT AT HIGHER FLUENCES. THE PULSE DURATION IS 20 NS AND FREQUENCY IS 355 NM. [50]

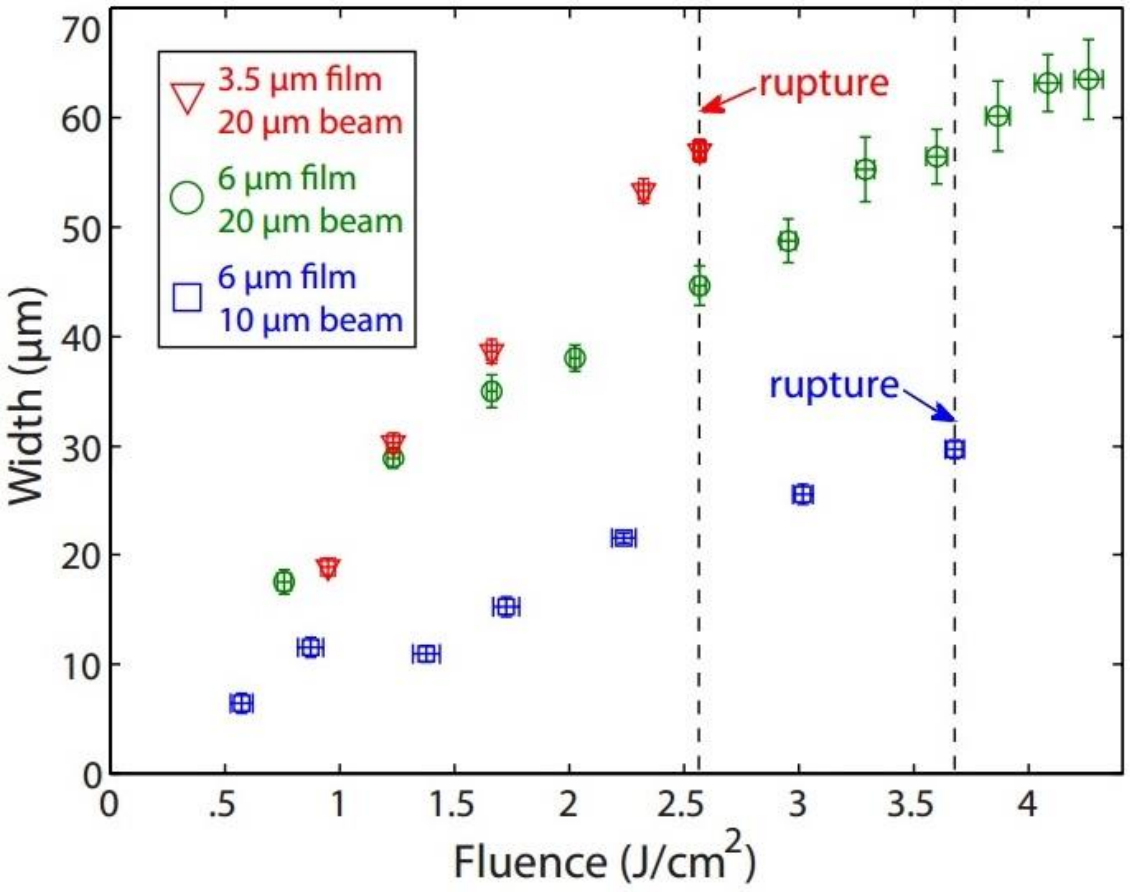

FIGURE 1-16: PLOT ILLUSTRATING HOW THE WIDTH OF BLISTERS INCREASES WHEN THE FILM IS THINNER (RED COMPARISON TO GREEN), AND THE BEAM PROFILE IS WIDER (GREEN COMPARISON TO BLUE)PRODUCED FROM A THIN FILM OF POLYIMIDE IS AFFECTED BY THE LASER FLUENCE AND BEAM WIDTH. EACH OF THESE ARE RECORDED AT DIFFERENT FLUENCES DEMONSTRATING THE INCREASING SHIFT AT HIGHER FLUENCES. THE PULSE DURATION IS 20 NS AND WAVELENGTH IS 355 NM. [50]

1.4.4 Effects of surface layer

In the Arnold group The films are often less than 6 µm thick, the layer of ink to be transferred is often thicker. So, a study by the Arnold group tested whether the transfer of a 10 µm- thick layer of the ink system of N-methyl-2-pyrrolidone (NMP) influenced the blister volume produced from a 6 µm polyimide film. Their results indicate little change in the volume of the formed blister, with or without ink, as shown in Figure 1-17, despite the relatively large mass increase.

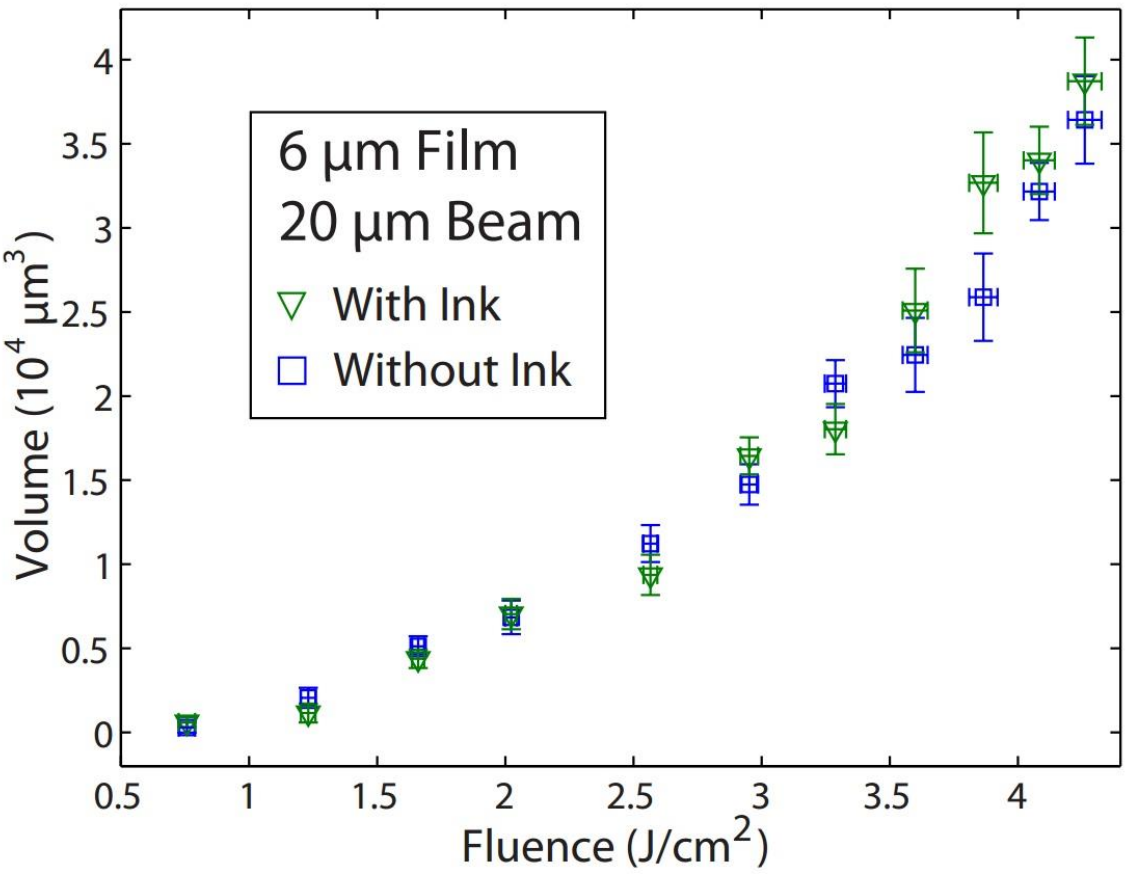

FIGURE 1-17: PLOT SHOWING NEGLIGIBLE INFLUENCE OF INK SURFACE LAYER (GREEN TRIANGLE WITH INK TO BLUE SQUARE WITHOUT) ON THE SIZE OF THE BLISTER FORMED FOR DIFFERENT LASER FLUENCES. THE PULSE DURATION IS 20 NS AND WAVELENGTH IS 355 NM. [50]

1.4.5 Variation in laser profile

No direct study of the laser profile influence on blister formation has been conducted; however, some studies have interchanged Top-hat and Gaussian laser profiles[50]. Beyond showing that both are a viable option for blister production, little more investigation was conducted.

1.4.6 Fluid ejection threshold

The Arnold and Kononenko groups tend to utilise blister sizes of roughly 20 µm in width; however, the Arnold group has also shown that there is a fluid ejection threshold. For blister sizes smaller than 2.5

µm, no ink jets are produced. As the size of the blister roughly corresponds to the width of the microjet, this creates a limit for the resolution of the printing technique. [42]

1.4.7 Beam dispersion

As the Arnold group uses BB LIFT to desorb fluids, and materials suspended in the fluid, the dynamics of the fluid keep the solvent and suspended particles together. Therefore, there is limited beam dispersion from distances of 100 to 800 µm. It's very applicable for printing; however, it limits the ability to study the particles in gas phase. For projection of dry nanoparticles, it was found that the scattering angle is dependent upon the fluence, with the maximum scattering angle being 40°, although no data was shown.[41]

1.4.8 Summary of literature

The BB-LIFT technique is clearly still a novel technique with a great many potential applications and studies yet to be done to fully understand the mechanism, and expand it beyond the currently tested thin film materials. So, whilst the expansion time frame, size and shape of the blisters are partially understood in relation to laser fluence and film thickness, a great deal can still be tested on materials for ejection and the optimisation of the technique. Furthermore, the technique seemingly hasn't been expanded beyond high resolution printing of gels and suspended particles.

2. Experimental Methods

BB-LIFT is based around a pulsed laser interaction at the interface of a transparent substrate and metal film; a metal film must be bonded to a transparent substrate atop which the particles of interest can be coated. This chapter describes the method of formation for these slides, the methods of transfer, and finally analysis of samples before, after or during transfer.

2.1 Substrate Preparation

2.1.1 Substrate cleaning

The initial substrate is a plate of transparent material. Often microscope slides of crown glass 1mm thick cut to 2.5 cm^2 are used. This is effective for visible and IR pulses; however for laser pulses in the UV, or if the substrate needed to endure high temperatures, quartz was used.

The transparent substrate is sonicated in a bath of distilled water and decon for ten minutes to remove large dust particles and oils. This is followed by ten minutes of sonication in methanol to remove further materials and any remaining surfactant. The substrate is then placed within a plasma chamber. The chamber is evacuated to 250± 50 mBar; and the radio frequency (RF) current is increased to 100% power. The pressure is controlled by adjusting an air intake valve which allows in a controlled amount of nitrogen and oxygen (ambient air) thus the majority of the plasma is nitrogen based. The plasma formation is checked for stability and held for more than 30 minutes. This destroys and vaporises any remaining surface impurities. The RF is then decreased and the chamber is vented. It was found that, without plasma cleaning, the metal films were still liable to show macroscopic defects which would increase the complexity of the system and reduce our ability to understand the mechanism. The sample was handled with tweezers from the initial cleaning phase onwards.

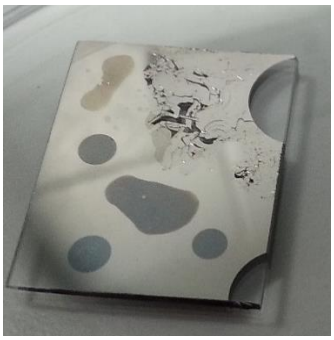

FIGURE 2-1: GLASS SUBSTRATE COATED IN TI VIA ELECTRON BEAM EVAPORATION (EBE) AFTER CLEANING BY SONICATION VIA SONICATION, BUT NO PLASMA CLEANING STEP. THUS, IMPURITIES REMAINING ON THE SURFACE INHIBIT THE FORMATION OF A HOMOGENEOUS METAL FILM.

The sample was then clamped within an Electron Beam Evaporator EBE via screws, which act as masks for small portions of the substrate, blocking the film formation at the screw sites. The EBE was then used to coat the transparent substrate with either, nickel, titanium, or copper. Some nickel, silicon and iron quartz substrates were prepared for the carbon nanotube direct growth studies, described in section 6.

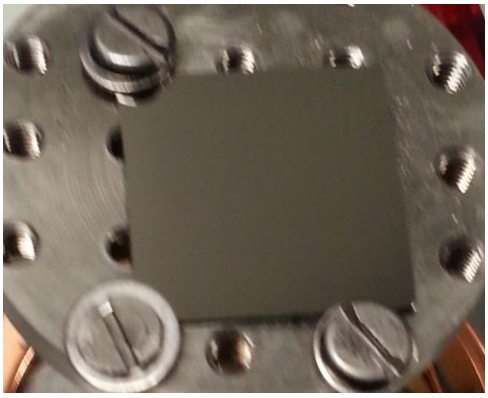

FIGURE 2-2: IMAGE OF TI COATED GLASS SLIDE ON THE SUPPORT WHICH IS PLACED WITHIN THE EBE. BOLTS ARE USED TO CLAMP THE GLASS TO THE SURFACE. THE BOLTS ALSO MASK THE GLASS FROM BEING COATED BY TITANIUM THUS ALLOWING A MEASUREMENT OF THE TITANIUM THICKNESS AT DIFFERENT POINTS ON THE FILM.

2.1.2 Electron beam evaporation

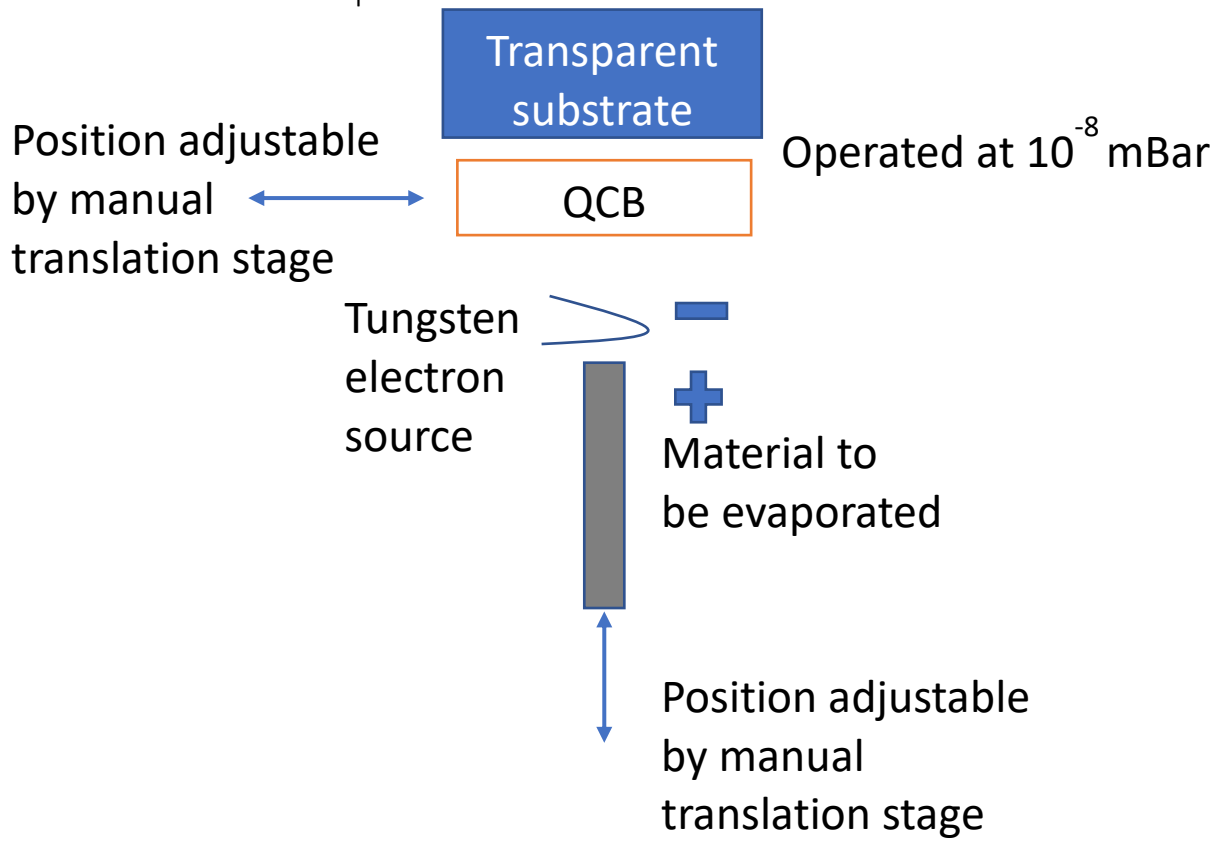

FIGURE 2-3: SCHEMATIC OF ELECTRON BEAM EVAPORATOR (EBE). THE TRANSPARENT SUBSTRATE IS CLAMED IN PLACE AS SHOWN IN FIGURE 2-2. A QCB CAN BE PLACED 150 MM INFRONT OF THE SUBSTRATE THUS BLOCKING DEPOSITION WHILST THE RATE OF DEPOSITION IS OBTAINED. THE ROD OR CRUCIBLE HOLDING THE MATERIAL TO BE EVAPORATED IS HELD ~150 MM BELOW THE QCB AND MUST BE KEPT IN THIS POSITION SO AS TO MAINTAIN A STEADY DEPOSITION. THE RODS WILL SLOWLY EVAPORATE SO USING THE TRANSLATION STAGE THEY MUST BE CONTINUALLY RAISED TO AS TO BE HELD AT THE CONSTANT DISTANCE FROM THE TUNGSTEN ELECTRON SOURCE.

The EBE has 4 slots, allowing different materials to be loaded at the same time, thus enabling evaporation of different substances without venting the chamber first. To evaporate the material, a high potential difference between the crucible containing the material, or the rod of pure material, and the electron source (tungsten filament) must be applied. The potential difference is between 500-1000V depending upon the material. The evaporation conditions for the different materials can be found, by finding the current and voltage at which the QCB detects a signal as it's being coated. A strong current, on the order of 2.5-4 Amps, is passed through the filament material, providing a high source of electrons. This current is also dependent upon the diameter of the tungsten filament, in that the thinner the filament, the lower the current needs to be, due to increased resistance. The potential difference between the filament and material is set and then the current through the filament is. During the

increase, the heat from the filament may cause some degassing of the chamber; and cooling water to the copper heat sink surrounding the filament must be turned on. If a shutter is in place, this must be open and the quartz crystal balance (QCB), which monitors the rate of deposition, is positioned between the surface to be coated and the material to be evaporated. This allows the determination of the appropriate current for the rate of deposition we desire. If the material is in rod form, this rod must be as close to the filament as possible, requiring continual adjustment of the rod position, utilising an externally adjustable translation stage. If the sample is too low within the holder, this cavity acts as a collimator, thereby reducing the spread of the beam and making the deposit more uneven on the substrate. Placing the substrate as close as possible to this filament, and aligning it vertically, reduces the current needed within the filament required to start the evaporation. It was also found that, to improve an even surface coverage, the sample should be placed directly above the evaporating material. Once the desired rate of deposition is achieved and stable, the current between the filament and the evaporating material should be recorded. This current combined with the voltage between the material and source is a measure of the power being applied to the system. This power must be kept constant to maintain the same deposition rate; however, as this power is being applied to a constantly shrinking material, the evaporation rate may have small oscillations. So, the quartz crystal balance must be brought back over the evaporating sample periodically in order to check the deposition rate.

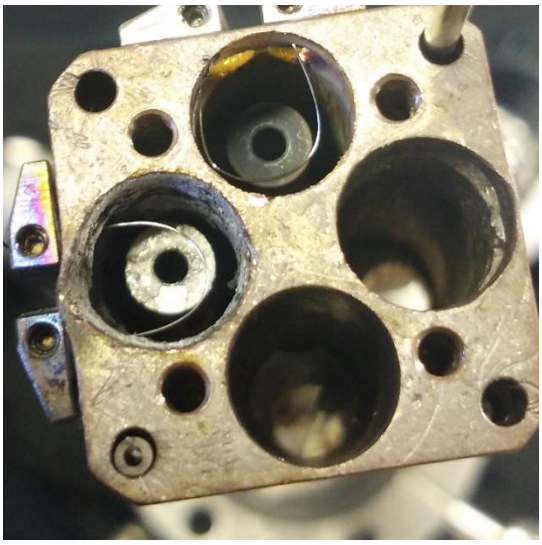

FIGURE 2-4: IMAGE OF HOLDERS FOR RODS AND CRUCIBLES WITHIN THE EBE. THE IMAGE SHOWS THAT THERE ARE MULTIPLE SLOTS TO HOLD SEPARATE MATERIALS. ALSO VISIBLE IS THE SUPPORT FOR THESE MATERIALS AND THE TUNGSTEN ELECTRON SOURCES.

Nickel, titanium, silicon and iron can all be deposited from rods because of their high melting points. In this situation, the rod must be continually raised using an external linear translation stage so as to maintain a consistent proximity to the filament. If the distance alters, the power supplied to the rod will decrease and the deposition rate will alter. Also, the spread of the deposition will become narrower due to the collimating effect mentioned above, resulting in a film thickness that is more difficult to determine.

In the case of copper deposition, the copper must be placed in a molybdenum crucible with a boron nitride liner. The melting point of molybdenum is sufficiently high to withstand the electron bombardment; however, if placed in contact with the copper, it will be wetted and the copper will creep out of the crucible. The copper does not wet the boron nitride ceramic and will therefore have as little contact with the surface as possible, thereby containing the copper within this well. The copper can be sourced from copper wires: however, the source of copper used for this research was spent copper gaskets which were cut into small enough pieces to place within the crucible. Filling the crucible with pieces cut in this manner leaves air pockets within the crucible and doesn't fill it completely. So, the evaporator was evacuated and the crucible heated until an initial yet small rate of deposition was detected upon the QCB. This indicated that the copper had melted. The crucible was then removed and more copper added if necessary so as to fill the crucible as much as possible. Not enough experimentation was done to determine the impact of having a very small amount of copper within the crucible; but, it was best to be avoided as it would unnecessarily create the risk of running out of copper during deposition, thus making an estimate of the deposited copper difficult.

Material	Rate of deposition /nmhour^{-1}	Source material P.D. /V	Filament current /A
Titanium	~60	1000	3.6
Nickel	~20	800	3.6
Copper	~30	800	3.5

2.1.3 Polyimide deposition via Spin-coating

To deposit polyimide the sample is cleaned as above and finished with plasma cleaning. However it is then transferred to a spin coater where 1-2 millilitres of polyimide are placed in the center of the film. The important factor is to ensure there is enough coverage (~1.5 cm diameter of the central droplet) so that when the spin coater is activated, it will start to accelerate at a slow rate, gently spreading the polyimide across the surface, before reaching full rotation speed, where the bulk of the polyimide is removed. The rotation speed controls the thickness of the film of polyimide on the surface. It was found via confocal laser focusing that 2000-4000 RPM formed 4-2 μm thick films after baking the polyimide.

The film was baked at 100°C for 1 hour under a constant flow of nitrogen into the oven. It was then baked for a further 15 minutes at 300°C. The films were measured for thickness in the AFM for the thinner films and the Raman spectrometer for the thicker films (using a confocal laser focusing technique) as the height exceeded the limit of the AFM.

2.2 Particle deposition upon films

To project particles into the gas phase, they must first be coated atop the thin films. The critical parameters are an even dispersal of material as the surface concentration of the particles is likely to affect the gas phase concentration after transfer. This meant that many of the particles had to be soluble to enable them to be dissolved within a solution, or robust enough to be transferred by evaporative heating. As all of the particles used were of high value, the technique of simply rubbing the dry particles on the surface, as used in LITD, was not tested.

Particles utilised for surface coating	Method of manufacture	Provider
SWNTs	high pressure disporoportionation CO_2	Carbon nanotechnologies inc.
MWNTs	chemical vapour deposition	Thomas Swan group
MWNTs grown directly to film		
C_{60}		
PCBM		
Gold coated silicon nanoparticles		

Molybdenum diselenide		

2.2.1 Spin-coating

The model of spin-coater used was the SPS Spin150. Spin-coating is a common technique in which a sample is held in place by a vacuum and spun at up to 4000 RPM. One can adjust the spinning program to have separate stages. The initial stage is acceleration, followed by rotation at a constant speed, leading to a last stage of deceleration. The slower the acceleration, the more gentle the spread. This can result in the majority of the solution gathering at one side of the film and all flowing off one edge. The final rotation speed determines the approximate thickness of the solution drying on the film. The faster the rotation. the thinner the solution layer and the faster the evaporation. A full investigation into this effect was not conducted; however, it was assumed that a faster rotation was appropriate for the desired results. Initially it was found that the solution would form rivulets when spun, and not cover the substrate uniformly. To counter this, the solution was placed to cover the substrate entirely from the onset, giving a uniform coating. To obtain the desired surface concentration once the initial coating was made, more controlled coating with ml portions dropped in the centre of the film was carried out.

This technique was used to deposit; C_{60} and PCBM in toluene, single walled carbon nanotubes (SWCNTs) in N-Methyl-2-pyrrolidone (NMP), Multiwalled carbon nanotubes in dimethylformamide (DMF). These solutions were prepared in concentrations below the critical micelle concentration, so as to avoid agglomeration.

2.2.2 Sandwich coating

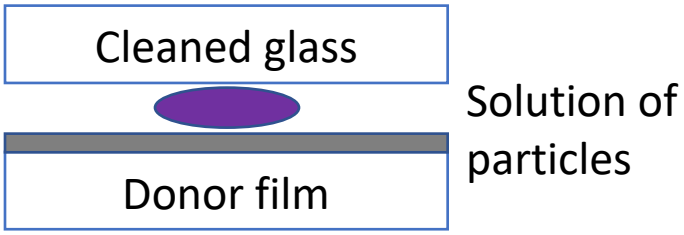

FIGURE 2-5: SCHEMATIC OF SANDWICH COATING TECHNIQUE. THE SOLUTION OF PARTICLES IS PLACES UPNO THE METAL SURFACE OF THE DONOR FILM. THEN A CLEANED GLASS SLIDE IS PLACED ATOP THIS, THUS SPREADING THE SOLUTION ACROSS THE DONOR FILM. THIS IS THEN ALLOWED TO DRY, LEAVING A RELATIVELY HOMOGENEOUS DEPOSIT ON THE SURFACE. THIS IS USEFUL FOR WHEN THE DONOR FILM SURFACE AND SOLUTION ARE EXTREMELY PHOBIC MAKING SPIN COATING NOT POSSIBLE.

Sandwich coating was developed to overcome difficulties depositing the gold coated silicon nanoparticles that were dispersed in an aqueous solution. The surface films were too hydrophobic and the solution rolled off the surface without leaving any nanoparticle deposit. This technique was also used for PCBM, where the fullerenes needed to be kept in a box out of direct light for risk of oligomerisation. The method is to place a droplet of the solution upon the clean film to be coated. A plasma-cleaned glass slide is then used to spread this droplet across the whole surface by laying it directly atop the film. The film can then be left to dry of its own accord, or gently heated to increase the speed of this process. The sandwich coating process results in a macroscopically uniform surface coverage; however, the particles tend to aggregate and form crystals.

2.2.3 Evaporative coating

This technique was only used to coat $C_{60,}$ as it can be effectively evaporated without damage to its structure. The evaporator itself was constructed within our labs and the sample is heated using resistive heating rather than electron impact. The temperature is measured by a thermocouple wrapped around the crucible. Once the appropriate current and voltage combination, which resulted in a top temperature of 450^{o}C, was found, a crucible with C_{60} was loaded into the holder and heated to this temperature (after being held at 100-150^{o}C overnight so as to degas the chamber and crucible). This temperature was held for 10-15 minutes allowing a deposit of ~100nm of C_{60} to be formed upon a film's surface, as shown below.

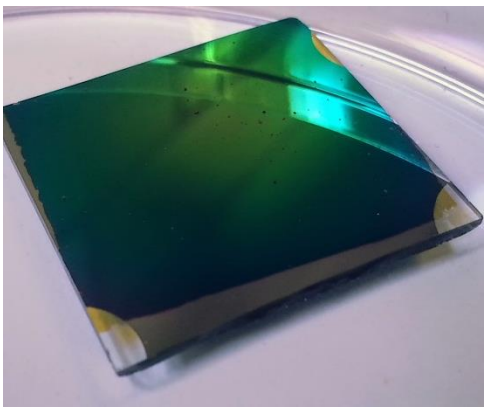

FIGURE 2-6: TITANIUM FILM ON GLASS SUBSTRATE COATED WITH 130NM OF EVAPORATED C_{60}. THE CLEANED GLASS SLIDE WAS CLAMPED INTO A HOLDER ABOVE AN HEATING FILAMENT BASED CRUCIBLE EVAPORATOR. THE TEMPERATURE WAS HELD AT 500˚C FOR 10 MINUTES BEFORE THE CRUCIBLE OF C_{60} WAS ALLOWED TO COOL AGAIN.

2.2.4 Direct growth of nanostructure on the film.

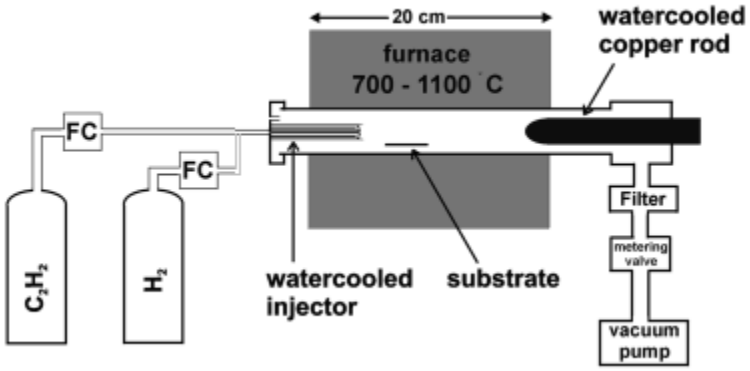

FIGURE 2-7: CHEMICAL VAPOR DEPOSITION CHAMBER (CVD). THE SUBSTRATE IS HELD WITHIN A QUARTZ TUBE. THE CHOSEN GASES ARE FLOWED THROUGH AT ATMOSPHERIC PRESSURE, WHILST THE ENTIRE SYSTEM IS HEATED TO A CONTROLLED TEMPERATURE WITH THE SAMPLE DIRECTLY BELOW THE THERMOCOUPLE. THE SYSTEM IS DEFINED IN MORE DETAIL BY NERUSHEV ET AL.[54]

MWCNTs were grown directly on a multilayer film, designed for BB-LIFT, without involving solutions or intermediary deposition steps which can damage or dirty the material. So, a film of ~10nm Ti, ~200nm Ni, ~5nm Si, and ~1nm iron nanotube growth catalyst upon a 1mm thick quartz substrate, was created with the EBE and the thicknesses checked via AFM. The Ti acts as a bonding agent between the Ni and quartz substrate. Without the bonding effects of the Ti, the nickel will detach from the quartz easily. A thick layer of Ti was also ineffective, as the Ti appeared to react and form silicides, becoming translucent to visible light. The silicon layer separates the iron from the Ni film, which forms a blister. If they were in contact, the iron layer would easily wet the nickel film and not form nanodroplets which are required for iron as a nanotube catalysis. This all needed to be adhered to a quartz film instead of glass due to quartz's ability to withstand the temperatures involved in chemical vapour deposition of MWCNTs, which would melt unfused silica.

Once the films were formed, they were placed in the center of the CVD growth chamber. The chamber was heated to 700°C at atmospheric pressure, under a gas flow of 600sccm Ar (99.996% purity) and 100sccm H_2 (technical quality). C_2H_2 (technical quality) was the carbon source and flowed into the furnace for 15 minutes at 8sccm. The Ar and H_2 were allowed to flow for 10 minutes at 700°C to ensure removal of all C_2H_2 hindering amorphous carbon growth as the chamber cooled. The samples were then removed and studied via Raman spectroscopy and electron microscopy to confirm CNT growth.

2.3 Translation stage

As the BB-LIFT technique removes the majority or all of the particles upon the surface once blistered and, this blistered area is now potentially damaged or altered in such a way that further laser pulses may not only cause a blister, the substrate needs to be moved, so a fresh area may be irradiated by the laser pulse. Therefore, an automated translation stage to adjust the position of the BB-LIFT film after each laser pulse was needed in order to make data collection and study on a larger scale, possible.

The samples are slotted into a holder, which is on the end of a long hollow pipe with a viewport on one end to allow the laser pulse to enter. The viewport end of the pipe is connected to a translation stage with bellows allowing movement of the viewport and sample whilst maintaining a stationary position for the rest of the setup. The 3D translation stage enables control over the distance from the laser focal point as well as allowing adjustment of the sample in the plane normal to the laser direction. The plane normal to the laser direction was automated using two recycled step motors and the addition of two external A4988 drivers, allowing the system to be moved in the vertical and horizontal plane, according to a program written and encoded onto an Arduino Uno microcontroller. (details in Appendix)

Control of the system's movement must be synced to a delay generator which is capable of producing a square wave pulse of 1ms in duration and 5V amplitude, which is strong enough to signal to the Arduino microcontroller that the laser has been fired. It was found that the signal direct from the laser sync (fs or ns) was not of the appropriate voltage or duration to trigger the microcontroller. This trigger is detected at an analogue input port on the Arduino (adjustable within the code). The Arduino has output ports which lead directly to hardware drivers. This accepts information from the Arduino controller about which direction to travel and when to step. The driver then translates it to logic gates allowing power from an external 12V 5A power supply to pass to the step motors. The motors themselves require ~1A each to provide enough power to turn consistently, and not be too high, so as not to overheat the drivers.

An example translation after a laser pulse would be as follows:

A pulse from the Arduino triggers the direction input (DIR), and this remains unchanged unless another pulse swaps it. The laser pulse triggers the delay generator, sending a pulse to the Arduino. This takes

the pre-programmed information of 100 steps, at 400 steps per second, and sends 100 pulses to the driver over 0.04s. Each step received by the driver applies a current through at least two of the output ports 1A, 1B, 2A, or 2B, thus shifting the position of the rotor within the motor by inducing an electrical field within it, pulling it round to its new location. If the driver has MS1, MS2 or MS3 enabled, it will enable more of the output ports 1A-2B to be triggered at the same time, enabling a finer degree of control over the motor. Once the step pulses from the Arduino have stopped, the driver will maintain the current through the last output ports which were enabled, holding the motor in that location until new steps have been triggered.

A stepper motor was specifically chosen over a DC motor as stepper motors provide very accurate positioning, whilst a DC motor, having only two brushes inside, takes a different amount of time to reach the chosen speed, based upon the starting position of the commuter in relation to the brushes. The internal configuration of a stepper motor is shown in Figure 2-8. The current and power are sent to the electromagnetic coils. This magnetically causes the multi-toothed rotor to be attracted to this coil. The tooth closest to the activated coil is the one most drawn to this position and then held there until another step pulse changes which coil is active, thereby attracting the closest tooth to the activated coil. Multiple coils can be activated at once, thereby pulling the teeth in multiple directions and holding them slightly off-center to the coil, allowing finer control of the motor.

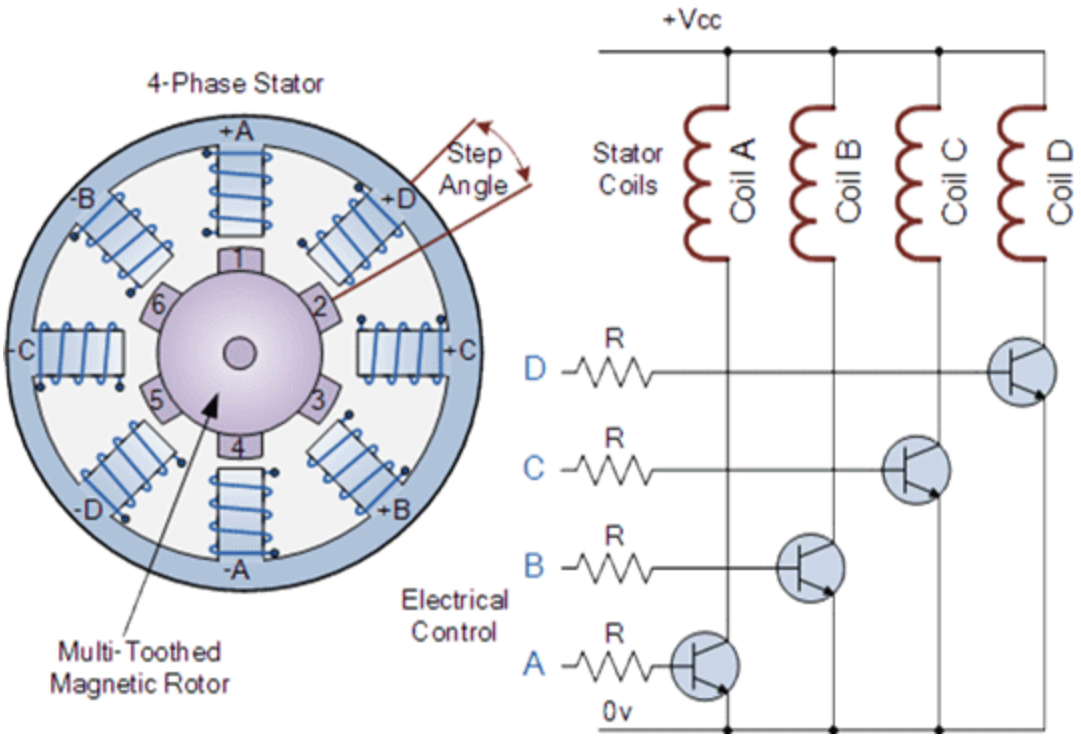

FIGURE 2-8: INTERNAL CONFIGURATION OF STEPPER MOTOR. EACH COIL CAN BE ACTIVATED INDIVIDUAL TO MAGNETICALLY ATTRACT THE MULTITOOTHED MAGNETIC ROTOR TO A NEW POSITION, OR AT THE SAME TIME MOVING INTO AN INTERMITTENT POSITION. THESE MUST BE SWITCH ON SEQUENTIALLY TO ALLOW A CONTINUAL ROTATION OF DEFINED STEPS.

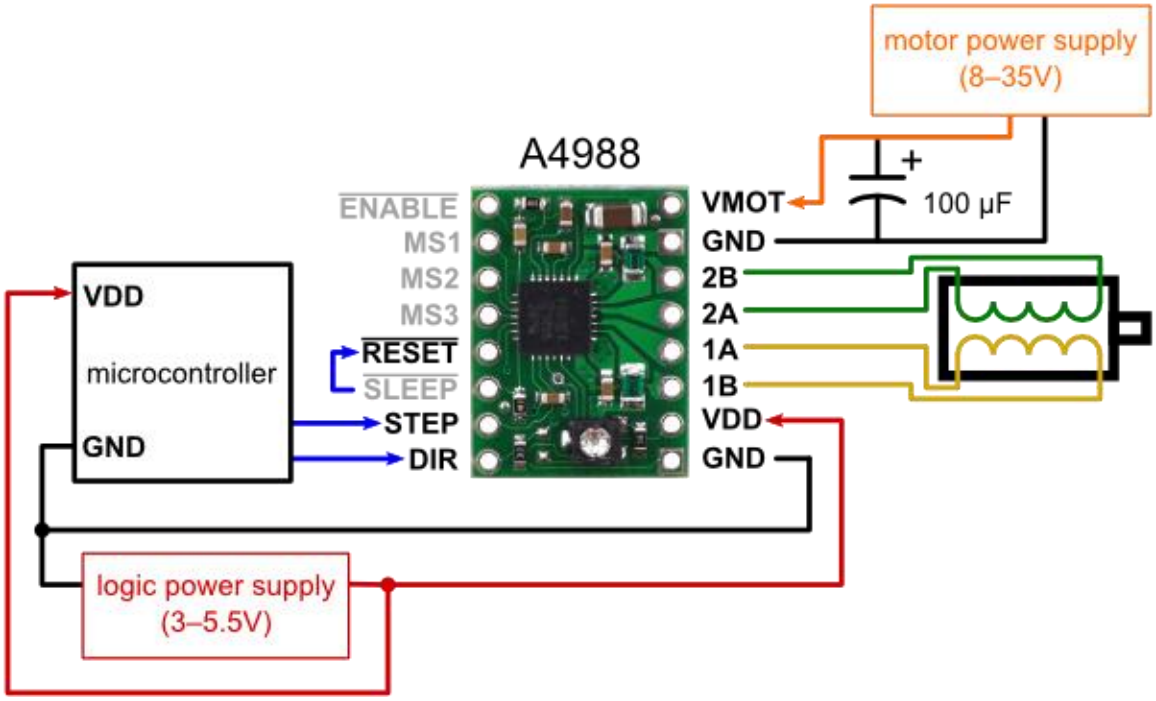

FIGURE 2-9: CIRCUIT DIAGRAM OF MICROCONTROLLER, STEPPER MOTOR DRIVER AND STEPPER MOTOR. THIS ALLOWS A PULSED INPUT FROM THE LASER TO THE MICROCONTROLLER SIGNALLING THAT THE LASER HAS FIRED. THE MICROCONTROLLER THEN SEND A SERIES OF PULSES TO THE DRIVER FOR EACH STEP, WHICH ALLOWS CURRENT THROUGH DIFFERENT COILS FOR EACH STEP. THUS ENABLING A CONTROLLED NUMBER OF STEPS TO BE TAKEN AND MOVING THE SAMPLE BY A DEFINED AMOUNT.

The program written onto the Arduino microcontroller (which controls the path of the motors) can be found within the appendix.

As the program is custom written, control and alteration of the pathway of translation must be written directly into the code.

The code is completely commented and allows easy adjustment of the velocity of the translation for each step, and the distance moved for each step, as well as the total distance to travel before changing row and travelling back in the opposite direction. Within this same step the total number of rows can also be adjusted.

In order to adjust each of these parameters there are four variables which must be altered; The rotation speed in x, and y, the distance for each step, (which is measured in steps, where 400 steps is one full

rotation of the motor, resulting in one mm of x or y movement). As movement is allowed in four directions (positive x and y, and negative x and y), where positive and negative indicate the direction, one must maintain the same signs; this also follows for the velocity control.
The total distance moved along each line and the number of rows is also measured in steps for the motor to take, and must be a multiple of the number of steps taken, otherwise the program will not recognise the position at which it must alter direction or stop.

2.4 Laser setup

Nanosecond (5-7 ns) and femtosecond (120fs) laser pulses were used to create the blisters which desorb the particles. The nanosecond laser was a Coherent Minilite II with 532nm output, with adjustable rep-rate from 1-15 Hz, and pulse energy of up to 25 J. The laser, for Mass spectrometry studies, which was used to ionise the particles, could be kept in sync with the LIFT laser and directed at the particle beam, ablating and/or ionising the particles. The pathways are shown in Figure 2-10. Two flip mounts are used to allow the two beam paths to be swapped without a time-consuming alignment procedure. This allows the fs and ns beam to be either the blister formation beam or ionisation beam. The power meter is shown in position in Figure 2-10 just after the final aperture with a diameter of 4 mm. The power was measured at the full repetition rate of the laser (15 Hz for ns, 1000 Hz for the fs beam). From this power and knowledge of the lens distance from the target film, the fluence can be determined. The lens focal position is in front of the film so the beam impacts over an area ~100-300μm in diameter.

To synchronise the two beams in order to photo-ionise the desorbed particles, the ns laser was enslaved to outgoing pulses of the fs laser. This was true in both modes of operation.

The power of the lasers after parsing the viewports into the chamber were also measured with the chamber opened so as to discover how much power was lost, due to the viewport windows via reflectance and absorbance.

A razor method was used to find the beam diameter and its characteristics in this optical setup, which has a non-negligible distance ~3 m and ~7 m from their source for the ns and fs lasers, respectively. The razor method involves raising a sharp edge through the beam, via a translation stage, and measuring the power at each point.

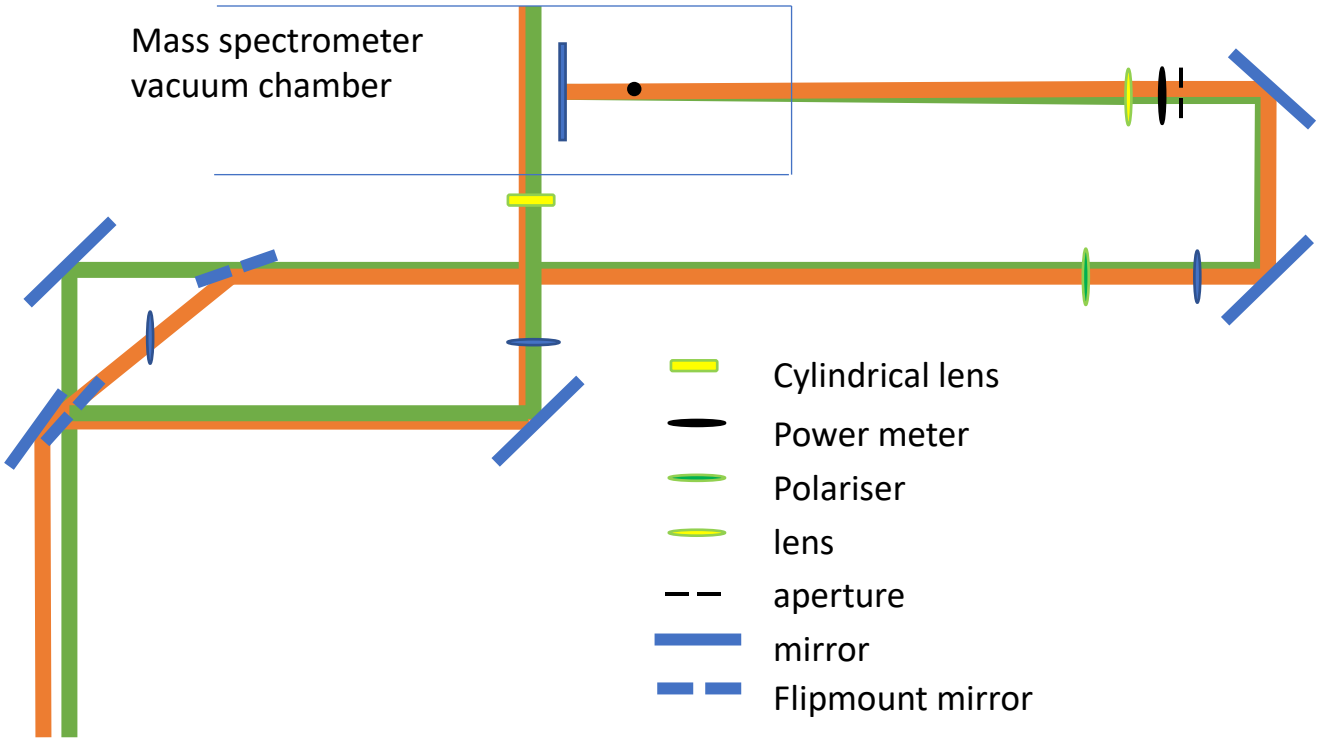

FIGURE 2-10: LASER PATHWAY, THE FS (ORANGE) AND NS (GREEN) LASER CAN BE SENT DOWN TWO POSSIBLE PATHWAYS ALLOWING THEM TO EITHER CAUSE BLISTERS OR IONISE THE EJECTED PARTICLES. THE LASERS ARE SYNCED TOGETHER VIA SIGNAL DELAY GENERATORS, ALLOWING ADJUSTABLE TIME DELAYS TO WITHIN 2 NS. THE LASERS PASS THROUGH A 4 MM APERTURE BEFORE PASSING THROUGH THE FOCUSING LENS TO CAUSE BLISTERS. IN ORDER TO IONISE THE PARTICLES THEY PASS THROUGH A CYLINDRICAL LENS FORMING A THIN VERTICAL BLADE TO IONISE THE PARTICLES. DETAILS OF SPECTROMETER GIVEN IN SECTION 2.5.5

2.5.1 Raman Spectroscopy

Raman spectroscopy is a common technique in chemical system identification. The Raman spectrometer is confocal and utilises either a 514, 488 or 718nm laser. The chosen laser is focused on the area of interest and excites electrons to imaginary energy states. As shown in Figure 2-11 the molecule's electron positions are either the ground state or in a partially excited state (vibrational state 1). The electrons receive energy from a photon which excites them to a virtual energy state, before they decay back to their; original position (Rayleigh), a higher energy state (stokes), or a lower energy state (Anti-stokes). The relaxation from a virtual state releases a photon with a defined energy specific to the polarizability of the sample thus allowing identification.

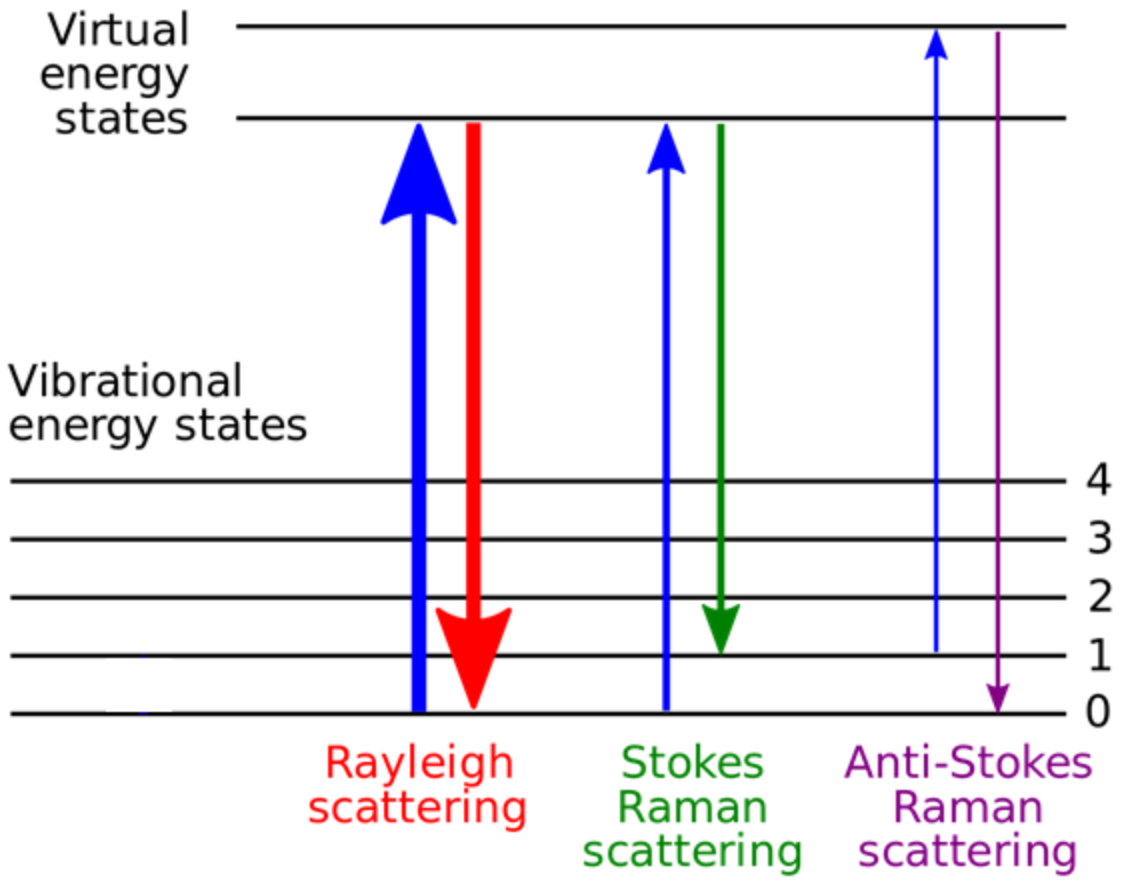

FIGURE 2-11: ELECTRON MOVEMENT IN RAMAN SPECTROSCOPY DEFINING; RAYLEIGH SCATTERING WHERE THE EMITTED PHOTON IS OF THE SAME FREQUENCY, STOKES EMITS A PHOTON OF LOWER ENERGY, ANTI-STOKES EMITS A HIGHER ENERGY PHOTON.

The intensity of the Raman scattering is proportional to the frequency of the incident light source, ν, the original intensity, I_0, the number of molecules the light is interacting with, N, and the polarizability of the sample, $f(\alpha^2)$.

$$I \propto \nu I_0 N f(\alpha^2) \qquad \text{EQUATION 2-1}$$

The polarizability is intrinsic to the sample and when exposed to an oscillating electric field, $\boldsymbol{E}$, such as that from the incident light source it will induce a dipole $\boldsymbol{\mu}$. As polarizability is spatially variable it must be written as shown in Equation 2-2 and Equation 2-3.

$$\boldsymbol{\mu} = \boldsymbol{\alpha E} \qquad \text{EQUATION 2-2}$$

Equivalently,

$$\begin{bmatrix}\mu_x\\ \mu_y\\ \mu_z\end{bmatrix} = \begin{bmatrix}\alpha_{xx} & \alpha_{xy} & \alpha_{xz}\\ \alpha_{yx} & \alpha_{yy} & \alpha_{yz}\\ \alpha_{zx} & \alpha_{zy} & \alpha_{zz}\end{bmatrix}\begin{bmatrix}E_x\\ E_y\\ E_z\end{bmatrix}$$ **EQUATION 2-3**

As the applied electric field is oscillating due it being a light source, It will cause the dipole moment to oscillate in relation to the frequency of oscillation ω, and time, t. The molecules own polarizability will also oscillate due the molecules vibrations Q_0^m and with a frequency of ω_m. Thus the induced dipole moment can be defined as shown in Equation 2-4.

$$\mu = \alpha_0 E_0 \cos(\omega t) + \frac{1}{2}\frac{\delta\alpha}{\delta Q_m} Q_0^m t E_0\{\cos(\omega - \omega_m) + \cos(\omega + \omega_m)\}$$ Equation 2-4

When a photon is emitted from the molecule it will have a frequency of defined be the oscillation of the induced dipole moment. Thus, defined by terms one, two and three of the Equation 2-4 where the frequency of emitted light will be either, ω (Rayleigh), $\omega - \omega_m$ (stokes), or $\omega + \omega_m$ (anti-stokes).

Experimentally we can increase the signal by, increasing the intensity of incident light, raise the laser power, expose the sample for a longer period of time, or similarly increase the number of accumulations. The choice of lens will also affect the Raman signal for similar reasons. An increased magnification increases the intensity, whilst also potentially increasing the proportion of interacting molecules N. The numerical aperture of the lens, which is a function of the lights seen through the aperture and the focal distance will alter the detection of emitted light from the scattering process. Where, the higher the numerical aperture the exponentially stronger the signal.

2.5.1.1 Raman spectra analysis of CNT

Carbon nanotubes have multiple vibrational modes. The most understandable is the radial breathing mode RBM in relation to a SWCNT. This is the energy required to cause the CNT to expand and contract along its radius. The amount of energy required shifts with a dependence upon the diameter of the nanotube.

The G mode comes from the planar stretching of the graphitic structure of the CNT, whilst the D-mode is due to the breathing modes of the 6 atoms rings; however, this is only allowed if there is a defect within the structure. As the G mode is allowed within a perfect graphitic structure, whilst the D mode is only allowed in the case of defects, the ratio of the G to D modes can be used as a gauge for the quality of the CNTs.

There are two important overtone modes as well, the G' and RBM+G. These and other overtones are caused by the combination of two vibrational modes, and are available due to the temperature of the CNT. Thus, they become stronger when the molecules have a higher internal energy and the molecule becomes an-harmonic. These are therefore not commonly used to identify the CNTs. The G' mode is the second derivative of the D mode and only observed in SWCNTs rather than MWCNTs.

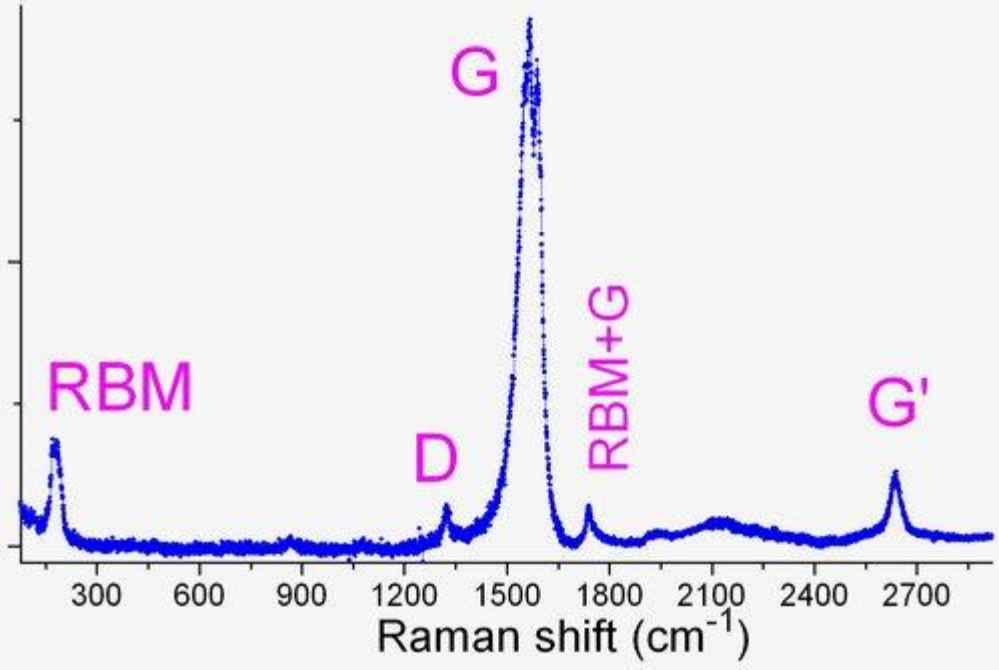

FIGURE 2-12: RAMAN SPECTRUM OF PRISTINE CARBON NANOTUBES. THE MAIN PEAKS USED WITHIN THIS THESIS WERE THE G AND D PEAKS, ALLOWING ANALYSIS OF THE QUALITY OF THE NANOTUBES.

2.5.1.2 Raman spectra analysis of Fullerene

C_{60} has seven allowed Raman transitions due to its I_h point group. The two main identifying Raman peaks are the A_g (2) and H_g (7) peaks, which are due to the translational vibration state within the pentagonal and hexagonal structure.

Within C_{60}, these peaks are at 1469 (A_g) and 1426cm^{-1} H_g. As can be seen these peaks shift based upon the internal and external structure effecting the shape of the graphitic structure. This is more noticeable in the Raman spectra of PCBM discussed below.

As shown in Figure 2-13 the fullerenes do degrade over time; and, it was found that this was a non-negligible effect in relation to our analysis as well.

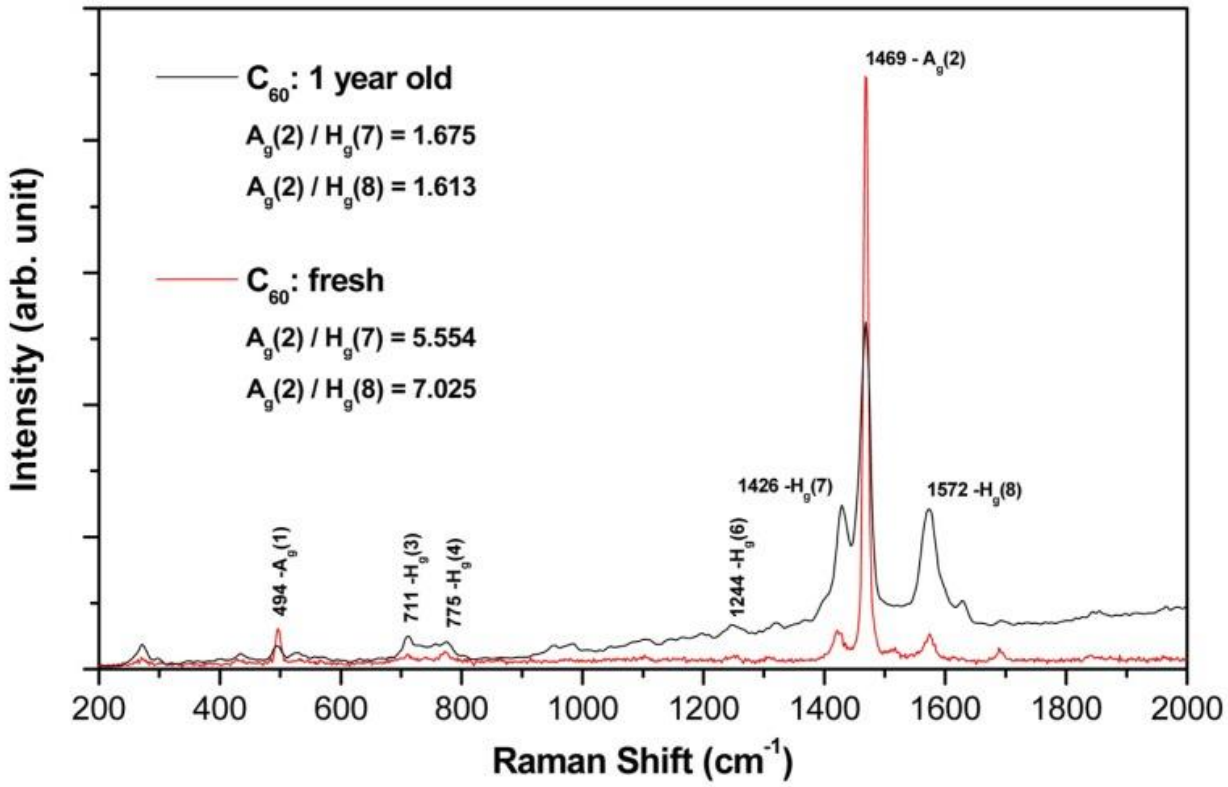

FIGURE 2-13: RAMAN SPECTRA OF SIGNIFICANT FULLERENE PEAKS WHERE THE RATIO OF THE $A_G(2)$ AND $H_G(7)$,$H_F(8)$ WERE USED TO SHOW THE QUALITY OF THE FULLERENES. IT CAN BE SEEN THAT OVER TIME THE RATIO DIMINISHES AND THUS THE FULLERENES START TO DECOMPOSE. [55]

2.5.1.3 Raman spectra analysis of PCBM

PCBM is a C_{60} fullerene with an exohedrally bonded phenyl butric acid methyl ester. Thus it has a similar Raman spectra to $C_{60;}$ however, the main peak is shifted to 1464 cm^{-1}. However, PCBM also oligomerises to a different structural formation when exposed to visible light, with a stronger effect towards the UV than Infrared. This effect will shift the Raman Spectra further as can be seen in Figure 2-15

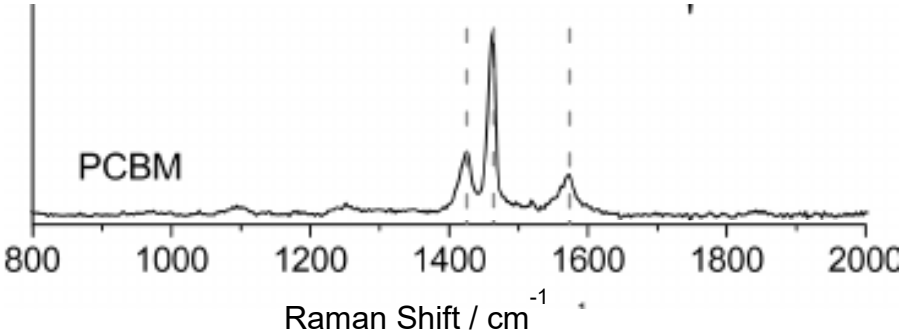

FIGURE 2-14: RAMAN SPECTRUM OF PCBM, SHOWS A SIMILAR PEAK STRUCTURE OF C_{60} YET IS IT SHIFTED SLIGHTLY DUE TO THE EXOHEDRAL COMPONENT ATTACHED TO THE C_{60}. LIKE C_{60} THE QUALITY THE PCBM CAN BE FOUND BY COMPARING THE RATION OF THE PEAK AT 1464 AND 1426 CM^{-1}.

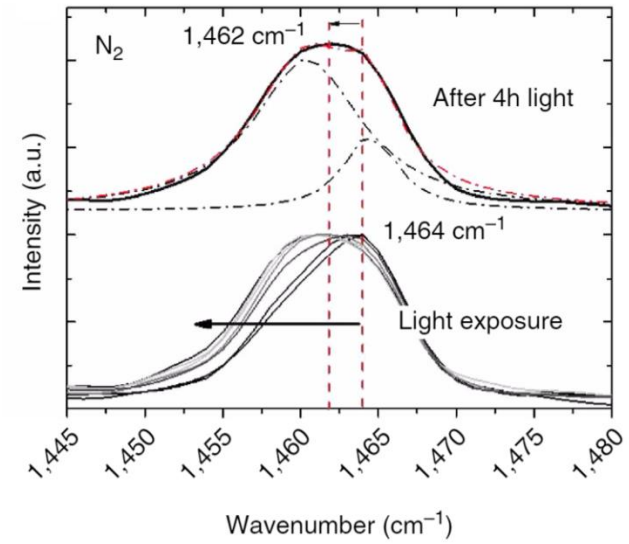

FIGURE 2-15: RAMAN SPECTRA SHOWING THE SHIFTING CENTRAL PEAK OF PCBM WHEN EXPOSED TO LIGHT. THIS SHIFT IS DUE TO THE OLIGOMERISATION OF PCBM BY A PHOTOCHEMICAL REACTION.[19]

2.5.1.4 Raman Spectra analysis of $MoSe_2$

Molybdenum di-selenide, as grown by Kituara et al.[56], also has a specific peak within the Raman spectrum, which allows identification to ensure that our sample is indeed $MoSe_2$ before and after transit, as well as the number of layers.

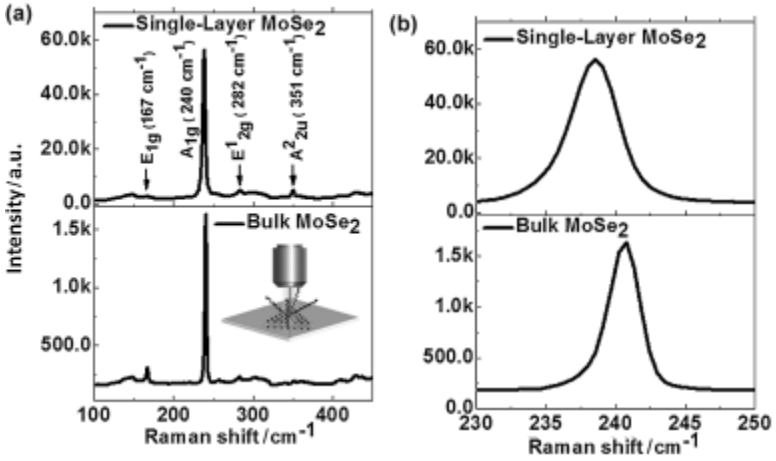

FIGURE 2-16: RAMAN SPECTRA OF $MoSe_2$ DEMONSTRATING THE VARIATION IN PEAK POSITION FROM BULK TO SINGLE LAYERED $MoSe_2$. IT CAN BE SEEN THAT SINGLE LAYERED $MoSe_2$ HAS A RAMAN SHIFT PEAK AT 242 FOR BULK $MoSe_2$AND 238 FOR SINGLE LAYERED $MoSe_2$ THUS ALLOWING THEM TO BE DISTINGUISHED VIA RAMAN SPECTROSCOPY. [57]

2.5.2 Atomic Force Microscopy

Atomic Force Microscopy (AFM) is a technique which uses a vibrating tip with a tip curvature of ~10 nm in diameter. The cantilever, shown in Figure 2-17 oscillates up and down allowing surface height measurements without continued contact with the surface, when in tapping mode. In contact mode the tip maintains a constant force along the surface which can allow nanomanipulation of the objects. So, the tip behaves like a Braille reader; the interaction of the tip with the forces on the surface control the vertical position of the tip. A continuous laser is directed at the reflective back surface of the cantilever, which hits a calibrated position on a detector. The tip's vertical position adjusts the angle of the cantilever, thereby altering the reflection angle and shifting the position at which the laser impacts the sensor. Thus measuring the topography of the surface. We utilise this technique to measure the thickness of evaporatively coated films. We can also use this technique to measure the surface coverage of the coatings applied via either spin coating or the sandwich technique.

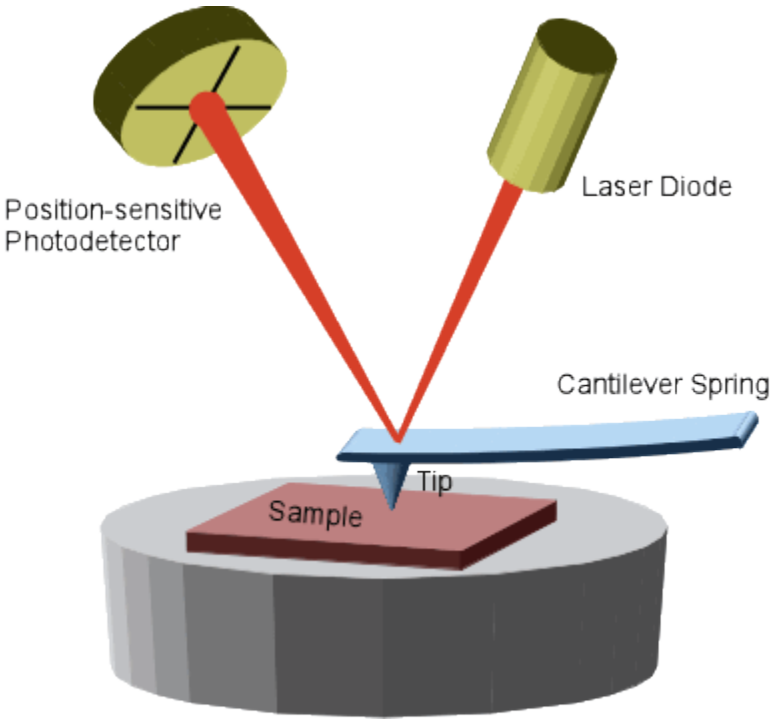

FIGURE 2-17: SCHEMATIC OF AFM. THE TIP WILL BE AT A HIGHER POSITION WHEN THE SAMPLE HEIGHT IS HIGHER, THUS THE ANGLE OF DEFLECTION WILL DIFFER AND THE LASER WILL HIT A DIFFERENT POSITION ON THE POSITION-SENSITIVE PHOTODETECTOR. THIS ALLOWS THE HEIGHT OF SAMPLES TO BE MEASURED TO SUB-NANOMETER RESOLUTION.

2.5.2.1 Film thickness measurements

The metal film formed in the EBE will have been clamped to the coating surface using bolts with a flattened head. This head acts as a mask which protects the glass slide from the forming metal surface, creating a small step, as shown in Figure 2-18 The AFM can measure the height of this step by placing it in tapping mode and aligning the step and the AFM tip, which is raster scanning, so the tip passes backwards and forwards, perpendicular to the step. With the AFM tip movement aligned perpendicular to the step a more accurate and easily analysed scan can be collected. Once the image is scanned, one must apply the flatten function to eliminate small impurities such as dust, and the plane fit function upon the glass (flattest) side of the image. This tells the program this surface is horizontal and adjusts the image to accommodate. These steps are necessary as the AFM nanoscope software will have adjusted the image to account for vibrations and slanted surfaces. Once the image is flattened and a clear vertical step is visible, the step height measurement function can be used. This measures the shift in height over the step as an average over the entire image. If the step is not parallel to the vertical edges of the scanned zone, this step will appear more like a slope. The plane fit function area can also be adjusted so as to assure that both the top surface and the glass surfaces are completely horizontal and not at an angle. If the flatten function was not used appropriately, it would maintain image artefacts which will cause some of the image to be distorted, also reducing the effectiveness of the step function

measurement.

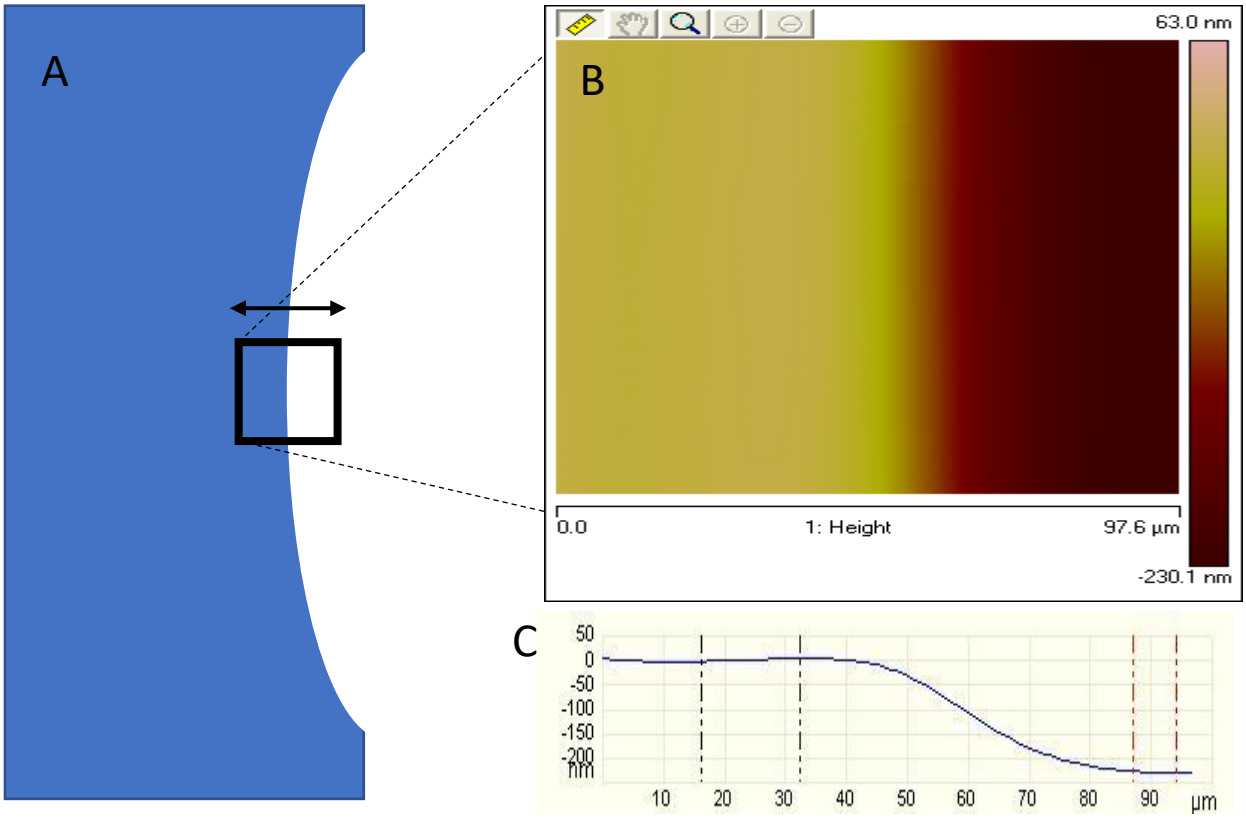

FIGURE 2-18: (A) EDGE OF TITANIUM FILM AND GLASS SUBSTRATE WHERE THE TITANIUM DEPOSITION WAS BLOCKED BY A SCREW HEAD AS DESCRIBED IN FIGURE 2-2. (B) AFM SCAN OF TITANIUM GLASS EDGE WITH A PICTORAL REPRESENTATION OF LOCATION AND DIRECTION OF AFM TIP MOVEMENT. (C) STEP HEIGHT MEASUREMENT OVER ENTIRE AFM SCAN SHOWING THE CHANGE IN HEIGHT OVER THE STEP. THUS USING AN AFM SCAN AT THE EDGE OF THE TITANIUM DEPOSIT WHERE THE BOLT HEAD BLOCKED THE METAL DEPOSITION ONTO THE GLASS, THE THICKNESS OF THE METAL DEPOSIT CAN BE DETERMINED.

2.5.2.2 Surface coverage measurements

When coating a film using spin coating or the sandwich technique, it's difficult to know the amount of material needed to provide full surface coverage. However, the AFM can scan the topography of this surface at the nanoscale. This allows us to find the surface roughness indicating an average particle surface coverage. We can also use this to measure whether the particles have been effectively removed from the surface and to what extent. This can be accomplished within the nanoscope editing software, allowing cross-sections and area roughness measurements.

2.5.2.3 Blank metal film analysis

Analysis of the changes of the metal film due to the laser irradiation, without any particles upon the surface,is also beneficial for understanding the BB-LIFT mechanisms. The AFM can highlight slight changes in the topography of the system; however, it is also capable of measuring changes in the phase

shift of the oscillating tip. If the tip is approaching an attractive surface, it will be pulled towards it; and, as it pulls away, as part of its oscillation, this retraction will be slowed by the attractiveness of the surface. This is inverted for a repulsive surface, and can help indicate surface changes to an extent.

2.5.2.4 Force Distance measurement

The AFM can apply a variable amount of force to the surface through the tip when in contact mode. This enables the function of force distance measurements. As the tip approaches the surface, the force remains unchanged. However, once in contact with the surface the tip will only move a distance with respect to the force exerted back on the tip from the sample. Thus, a measurement of the distance moved in relation to the force applied can be found. This was used for measuring the responsive force of blisters caused by ns BB LIFT and fs BB LIFT.

2.5.3 Scanning Electron Microscopy

Scanning Electron Microscopy (SEM) uses the scatter of an electron beam to determine the shape and, loosely, the material characteristics of particles on a conductive surface. However, as an electron will have a wavelength of less than 0.01nm, according to the de Broglie equation, the theoretical resolution is orders of magnitude lower. However, experimental challenges present themselves and the main resolution defining feature is the electron beam width; so, most scanning electron microscopes have a resolution on the order of 10nm. The particles that are being analysed must be conductive; and, it must be on a conductive surface otherwise charge can build up upon the particles, causing a disrupted image and also damaging the particles. Using this technique, we can get very fine resolution of some of the particles, such as the carbon nanotubes or auroshells, allowing us to analyse whether they had incurred any damage during the transfer from one film to another.

2.5.4 Optical evaluation

It's important not to overlook the use of a microscope allowing direct images of the surfaces and particles on the micron scale. The Raman microscope can be conveniently used to find the height, to the nearest half micron, by focusing the laser upon the surface, then shifting it slightly to the feature/step we wish to check the height of, and then readjusting to refocus the laser by shifting the translation stage up or down. The difference in the stage position gives us the vertical shift in topography. This is shown in Figure 2-19 where, once the laser has been moved, it now forms a wider unfocused spot upon the surface; and, adjusting the height of the translation stage (which can be done to an accuracy of 0.2 microns) will refocus the beam.

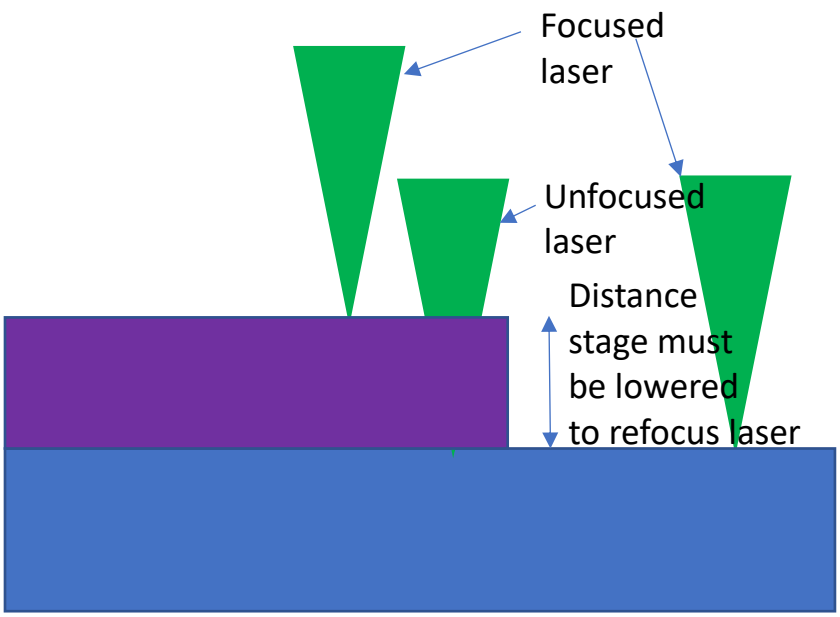

FIGURE 2-19: OPTICAL FOCAL ANALYSIS OF HEIGHT VARIATION. IF THE CONFOCAL LASER IS MOVED OVER A STEP THE LASER WILL BECOME UNFOCUSED. AFTER REFOCUSING THE LASER BY ADJUSTING THE POSITION OF THE SAMPLE IN THE Z DIRECTION VIA STEPPER MOTORS WITHIN THE RAMAN SPECTROMETER THE DIFFERENCE BETWEEN THE Z POSITIONS CAN BE USED TO DETERMINE THE HEIGHT OF THE STEP TO WITHIN 500 NM.

Within optical evaluation we can analyse the spread of the particles, which is often slightly larger than the diameter of the original blister. This is done by using the radial analysis tool within the open source software Image, which creates a radial plot based upon the intensity of the spots within a specific location on the film.

In some cases, such as for molecules, it is very difficult to find the position of the ejected particles upon a receiver plate. To overcome this issue a glass receiver plate is used, where light can then be shone through the plate from edge. This forces the light to totally internally reflect off the front and back surface of the glass film, unless it finds an object which has a more amenable index of refraction than air. This technique was developed and used for finding the landing position of the fullerenes.

Using either this technique or normal optical imagery, we can find the spread of gold coated silicon nanoparticles, fullerenes or carbon nanotubes.

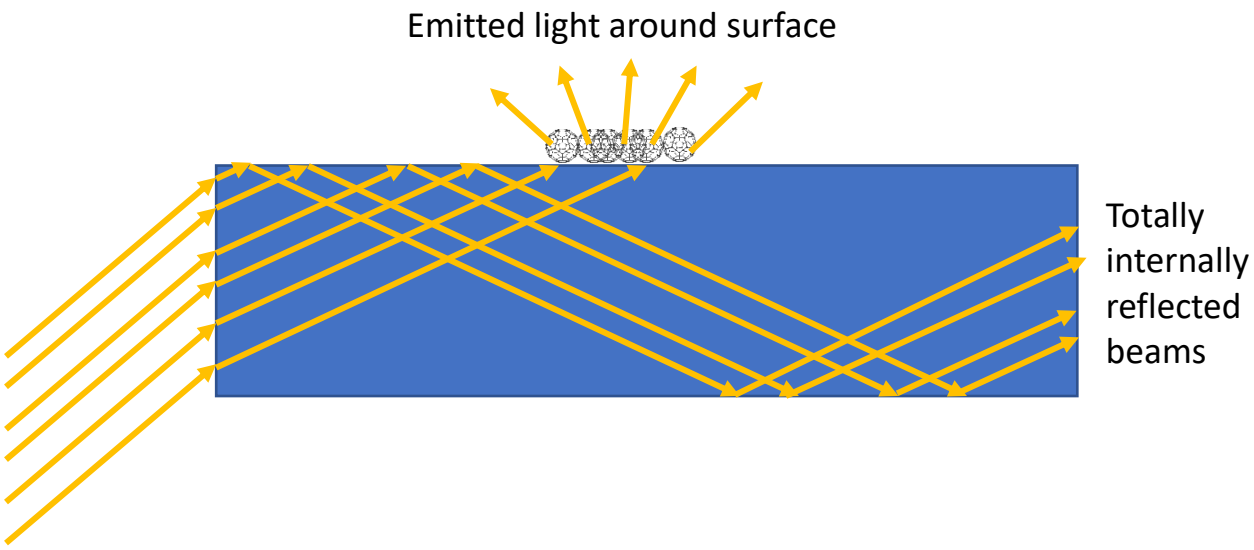

FIGURE 2-20: INCOMING LIGHT FROM THE SIDE OF THE FILM IS TOTALLY INTERNALLY REFLECTED UNLESS IT ENCOUNTERS PARTICLES UPON THE SURFACE. THE PARTICLES ON THE SURFACE HAVE A MORE AMENABLE CHANGE IN INDEX OF REFRACTION THAN THE GLASS AIR INTERFACE. THUS THEY ALLOW THE LIGHT TO ESCAPE FROM THE GLASS AT THESE LOCATIONS. THIS ALLOWS NANOSCALE MOLECULES SUCH AS FULLERENE TO BE VISUALISED ON THE SURFACE WHEN IN VERY SMALL QUANTITIES.

2.5.5 Mass Spectroscopy

Mass spectroscopy was used to analyse the particles desorbed by the BB-LIFT technique. It allowed us to analyse what the particles were, as well as their velocity distribution, due to the ability to adjust the delay time of the ionising laser pulse.

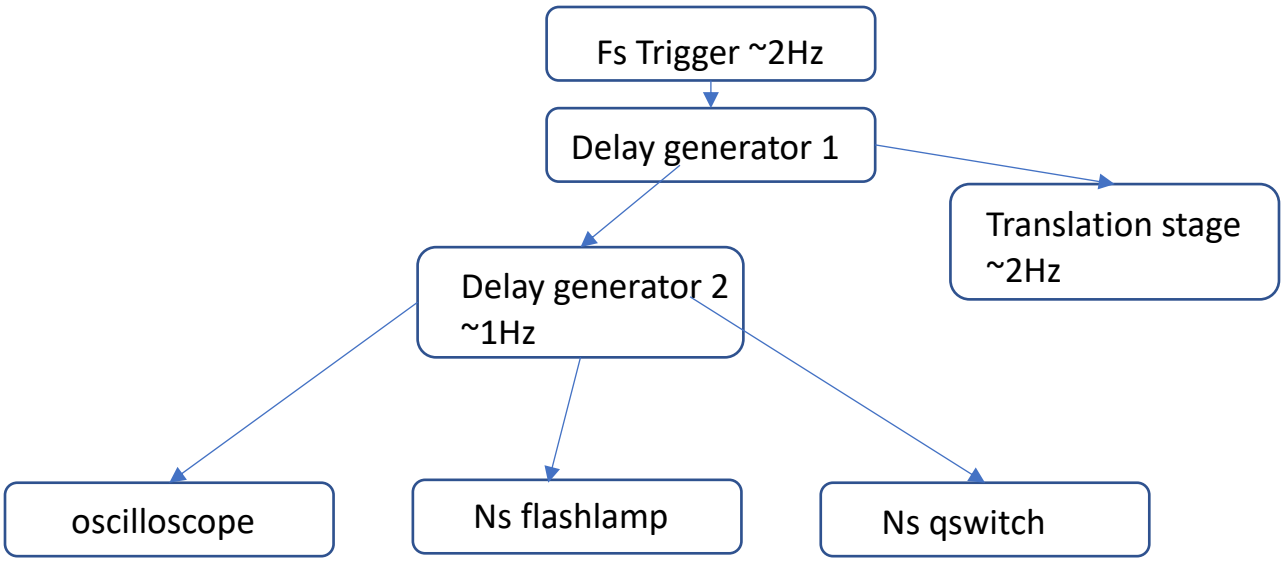

FIGURE 2-21: FLOW DIAGRAM SHOWING SYNCHRONISATION PATHWAY FOR USE OF MASS SPECTROMETRY SYSTEM WHEN THE FS LASER IS CAUSING THE BLISTERS. THE FS LASER MUST HAVE IT'S REPRATE REDUCED FROM 1 KHZ TO ~2 KHZ, AS THE NS LASER CAN ONLY FIRE WITH A REPRATE ~10 HZ AND THE TRANSLATION STAGE MUST ALSO BE GIVEN TIME TO MOVE. THE FS LASER TRIGGERS THE FIRST DELAY GENERATOR WHICH AMPLIFIES AND SHAPES THIS SIGNAL TO A SQUAREWAVE 1MS IN LENGTH WHICH CAN TRIGGER THE ARDUINO MICROCONTROLLER FOR THE TRANSLATION STAGE. IT ALSO TRIGGERS THE SECOND DELAY GENERATOR WHICH HALVES THE REPRATE TO 1 HZ THAT CONTROLS THE OSCILLOSCOPE AND NS FLASHLAMP AND QSWITCH ALL AT DIFFERENT DELAYS BUT STILL OPERATING AT A REPRATE OF 1HZ.

The mass spectroscopy system, Figure 2-22, uses a laser to ionise particles within an extraction field. The ionisation laser passes through a cylindrical lens, which creates a vertical blade; therefore, we were more likely to ionise the particles without having an extremely finely tuned alignment. The length of the extraction field is adjustable, as is the position at which the particles are ionised. The mass spectrometer itself is a time of flight mass spectrometer. The particles first pass through an extraction field which has a from positively charged plate to grounded mesh on the order of <2 cm. They then enter an area of free field until they approach the microchannel plates (MCP). There are two MCPs with a strong electric field of 4.3kV between the two of them and the back MCP is approximately 100 V above ground level. This signal is detected on the oscilloscope which averages over a series of blisters, before storing this data in a labview program. The entire system is pumped down to ~10^{-7} mBar via a turbo pump and fore pump system. This was altered from a diffusion pump, because the diffusion pump releases large amounts of oil into the chamber, giving a very noisy background. The spectra were recorded as an

average number of 5-10 blisters pulses and ionisations upon the oscilloscope, after which they were transferred to a labview program and stored.

A gas inlet tube was also added, allowing the gentle addition of either nitrogen or argon for venting and calibration; and, there is easy potential to allow other gases to be added to the chamber.

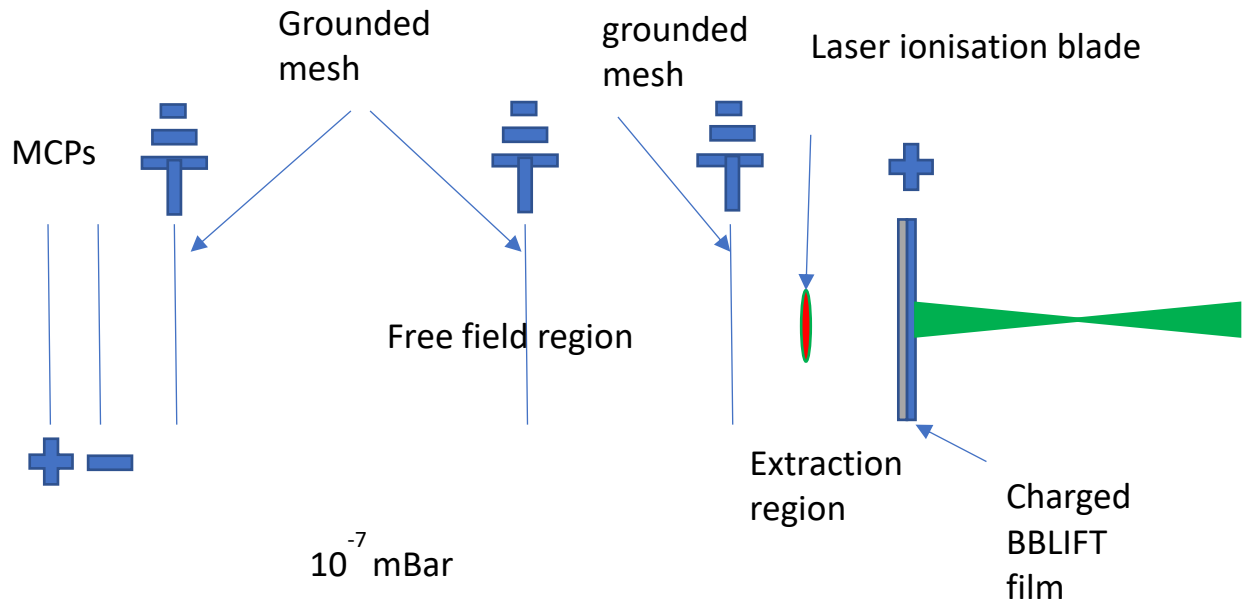

FIGURE 2-22: INSIDE MASS SPECTROSCOPY SETUP. THE PARTICLES ARE EJECTED BY A LASER PULSE ON THE POSITIVELY CHARGED BBLIFT FILM. THE EJECTED PARTICLES TRAVEL A KNOWN AND ADJUSTABLE DISTANCE BEFORE BEING POSITIVELY IONISED BY A DELAYED IONISATION BLADE. THE POSITIVELY CHARGED IONS ARE ACCELERATED TOWARDS THE GROUNDED MESH FILM BEFORE TRAVELING ACROSS A FREE FIELD TO THE CHARGED MCPS WHICH DETECT THEIR ARRIVAL SENDING A PULSE TO THE OSCILLOSCOPE. THUS FORMING A MASS SPECTRUM FOR EACH OF THE DIFFERENTLY MASSED PARTICLES.

3. Blister formation mechanisms on thin films.

Laser-Induced Forward-Transfer (LIFT) was the initial basis for Blister-Based LIFT. LIFT employs a very similar starting basis; yet, the film itself is the transferred material, unlike BB-LIFT which transfers the material atop the metal/polymer film. The development of this work was undertaken based upon the initial work by Kononenko et al[41]. Their initial work was done using 50 ps pulse blister expansion. In contrast, our work was accomplished at two different pulse durations of 120 fs and 5-7 ns. This larger pulse duration range allowed us to study the mechanism on a broader scale. An investigation into the effects due to varying laser pulse duration was warranted due to the strong variation in effects upon materials due to the pulse duration.[58] The results presented in this chapter were published and are presented within the appendix.

3.1 Effects of pulse duration on matter

The pulse duration has a strong effect on the impacted material, due to the electron and lattice interactions. Within a material system, the electrons have the highest velocity and operate on the atto/femtosecond timescale, whilst nuclei can be approximated at being stationary in relation, as they operate on a picosecond timescale. The photons are absorbed by the electrons. The electrons then transfer this energy to the nuclei on the picosecond timescale. While heat transfer on the nanometer scale via nucleic vibrations, operates on the nanosecond timescale. So, a pulse on the femtosecond timescale will impart all of its energy to the electrons through multiphoton excitation, which means they will absorb all of this energy without the chance to transfer it to the lattice, and thus reduce their energy level. Conversely, if the incoming pulse is on the nanosecond timescale, the electrons transfer the energy to the lattice in a far shorter timeframe than the laser pulse length. Therefore, nanosecond laser pulses can be viewed as imparting their energy to the lattice inducing a steady build-up of lattice vibrational energy.

The penetration depth of the laser (L) is also dependent upon the fluence, wavelength and duration of the laser pulse. Where

$$L = \alpha^{-1}\ln(I_a\tau_L) \qquad \textbf{EQUATION 3-1}$$

α is the material absorption coefficient, τ_L is the pulse duration and I_a is the laser intensity.[59] Thus femtosecond laser pulses have a dramatically reduced penetration depth in relation to nanosecond laser pulses.

3.1.1 Effect of pulse duration upon blister formation

There are two mechanisms we propose in relation to nanosecond and femtosecond laser pulses, from experiments that are still to be described. The nanosecond pulses heat the film throughout, causing an expansion proportional to the materials coefficient of thermal expansion. Due to the constraints upon the film in all directions, but normal to the substrate, the film expands in this direction. Femtosecond laser pulses ablate the film at the interface, changing the phase of the film to one which occupies a much higher volume. This gas expansion stretches the film with regard to the Young's modulus of the material itself.

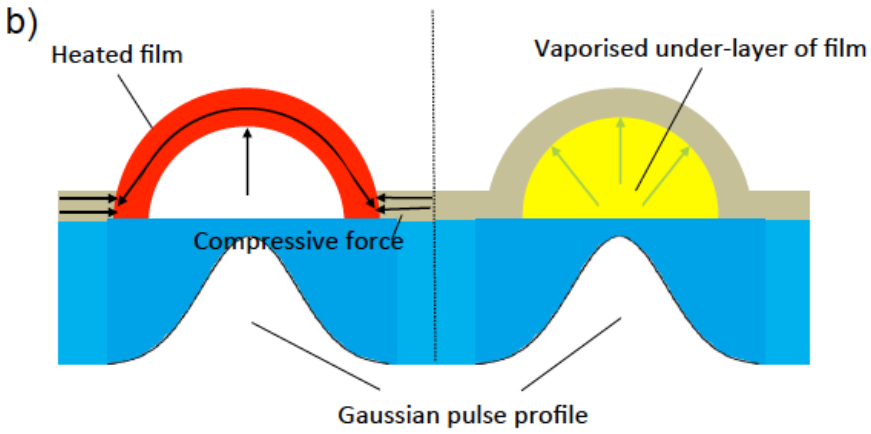

Figure 3-1. Cartoon of blister expansion mechanisms. (a) ns incident pulse. *The film expands due to heating of the film; and, this expansion projects the film and particles in the direction normal to the substrate. (b) fs incident pulse. Ablation of the film at the substrate interface creates a trapped plasma/gas which expands, thus stretching the film to form the blister. Not to scale, dimensions in the vertical direction are greatly exaggerated for illustration purposes.*

3.2. Experimental Details

Films of titanium, with thickness ranging from 300-400nm ,were deposited upon crown glass microscope slides. Titanium has a thermal expansion coefficient of 9 x 10^{-6} K^{-1}, a thermal conductivity of ca. 20Wm^{-}

$^{1}K^{-1}$and a high melting point of 1941K[60], combined with a high tensile strength at high temperature.[60] Titanium's strong adhesion to the glass substrate, rate of deposition and high melting point make it an effective donor film. The blisters were formed upon the films in a vacuum chamber with a base pressure of 3 x 10^{-7}mbar. The parameters of the laser systems were the second harmonic output of a Nd:YAG laser with 7ns pulse duration at 532nm (1/e beam diameter of 370±30µm at the metal film position, fluence range 220-370mJcm^{-2}) and the fundamental output from a Ti:Sapphire laser at 800nm with 120fs pulse duration, (1/e beam diameter of 300±30µm, fluence range 180-210mJcm^{-2}), where the required fluence to induce BB-LIFT is expected to depend on film thickness, as shown previously by Kononenko et al. for 50ps duration 532nm pulses.[41] The reflection coefficients R from the films were 0.39 and 0.42 for 532nm and 800nm respectively. The femtosecond and nanosecond lasers had shot-to-shot fluctuations of 5% and 15% respectively, giving errors in the stated fluence of 20-25%. The substrates were studied via optical microscopy and AFM.

3.3 Results and Discussion

3.3.0.1 Blister Morphology

Figure 3-2 shows blisters formed via back irradiation from nanosecond and femtosecond laser pulses on clean films. The nanosecond blisters appear flat after the irradiation. This is in line with the heating model of blister formation, as the film will recontract after the heat has dissipated to the rest of the system. The blister itself was also within the regime for cracking on the surface, as described by Kononenko et al.[41]; and the AFM shows these cracks protrude out of the flat surface. This indicates that the cracks may have been formed due to high compressive pressure similar to mountain ranges. If these cracks were formed by a tear in the film, and the escape of an expanded gas the expectation would be of a folded back film.

The fs induced blister shows a locally expanded surface area which has remained after the film has cooled. This indicates that the surface has been irreversibly stretched. The blister also appears to show a collapse in the centre of the blister, resulting in what appears to be waves upon the surface of the film. This is in line with the ablation model of blister formation.

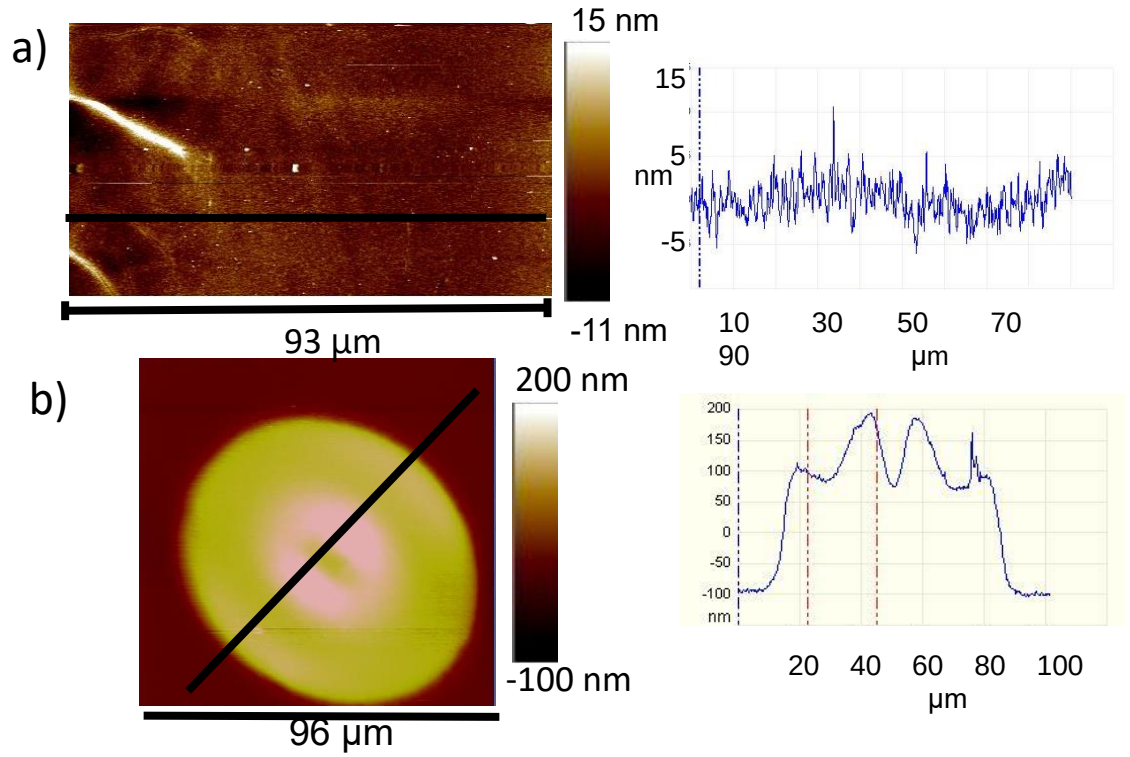

FIGURE 3-2; (A) EDGE OF BLISTER FORMED BY SINGLE SHOT, NANOSECOND LASER PULSE AT 220MJCM^{-2} ON 380NM FILM AND AFM DERIVED CROSS SECTION, SHOWING A FLAT SURFACE. (B) SINGLE SHOT, FEMTOSECOND LASER PULSE AT 190 MJCM^{-2} ON 200 NM FILM, WITH AFM DERIVED CROSS SECTION, INDICATING AN EXPANDED AND SEMI-CONTRACTED BLISTER. THIS SUPPORTS THE PROPOSED SEPARATION OF MECHANISMS SUGGESTED BY FIGURE 3-1.

3.3.0.2 Nanosecond Irradiation

Nanosecond blister formation leaves a quasi-flat surface with a slight depression of ≈ 5nm surrounding the blisters, as seen in Figure 3-2 at ≈30µm. At higher fluences, a greater number of cracks are formed before the metal film is removed at fluences beyond 400mJcm^{-2}, for the 300-380nm thick films, Figure 3-3.

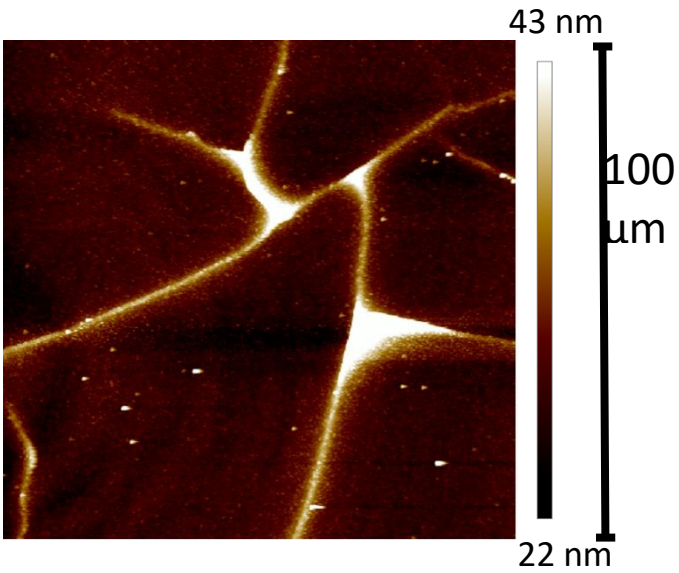

FIGURE 3-3: AFM SCAN OF CRACKED NS BLISTER, FORMED BY 7 NS LASER PULSE WITH A FLUENCE OF 220MJCM^{-2}. THE SCAN AREA IS 100X100 MM^2 AND IS A ZOOMED IMAGE THE BLISTER SHOWN IN FIGURE 3-4 (A). THE INTERSECTING LINE 'CRACKS' ARE ACTUALLY RAISED ABOVE THE SURFACE INDICATING THEY ARE CAUSED BY COMPRESSIVE STRESS SIMILAR TO THAT WHICH FORMS MOUNTAIN RANGES AS TWO PLATES ARE PUSHED TOGETHER.

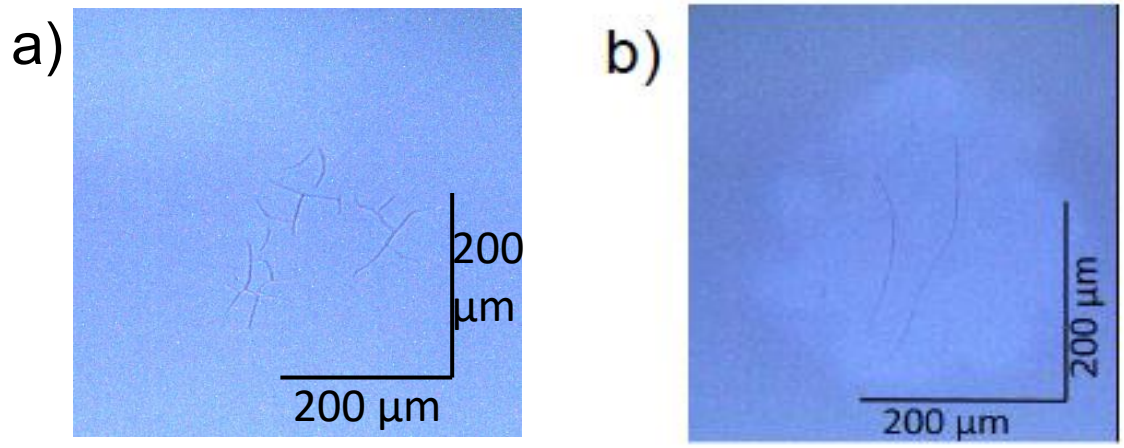

FIGURE 3-4: OPTICAL MICROSCOPE IMAGE OF TI FILM, IRRADIATED FROM THE BACK AT 220 MJCM^{-2}. (B) TI FILM WITH THE TI SURFACE DIRECTLY IRRADIATED AT 315 MJCM^{-2}. DUE TO THE DIFFERENT REFLECTIVITIES, THE ABSORBED ENERGY IS SIMILAR IN BOTH CASES (135 MJCM^{-2} AND 160 MJCM^{-2} RESPECTIVELY.) SAME FILM 200-300 NM THICK.

Figure 3-4 utilises front and back laser irradiation to demonstrate the heat model of expansion in nanosecond blisters. As the laser pulse transfers heat to the film, the side of the film which the pulse

irradiates is unimportant. Figure 3-4 demonstrates a similar surface structure, indicating a lack of ablation by the laser, but rather a heating of the film. Evidence of film heating was also found when the film has a surface coverage. Figure 3-5 shows separate zones which can form within some nanosecond blisters.[53] The surface was coated in auroshells before the blister was formed and these have been largely removed from the central region. There is a region surround the center that contains a lower density of particles. The central zone is formed by a combination of melting and the Marangoni effect. The Marangoni effect creates a convection current, which transfers some surface particles towards the colder section of the film. This creates a small wall around the central region. A schematic of this effect upon the auroshells is given in Figure 3-6.

An alternative mechanism for the multiple regions can be hypothesised as due to the varying speeds of expansion of the blister, with the central region expanding faster than the outer radius, and threshold of adhesion for the surface particles. As described by Meshcheryakov et. Al[61] the center of the blister will theoretically travel faster than the edge as calculated for SnO_2 bubbles. This is due both to the increased stress at the central region aswell as the greater distance over which the region will cover. Taking into account that in a multi-layered structure the particles closer to the surface will feel a stronger attraction to the surface than those in the layers above, where the surface interaction force is reduced due to the distance, It can be presumed that it is possible to desorb the upper layers with less force of ejection, provided by the deceleration of the blister, than required to desorb the surface monolayer. Thus, a particle on the surface in the center of the blister may be ejected whilst a particle on the surface at the edge of the blister may not. Importantly this is a threshold effect and therefore there will be a defined rate of deceleration at which the surface particles will no longer be ejected. Thereby creating a central zone where there is enough energy to remove the surface layer, and a secondary zone where only the layers above will be ejected as seen in Figure 3-5. It can also be seen that the height of the particles in the second zone is less than that of the outer non-blistered region, in conjunction with this theory. This theory does not explain the ring of particles surrounding this central zone and therefore relies on the effect of backscattered ejected particles.

The above model relies on the interaction of particle to particle effects to be less than that of surface particle interaction which is not true in many cases. Furthermore, it is unlikely that the sharp ring ~one particle diameter wide, could be formed due to the backscatter from some of the ejected particles. However, problems also face the Marangoni effect explanation. Figure 3-7 calculates the length of time at which the system cools indicating that the temperature will drop by 100˚C, and thus reduce in fluidity

within 100 ns indicating that the rate of flow for the particles on the surface must be greater than 100 ms^{-1}. Whilst this rate of flow may be possible it is beyond the scope of this project to calculate the systems fluid mechanics, or conduct a time resolved photoluminescent study to track the gold particles movement.

One method to if this effect is due to the Marangoni effect or ejection thresholds experimentally is through the use of a Time-resolved interferometric micrometer as used by Kononenko et al.[62] to study the surface structure of the blister as it evolves over time. This would show whether the surface is changing phase, as the blister shape would distort at the regions of altered state.

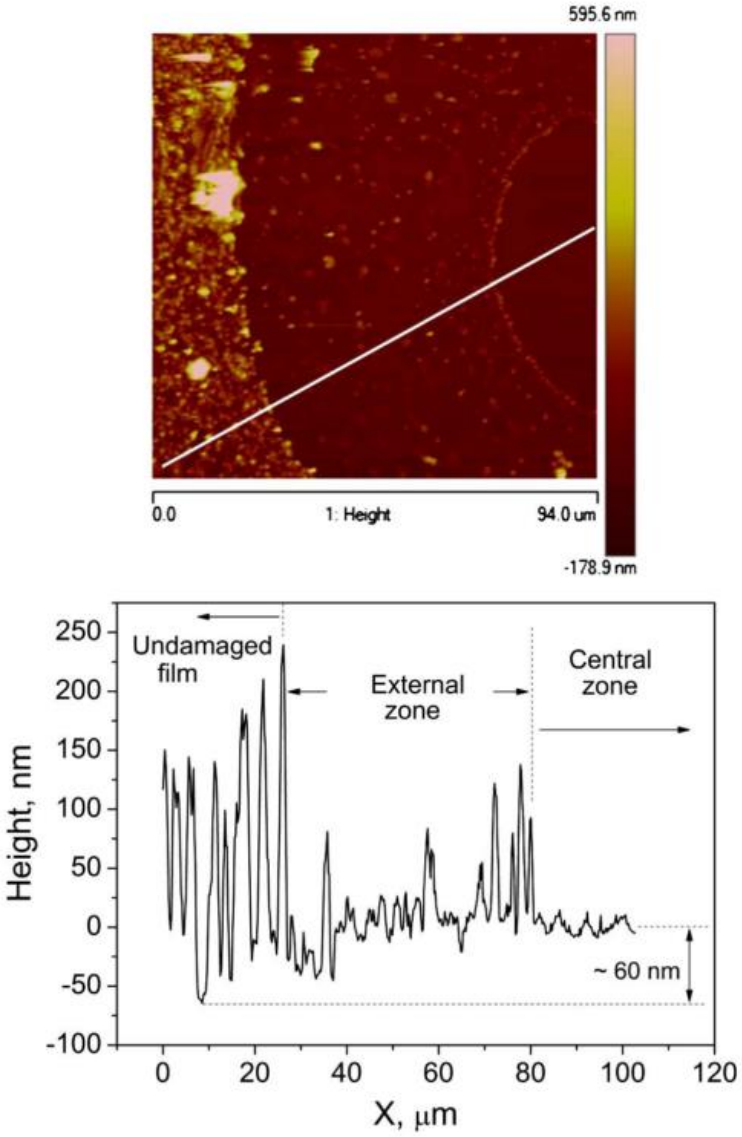

FIGURE 3-5: AFM SCAN OF BLISTER FORMED ON A TITANIUM SURFACE COATED IN 150NM AUROSHELLS. THREE DISTINCT ZONES CAN BE OBSERVED. ONE WITH A COMPLETE LACK OF AUROSHELLS, ANOTHER WITH A SPARSE DENSITY' AND FINALLY, OUTISDE THE BLISTER WITH

A HIGH DENSITY EQUIVALENT TO THAT OF A NON-IRRADIATED SECTION. 7 NS LASER PULSE, ~220 NM TITANIUM FILM, ~250 MJCM^{-2} FLUENCE.

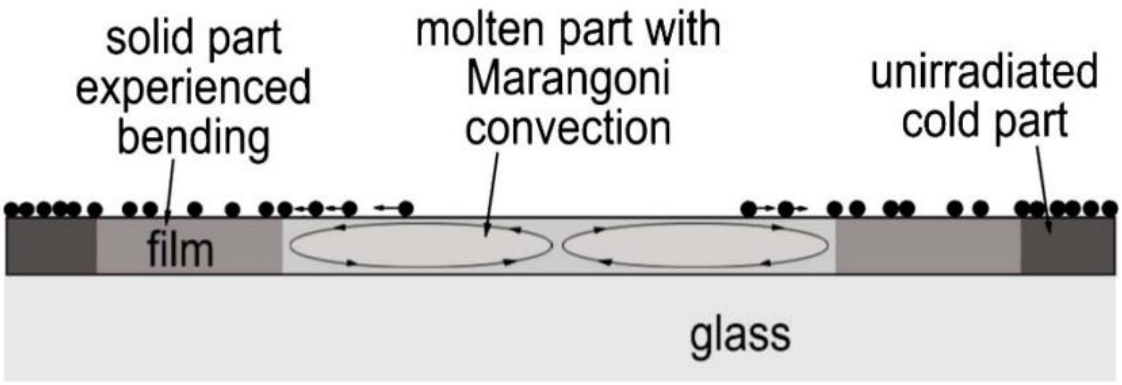

FIGURE 3-6: CARTOON OF THE MARANGONI EFFECT LEADING TO THE SEPARATE ZONES OF NANOSECOND BLISTER UPON TITANIUM COATED IN AUROSHELLS DESCRIBED IN FIGURE 3-5. THE MARANGONI EFFECT IS A POSSIBLE MECHANISM AS THE VARIATION IN TEMPERATURE OVER THE SURFACE WILL CAUSE CHANGES IN SURFACE TENSION LEADING TO THE FLOW OF LIQUID FROM THE HIGH TEMPERATURE REGION TO THE LOWER TEMPERATURE REGIONS.

The surface temperature was calculated by computational models created by S. Starinskiy to test these hypotheses about heat transfer upon a titanium thin film.

The model creates a time-resolved temperature profile along one dimension, using a thermal model from Bulgakova et al.[63,64] We can study the heat transfer in the titanium when $z > 0$ and in the glass substrate for $z < 0$.

$$\left(c_f \rho_f + L_m \delta(T - T_m) + L_t \delta(T - T_t)\right) \frac{\partial T}{\partial t} = \frac{\partial}{\partial z} \chi_f \frac{\partial T}{\partial z} + S(t, z)\,, \qquad z > 0$$

EQUATION 3-2

$$c_g \rho \frac{\partial T}{\partial t} = \frac{\partial}{\partial z} \chi_g \frac{\partial T}{\partial z}\,, \qquad z < 0$$

EQUATION 3-3

In the above equations, the indices *f* and g refer to the film and glass, respectively. The mass density is given by ρ, heat capacity by *c*, and thermal conductivity is χ. The initial terms $L_m \delta(T - T_m)$ and $L_t \delta(T - T_t)$ allow the modelling of temperature, excluding phase transitions[65], where the indices t and m refer to the transition and melting point of the system respectively. L is the latent heat whilst T is temperature. There is no ablative transition term as the laser fluence modelled is too low for this transition. This is all

differentiated over time t. The term $S(t,z)$ refers to the source, ie, the laser pulse. $S(t,z) = (1-R)\alpha_f I(t)\exp(-\alpha_f z)$ where R is the reflectivity, α_f is the absorption coefficient, and $I(t)$ is the incident laser beam intensity.

The boundary conditions for Equation 3-2 and Equation 3-3 are shown,

$$T(0,z) = T_0, \qquad \chi_f \left.\frac{\partial T}{\partial z}\right|_{z=0} = \chi_g \left.\frac{\partial T}{\partial z}\right|_{z=0}, \qquad \chi_f \left.\frac{\partial T}{\partial z}\right|_{z=l} = 0 \qquad \chi_g \left.\frac{\partial T}{\partial z}\right|_{z=-d} = 0 \quad \text{EQUATION 3-4}$$

Where T_0 is the initial temperature of the system. l and d are the thickness of the film and glass substrate respectively. In this model, however, the glass substrate is taken as 5µm rather than 1mm. However, this is still far larger than the 300nm of the Ti, and it was found that further increases of the glass thickness did not affect the modelled film temperature.

These equations were used to model the experimental setup described in Chapter 2 for nanosecond laser pulses. As such, the term values are given in table 0-1.

TABLE 3-1 PROPERTIES OF MATERIALS USED IN THE CALCULATIONS FOR NS IRRADIATION AT 532 NM

Parameter	Titanium	Glass
ρ / gcm^{-3}	4.55-0.000147T, T < 1941 K [20] 4.12, T > 1941 K [20]	2.2*
C / Jkg^{-1} K^{-1}	488+0.00293T+0.00048T^2- 3.55e-7T^3, 300 < T < 1200 K [20] 2055-2.94T+0.0019T^2- 3.63e-7T^3, 1200 < T < 1941 K [20] 989.2. T > 1941 K [20]	800 [21]
χ / Wm^{-1}K^{-1}	-0.013(T-300)+22.2, 300 < T < 500 K [20] -0.00053(T-500)+19.6, 500 < T < 1156 K [20] 0.01693(T-1156)+19.95, T > 1156 K [20]	0.8 [21]
α_f / cm^{-1}	6×10^5 [22]	-
T_m, /K	1941 [14]	-
L_m / kJmol^{-1}	14.15 [14]	-

T_t / K	1250 [18]	-
L_t / kJmol^{-1}	4.3 [19]	-
R	0.36*	0.04*

*measured

The 1-dimensional temperature model indicates that the titanium film heats to its peak temperature 10 nanoseconds after the peak of the initial gaussian pulse as shown in Figure 3-9 The temperature range spreads from 1400 K at 0.17 Jcm^{-2} to 2040K at 0.32 Jcm^{-2}. It's important to note that the melting point of titanium is 1941 K. This is consistent with the previous discussion upon the potential for the melting of the film and potential Marangoni effects.

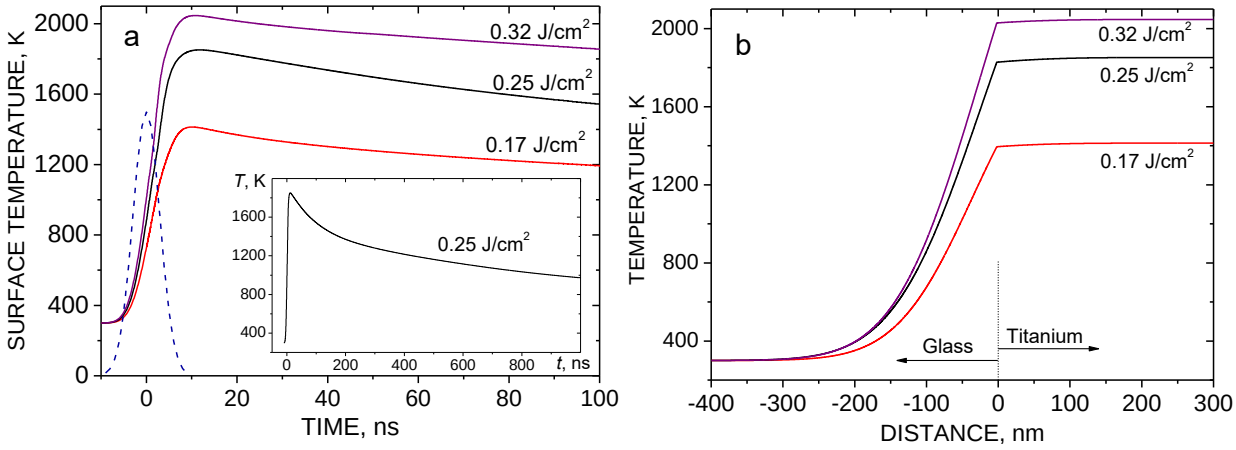

FIGURE 3-7: 1D CALCULATIONS FOR A TITANIUM FILM, AS HEATED BY NS BB-LIFT FOR DIFFERENT LASER FLUENCES. (A) SHOWS A TIME RESOLVED EVALUATION OF THE UPPER SURFACE OF THE TITANIUM FILM. THE DASHED LINE IS THE INITIAL LASER PULSE; AND THE INSET DEMONSTRATES THE TEMPERATURE EVOLUTION OVER A LONGER TIMEFRAME. (B) SHOWS THE TEMPERATURE DISTRIBUTION THROUGH THE FILM AND GLASS SUBSTRATE AT 10NS WHEN THE MAXIMUM FILM SURFACE TEMPERATURE IS REACHED.

The cracking in the film as evidenced by the previous figures, with a clear AFM scan in Figure 3-3, can also be related to a simple expression of thermal stress σ.

$$\sigma = \frac{Ek_e\Delta T}{2(1-\upsilon)}$$ **EQUATION 3-5**

Where E is the Young's modulus of the film (103 GPa for thin films of Ti[60]), k_e is the coefficient of linear thermal expansion 9 x 10^{-6} K^{-1}, [66] ΔT is the average temperature change over the given time period which is assumed to be $T_{max}/2$. υ is the Poisson ratio of 0.32-0.34. When the yield stress exceeds 700MPa for a thin film[67], the films will crack. This is liable to occur at 1800K or above, which corresponds to laser fluences of ~250 $mJcm^{-2}$.

3.3.0.3 Theoretical rate of blister expansion via Ns irradiation

The work presented in this section is based upon that done by Yuri P.Meshcheryakov et al.[61] on the microbump formation within SnO_2, and is intended as a guide for understanding the theoretical modelling behind nanosecond induced blister/microbump formation. However, due to the complexity and processing time of these calculations recreating this model for titanium is beyond the scope of this project. Furthermore, the authors state that assumptions used within this model for SnO_2 mean that it can only be used to justify a qualitative understanding of the process. Therefore, the time and expense required to adjust the parameters from SnO_2 irradiated below it's ablation threshold in a LIFT scheme to the parameters necessary for Ti under the same scheme and sub-ablatation irradiation threshold was deemed as unjustified.

To study blister formation, a 1D model of thermoelasticity and the axis stress waves induced by rapid heating via a nanosecond heating of 200 nm of SnO_2 on a quartz substrate was created. Due to the timescale of nanosecond laser heating the electronic and lattice subsystems are considered to be in equilibrium. It should be stressed that this is not the case for femtosecond irradiation and thus this model cannot be so easily transposed.

The governing equations underlying the numerical calculations are;

$$c(T)\rho \cdot \frac{\partial T}{\partial t} = \frac{\partial}{\partial x}\left(\lambda \frac{\partial T}{\partial x}\right) - \frac{c\rho\eta}{k_\varepsilon} \cdot \frac{\partial^2 u}{\partial t \partial x} + S(x,t) \qquad \text{EQUATION 3-6}$$

$$\rho \frac{\partial^2 u}{\partial t^2} = E_1 \frac{\partial^2 u}{\partial x^2} - E_2 k_\varepsilon \frac{\partial T}{\partial x} \qquad \text{EQUATION 3-7}$$

$$E_1 = \frac{E(1-v)}{(1+v)(1-2v)}, \qquad E_2 = \frac{E}{1-2v}$$ **EQUATION 3-8**

$$S(x,t) = \frac{2F_0(1-R)\alpha\sqrt{\ln 2}}{\tau\sqrt{\pi}} \exp\left(-4ln2 \cdot \left(\frac{t}{\tau}\right)^2\right) \times \exp(-\alpha x)$$ **EQUATION 3-9**

Where T, c, λ, k_ε, are the temperature, heat capacity, thermal conductivity and liniear expansion coefficient, respectively. Further, u, ρ, E, is the material displacement, density and Young's modulus with v being the Poison ratio and η is the thermomechanical factor $3Gk_\varepsilon T_0/c\rho$. T_0 is the initial temperature and $G = E/(3(1-2v))$. And for the laser irradiation effects F_0 is the fluence, R and α are the reflection and absorption coefficients whilst τ is the pulse duration. Thus using these equations the 1D expansion of the film over time with relation to temperature (Equation 3-6), which can be related to stress induced effects incorperated by Equation 3-7 and Equation 3-8. Finally the laser parameters are then incorperated through the use of Equation 3-9. Whilst the euqations above relate the physical effects to the expansion of the system based upon it's properties, they do not define the movement of the cells in the model. Thus, the dynamic equations;

$$\begin{gathered}
\frac{\partial\sigma_{rr}}{\partial r} + \frac{\partial\sigma_{rz}}{\partial z} + \frac{\sigma_{rr}-\sigma_{\theta\theta}}{r} = \rho\frac{\partial^2 u}{\partial t^2}, \\
\frac{\partial\sigma_{rz}}{\partial r} + \frac{\partial\sigma_{zz}}{\partial z} + \frac{\sigma_{rz}}{r} = \rho\frac{\partial^2 \omega}{\partial t^2}, \\
\sigma_{zz} = \lambda div\boldsymbol{D} + 2\mu\frac{\partial\omega}{\partial z}, \\
\sigma_{rr} = \lambda div\boldsymbol{D} + 2\mu\frac{\partial u}{\partial r} \\
\sigma_{\theta\theta} = \lambda div\boldsymbol{D} + 2\mu\frac{u}{r} \\
\sigma_{rz} = \mu\left(\frac{\partial u}{\partial z} + \frac{\partial\omega}{\partial r}\right)
\end{gathered}$$ **EQUATION 3-10**

From the theory of elasticity as expressed in cyclindrical coordinates must be used. Where; σ_{zz}, σ_{rr}, $\sigma_{\theta\theta}$ and σ_{rz} are components of the stress tensor; u and ω are components of the displacement vector $\boldsymbol{D}$. λ and μ are Lamé constants as expressed via of the Young's modulus and poisson ratio as

$$\lambda = \frac{Ev}{(1+v)(1-2v)}, \quad \mu = \frac{E}{2(1+v)}$$ **EQUATION 3-11**

In order to capture possible plastic flows the addition of the von-Mises yield criterion were used

$$K = 2J - {}^{2}/_{3}\,(Y^{0})^{2},$$

where

EQUATION 3-12

$$2J = [(S_{rr})^2 + (S_{zz})^2 + (S_{\theta\theta})^2] + 2(S_{rz})^2$$

Where J is the deviatoric stress, and $S_{rr}, S_{zz}, S_{\theta\theta}, S_{rz}$ are the components. If $K > 0$ the material is viewed as non elastic and if $K \leq 0$ the material is in the elastic regime.

The numerical calculations involved in this are demanding and thus the model blister size was reduced by 2 orders of magnitude to a 5 µm radius. Thus allowing the simplified model of microbump formation over time for SnO_2. The mechanical and thermal properites of SnO_2 are viewed as similar enough to Ti as to be negligible in comparison to the other simplifications made in this model, where the authors state this data can only be viewed as qualitative.

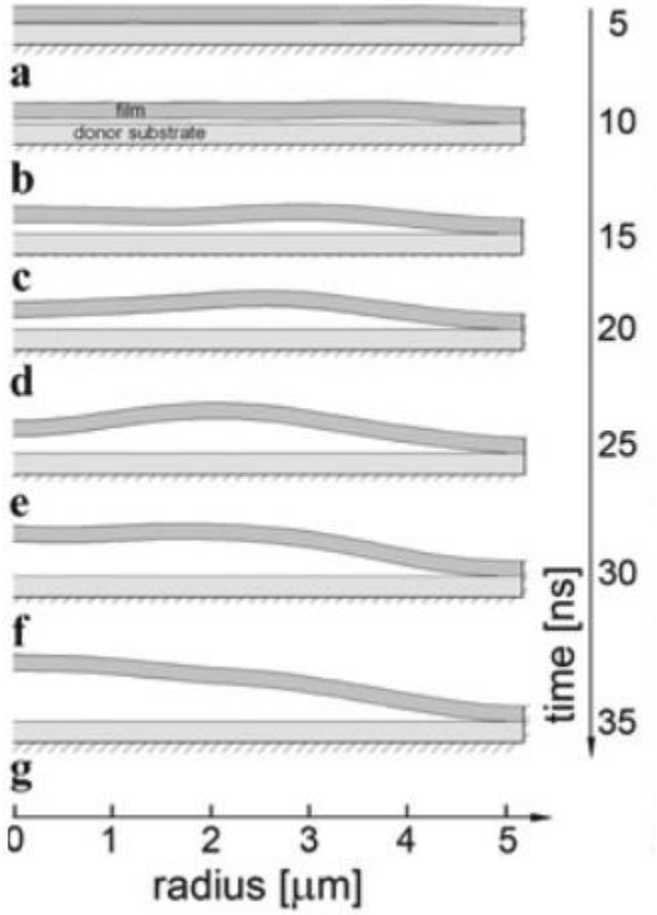

FIGURE 3-8: QUALITATIVE MODEL OF BLISTER EVOLUTION OVER TIME FOR SnO_2 ILLUSTRATING THE EFFECTS OF THERMAL INDUCED STRESS UPON THE SURFACE. THIS WAS CALCULATED FOR SnO_2 FILM WITH THICKNESS OF 200 NM DELAMINATED FROM FUSED SILICA BY A 30 NS UV LASER PULSE WITH 250 MJCM^{-2} FLUENCE. NOTE THAT THE CENTER OF THE BLISTER,

(RADIUS = 0) G EXPANDS THE MOST FORMING AN ARC WHILST THE EDGE REMAINS CLOSER TO THE SURFACE. THE RATE OF EXPANSION IN THE C

The evolution of blister formation over timeFigure 3-8 indicate that the blister reaches a maximum velocity towards the end of the blister expansion. It also shows that this expansion forms more as a compressive wave moving from the edge of the blister inwards. This means that the whilst the edge of the blister has the slowest expansion rate, this rate does not increase in a linear fashion as it approaches the center. This data was calculated for the expansion of SnO_2 from a 30 ns laser pulse of fluence 250 $mJcm^{-2}$, and the maximum velocity obtained at the center was ~60 ms^{-1}. However, due to the assumptions made by the calculation and the author's stress of the qualitative nature of the results, it's believed that this can be used as a reasonable model for the expansion of the titanium blisters formed in this thesis.

3.3.0.4 Femtosecond laser irradiation

The morphology of the femtosecond laser blisters is considerably different to the ns blisters, as seen in Figure 3-2. The blisters maintain some protrusion above the surface of the film; and their diameter is also significantly smaller (ca. 100 µm blister, 300µm diameter laser spot), whilst the nanosecond blisters diameter closely matches the size of the irradiation zone.

The topological variation in the fs and ns blisters is in line with their respective ablation and heat formation mechanisms put forward previously. The femtosecond laser energy is absorbed within the irradiation penetration depth α of 19nm as $\alpha = \lambda/4\pi k$ where λ is the wavelength of 800nm and k =3.33 is the extinction index of Ti.[68] The laser fluence used is also significantly larger than the ablation threshold for titanium of 50 $kJcm^{-3,}$ as determined by Zhu et al.[69]

The heat affected zone can be modeled by calculating the heat transfer rate from the electron subsystem to the titanium lattice. The heat conductivity of the electron system can be described by

$$k_e = \frac{v_F^2 C_e(T_e)}{3(AT_e^2 + BT_l)}$$ **EQUATION 3-13**

Where v_F is the Fermi velocity, C_e is the electron heat capacity, T_e and T_l are the electron temperature and lattice temperature, respectively.[70] A = 6.16 x 10^4 $K^{-2}s^{-1}$, B = 1.21 x 10^{13} $K^{-1}s^{-1}$,[70] and $v_F = 3x10^5$ ms^{-1}. Using the heat transfer equation, the heat propagation distance (Δx) can be estimated as $\Delta x \sim \sqrt{\chi_e \Delta t}$ where χ_e is the thermal conductivity. Considering titanium's extremely high electron lattice

coupling factor of >10^{18} $Wm^{-3}K^{-1}$,[71] this implies that the electrons will transfer their heat to the lattice within the first picosecond, and the size of the heat-affected zone can be estimated as follows;
For a single 120fs pulse at 200mJcm^{-2} the electron temperature will increase to 32000K after 1ps. As the metal will ablate after ca. 10ps,[72] the heat affected zone will have only spread to be ~16nm. Whilst the heat only penetrates to a shallow depth, the lattice temperature will increase to above 10000K, leading to ablation with particles traveling at several kms$^{-1,}$ providing the surface with a recoil force over this area.[72]

To check that the fluence of the femtosecond laser used for blister formation was above the ablation threshold,as mechanistically predicted, the titanium was directly irradiated with a fluence of 200mJcm^{-2} (Figure 3-9). This corresponds to an absorbed fluence of 90 mJcm^{-2}, due to the reflectivity of titanium being 0.55 for 800 nm[68], which is similar to the absorbed fluence in Figure 3-2. where R = 0.45. Figure 3-9 shows little relation to Figure 3-2, showing the blister, unlike the nanosecond irradiated zone in Figure 3-4, that look the same, whether the laser impacted the front of back side. Instead, there is clear evidence for ablation removing some material, and a raised edge, possibly due to the shockwave from the ablation process.

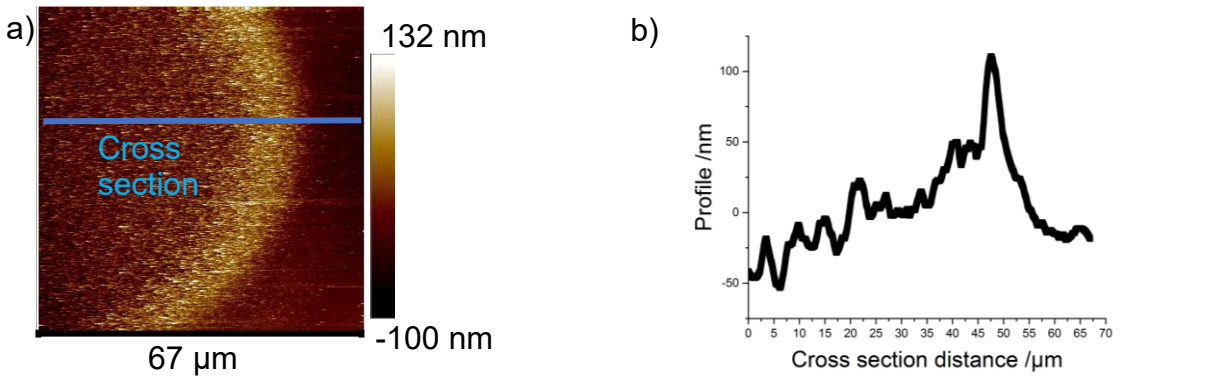

FIGURE 3-9 AN AFM IMAGE (A) AND THE CROSS-SECTION (B) OF A TITANIUM FILM IRRADIATED WITH A FEMTOSECOND LASER PULSE WITH A FLUENCE OF 200MJCM^{-2} WHERE THE ORIGINAL SURFACE IS AT ~-20 NM. THIS SHOWS THAT WE ARE ON THE ABLATION THRESHOLD FOR FS LASER INTERACTION WITH THE FILM. THE CLEAR VARIATION BETWEEN THE TITANIUM FILMS IRRADIATED FROM THE FRONT (FIGURE 3-3 AND FIGURE 3-4) BY NS PULSES COMPARED TO FRONT IRRADIATION BY FS PULSES ALSO PROVIDES FURTHER EVIDENCE TO THE SEPARATE BLISTER FORMATION MECHANISMS.

Therefore, it's proposed that femtosecond laser pulses ablate the film within the area of irradiation, creating a vapour and projecting the area of ablation away from the glass substrate. This blister

stretches the titanium film to a degree dictated by the thickness of the film and the Young's modulus of the material (discussed further in chapter 4). This leaves a bump remaining on the surface with a relatively flat top and edges stretching out of the plain of the film as seen in Figure 3-2.

3.3.0.5 Theoretical rate of blister expansion via femtosecond irradiation

The Young's Modulus for a material, shown in Equation 3-14, demonstrates how the change in thickness will have caused the change in velocity.

$$\Delta L = \frac{FL_0}{EA_0} \qquad \text{Equation 3-14}$$

ΔL defines the change in length where the final cross sectional surface length of the blister will be $\Delta L + L_0$. F is the force stretching the film, which is provided by the rapid change of phase of the film from solid to gas, at the interface of the glass and film. E is the Young's Modulus which is film dependant. A_0 is the cross sectional area of the film, in relation to the direction it's being stretched. These are each illustrated in Figure 4-11. It can be seen that as A_0 decreases, $\Delta L + L_0$ increases, thus the blister will be larger, increasing h. The force is created by the pressurised gas, and it's presumed that the rate of formation and dissipation through condensation is unchanged in relation to the film thickness. Thus, the blister expansion will take place over a similar time frame. Therefore, if h increases over the same time period for thinner films, the surface particles will therefore be traveling faster when the blister expansion stops.

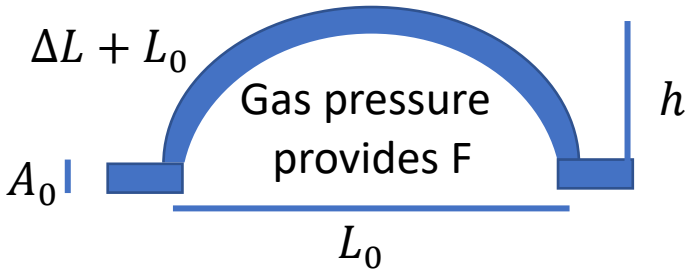

FIGURE 3-10: SCHEMATIC OF FS BB LIFT BLISTER EXPANSION IN RELATION TO THE YOUNG'S MODULUS SHOWN IN EQUATION 3-14. THE HEIGHT OF THE BLISTER IS REPRESENTED BY H, THE THICKNESS OF THE FILM IS A_0, L_0 IS IT'S AREA WHILST $L_0 + \Delta L$ CROSS SECTIONAL DISTANCE OF THE BLISTER.

To estimate the pressure at this interface, the Equation 3-15 from Lei et al. was used.[73]

$$P(r) = (1 - R)\frac{F_a(r)}{A_0}(1 - e^{-2A_0\alpha})$$ Equation 3-15

Where $P(r)$ is the pressure with respect to radius, F_a is the fluence, R is the reflectivity of the titanium, A_0 is the thickness of the film, and α is the inverse optical penetration depth. From which Figure 3-11 can be plotted, where the pressure for the entire blister was estimated as the average over this surface.

Figure 3-11, and the expressions for plastic collapse pressure and initial impulsive velocity (Equation 4-5 and 4-6) from Micallef et al., can be used to demonstrate that we are in the plastic deformation regime, and find the velocity of the blister expansion.

$$p_c = \frac{6\sigma_0 A_0^2}{4r^2}$$ **EQUATION 3-16**

Equation 3-16 defines the plastic collapse pressure, where the material deforms beyond its point of elasticity. It can be seen from the previous figures of femtosecond blisters that the material is deformed and remains as such, thus corroborating the calculation of p_c. σ_0 is yield stress for thin titanium films with a value of 700 MPa from Shan et al.[67]

$$v_0 = \frac{\xi\eta\tau p_c}{\mu r^2}$$ **EQUATION 3-17**

Equation 3-17 defines the velocity of the film due to the pressure at the interface, where ξ is blister position and can be simplified to r^2. η is the dynamic load factor which can be defined as $\frac{p_0}{p_c}$,where p_0 is the maximum overpressure. The timeframe of the expansion is given by τ, which is the time taken for the gas to change phase back to solid. The titanium blister region is defined by μ which is the film mass per unit area. This allows the expression to be simplified further to Equation 3-18.

$$v_0 = \frac{\tau p_0}{\mu}$$ **EQUATION 3-18**

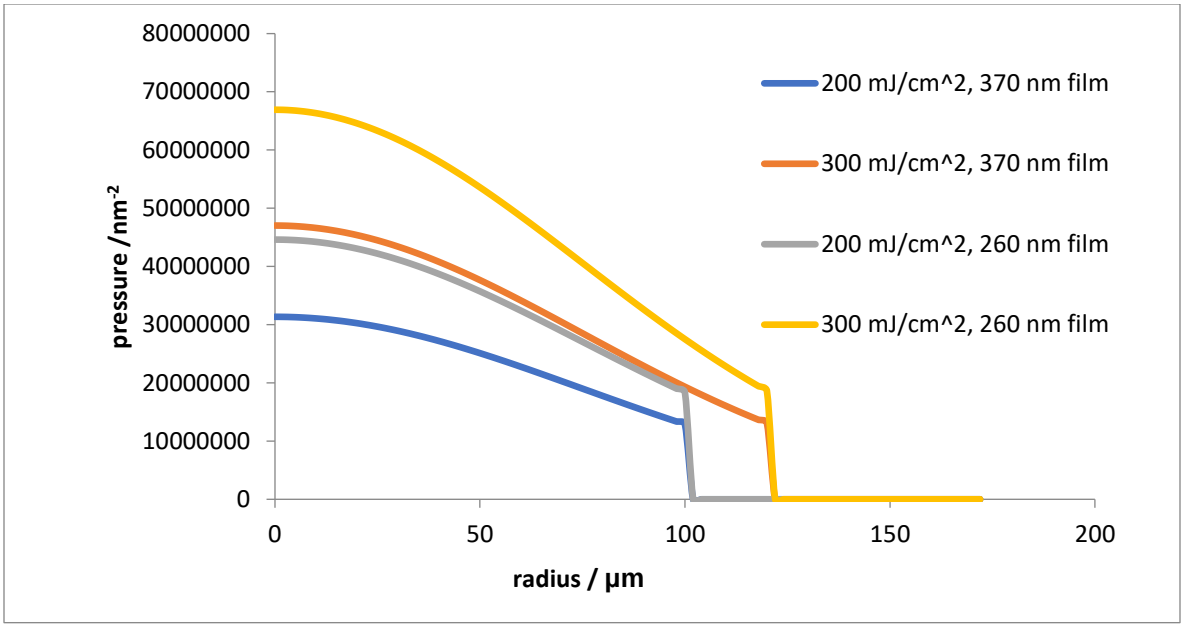

FIGURE 3-11: PRESSURE AT FILM INTERFACE DEPENDENT UPON THE RADIUS R FOR A 370 NM FILM. THE FIGURE SHOWS TWO FLUENCES 300 MJCM^{-2} (ORANGE) AND 200 MJCM^{-2} (BLUE). THE SHARP PRESSURE CUT-OFF, SEEN AT 100 MM AND 125 MM IS DUE TO THE ABLATION THRESHOLD OF TITANIUM. THE PRESSURE FOR THE ENTIRE BLISTER WAS TAKEN AS THE AVERAGE OVER THE GRADIENT.

Thus from Figure 3-11 and Equation 3-18, the velocity of the blister explanation can be estimated as 7.5 ms^{-1}and 10ms^{-1} for fs fluences of 200-300 mJcm^{-2} for a 370 nm film. This matches well with our experiments shown in Chapter 4; and, whilst the calculation for the thinner 260 nm film give values of 15 and 20 ms^{-1} for the same fluences, this qualitatively describes the trend, where a reduced film thickness will result in a faster velocity for the desorbed particles. These calculations provide a reasonable description of the system and manage to qualitatively relate the effects of pressure caused by confined gas formation at a titanium glass interface, aswell as the thickness of the titanium film to the expansion of the blister, when irradiated by a fs laser pulse. Whilst these equations are surprisingly close to the experimental values in Figure 4-12, and qualitatively follow the same pattern, of thinner films allowing a higher velocity, as shown in Figure 4-14. It's believed that due to the size of the assumptions and simplicity of the model, that this can currently only be used to qualitatively model the parameters surround fs-BB-lIFT.

3.3.1 Direct comparison of femtosecond and nanosecond blisters

3.3.1.1 AFM force distance measurements

As the femtosecond blisters leave a surface protrusion, it's believed to be a titanium shell which, when depressed with a force, should flex. As the nanosecond blisters leave a largely flat surface, they should be unable to adjust in relation to applied force. The tip of the AFM was used to try and move a distance into femtosecond and nanosecond blisters, as shown in Figure 3-12. In Figure 3-12b, the force distance curve in the centre of the blister has a gentler gradient than outside the blister, indicating the surface flexes as force is applied to it. Conversely the force distance curves are parallel as the centre of the

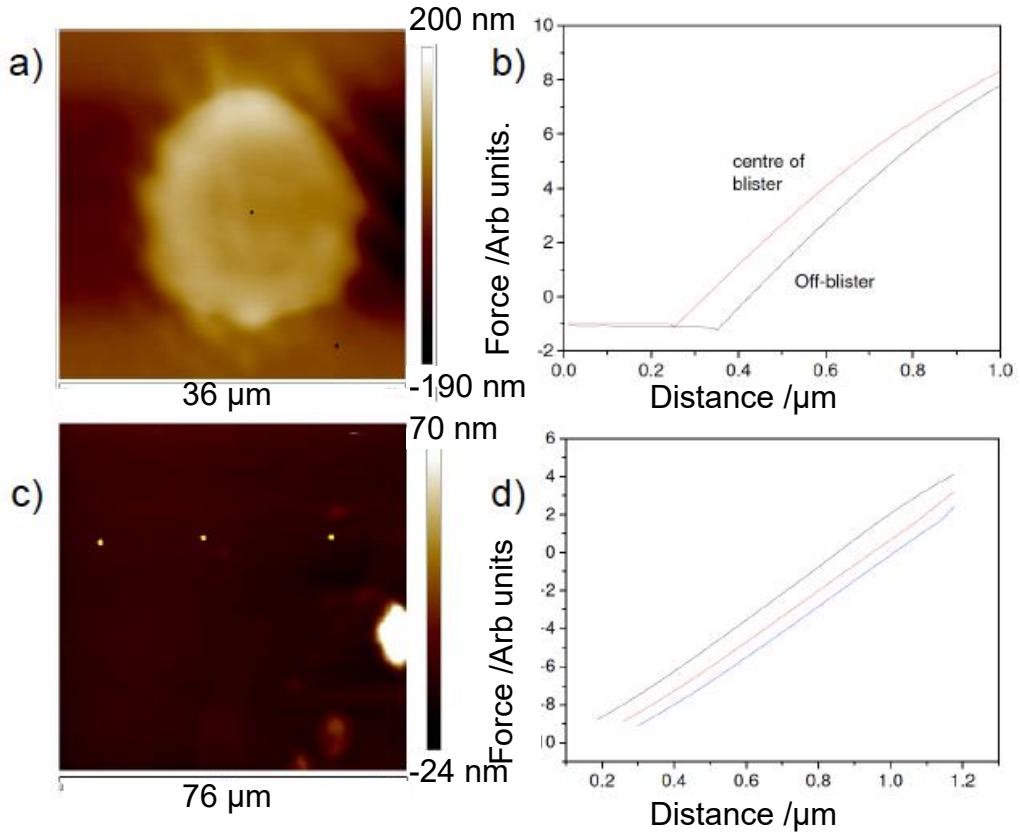

FIGURE 3-12: AFM IMAGES OF FEMTOSECOND, 185 MJCM^{-2} (A) AND NANOSECOND 270 MJCM^{-2} (C) BLISTERS, WITH DOTS INDICATING THE POSITIONS WHERE FORCE WAS APPLIED VIA THE AFM TIP. THE FORCE DISTANCE CURVES ARE CORRESPONDINGLY SHOWN IN (B) AND (D) FEMTOSECOND AND NANOSECOND RESPECTFULLY. THE SMALLER GRADIENT OF THE CURVE IN THE CENTRE OF THE BLISTER (B) INDICATES THAT THE MATERIAL IS MORE FLEXIBLE AT THIS POINT. WHILST THE UNCHANGING SLOPE FOR THE NS BLISTERS INDICATES THAT THE BLISTERS STILL LIE IN THE SAME POSITION WITH RELATION TO THE SURFACE.

nanosecond blister is approached. Thus, the surface has no change in movement, irrespective of where upon the blister force is applied.

3.3.1.2 Multiple pulses

The behaviour of different pulse durations can also be seen in Figure 3-13, which demonstrates the effect of multiple laser pulses upon the same location. In the case of femtosecond blisters, the size of the affected zone increases with each pulse, which leaves rings like stretch marks on the blister. The blisters eventually burst, likely due to a shear fracture in the titanium foil. The nanosecond blisters however, show a rather limited variation apart from the potential for an increase in the number of cracks as the pulses cause continued expansion and contraction.

This shows good relation to the mechanisms of blister formation proposed. The femtosecond laser pulses ablate the titanium film over an area, providing an ablative force to this region. The region is then propelled away from the substrate, and a combination of the ablation and ablated material stretch the film. The titanium films become weaker and thinner with each ablation and gas pressure induced stretch, eventually leading to a rupture in the blister.

In relation to the nanosecond blisters, which typically appear to obey the heat expansion formation, the film is heated to near melting point. The heat causes the titanium to expand and push away from the glass substrate. As the film cools, it recontracts forming a largely flat surface. The following irradiation pulses cause the blister to expand and contract continually.

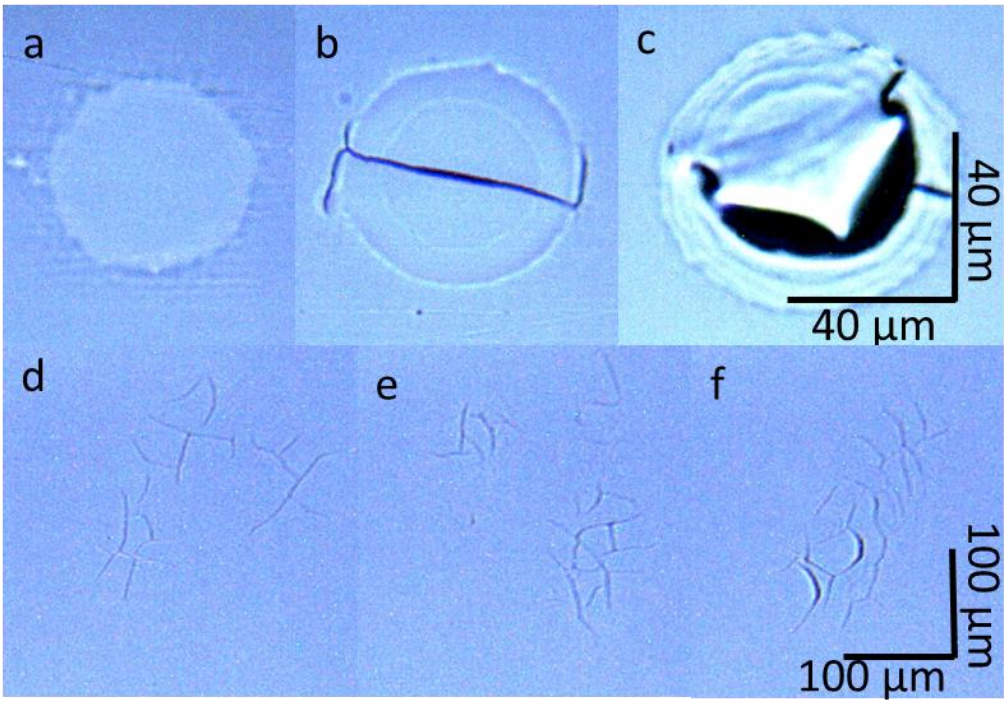

FIGURE 3-13: OPTICAL MICROSCOPE IMAGES OF FEMTOSECOND BLISTERS, 210MJCM^{-2} (TOP ROW) AND NANOSECOND BLISTERS, 270 MJCM^{-2} (BOTTOM ROW) IRRADIATED BY A VARYING NUMBER OF LASER PULSES. (A) AND (D) ONE SHOT, (B) AND (E) TWO SHOTS, (C) 7 SHOTS, AND (F) 10 SHOTS.

3.4 Conclusion

AFM and optical microscopy studies of blister formation by nanosecond and femtosecond blisters have shown good agreement with computational models, indicating that the pulse duration has a strong effect upon the formation of the blisters. Two different models of blister formation have been put forward which can be used to explain the varied effects observed and calculated in this chapter. Nanosecond-BB LIFT appears to form blisters via heating of an irradiated area within 10ns, causing the titanium film to expand and protrude forward at a speed capable of desorbing particles upon the surface. The protrusion then collapses back to a flat surface as the film cools. The initial heating can cause melting, leading to zones within the blister; and, the rapid expansion can cause cracks to form in the surface, due to shear stress on the titanium. However, blisters can still be formed below this cracking and melting threshold. Femtosecond-BB LIFT appears to form blisters due to the initial ablation over an area at the interface of the film and glass. These ablations create a force and a confined gas plume which serve to stretch the titanium film into a titanium shell with a largely flat top and steep

sides.

These two mechanisms will have differing effects upon the ejected particles. In ns-BB LIFT there is the potential that the particles may be heated, thus damaging them. The expansion rate of the blister is also largely controlled by the thermal expansion coefficient of the film material, leading to similar velocities of the ejected particles. Fs-BB LIFT likely avoids the potential for heating the particles, due to an increased surface temperature. The expansion caused by a direct force acting upon the film from the direction of the substrate also means the expansion is largely governed by the Young's Modulus of the material. Therefore, adjustments to the ease of stretching the material such as thickening or thinning it will cause varying rates of expansion of the blisters. This potential is discussed further in Chapter 4.

4. Characterisation of desorbed particles spatial and velocity distribution

Gas phase beams often require some form of collimators to block the radial components. This is because gas phase sources typically do not produce highly directional beams. It was possible that BB LIFT also produced a dispersion of particles, rather than a directional pulse. So, to discover potential implementations for BB LIFT and potential insight into blister formation, the spread of the particles upon a receiver plate was investigated. The receiver plates used were either glass slides or titanium films; the particles tested were sandwich-coated auroshells and spin-coated $C_{60;}$ and, the experiments were conducted with 7 ns laser pulses upon titanium and nickel.

Knowing the velocity distribution of the beam was also necessary in order to apply this method for gas phase experimentation, as-well as to obtain further insight into the mechanics of beam formation. Velocity distribution measurements were conducted using C_{60} spin-coated upon titanium films with thicknesses ranging from 200 to 370 nm. Furthermore, the variation between nanosecond and femtosecond BB LIFT was explored.

4.1 Particle spatial spread

Kononenko et al.[41] measured the spread of emitted diamond nanoparticles to be 40˚ from the 40µm blisters produced by irradiation with a 50 picosecond laser. This was found by placing a receiver in front of the film and measuring the scattering angle. However, Kononenko et al. did not describe how this scattering angle was measured.

4.1.1 Particle spread for ns BB LIFT

The method used in our experiments is similar; however, the scattering angle was found by measuring the radial distribution of the particles deposited upon the receiver plate. The particles appear significantly darker than the receiver plate, as seen in Figure 4-1. Therefore, the radial distributions of these particles' splatter can be found, via the pixel intensity of the image.

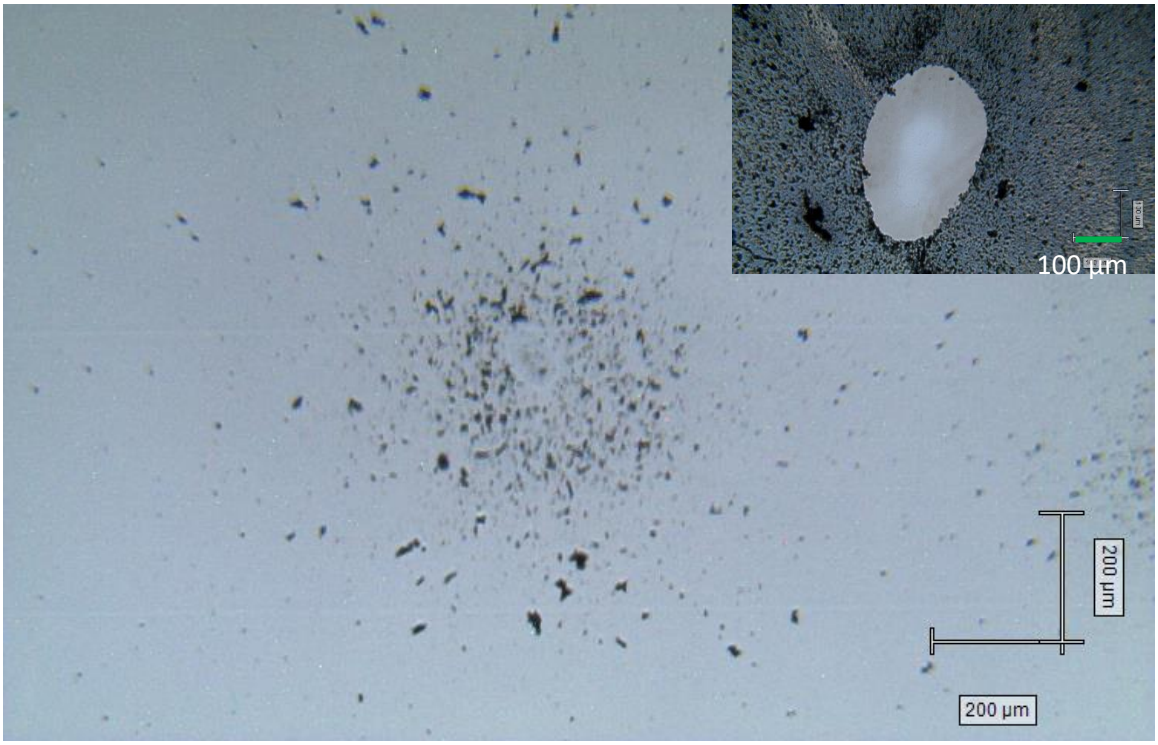

FIGURE 4-1: 250 MJ CM^{-2} NANOSECOND BLISTER (TOP RIGHT) AFTER THE TRANSFER OF AUROSHELLS TO A RECEIVER PLATE 2MM AWAY (CENTRE) FROM A SINGLE PULSE.

Analysis of ~50 blister deposits, similar to that shown in Figure 4-1, reveals the plot shown in Figure 4-2. Thus, with knowledge of the receiver distance and the point at which particle intensity decays to background, the spread of the particles can be found via

$$\tan^{-1}\frac{deposition\ radius - Blister\ radius}{receiver\ and\ donor\ distance} \qquad \textbf{EQUATION 4-1}$$

As shown in Figure 4-2 the deposition radius is ~300 µm. This is irrespective of whether the blister burst or the film remained intact. Thus, with a 2 mm distance and a 100 µm average radius of a nanosecond blister, the spread of the particles is ~5˚ at 250 mJ cm^{-2} from a 260 nm thick titanium film.

The plots in Figure 4-2 show the spread from blisters which have burst and those which remained intact, ~10 and ~30 respectively. However, they show very similar characteristics. This could indicate that particles are emitted before the blisters' structural collapse. There is also a flat section of the plots which extends to ~90 µm. As the blisters' themselves have a radius of ~100 µm this could be an indication that a large section of the deposit is emitted in a straight line from the donor film. This correlates well with the theory of blister formation, since the film is heated over an area rather than a

point position. So, the film expands normal to the surface initially. This implies that the particles receive most of their momentum in this normal vector. Once the film has fully expanded the shape may be hemispherical; however, the particles do not need to leave the surface normal to the final blister shape. This holds especially true for the particles from blisters which have burst. The burst blister topography tends to be very jagged making AFM analysis very difficult.

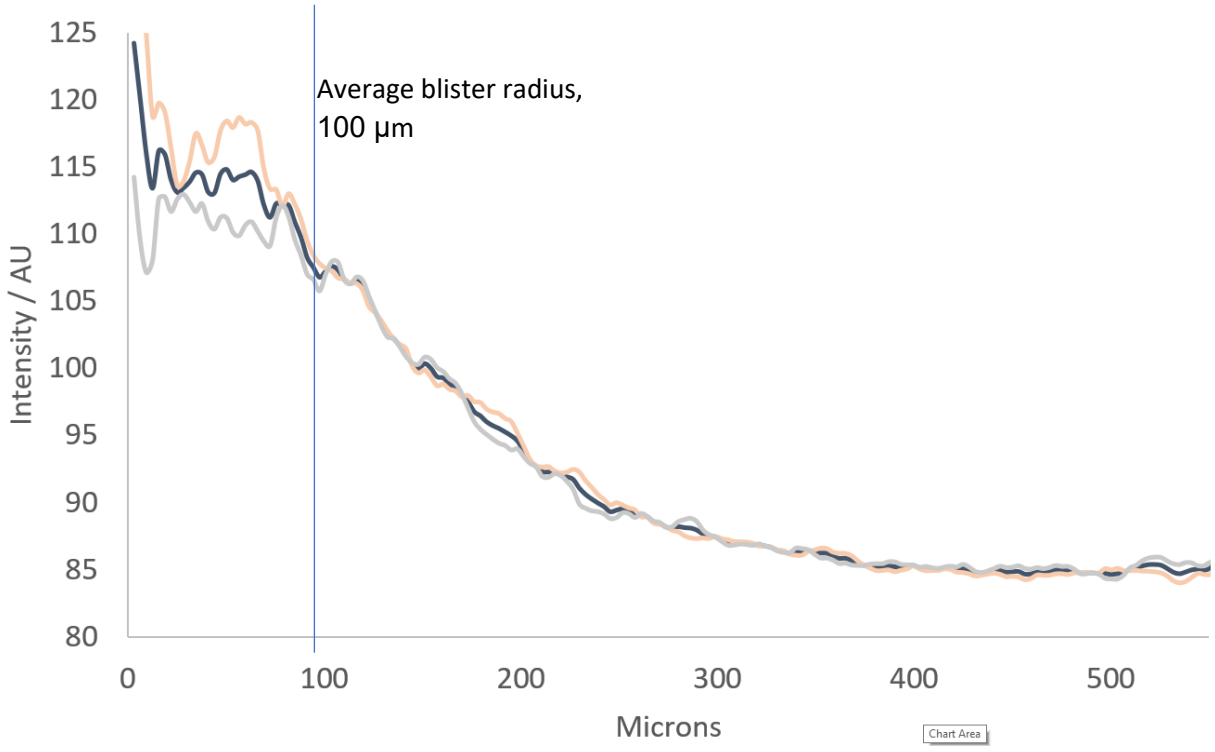

FIGURE 4-2: RADIAL DISTRIBUTION OF 40 BLISTER DEPOSITS FROM NS LIFT AT 250 MJ CM^{-2} OF AUROSHELLS (DARK BLUE)~30 BLISTERS. RADIAL DISTRIBUTION OF BURST BLISTER DEPOSITS (LIGHT RED)~10 BLISTERS. RADIAL DISTRIBUTION OF INTACT BLISTER DEPOSITS (GREY). THE VERTICAL LINE IS THE AVERAGE BLISTER RADIUS.

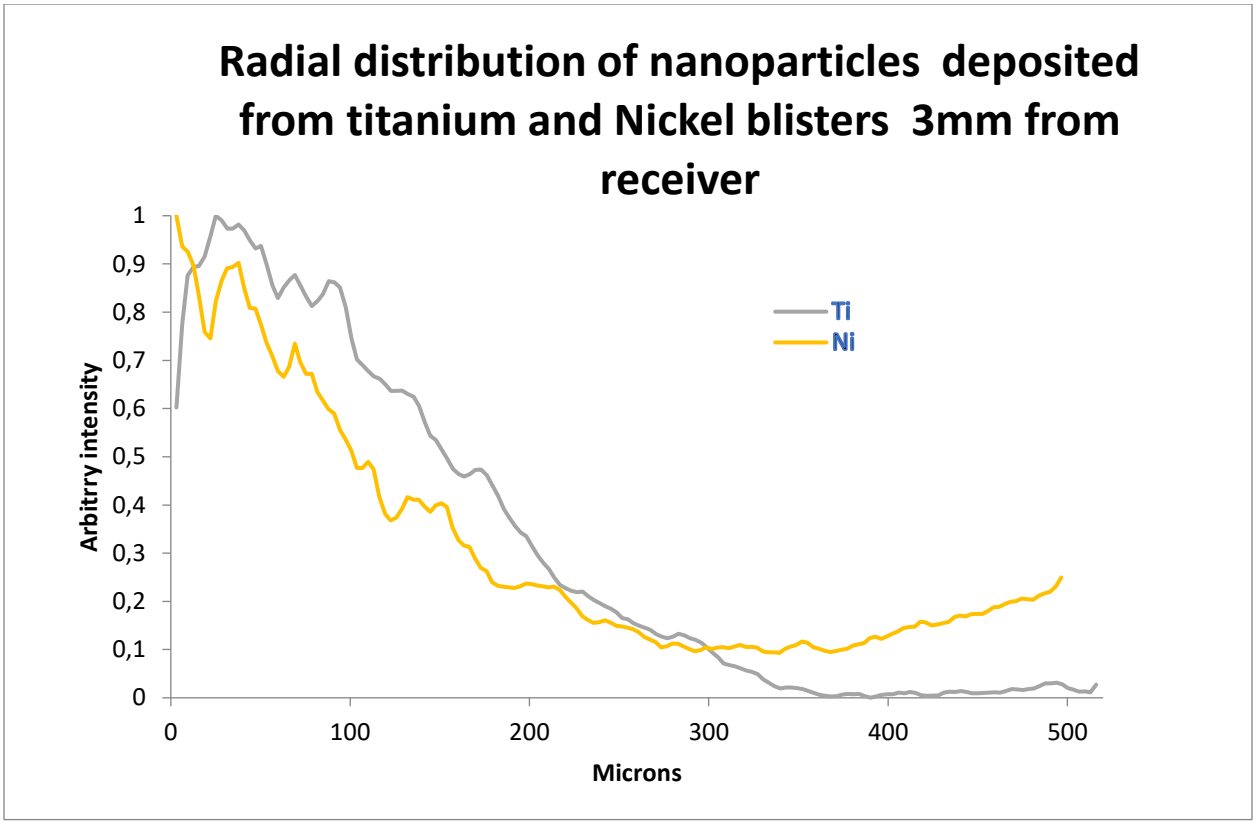

FIGURE 4-3: COMPARISON OF PARTICLE SPREAD FROM BLISTERS FORMED ON NICKEL (YELLOW) AND TITANIUM (GRAY) AT 3MM DISTANCE FROM TARGET. 200-250 NM FILM THICKNESS AT 250-300 MJCM^{-2} FLUENCE NS LASER PULSE.

A brief study into particle deposition from nickel films was conducted; however, this research was only done on eight nickel deposits. Nevertheless, we found that the particles are indeed removed and decay to the background level at ~300 µm, thereby giving a spread of ~4˚. The accuracy of this value is contestable due to the low sample size; however, it does indicate that nickel and titanium form blisters in a similar manner. The titanium film appears to show a very similar structure to the previous titanium deposits shown in Figure 4-2 and gives a similar spread of ~5˚.

Further experiments were done via ns BB LIFT with C_{60} instead of the auroshells, where the thermal heating of the film can also desorb more molecules, discussed in section 4.1.2 resulting in a wider spatial distribution. Due to the poor visibility of C_{60} in the mircroscope images, ~200 blisters were formed and transferred to a single location on a receiver plate. The receiver plates were 2.8 and 4.0 mm from the donor film and illuminated via the technique described in Chapter 2. Figure 4-4 shows one of these deposits. Visually, the deposit appears to be far larger than those of titanium or nickel. However, the

plots from when the receiver plate is 4 mm away, in Figure 4-5, show they still maintain the flatter initial radius before decaying.

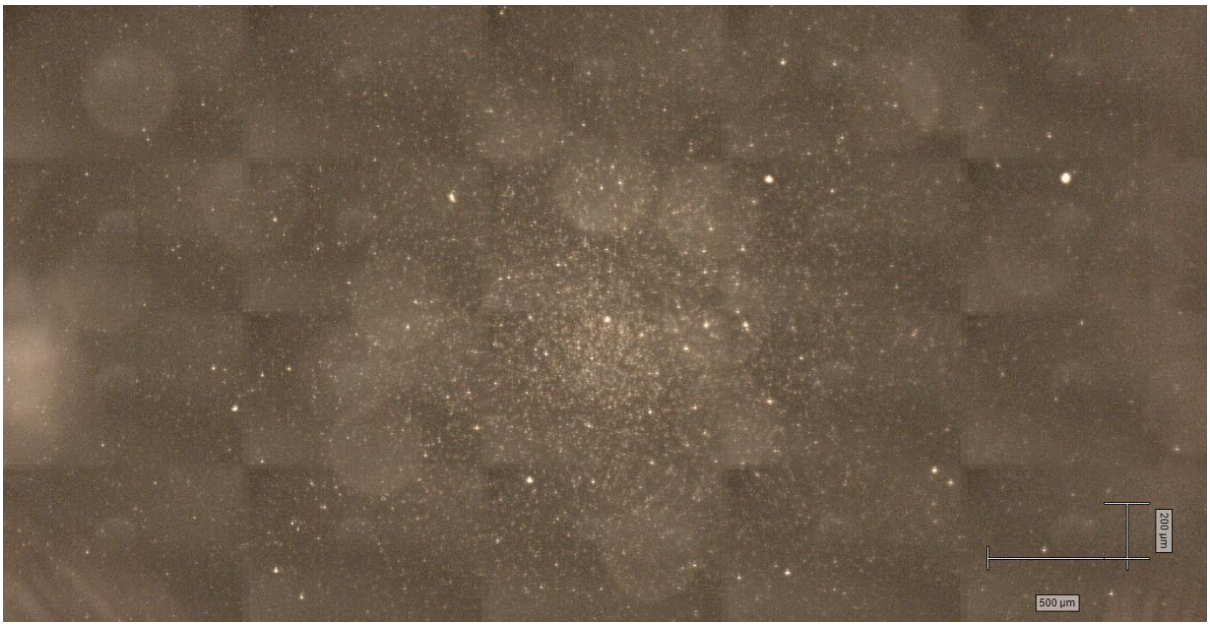

FIGURE 4-4: C_{60} DEPOSIT ON GLASS RECEIVER PLATE, 4 MM FROM THE DONOR FILM VIA NS BB LIFT. THE C_{60} IS ILLUMINATED DUE TO TOTALLY INTERNALLY REFLECTED LIGHT ESCAPING FROM THE GLASS AT THE FULLERENE GLASS INTERFACE. THE DONOR FILM BLISTERS HAVE A DIAMETER OF ~200 NM WHERE THE LASER FLUENCE IS ~250 MJCM^{-2}

The size of the deposits push the radial distribution measuring system to its limit as the particles reach background levels at the edges of the plots shown. However, measurements of the background intensity level were taken, confirming that it lies at the edge of where the shown plots display. From Figure 4-5 we can estimate the spread of the fullerene to be 10-15˚.

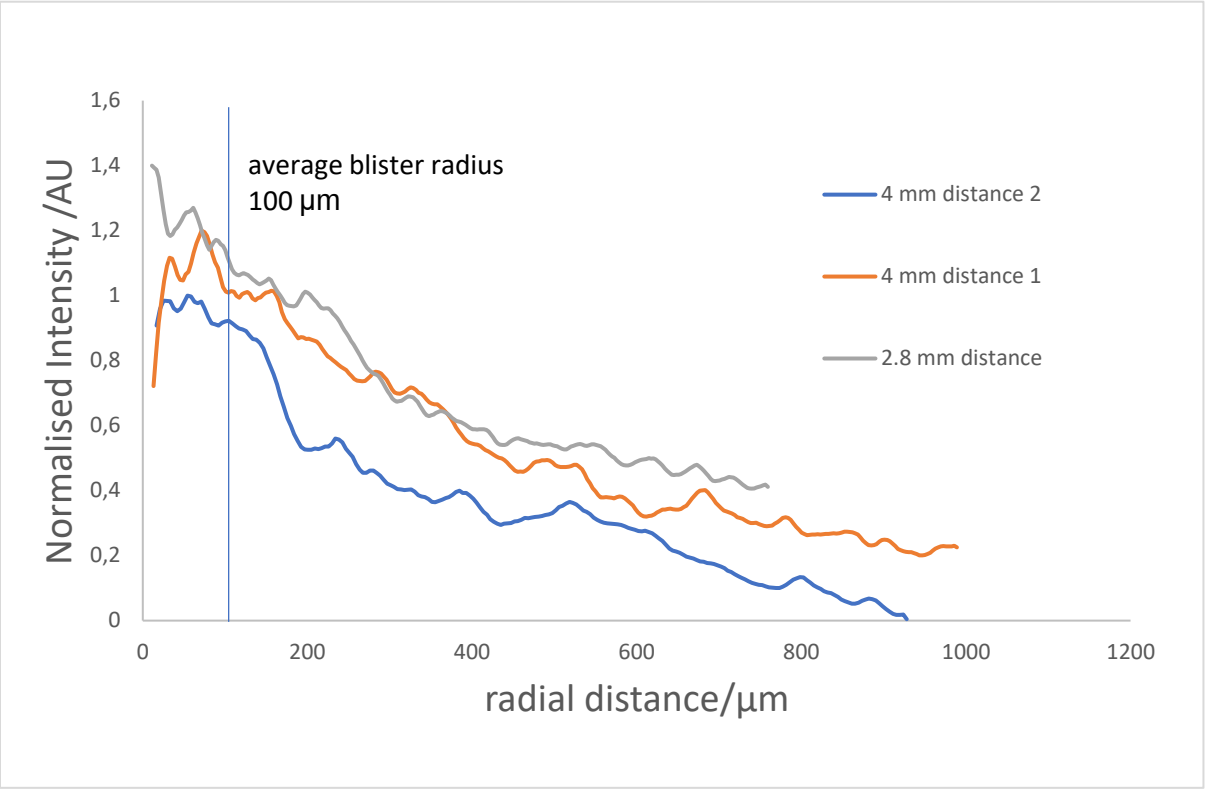

FIGURE 4-5: RADIAL DISTRIBUTION PLOTS FROM~200 C_{60} DEPOSITS UPON A GLASS RECEIVER PLATE. TWO OF THE PLOTS (ORANGE AND BLUE) ARE FROM WHEN THE RECIEVER PLATE WAS 4 MM FROM THE DONOR FILM, AND THE GRAY PLOT IS WHEN THE RECIEVER IS 2.8 MM FROM THE DONOR FILM. THE LINE IS THE AVERA GILM BLISTER RADIUS.

Comparison of the particle spreads of fullerene and auroshells show some discrepancy, yet both are significantly more collimated than the spread previously reported by Kononenko et al.[41] for diamond nanoparticles desorbed with ps pulses. This may indicate the spreads are related to the particle being transferred, rather than the pulse duration of the laser. As discussed in 4.2.1 ns BB LIFT also transfers via thermal desorption which could result in a wider spatial distribution. Yet, another conclusion can be drawn from analysis of the methods. The method of analysing deposits of auroshells involved many different locations of blister deposits, each 1 mm from each other. Whilst the fullerenes were all deposited upon the same location, so they stack atop each other. In relation to the auroshells method, it is possible that the background intensity level is higher than for the clean glass receiver. This may be due to some unintentional overlapping of the deposits. Therefore, they may have reached what appears to be a flat intensity before the true background level. Figure 4-5, like Figure 4-4, does show two separate slopes in each of the curves. The plots have a shallower gradient out to 170 µm before a drop

which asymptotically approaches the background level. At this edge, the intensities undergo a rapid drop off before levelling off to background.

4.1.2 Particle spread for fs BB LIFT

The spread of fullerenes, desorbed by femtosecond blisters, was found by depositing from a titanium donor film, with evaporated fullerene, to a receiver plate 2 mm from the donor film. The fullerene film can be applied in thicker and denser deposits than via spin coating, and also comes off in larger more visible fragments. An example blister can be seen in Figure 4-6, which shows a central area largely devoid of fullerenes. The titanium that is visible has two distinct sections. The inner section is ~50 µm in diameter, and slightly brighter than the external region, just before the magenta fullerene deposit. This central region is likely to be the blister. The external, darker titanium region may be titanium which remained adhered to the surface. The exterior coloured region is fullerene which has had some of the top layer removed, with the bulk removed from the central area. The colours are given by the interference patterns of the light reflected from the top of the titanium film and the light reflected off the titanium which has passed through the film. Fifty of these blisters were used to deposit C_{60} upon the receiver plate which can been seen in Figure 4-7. The deposit on the receiver plate is thick enough to be clearly visible; and, a radial spread plot was formed from this as shown in Figure 4-8.

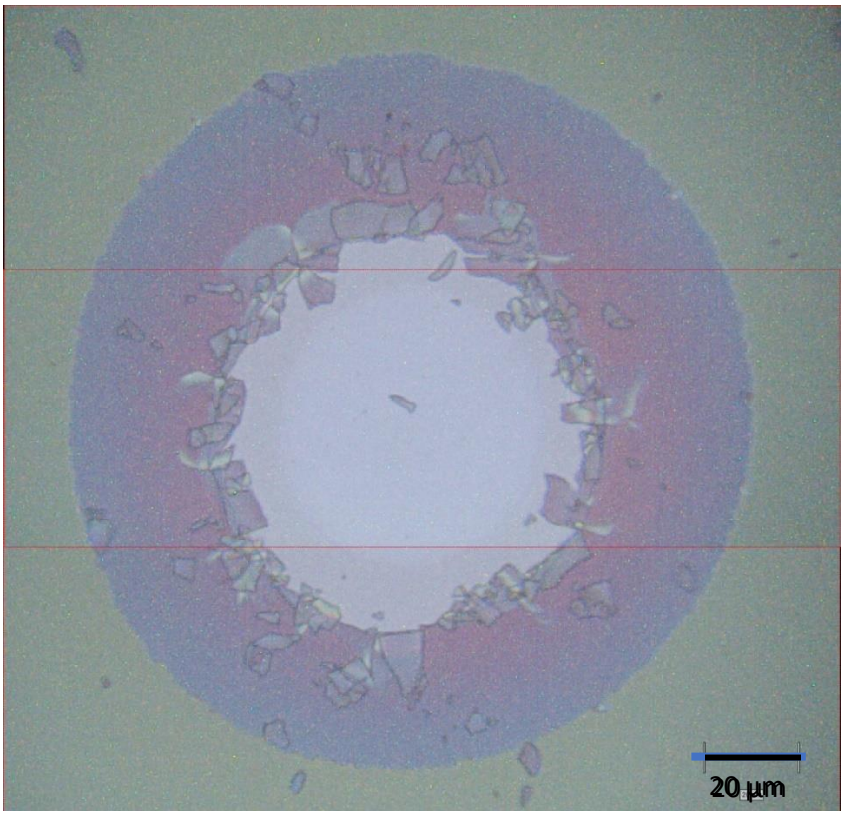

FIGURE 4-6: FEMTOSECOND BLISTER 180 MJCM^{-2}, 330 NM TI, 180 NM C_{60} EVAPORATED FILM.

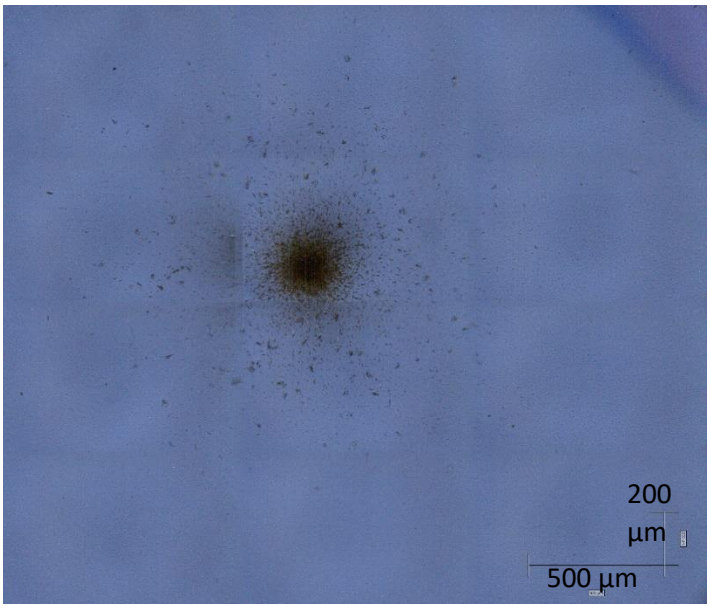

FIGURE 4-7: FULLERENE DEPOSIT FROM 50 BLISTERS AS SHOWN IN FIGURE 4-6.

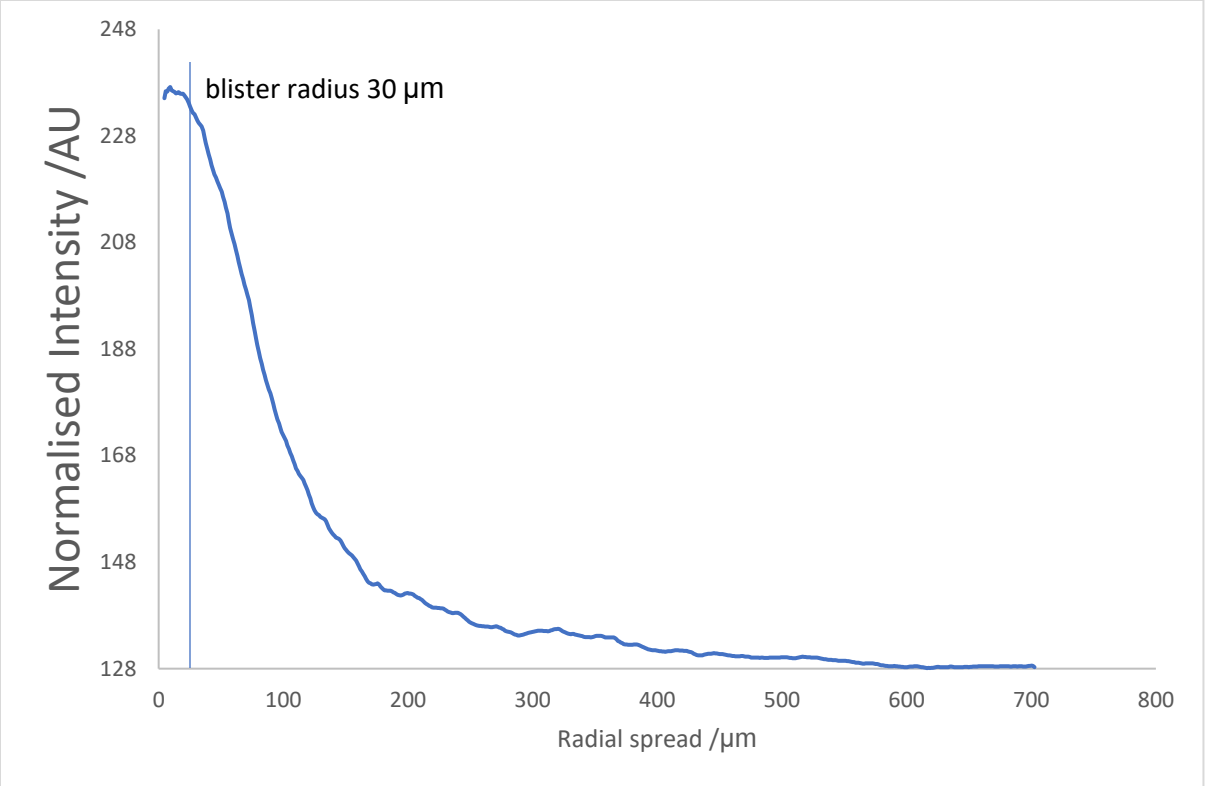

FIGURE 4-8: RADIAL DISTRIBUTION OF C_{60} FROM 50 BLISTERS ON 310 NM TITANIUM FILM WITH 180 NM EVAPORATED C_{60} AT 2 MM FROM DONOR FILM, VIA FS PULSES AT 180 MJCM^{-2}. THE VERTICAL LINE IS THE AVERAGE BLISTER RADIUS.

It can be seen that the fs radial spread has a steeper drop off when compared to the ns deposits. There is a semi-flat center extending to 20 µm which is the approximate radius of the central brighter titanium section of the blisters as seen in Figure 0-6. This is similar to that seen from the nanosecond blisters. Ninety percent of the deposit is found within a radius of 330 µm indicating a spread from the blisters (entire area of desorbed fullerene of 70 µm radius) of ~7˚. This is narrower than for the nanosecond spread of 10°-15° indicating the fs mechanism is more directional than for the heating mechanism. From Figure 3-2 of a fs blister cross section it can be seen that the cross section if fully expanded would be more akin to a column with a rounded top rather than a hemisphere.

4.2 Velocity Distributions

As discussed in Chapter 3 there is a variation in blister formation due to the irradiating pulse duration. This variation in laser pulse width was found to correlate with differences in the measured velocity distributions of emitted particles. As the nanosecond pulses cause inflation of the blister, due to heating of the film, it was found that this could also induce two velocity components within evaporable particles, as the film would rise to over 1700 degrees, causing evaporative emission alongside the BB LIFT

emission. Femtosecond blister formation doesn't appear to create this residual heating effect. However, the film thickness does appear to cause a variation in the velocity distribution as discussed below.

4.2.1 Nanosecond velocity distributions

Initial testing of nanosecond BB LIFT was conducted upon titanium films sandwich-coated in auroshells. Due to the 150 nm size, with a gold coating (25 nm) and silicon core (125 nm), they are not possible to transfer via thermal evaporation. However, utilising the setup discussed in the appendix, and the lab of Dr. Buglokov- in Novosibirsk which utilised a 193 nm ionising, laser pulse It was possible to ablate the surface of the auroshells, and find the velocity distribution of the desorbed particles, by detecting the the ionised material.

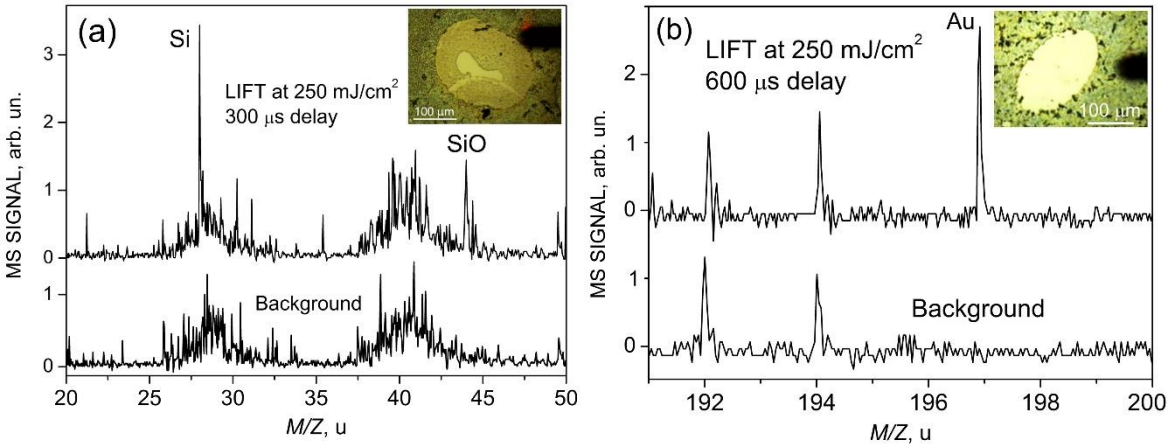

FIGURE 4-9: MASS SPECTRA OF IONS FROM ABLATION OF AUROSHELLS, AFTER EMISSION FROM THE SURFACE. THE LOWER SPECTRA IN (A) AND (B) DISPLAY THE BACKGROUND SPECTRA IN THE CHAMBER AND THE INSETS ARE IMAGES OF THE BLISTER WHICH EMITTED THE PARTICLES. (A) GAUSSIAN NS LASER PULSE (532 NM AND 250 MJCM^{-2}) WITH 400 NM IONISING FEMTOSECOND LASER PULSE, WITH A TIME DELAY CORRESPONDING TO A VELOCITY OF 50 MS^{-1}. (B) TOP HAT NS LASER PULSE (532 NM, 250 MJCM^{-2}) WITH 193 NM NS IONISING PULSE AT A TIME DELAY CORRESPONDING TO A VELOCITY OF 60 MS^{-1}.

Figure 4-10 demonstrates that the particles are emitted over a narrow region of velocities from 50-60ms^{-1}. This is below the estimated 100 ms^{-1} by Kononenko[62], as irradiated by 50 ps pulses. However, due to the change in pulse duration, there is some leeway for the change in velocity.The velocity of 60 ms^{-1} does show a closer relation to the maximum velocity of movement for a film, calculated for SnO_2,

under more similar irradiation conditions.[74]

Figure 4-10(C) shows data from fs ablated auroshells. However, detection of the gold from the auroshells was not observed, whilst silicon and SiO are observed. The absense of gold is probably because the ultrashort ionisation pulses are likely to cause spallation[75,76], where the gold is removed as large particles rather than ablated ions. However, the longer (ns) UV ionisation pulse creates thermal ablation conditions, which are more favourable for the emission of gold ions.

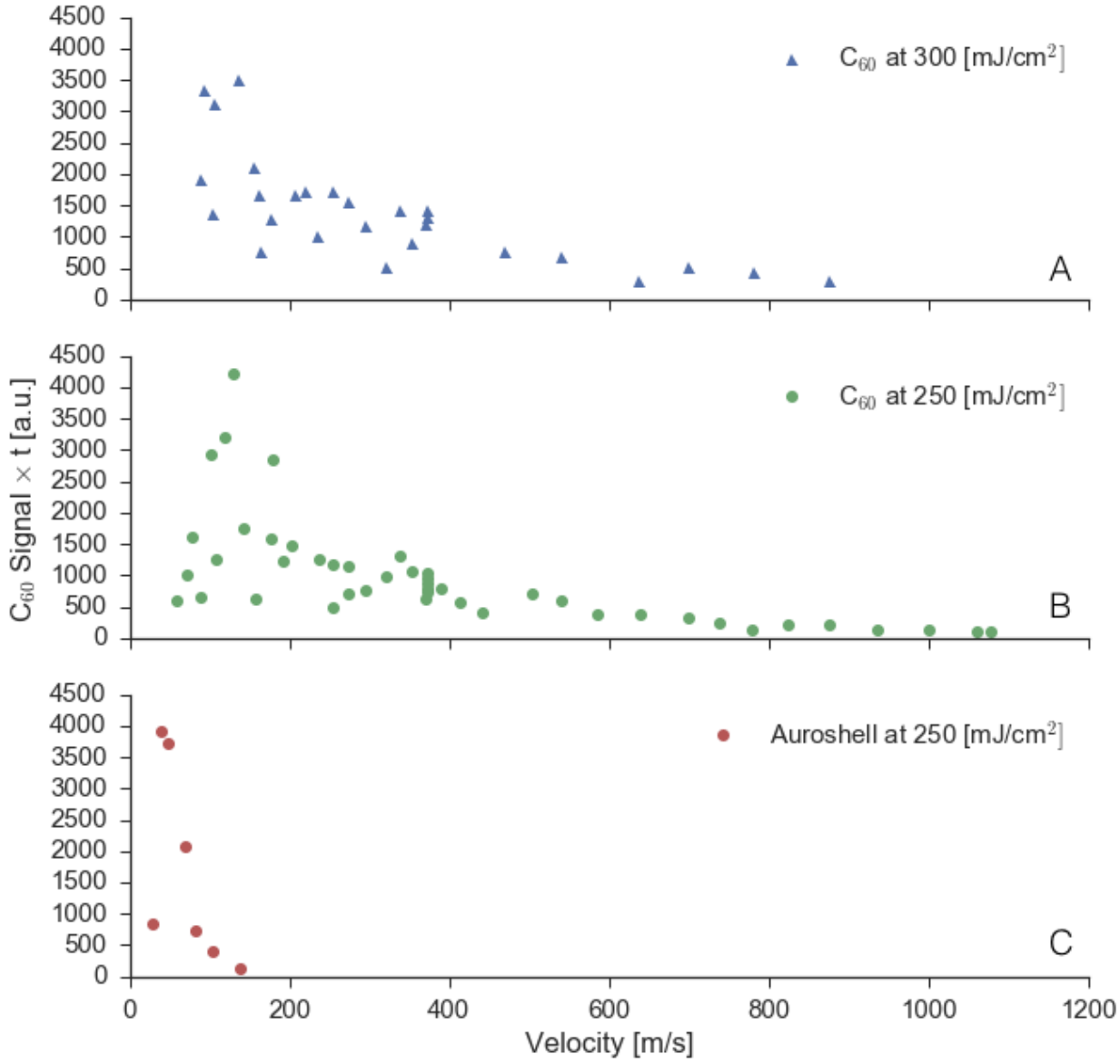

FIGURE 4-10: VELOCITY DISTRIBUTIONS FROM NANOSECOND BB LIFT OF C60 AT 300 MJCM^{-2}(A), AND 250 MJCM^{-2}(B), AS-WELL AS AUROSHELLS, (C). THE FILM THICKNESS WAS 265 NM OF TITANIUM.

Velocity distributions are shown in Figure 4-10 (A,B) for fullerenes desorbed from a 265 nm titanium film with ns pulses of 250 and 300 $mJcm^{-2}$. These are shown in comparison with the data for the auroshells in Figure 4-10(C). The figure shows two distinct regions of C_{60} desorption where the highest signal is detected at time delays corresponding to ~100 ms^{-1} which would imply a temperature of 400 K. This temperature does not correspond with the calculated temperatures of the film after irradiation, discussed in Chapter 3, and the shape of the curve does not fit an M-B distribution. The fitting of M-B curves to the remaining emitted fullerenes was an attempt to find the surface temperature. However, as the temperature of the film surface changes considerably over the microsecond timescale, as shown in Figure 3-9, this approach is incompatible without a time-resolved component. Figure 4-10 clearly shows there are fullerenes removed at lower intensities, yet higher velocities; however, these emissions are not visible for the non-evaporable, auroshell particles the velocity of which is similar to the blister-emitted fullerene velocities.

Figure 4-10 also demonstrates a varying-intensity particle desorption for various velocities in relation to the fluence of the laser pulse. Whilst this variation is expected, due to the difference in temperature, the varying fluences will elevate the film to a greater height. The separation is within our margin of error, therefore decreasing our ability to draw further conclusions.

4.2.2 Femtosecond velocity distribution

The velocity distributions of the particles desorbed using femtosecond pulses were measured for $C_{60,}$ as the auroshells did not produce as strong a signal for detection as the $C_{60,}$ due to the difficulties of causing ablative ionisation in contrast to direct molecular ionisation, since no VUV laser was available in the Edinburgh laboratory, and no fs laser was available in Novosibirsk.

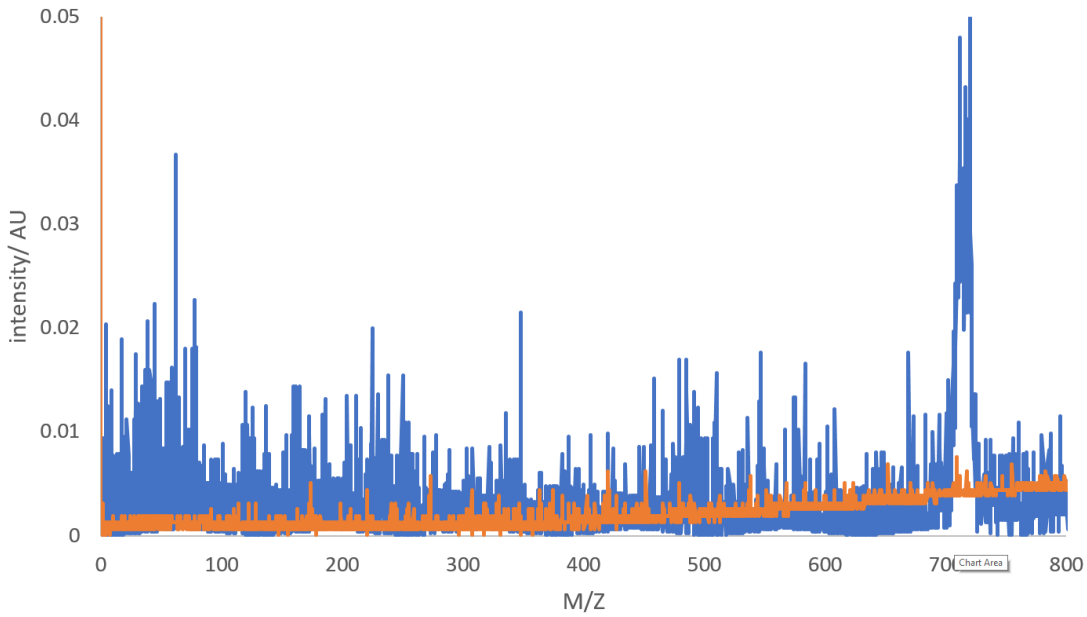

FIGURE 4-11: EXAMPLE MASS SPECTRA OF C_{60} DESORBED BY A FS PULSE WITH FLUENCE 280 MJCM^{-2} FROM A 370 NM TITANIUM FILM AND IONISED WITH A NS PULSE WITH A DELAY EQUATING TO ~15 MS^{-1} (BLUE). A BACKGROUND WITH NO NS IONISATION IS SHOWN (ORANGE). THE INTEGRAL OF THE C_{60} PEAK WAS TAKEN AS THE INTENSITY OF PARTICLES IN THE GAS PHASE AT THIS VELOCITY.

As discussed in Chapter 3, the femtosecond BB LIFT mechanism is caused by the expansion of plasma confined between the film and the transparent substrate. This applies a force stretching the film into a blister. The results in Figure 4-12 demonstrate that this stretching can be limited by a thicker film, and therefore reduce the velocity of the emitted particles. The velocity distribution was found by integrating over the C_{60} peak in mass spectra similar to that shown in Figure 4-11 at various time delays between the fs blister pulse and ns ionisation pulse. Figure 4-12, in contrast to Figure 4-13, which is of the velocity distribution of particles from nanosecond BB LIFT, shows a clear velocity variation.

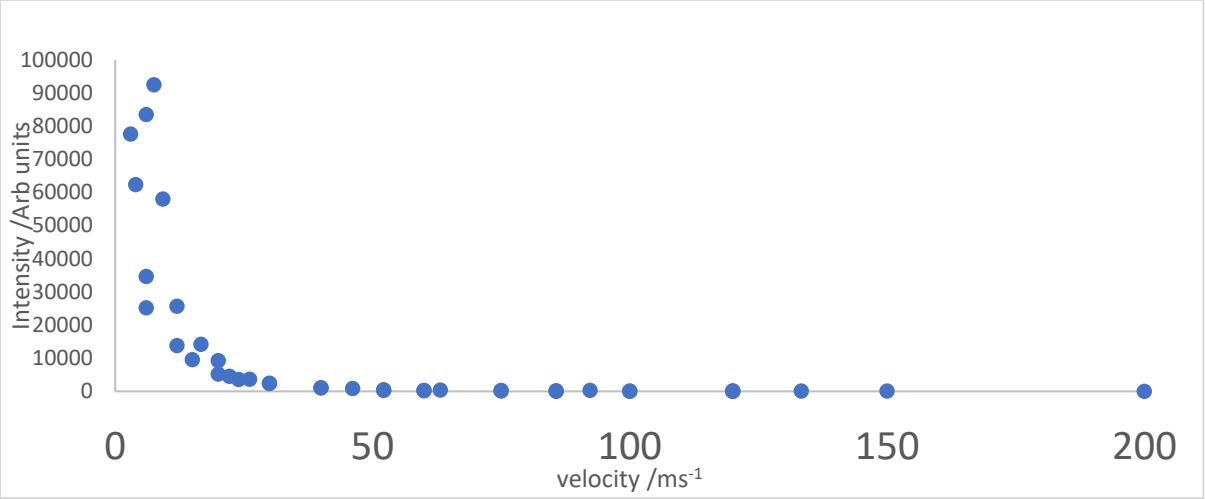

FIGURE 4-12: VELOCITY DISTRIBUTION OF C_{60} FROM 370 NM TITANIUM FILM DESORBED BY FS BB LIFT 280 MJCM^{-2}. THIS EXPERIMENT WAS FOUND BY PERFORMING FS BB-LIFT AND NS IONISATION ON THE SAME FILM AS THE VELOCITY DISTRIBUTION SHOWN IN FIGURE 4-13.

Figure 4-12 shows a very low and confined velocity distribution from 5-10 ms^{-1}, in relation to ns BB-LIFT, Figure 4-13. There is also no evidence of higher velocity fullerenes, potentially caused by thermal evaporation from the film. The effect of reduced velocity is not replicated in Figure 4-13 showing nanosecond BB LIFT from the same film.

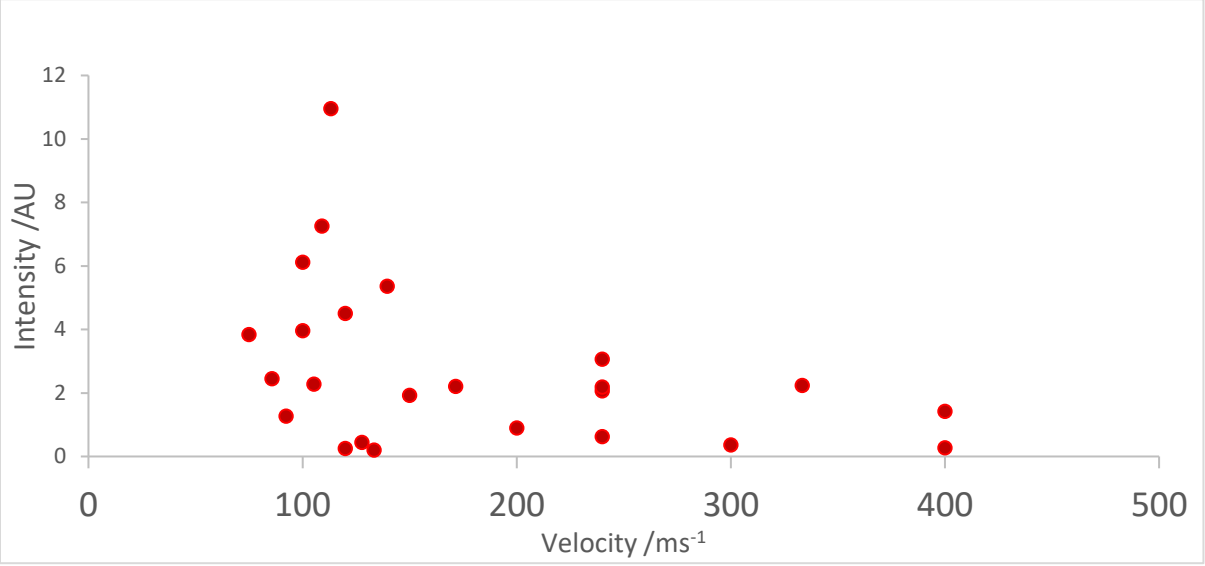

FIGURE 4-13: VELOCITY DISTRIBUTION OF C_{60} FROM 370 NM TITANIUM FILM DESORBED BY NS BBLIFT 230 MJCM^{-2}. THIS EXPERIMENT WAS FOUND BY PERFORMING FS BB-LIFT AND NS IONISATION ON THE SAME FILM AS THE VELOCITY DISTRIBUTION SHOWN IN FIGURE 4-12.

Figure 4-13 demonstrates similar results to the other ns desorbed velocity distribution curves. The peak velocity is ~120 ms^{-1} and has a greater spread than for femtosecond BB LIFT. There is also clear evidence of higher velocity fullerenes, liable to have been evaporated shortly after blister formation.
The clear difference between the two velocity distributions, from blisters formed upon the same film with varying pulse durations, demonstrates how the different mechanisms discussed in chapter 3 affect the velocity of the desorbed particles. The film thickness does not affect the expansion of the nanosecond induced blisters, within the investigated range, because the pulse is heating the film. The primary formula describing nanosecond blister formation is shown in Equation 4-2

$$\Delta L = L_0 \alpha \Delta T \qquad \text{Equation 4-2}$$

Where ΔL is the change in length from L_0, due to the change in temperature ΔT, and α is the thermal expansion coefficient for the film. The laser fluence effects ΔT as discussed in Chapter 3; yet, the region of fluences available for nanosecond BB LIFT is small, thereby reducing our ability to control the particle emission via fluence. However, if the film material is altered this may have a more drastic impact upon the expansion rate. That being said, the film's melting point will limit the ΔT available to cause adequate blister expansion. Thus, in order to increase the velocity distribution of nanosecond BB LIFT, αT_m must be high, where T_m is the melting point of the film material. If this product is low then, provided the film is still heated on the timeframe of the laser pulse, the velocity of blister expansion, and thus of the emitted particles, will be low.

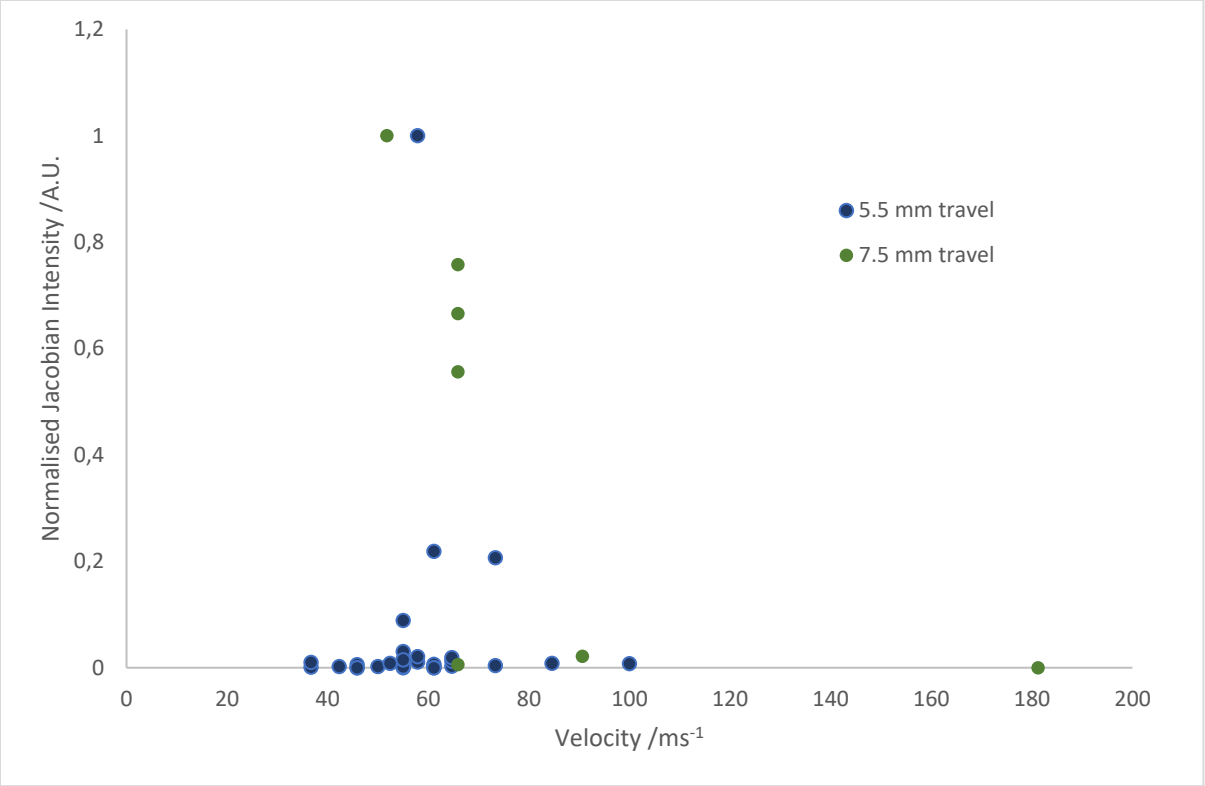

FIGURE 4-14: FULLERENE VELOCITY DISTRIBUTION FROM 260 NM TITANIUM FILM INDUCED BY FS BB LIFT, FLUENCE ~250 MJCM^{-2}. THE DISTANCE THE FULLERENES TRAVELLED BEFORE NS IONISATION WERE 5.5 MM (BLUE) AND 7.5 MM (GREEN). THIS PLOT SHOWS CONFIRMATION OF VELOCITY DISTRIBUTIONS BY CHANGING THE DISTANCE THE PARTICLES MUST TRAVEL BEFORE IONISATION, AND CONSEQUENTLY FIND THAT THIS APPROPRIATELY AFFECTS THE DELAY TIME NECESSARY FOR FULL IONISATION. IT SHOULD BE NOTED THAT WITHIN THIS PLOT THE VALUES OF THE HIGHEST DETECTION ARE FROM SATURATION OF THE DETECTOR. THIS PATTERN SAME VELOCITY IS REPEATED ON A LOWER LEVEL WHEN THESE ARE IGNORED.

These results are in strong agreement with the theoretical calculations performed within chapter 3, which indicate a higher velocity distribution for thinner films when performing fs-BB-LIFT. Whilst the velocity for the thinner film does not agree completely numerically with the theoretical calculations, they follow the same qualitative pattern showing a strong dependence of velocity upon the thickness of the film.

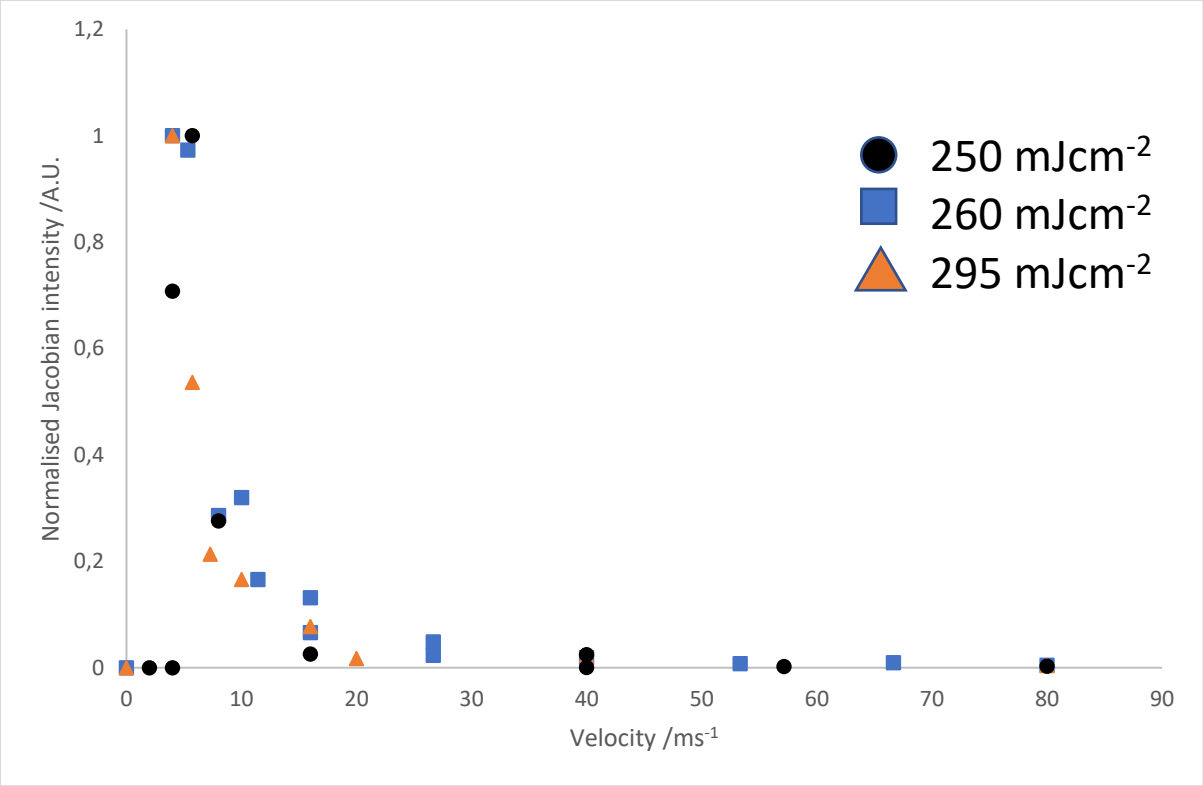

Figure 4-15: C_{60} velocity distribution at 250 mJcm^{-2} (black circle), 260 mJcm^{-2} (blue square), and 295 mJcm^{-2} desorbed via fs BB LIFT from a 370 nm titanium film.

Figure 4-15 shows the velocity distribution of C_{60} desorbed from a 370 nm film of titanium at 3 different fluences. However, potentially due to the low varition in fluence, there is limited change to the velocity of the desorbed C_{60}. Demonstrating that over the range tested the fluence has a negligible effect upon the velocity distribution in relation to the film thickness. Whilst the theoretical calculations shown in chapter three indicated that a change in velocity should be found as we adjust the fluence. We are not experimentally able to find this due to the innate uncertainties within the experiment.

Figure 4-14 demonstrates that the change in thickness of the film from 370 nm to 260 nm increases the velocity of the desorbed fullerenes. This is in good agreement with the theory explained in chapter 3, that the film stretches under the pressure of a confined gas.

4.3 Conclusion

Through experimental measurements and theoretical approximations it was found that the particle spread is from 10-15˚ for ns BB LIFT and ~7˚ for fs BB LIFT of a fullerene film. The impact of the particles being desorbed upon the spatial distribution of the particles is yet to be fully characterised, and it's suggested that this also be done in conjunction with adjusting the size of the blisters to determine if the

central area (radius of blister in relation to the deposits) does vary with the size of the blister. However, this data suggests that BB LIFT provides the desorbed particles a velocity with a confined spatial distribution. It's presumed this is due to the blister being formed by laser pulse impact over an area rather than at a point position, thus altering the dynamics of blister expansion. If the blister was formed by the laser a fine focal point it is presumed that it would expand hemispherically from this position. The velocity distribution of the particles shows a strong relation to the pulse duration. This is in line with the previous research into pulse duration effects upon blister formation as discussed in Chapter 3. Ns BB LIFT provides the auroshells with a velocity of ~50 ms^{-1} and desorbs C_{60} a velocity of ~100 ms^{-1} with a small dependence upon the fluence, yet the titanium film thickness does not affect velocity distribution. However, for fs BB LIFT the velocity of the desorbed fullerene varies from 7-65 ms^{-1} with a strong dependence upon the film thickness and a weaker theoretical dependence upon the fluence. This is due to the two different mechanisms discussed in Chapter 3.

5. Low damage 0, 1 and 2-dimensional particle transfer

The ability to place particles into the gas phase can aid in understanding the fundamental science related to that particles structure and potential interactions. This is because they are in a vacuum, traveling with a known velocity. This enables use in many spectroscopic techniques which can gather a more detailed analysis. The successful transfer of particles to a specific location has numerous practical applications which can also be of tremendous use in industry. However, most beam sources can damage the particles due to aggressive charging, heating or radiation. This tends to define an upper limit of complexity for particles which can be successfully transferred to the gas phase. Furthermore, methods such as MALDI or electrospray require the particles to be soluble inside a specific matrix or solution. However, BB-LIFT has shown itself capable of gently transferring large complex structures from "0-dimensional" point particles, like small molecules, to 150nm nanoparticles, crystals, 1-dimensional carbon nanotubes, and even 2-dimensional molybdenum di-selenide films.

5.1 Molecular transfer

Large, complex and fragile molecules are notoriously difficult to study[1] due to fragmentation and deformation of the molecular structure during gas phase transfe, to the spectrometer or for direct printing. Molecules like C_{60} are fairly robust and can be evaporated without suffering thermal decomposition. However, Phenyl-C_{61}-Butyric acid Methyl ester (PCBM), Figure 5-1, is more complex than C_{60} and suffers full thermal isomerisation at 300˚ over a period of 20 minutes, where the reactant and product are given in Figure 5-1.[19] It can be seen that a new, five-membered cyclo-adduct isomer is given. Typical gas phase analysis of PCBM is accomplished via sublimation, under vacuum, at over 300˚[77]. Therefore, the true molecule studied has instead been iso-PCBM.[19] The technique that is developed within this thesis could provide a method for the study of non-isomerised PCBM.

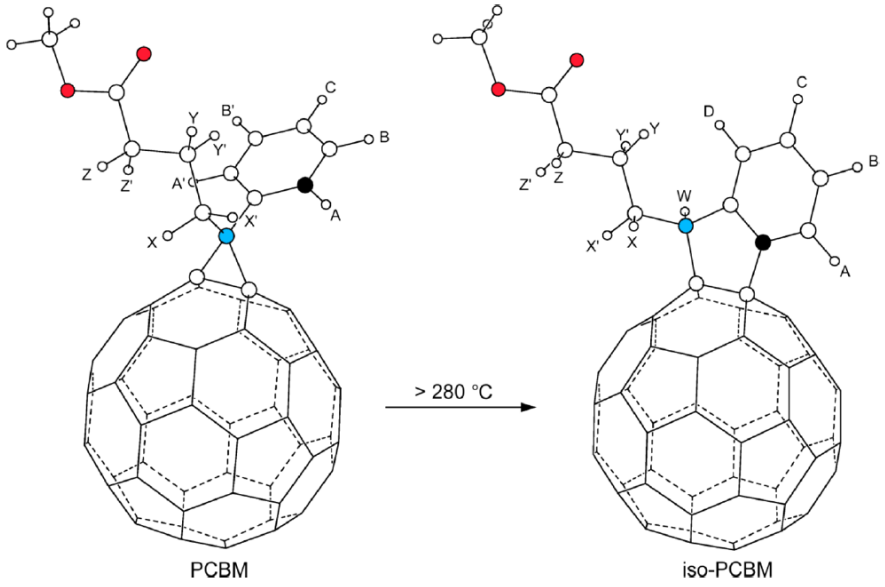

FIGURE 5-1:: DFT-MODELLED, THERMAL ISOMERIZATION OF PCBM TO ISO-PCBM, WITH NMR-ASSIGNED HYDROGEN ATOMS. ISOMERISATION WAS FOUND TO OCCUR ABOVE 280˚C, WHERE 80% IS ISOMERISED BY HEATING FOR 20 MIN AT 340° [19]

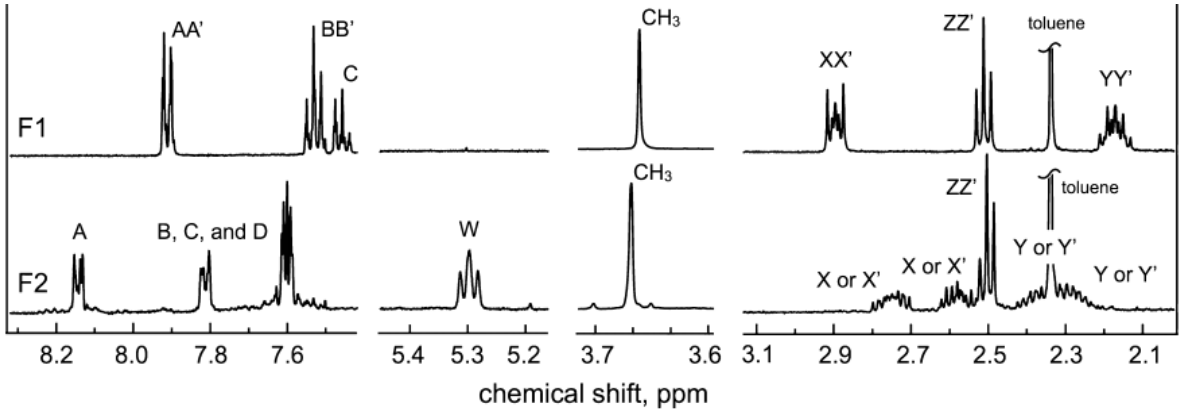

FIGURE 5-2: 1H NMR SPECTRA (400 MHZ, CDCL3 SOLVENT) OF PCBM (TOP); AND ISO-PCBM (BOTTOM). THE LARGE SINGLET PEAKS AT 2.36 PPM ARE A RESULT OF TOLUENE IMPURITIES.[19] **THE TWO PLOTS SHOW THE EFFECTIVENESS OF IDENTIFICATION VIA 1H NMR.**

Whilst studies indicate that PCBM and its isomer have similar electrochemical properties[19], ^{1}H NMR is effective at identifying and distinguishing the two isomers, as seen in Figure 5-2, where variation in the PCBM peaks between the chemical shift of 7.4 and 8.2 can be clearly observed. Therefore, analysis of the variation in PCBM, when transferred via ns BB-LIFT, where significant heating (Titanium film can

reach >1700 ˚C) is liable to occur, will enable further understanding of the potential damage to the molecular structure of desorbed molecules under these conditions.

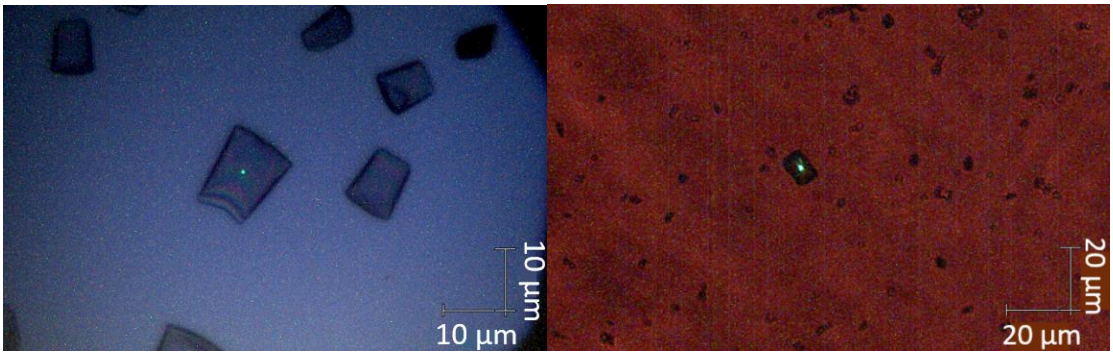

FIGURE 5-3: OPTICAL IMAGE OF $PC_{60}BM$ WITH THE RAMAN LASER (BRIGHT SPOT) FOCUSED ON THE CENTRE OF A CRYSTAL. THE CRYSTALS WERE MEASURED TO BE APPROXIMATELY 10 µM ACROSS AND 5 µM HIGH (HEIGHT MEASURED USING CONFOCAL FOCUSING TOPOGRAPHY TECHNIQUES). THE IMAGE ON THE RIGHT IS OF SOME OF THE TRANSFERRED PCBM, UNDER RED LIGHTING TO AVOID OLIGOMERIZATION.

As the PCBM was transferred to the surface via the sandwich method (methods 2.2.2), large crystals, typical of PCBM, were formed, as can be seen in Figure 5-3(a). The crystals are also successfully transferred, as seen in Figure 5-3(b). The Raman spectra, before and after transfer, are shown in Figure 5-4. From the Raman spectra (514 nm excitation laser), it can be seen that some light-induced oligomerisation has taken place, creating a shoulder on the central peak at 1460 cm^{-1}.[19] This is likely due to exposure between chambers, as-well as whilst trying to find the PCBM upon the receiver plate. The shift does not correspond with complete loss of the phenyl butric acid ester, which would result in a shift towards 1469 $cm^{-1,}$ which is the characteristic C_{60} peak.

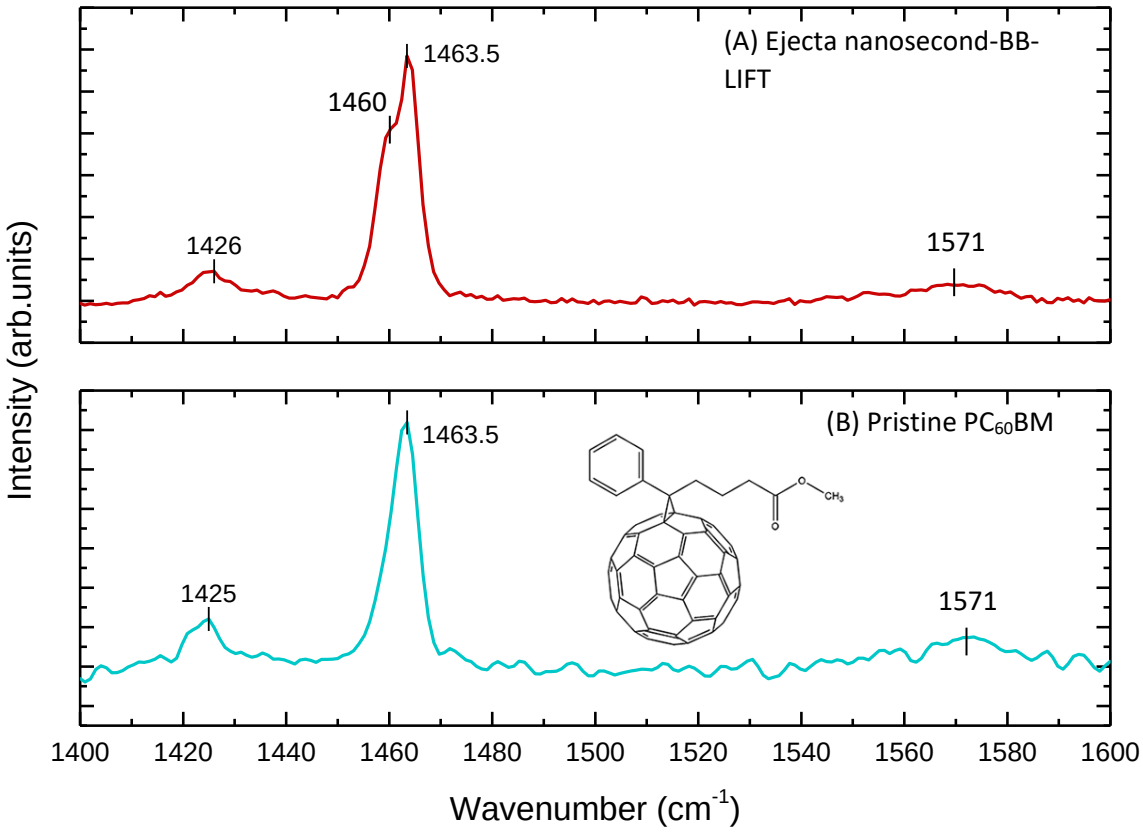

FIGURE 5-4: RAMAN DATA RECORDED USING A RENISHAW INVIA RAMAN MICROSCOPE, AT AN EXCITATION WAVELENGTH OF 514 NM. (A) EJECTA COLLECTED FROM NANOSECOND-BB-LIFT. (B) PRISTINE $PC_{60}BM$ STANDARD (>99% PURE M111 OSSILA).

The NMR spectra were measured with a Bruker Avance, 4-channel 800MHz spectrometer (18.8 T), using a 5mm, triple-resonance CryoProbe, optimised for H NMR. The deposited PCBM was dissolved in 0.6 ml of deuterated chloroform, and analysed over 1.5 hours. Due to the low signal from the transferred PCBM (very low concentration), a tailored double pre-saturation of the $CDCl_3$ carbon-12 peak was performed. The data shown in Figure 5-6 show clearly defined PCBM peaks, with no detection of isomerisation. However, due to the very high detection efficiency, some impurities can be seen at 7.43 ppm. This indicates that the PCBM does not undergo thermal isomerisation during the LIFT experiment. Therefore, whilst the PCBM may undergo some heating due to the ns-BBLIFT, it is not significant enough or over a long enough time period to cause destabilisation of the molecule. Thus, nanosecond BB-LIFT could potentially be applied to printing or gas phase analysis of other functionalised fullerenes and

thermally unstable molecules, after further testing.

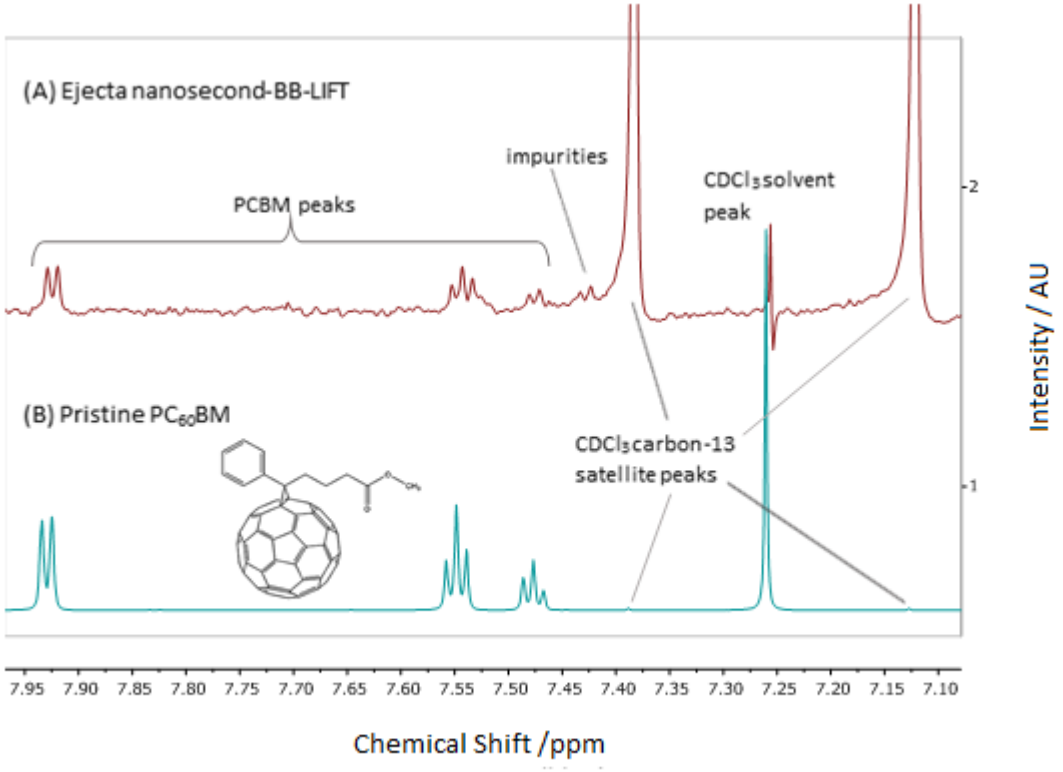

FIGURE 5-5: ^{1}H NMR SPECTRA, RECORDED USING A BRUKER AVANCE 800 MHZ SPECTROMETER. (A) EJECTA COLLECTED FROM NANOSECOND-BB-LIFT, WHERE A DOUBLE PRE-SATURATION. WAS PERFORMED FOR THE TRANSFERRED PARTICLE NMR TO REDUCE THE $CDCL_3$ PEAK. (B) PRISTINE $PC_{60}BM$ STANDARD (>99% PURE). NS BB-LIFT AT ~250 MJCM^{-2} FROM ~250 NM TI FILM.

As discussed in Chapter 3, Figure 3-9, the surface of the titanium film does not reach its full temperature until ~13 ns after the ns pulse begins to irradiate the film. The lower section of the film will rise in temperature more quickly than the upper layer, and thus begin to expand. The lack of detectable heating of the desorbed particles indicates that they may be removed before the surface layer can transfer this energy to the particles. From Figure 3-9 there is a reduction in the rate of heating after 7ns, which would result in a reduced velocity of expansion. Thus, the particles on the surface may be moving with more velocity than the expanding film. It's possible this is why a non-significant amount of thermal energy is transferred to the surface particles.

5.2 Auroshells

Gold coated silicon nanoparticles are a much larger system than the fullerene molecules, with a diameter of 150 nm (100 nm silicon core, 25 nm thick gold coating). Aerodynamic lenses are the typical means of streaming gas phase nanoparticles into a beam; however, the requirements of carrier gases and pumping may limit the available applications.

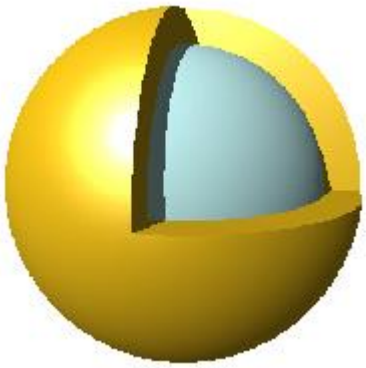

FIGURE 5-6: SCHEMATIC OF AUROSHELL, SHOWING SILICON CORE (50 NM RADIUS) WITH THIN SURROUNDING LAYER OF GOLD (25 NM RADIUS).

Figure 5-7 is a scanning electron microscopy image of the auroshells on a titanium film before transfer; whilst Figure 5-8 is an example image of the auroshells post transfer. Gold has a melting point of 1064˚C, however, it was observed that if SEM focused upon the particles, they would start to disintegrate within seconds.

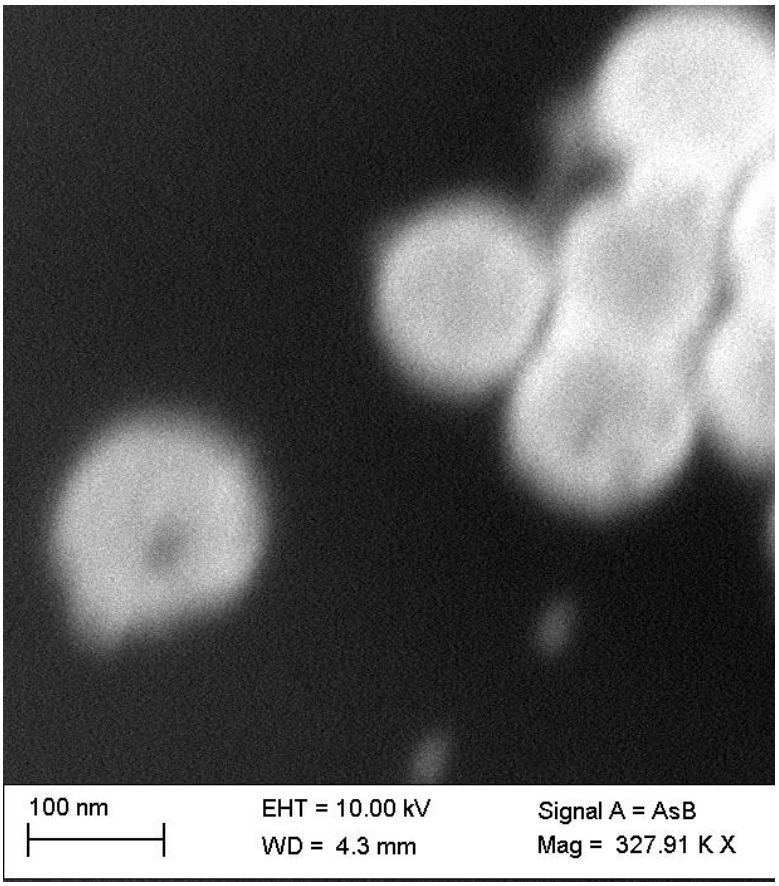

FIGURE 5-7: GOLD-COATED SILICON NANOPARTICLES BEFORE NS BB-LIFT DESORPTION. NS BB-LIFT AT ~250 MJCM^{-2} FROM ~250 NM TI FILM

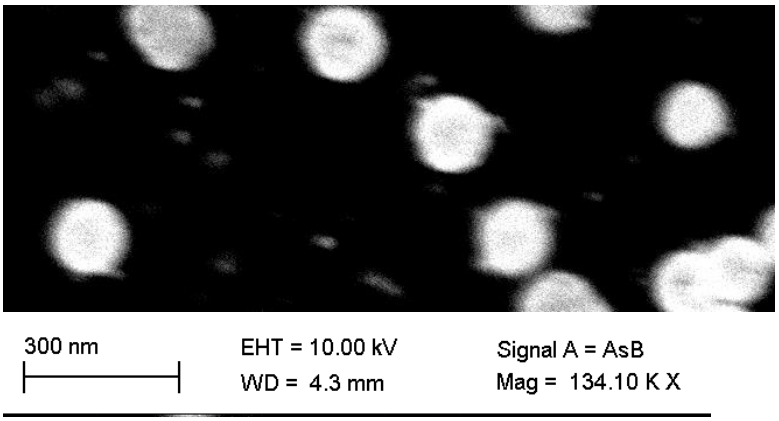

FIGURE 5-8: GOLD-COATED SILICON NANOPARTICLES POST NS BB-LIFT DESORPTION. NS BB-LIFT AT ~250 MJCM^{-2} FROM ~250 NM TI FILM.

The images show the coating remains intact after transfer, as can been seen by their high intensity, and similar colouration. Furthermore, the size of the nanoparticles remain uniform with no signs of cracking. There is some material residue, approximately 10 nm wide however, this residue is visible in the gold nanoparticle deposits both before and after transfer. XRD spectra were also taken on positions within the blisters previously containing an auroshell coating, as shown in Figure 5-9 and Figure 5-10, which found no evidence of gold upon the surface, indicating that little to no gold was broken off or melted into the blisters; whereas, a spectrum taken upon a non-blistered region indicates a high proportion of gold.

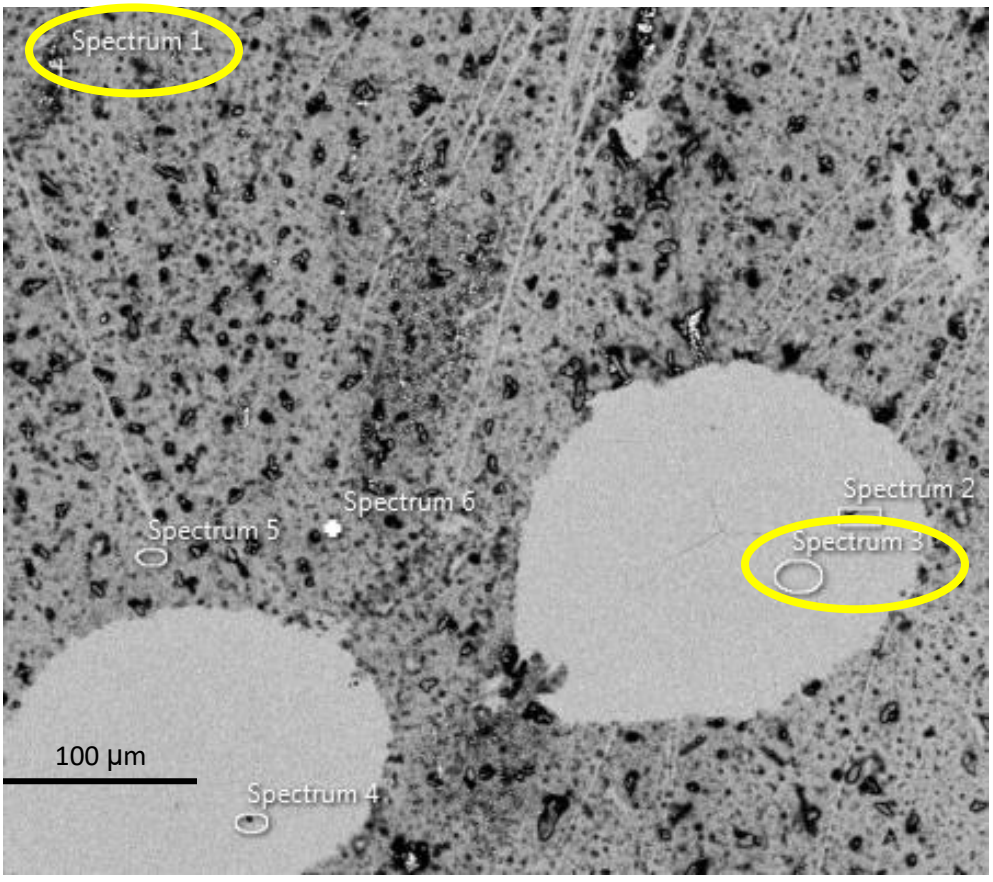

FIGURE 5-9: SEM IMAGE OF XRD SPECTRUM LOCATIONS. FOR NS BB-LIFT AT ~250 MJCM^{-2} FROM ~250 NM TI FILM WITH AUROSHELL COATINS.

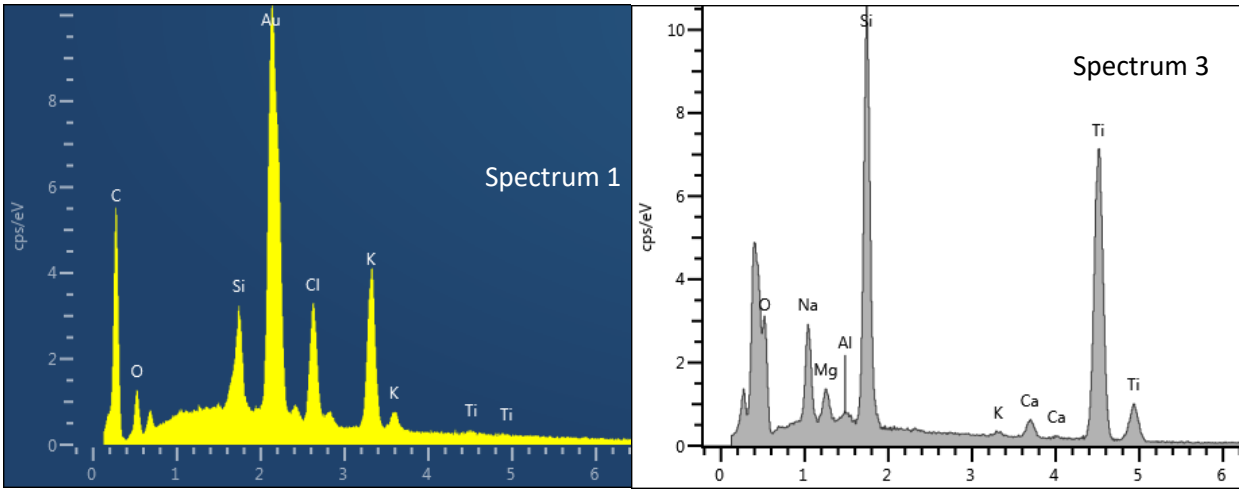

FIGURE 5-10: EDX SPECTRA IDENTIFYING PREDOMINANT MATERIAL IN THE TARGET AREA. SPECTRUM 1 IS AN AREA OFF THE BLISTER. SPECTRUM 2 IS AN AREA ON THE BLISTER. THE SILICON DETECTED IN BOTH IS LIKELY DUE TO THE X-RAYS PENETRATING THE TITANIUM FILM, AND DETECTING THE GLASS BELOW. NO GOLD FROM THE AUROSHELLS IS DETECTED FOR THE SPECTRA ON THE BLISTERS AS REPRESENTED BY SPECTRUM 3.

5.3 Carbon nanotubes

Carbon nanotubes are often described as quasi-1-D materials due to the orders of magnitude difference between their diameter and length. Transfer of these materials has been accomplished successfully using a LIFT system. However, the transferred MWCNT were imbedded within polyvinylpyrrolidone and poly(acrylic acid) forming a 1.5µm polymer and MWCNT compound.[39] Similarly, single-walled CNT have been transferred whilst encapsulated within a silver paste.[78] Therefore, the transfer was not of pure and dry CNTs.

Transfer of pure SWCNT has been accomplished via LIFT from a triazine polymer substrate.[40] However, this technique vaporises and transfers some of the triazine alongside the CNT, and the resulting I(D)/I(G) ratio, as ascertained by raman spectroscopy, rose from 0.098 to 0.112, indicating the nanotubes were not transferred without attaining some damage. Thus, each of these methods contains inherent problems due to impurities, based upon the CNT encapsulation and damage to the CNT from ablated triazine plasma or the laser itself.

The BB-LIFT technique differs from previous published laser transfer attempts, as the particles are un-encapsulated and free of impurities, whilst also protected from thermal or ion damage during the laser transfer.

Three different methods of transfer were successfully achieved. SWCNT and MWCNT were spin coated on separate ~200 nm thick titanium surfaces, as described in Chapter 2. In another experiment, a sample of MWCNT was grown directly on the surface of a multi-layered substrate consisting of ~10 nm titanium base, ~200 nm nickel coating, ~5 nm silicon separating layer and an ~1 nm iron catalytic layer as used for previous CVD CNT growth.[79] These were then transferred via fs BB-LIFT to titanium coated receiver plates placed 3.6 mm away.

The deposits from the spin-coated prefabricated CNT were imaged via AFM, as their concentration was too low for visibility via SEM atop the titanium, whilst the CVD grown MWCNT were imaged with SEM, as their high density and rough topology made AFM inviable.

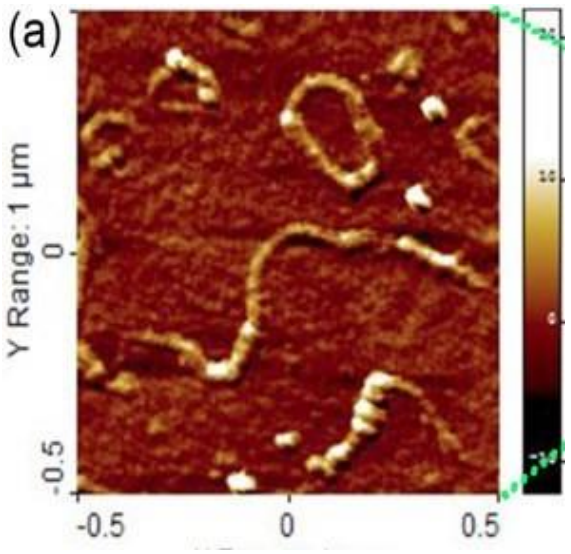

FIGURE 5-11: EXAMPLE AFM IMAGE OF MWCNT, DEPOSITED UPON TITANIUM SURFACE VIA FS BBLIFT WITH A FLEUNCE OF ~200-300 MJCM^{-2} ~250 NM TI FILM.

From the AFM scans of the nanotubes, it's possible to determine the radius of the nanotubes before and after deposition as 3.3 ± 0.6 nm and 9.5 ± 1 nm for the spin coated SWCNT and MWCNT respectively before transfer. The diameter of the nanotubes after transfer remains similar, at 3.1 ± 0.9 nm and 8 ± 3 nm respectively. The SEM images show effective transfer of large bundles of nanotubes transferred from the CVD grown system, as seen in Figure 5-12. However, it can also be observed that other ribbonlike structures were transferred alongside the MWCNT. Whilst analysis of these non-CNT materials proved difficult, It's believed they may be silicon from the separation layer.

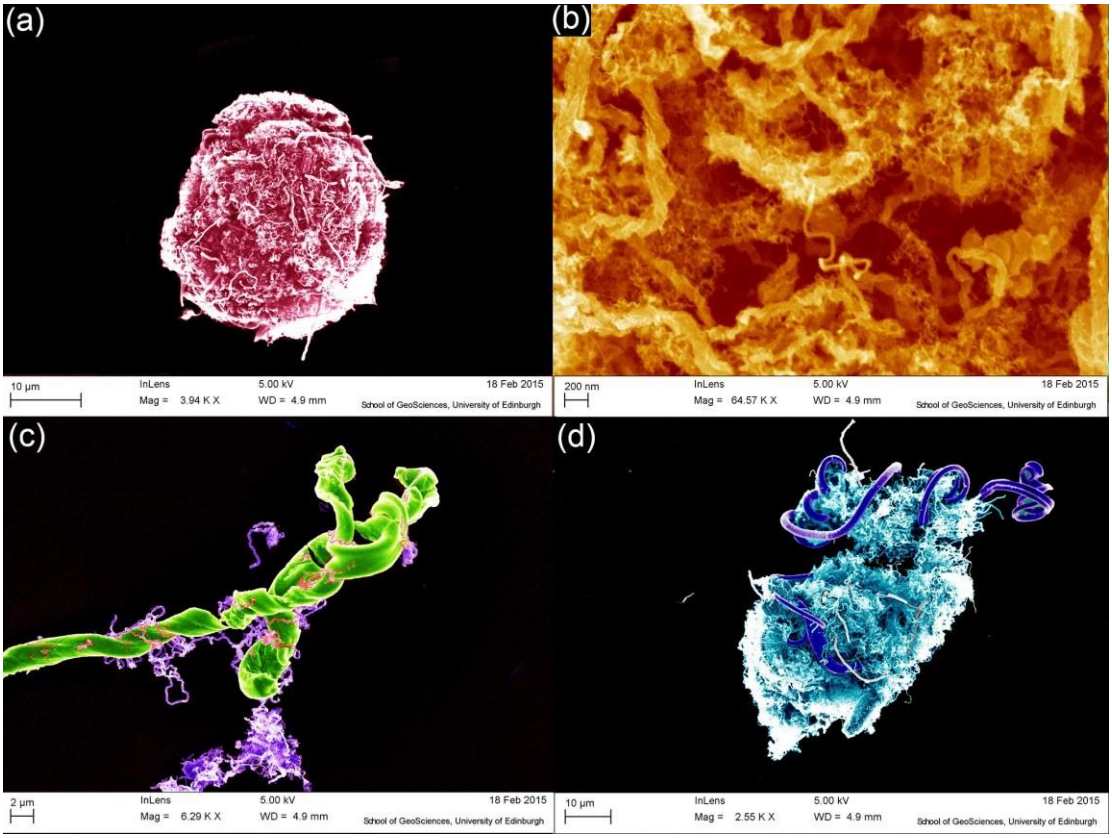

FIGURE 5-12: FALSE COLOUR SEM IMAGE OF TRANSFERRED CVD GROWN MWCNT. THE FS PULSE FLUENCE WAS 600 MJCM^{-2} FROM MULTI-LAYERED FILM DESCRIBED IN CHAPTER 6

Raman spectra of the transferred and non-transferred CNT were obtained, which provide a diagnostic of any defects in the CNT after transfer, where an example is given in Figure 5-13.

From these spectra, the I(D)/I(G) ratios for the MWCNT were found to be largely similar or lower than previously. The CVD grown MWCNT had a ratio of 0.9 ± 0.1 and 0.8 ± 0.1 before and after transfer respectively, thereby maintaining a similar if not decreased level of imperfections. As for the spin-coated MWCNT, the ratio appears to have decreased from 0.99 ± 0.08 to 0.5 ± 0.2 after transfer. This is an interesting outcome, and likely to be due to the reduced concentration of MWCNT upon the receiver plate, which reduced the signal strength. Similarly, the transferred SWCNT concentration was too low to obtain a strong enough reading to measure the I(D)/I(G) ratio.

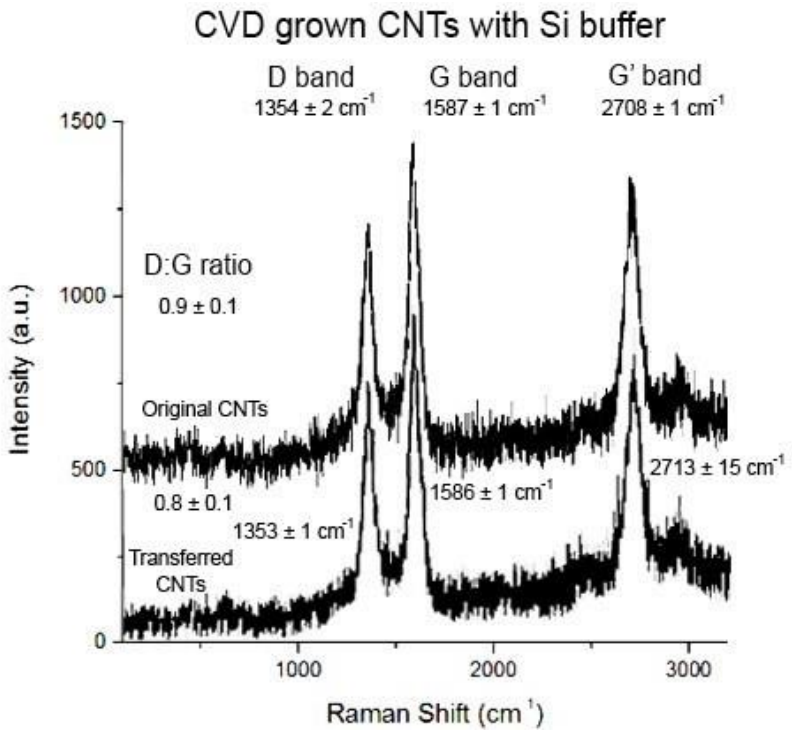

FIGURE 5-13: RAMAN SPECTRA OF CVD GROWN MWCNT, BEFORE AND AFTER FS BBLIFT TRANSFER. THE PLOT INDICATES VIA THE UNCHANGED D:G RATIO THAT THE NANOTUBES WERE UNDAMAGED BY THE TRANSFER.

The BB-LIFT technique is an improvement upon the previously attempted CNT transfer technique found within the literature, because of its ability to transfer the 1-D materials, showing no evidence of induced damage and lack of reliance upon imbedding the CNT within another system being simultaneously transferred.

5.4 Macro/crystalline structures

It has been shown that BB-LIFT can transfer molecular and nanoparticle materials without damage. However, it also appears capable of transferring crystalline structures such as PCBM crystals, as seen from Figure 5-3. This shows a large crystal ~ 10 µm in size, transferred from the donor film to the receiver plate, 2mm away. From x-ray crystallography studies of glass transition temperatures by Cho et al[80], it's known that PCBM crystals become amorphous above 200˚C when undergoing heating at 10˚C/minute. Thus, it can be assumed that the desorbed crystalline PCBM was not given enough energy to significantly raise the temperature above 200˚C during transfer, deposits more akin to splattered crystals would have been observed.

Similar results were found during transfer of C_{60} thin films (150-180nm), since the films appeared to transfer as macro scale thin films, as seen in Figure 5-14. These deposits were studied with Raman spectroscopy for ns and fs BB-LIFT transfer, as shown in Figure 5-15, which indicated they are deposits of fullerene. Fullerene crystals, unlike PCBM, undergo direct sublimation before melting. Therefore, it cannot be used as evidence for a gentle low heat transfer. However, their relatively flat and macro scale transfer indicates the possibility for other thin film transfer as discussed in Chapter 5 section 5.

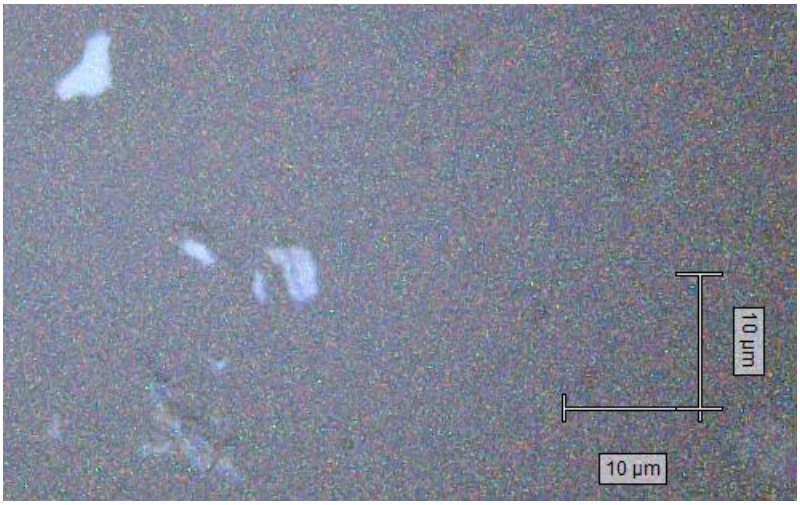

FIGURE 5-14: FS BB LIFT TRANSFERRED FULLERENE THIN FILM AT THE EDGE OF MULTIPLE DEPOSITS FROM A TITANIUM FILM ~330NM THICK WITH A FEMTOSECOND LASER WITH A FLUENCE OF 200 MJCM^{-2} .

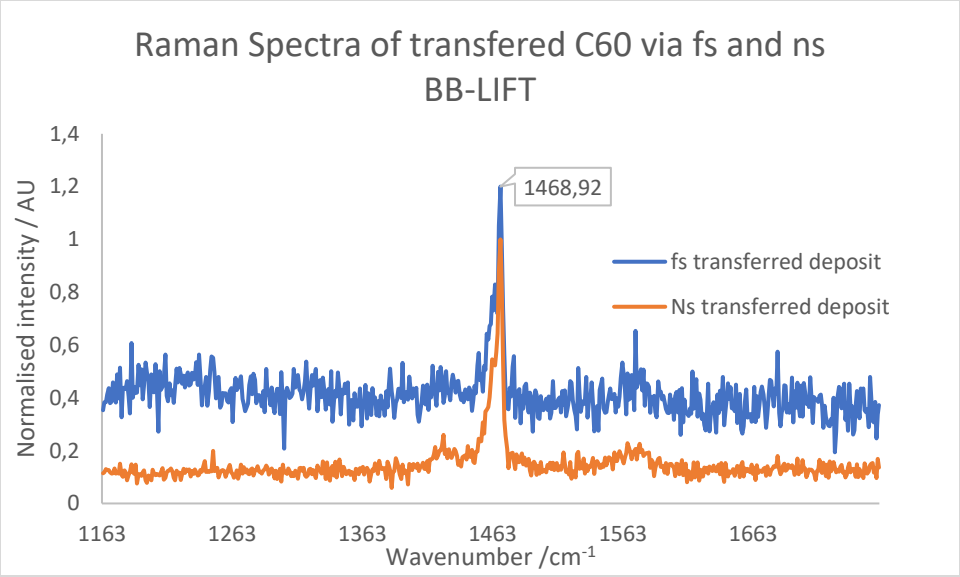

FIGURE 5-15: RAMAN SPECTRA TAKEN WITH 514NM LASER UPON TRANSFERRED FULLERENE THIN FILMS VIA NS AND FS BB LIFT.

The successful transfer of thin films and crystalline structures opens further possibilities for BB LIFT. However, it does present a potential problem with regard to the method of donor film surface coverage, as BB-LIFT is likely to transfer the material as clusters instead of individual molecules. There is the potential for this issue to be overcome by gentle surface heating to raise the molecules energy close to their lattice binding energy, or through secondary gas phase cluster size reductions.

5.6 Molybdenum diselenide

Successful transfer of thin films is demonstrated in the previous section. However, the transferred films are >100nm in thickness. Transfer of 2-Dimensional films, which have thicknesses on the atomic scale, tend to behave drastically different than their bulk composites, making them key areas of modern research. Molybdenum diselenide, $MoSe_2$, is an example of one such 2D material with potentially very useful opto-electrical properties stemming from its semi-conductive nature. In order to study the potential of BB-LIFT to cleanly transfer 2-D crystals, a few films of titanium 220-350nm thick were coated in molybdenum diselenide by the Kitaura research group at Nagoya University, via dispersal from solution. An example of a typical deposit is shown in Figure 5-16.

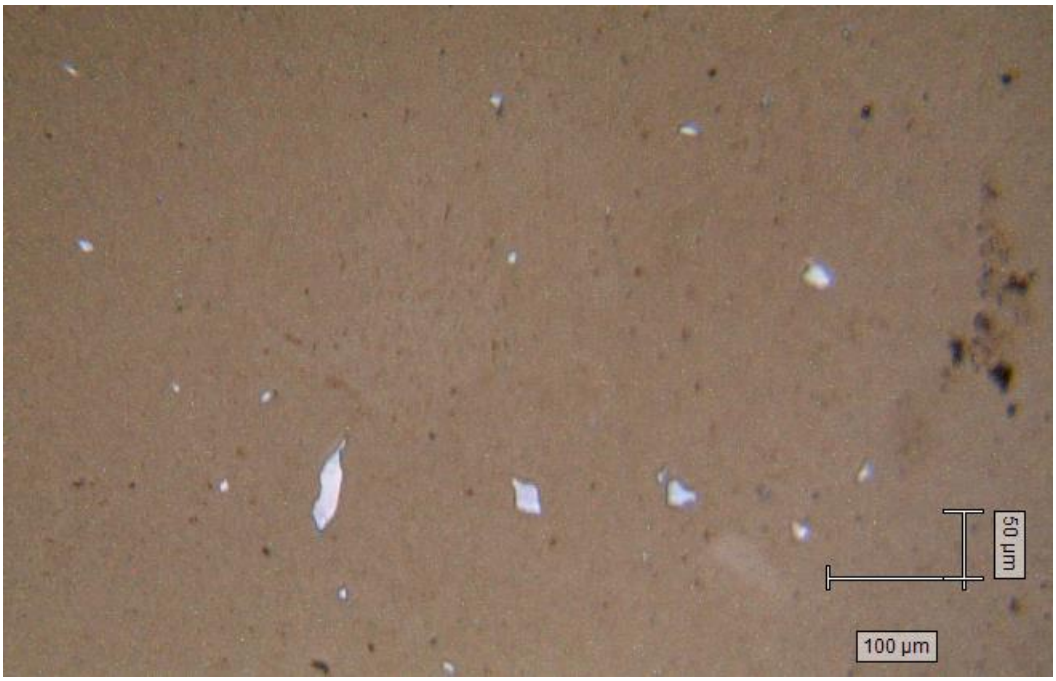

FIGURE 5-16: $MoSe_2$ CRYSTALS, ARRANGED ON TITANIUM DONOR FILM SURFACE, IMAGED VIA AN OPTICAL MICROSCOPE.

A position marker was made on the donor film by using multiple high intensity fs laser pulses. However, this caused ablation of the silicon receiver film, which patterned much of the $MoSe_2$ in silicon nanoparticles. This silicon nanoparticle deposition was very dense near the marker, and still prevalent at the furthest distances from the marker as seen via AFM in Figure 5-17.

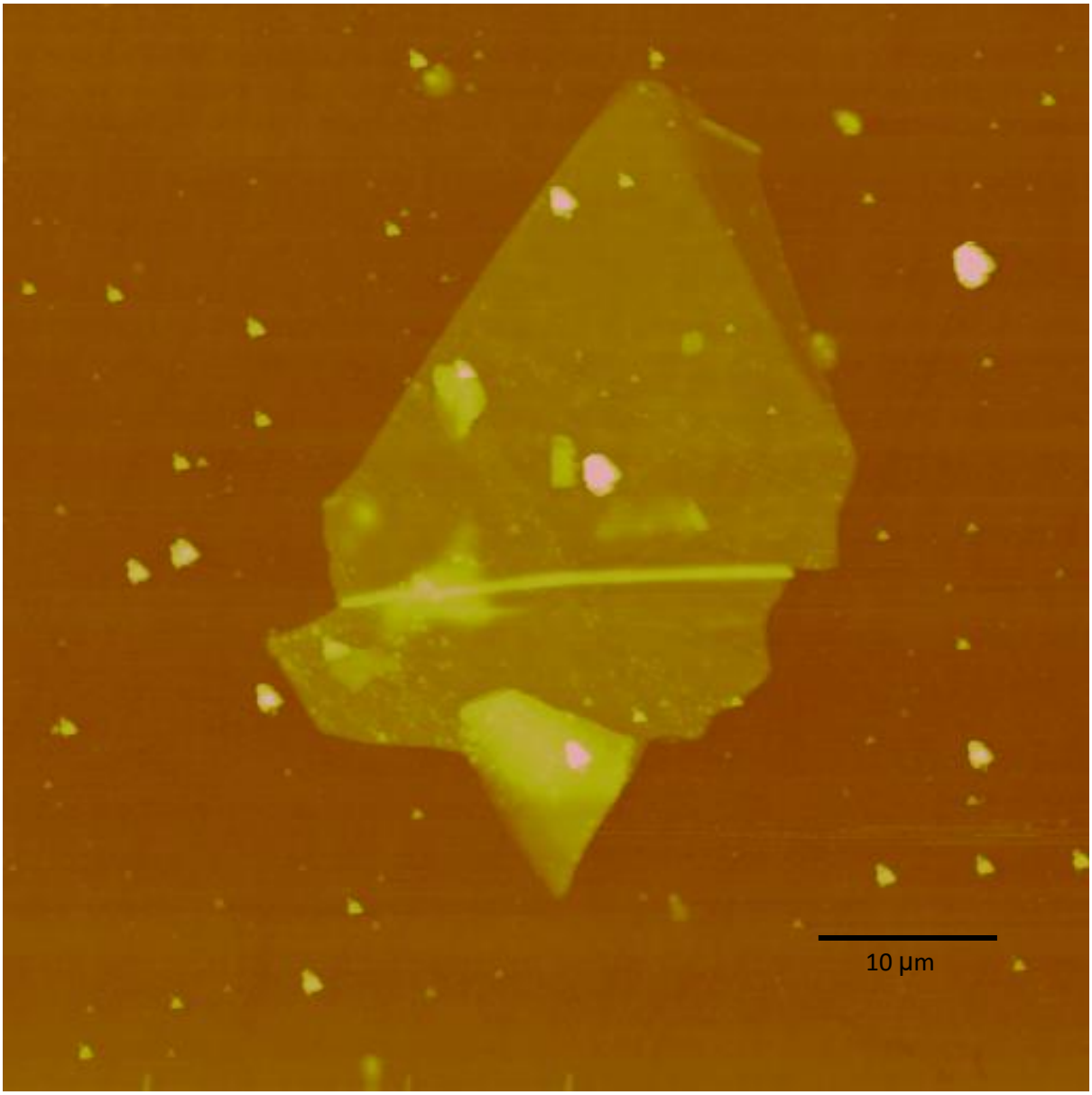

FIGURE 5-17: AFM SCAN OF $MoSe_2$ FILM ON TI DONOR FILM SURFACE. THE SURFACE HAS ALSO BEEN COATED IN SMALL NANOPARTICLES OF SILICON FROM ABLATION BACKSCATTER OF THE RECEIVER PLATE.

The $MoSe_2$ thin films were transferred to silicon and glass receiver plates 2mm from the donor film, via fs BB-LIFT. As can be seen in Figure 5-18, the ablated silicon nanoparticles were also transferred, creating a rough texture on the otherwise flat and successful $MoSe_2$ transfer. It can also be seen that the size of the transferred crystals can be within the tens of micrometer scale, thus fitting within the fs

blister. Figure 5-19 demonstrates that if the $MoSe_2$ is larger than the blister, the 2D film is still transferred; however, it may break upon desorption from the titanium donor film.

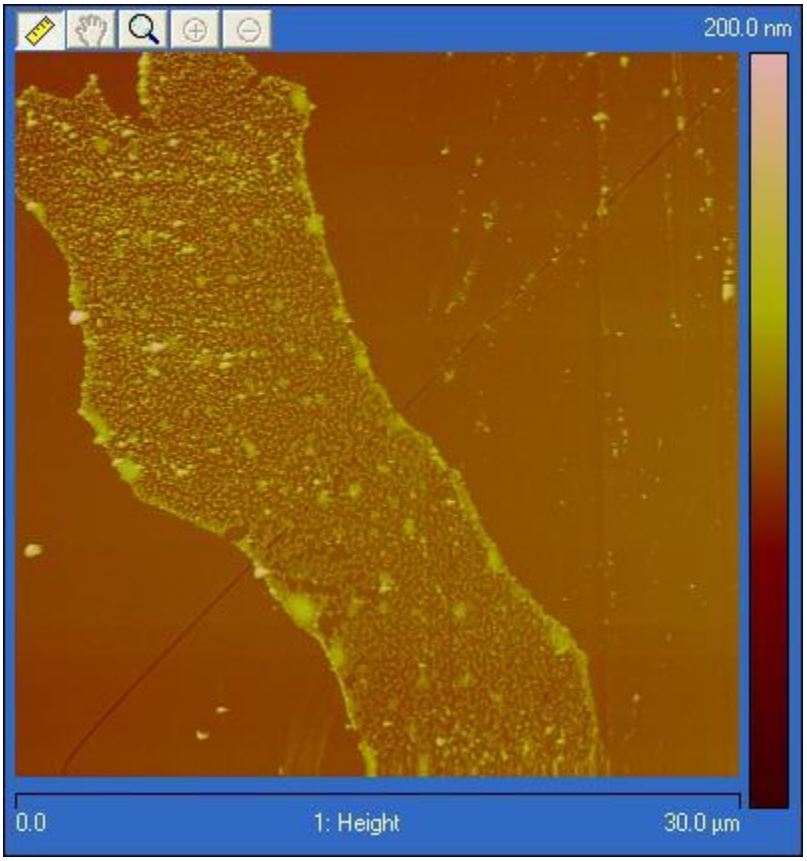

FIGURE 5-18: TRANSFERED $MoSe_2$ ON GLASS RECEIVER PLATE. THE $MoSe_2$ SURFACE HAS A ROUGH TOPOGRAPHY, DUE TO THE ABLATED SILICON NANOPARTICLES ON THE GLASS $MoSe_2$ SIDE OF THE FILM.

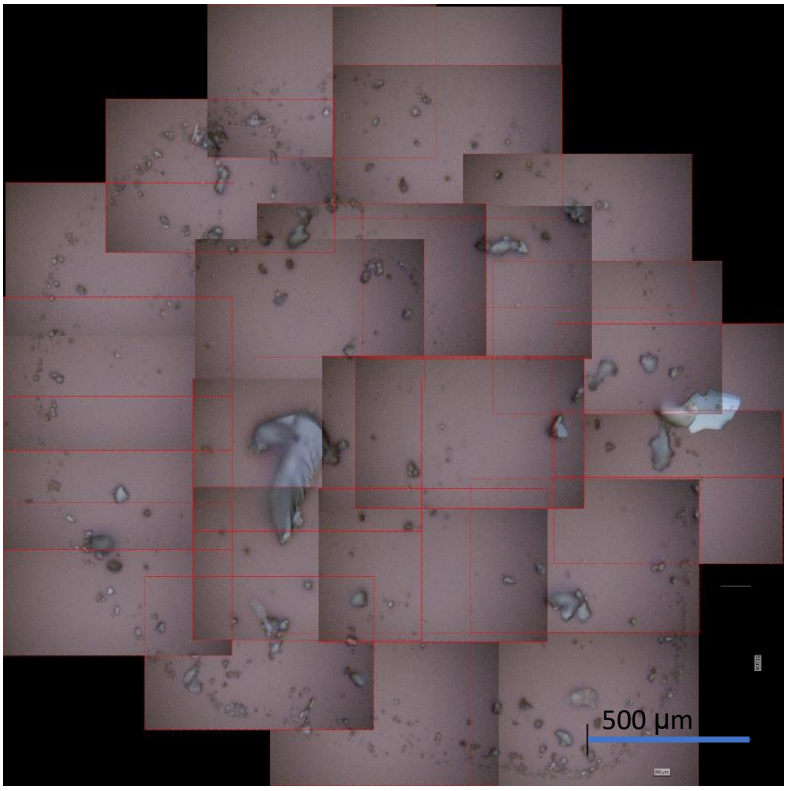

FIGURE 5-19: FRAGMENTED $MoSe_2$ ON SILICON RECEIVER PLATE. THE LARGE CENTRAL FRAGMENT WAS NOT DEPOSITED PARALLEL TO THE RECEIVER PLATE, AS SEEN FROM THE BLURRING OF THE CENTRAL THIN FILM. A RING OF FRAGMENTS SURROUNDING THIS FRAGMENT ALSO SUGGESTS THAT THE FILM WAS BROKEN CLOSER TO THE DONOR FILM ALLOWING THE SPREAD OF THE FRAGMENTS.

The $MoSe_2$ samples were measured via Raman spectroscopy with a 514nm wavelength before and after transfer, demonstrating that the crystals are unchanged, as seen in Figure 5-20.

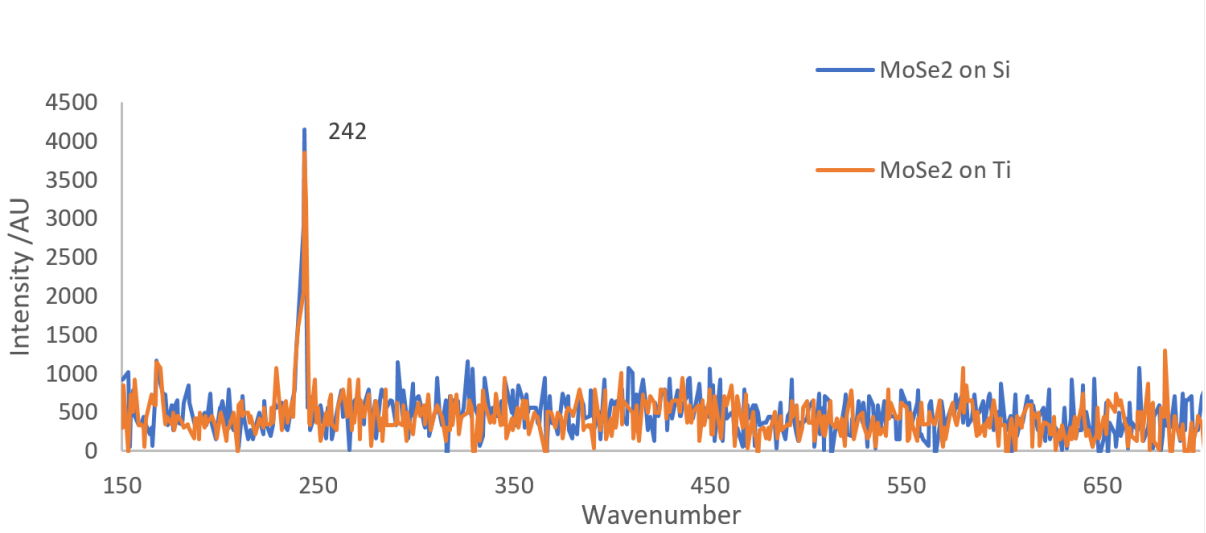

FIGURE 5-20: RAMAN SPECTRA OF $MoSe_2$ ON DONOR FILM (TI) AND RECEIVER PLATE (SI), TAKEN WITH 514 NM WAVELENGTH. THUS SHOWING THAT THE $MoSe_2$ REMAINS UNCHANGED DURING THE TRANSFER. TRANSFERRED VIA FS BB-LIFT AT ~250 MJCM^{-2} FROM ~270 NM TI FILM

The entire donor film was scanned before transfer, to identify the crystals before transfer. Many of the transferred crystals were also imaged, to compare to the original film. A successful transfer of a crystal before and after transfer can be seen in Figure 5-21, where the image on the donor film has been inverted to provide the same orientation as the deposited image.

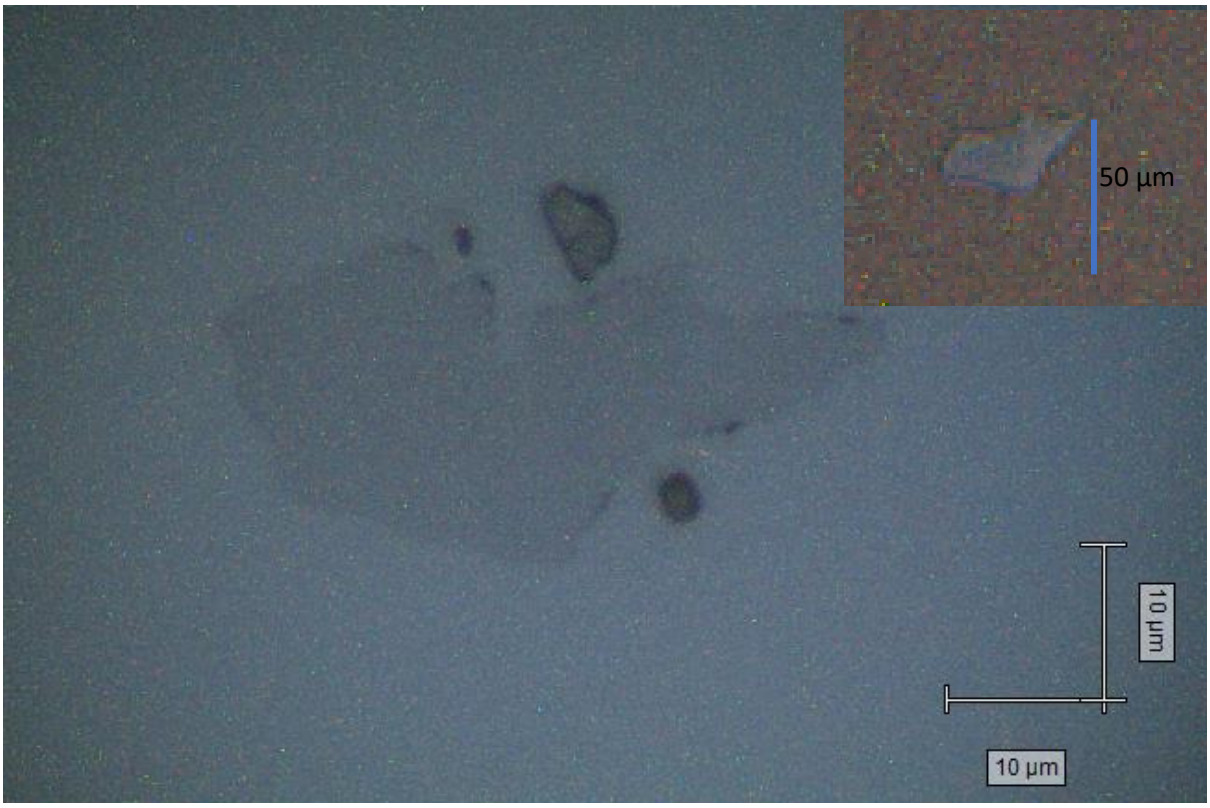

FIGURE 5-21: IMAGE OF TRANSFERRED $MoSe_2$ AFTER TRANSFER (CENTER), AND BEFORE TRANSFER (TOP RIGHT). THUS INDICATING MINIMAL DAMAGE TO A LARGE FRAMENT.

In this instance, the film appears to have fragmented slightly during transfer; however, the majority of the film remains intact. Unfortunately, the resolution of the donor film image is quite poor, due to the necessity of imaging at lower magnification and storing as a lower quality image.

It has been demonstrated that the BB-LIFT technique can successfully transfer a large variety of materials into the gas phase, or printed onto another substrate. The technique does not heat the sample to a high temperature, as demonstrated by PCBM molecular and crystal transfer. It can also transfer complex nanoparticles without damage, as demonstrated via the 150 nm auroshells. Furthermore, it can transfer materials of multidimensional complexity, without causing undue structural damage, as illustrated by CNT, $MoSe_2$ and fullerene crystals.

5.7 Molybdenum disulphide

2D Molybdenum disulphide is a potentially very useful material with uses in dehydrosulphurisation[81], photosensitive thin films[23] and even lithium-ion batteries[25]. The ability to transfer 2D MoS_2 can potentially advance each of these areas, in terms of study or production.

The MoS_2 was grown using CVD by the Warner research group, as described in the cited paper.[82] It was transferred to a 250nm titanium film on a 1mm glass substrate, with a dry transfer method, utilising a dry transfer technique, as described by Sheng et al[83]. The PMMA coating on the MoS_2, was removed by soaking in acetone for three hours, followed by a further acetone rinse.

The Raman spectra were measured before and after transfer to a plasma-cleaned glass receiver plate, 3mm from the donor film. The MoS_2 was transferred via fs laser pulses of fluence 215 $mJcm^{-2}$ with blister size approximately 80 µm, as seen in Figure 5-22. It can be seen that no MoS_2 remains in the regions of and surrounding the blisters.

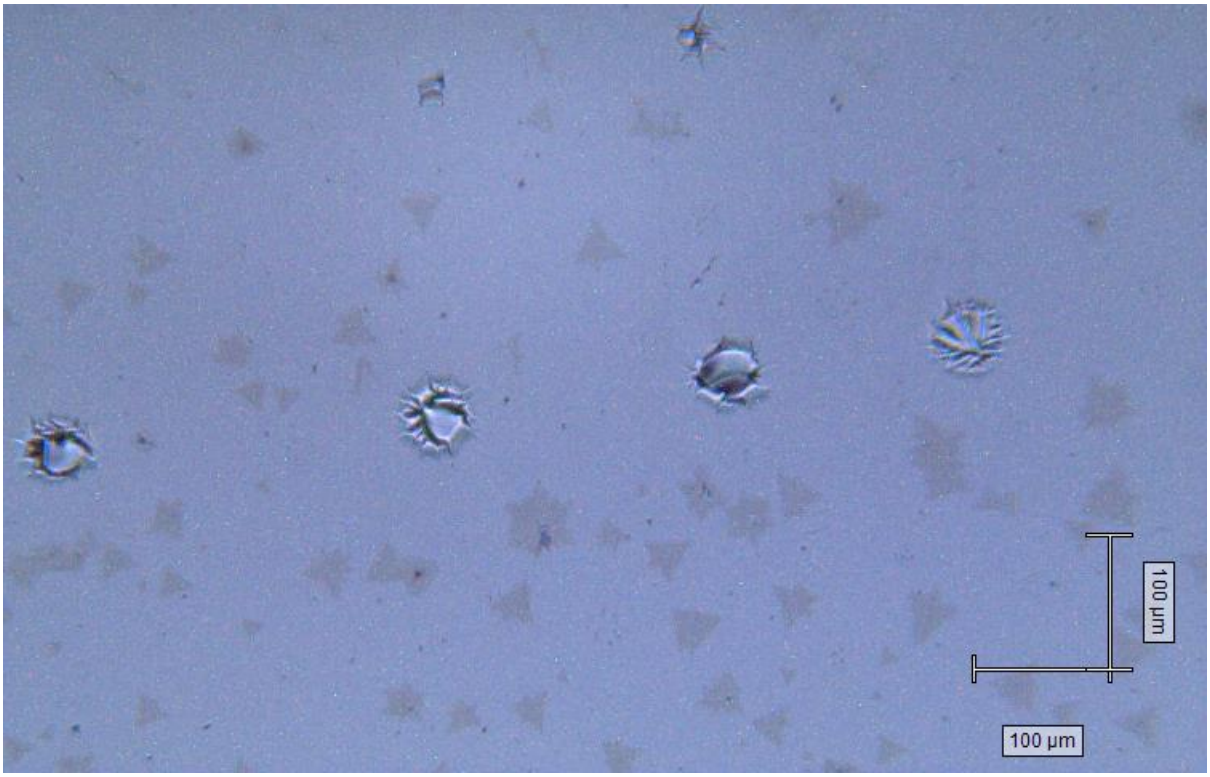

FIGURE 5-22 EXAMPLE BLISTERS ON TITANIUM SURFACE, IN THE REGION OF THE MoS_2 CREATED WITH AN FS PULSE OF FLUENCE 215 MJCM^{-2} ON A 260 NM TI FILM.

The procedure to transfer the MoS_2 was successful at transferring two-dimensional films smaller than the size of the blister. Figure 5-23 shows Raman spectra of MoS_2, before BB LIFT transfer (blue) and after transfer (green). From Changgu Lee et al. and Hong Li et al. it's known that, as the number of layers increases, the separation within the Raman spectra increases due to interlayer electron interactions.[84,85] The Raman peak separation with a 514 nm activation laser of single and bi-layer MoS_2 are 18.7 cm^{-1} and 21.6.[84] We have measured peak separation as 20 ± 1 and 19 ± 1, before and after transfer. The measured Raman peaks also match appropriately at 384-385 ± 0.5 and 404.7 ± 0.5. Thus, transfer of 2D MoS_2 was successful.

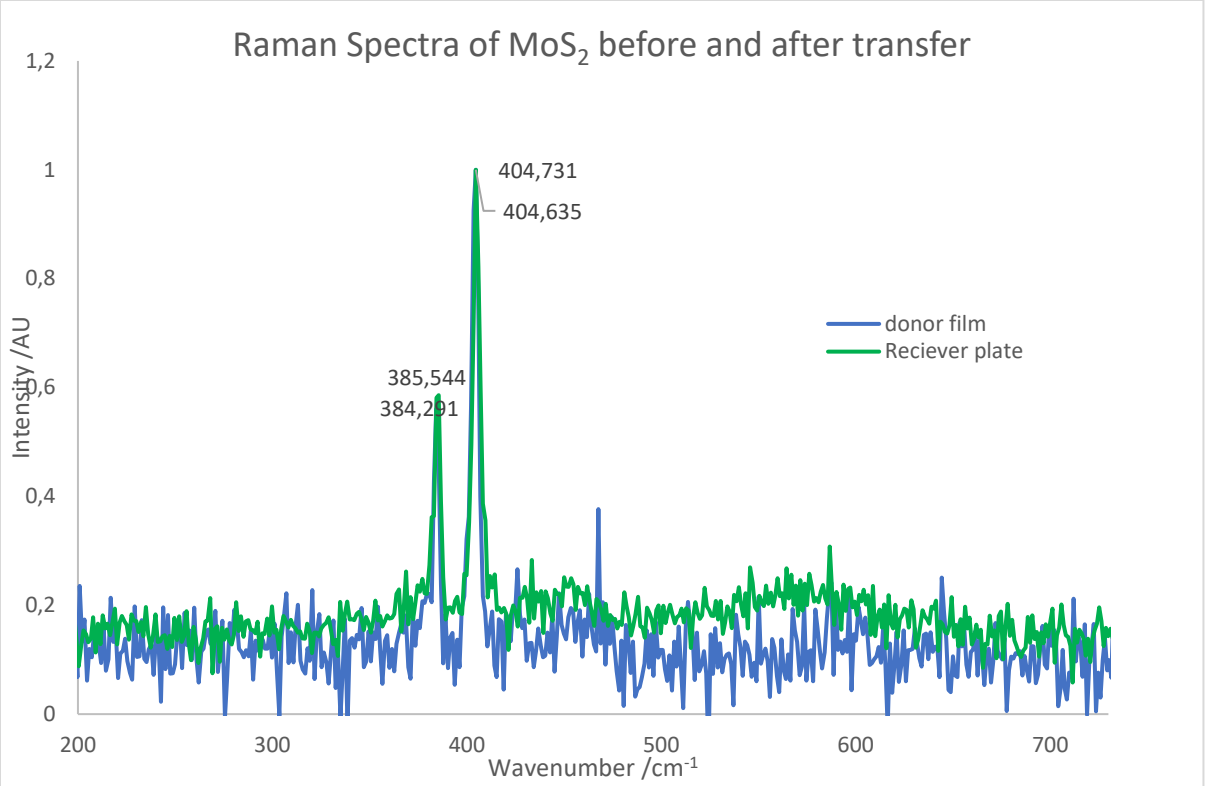

FIGURE 5-23: RAMAN SPECTRA OF MoS_2 CRYSTALS TAKEN WITH A 514 NM LASER, BEFORE AND AFTER. THE SPECTRA INDICATE THAT THIN FILMS ARE CAPABLE OF BEING TRANSFERRED VIA BB LIFT WITHOUT ALTERING THEIR TWO DIMENSIONALITY.

AFM scans of the films before and after transfer, with associated cross sections giving the height of the films, indicate that the initial films were ~3 nm thick on the donor film and a sample found on the receiver film was ~6 nm thick, indicating a single layer on CVD grown deposit and 2 layers on the receiver film. There is potential that there are more single layered MoS_2 films on the receiver plate, as indicated by multiple Raman spectra of different samples. However, due to the transparency of the receiver plate, detection of the deposited MoS_2 was extremely difficult.

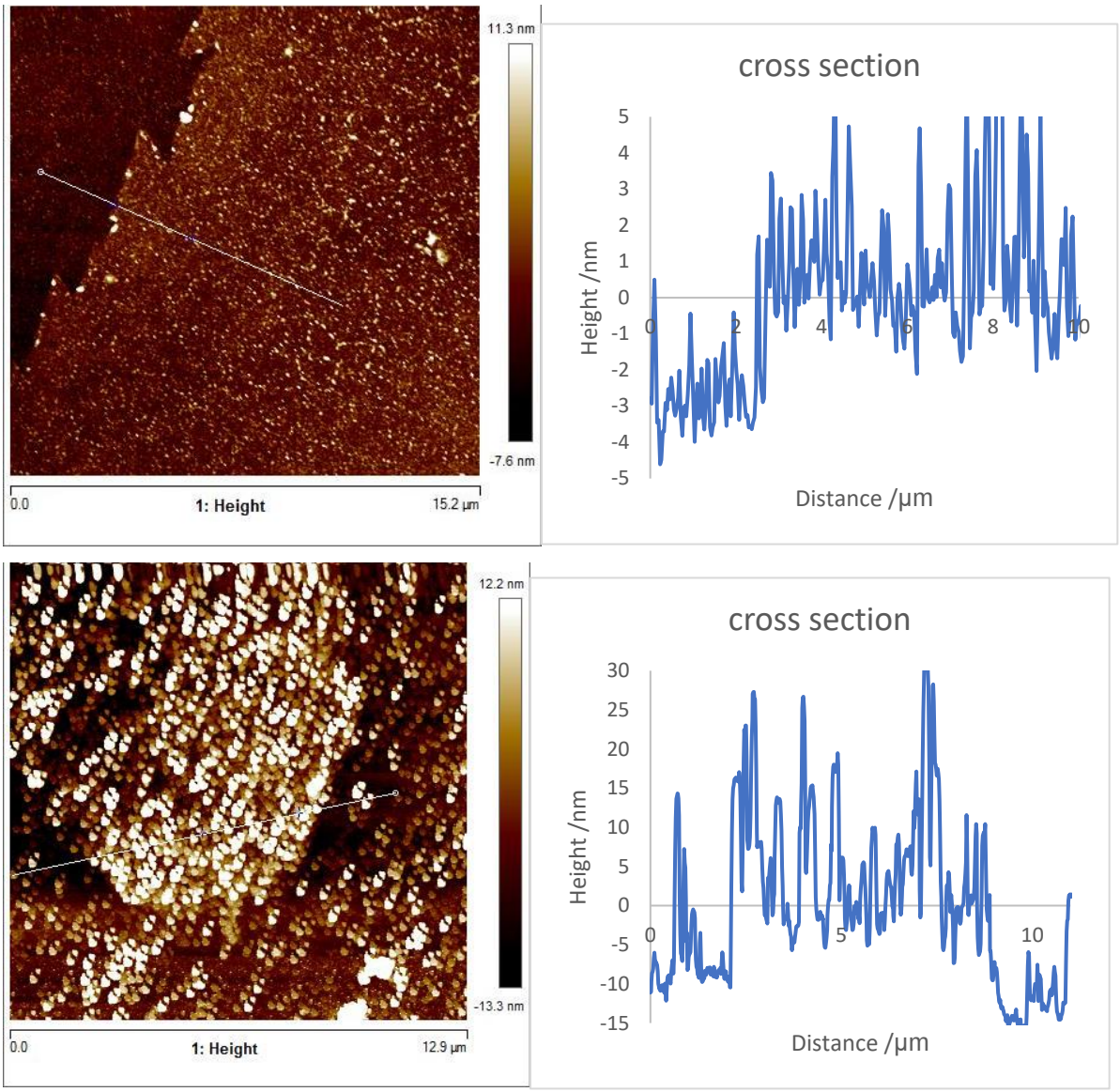

FIGURE 5-24: AFM IMAGE OF MoS_2 ON DONOR FILM (TOP) AND GLASS RECEIVER PLATE (BOTTOM). THE CROSS SECTIONS TO THEIR RIGHT DEMONSTRATE THAT THE SCANNED DONOR FILM CRYSTAL IS MONOLAYERED AND ~3.5 NM THICK WHILST THE TRANSFERRED MoS_2 CRYSTAL IS ~7 NM THICK AND THEREFORE HAS 2 LAYERS. THE NOISE ON THE SCANS IS LIABLE TO BE RESIDUAL PMMA.

Similarly to the $MoSe_2$ discussed in the previous section, the blisters have the ability to crack and break the 2D MoS_2 films, as they can be much larger than the blister, as shown in Figure 5-25. As the blisters do not directly target the location of the MoS_2,they can cause some of the films to be off-center to the titanium expansion, and thus potentially cause rotation within the transferred MoS_2, thereby meaning it may not land as a flat crystal. A Raman scan of one such deposit is shown in Figure 5-26. The peak

separation and position indicate that this is bulk MoS_2.[85] Thus, it's likely that the film folded or compressed upon landing, forming a bulk-like deposit.

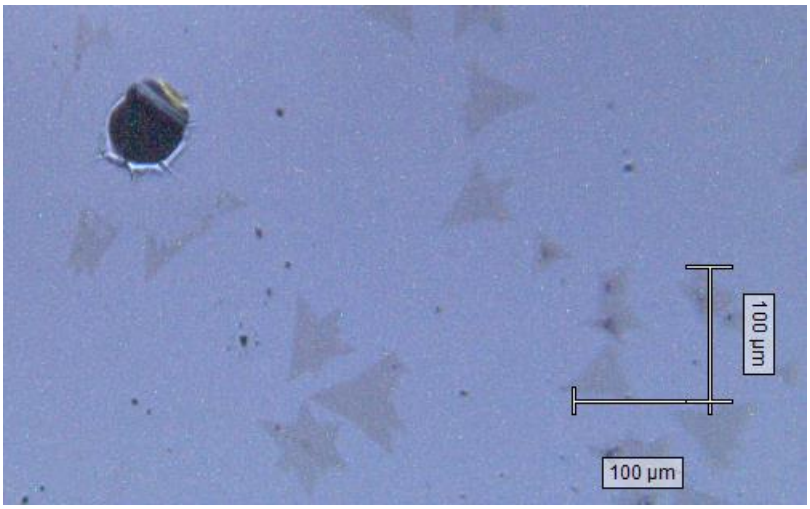

FIGURE 5-25: IMAGE OF A BURST FS BLISTER IN THE REGION OF THE MoS_2 DEPOSIT. THE BLISTER DID NOT TRANSFER THE ENTIRE MoS_2 CRYSTAL. SOME OF THE SURROUNDING CRYSTALS HAVE REMAINED AS FRAGMENTED SECTIONS.

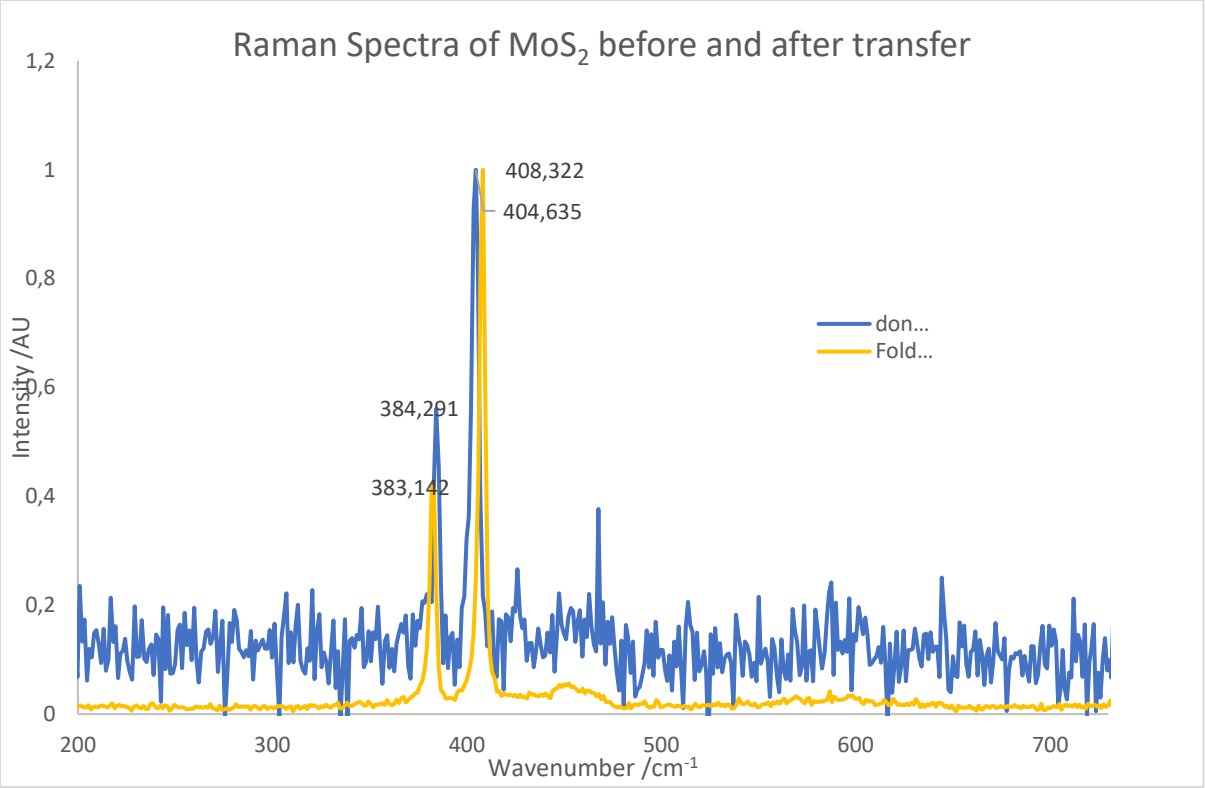

FIGURE 5-26: RAMAN SCAN OF MoS_2 DEPOSIT ON RECEIVER PLATE (YELLOW) AS COMPARED TO MoS_2 ON THE DONOR FILM.

The successful transfer of MoS_2 2D films still requires more work; yet, this advancement may allow more successful study of other 2D films due to the ability to directly transfer the MoS_2 to a specific location. Further study should adjust the receiver plate to allow better detection and identification of the MoS_2. The blisters should be enlarged, allowing transfer of larger crystals. Furthermore, the optical properties of the MoS_2 after transfer could give greater insight into the process. As will be discussed in the next section, it's possible to grow materials directly to the donor film, utilising CVD; and therefore, this could potentially be applied to the MoS_2, thereby allowing us to transfer the MoS_2 from the growth film. We would thus be able to bypass the dry transfer process, which causes impurities within the sample.

5.8 Conclusion

BB LIFT has shown that it can gently transfer a wide variety of particles from nanoparticles, and fragile molecules to quasi 1 and 2 dimensional structures. The ability to gently transfer fragile molecules and nanoparticles, with a high concentration, has potential for furthering fundamental research into these materials. The ability to print microstructures such as the bulk and quasi-2D crystals also has

applications into fundamental research around these structures by allowing clean transfer to specific locations which can enable solid state studies into their underlying physics. Furthermore, the ability to continuously print these structures can aid in industry for manufacture of devices made from these materials. The previously conducted experiments on 1D and 2D structures also suggest a possible advancement in development of these materials for study when combined with the first principle experiments of direct growth and transfer from the same film as discussed in Chapter 6.

6. Direct growth and transfer from donor film

The previous chapter discusses transfer of a large variety of materials from titanium donor films. However, as discussed within chapter 2, these films must be coated with the material of interest by either spin coating, sandwich technique, or PMMA transfer. Whilst this is effective, it requires that the materials be soluble, apart from PMMA transfer. The solute potentially adds impurities to the sample; and, controlling the surface concentration can be difficult. Direct growth of the material upon the donor film overcomes surface deposition problems, whilst also allowing for further advancement of BB LIFT into printing and gas phase studies.

6.1 Chemical vapour deposition of CNT

Chemical Vapour Deposition, CVD, is an old technique used for a wide variety of applications.[86] The process involves heating a catalytic substrate, under an atmosphere containing a non-reactive carrier gas, with a small concentration of gas which will chemically react with the surface of the substrate, creating a deposit of a new catalytically grown material. CVD of carbon nanotubes can be conducted with a large variety of catalytic surfaces, (Fe, Co, Ni).[87] However, the topography of the catalyst affects the CNT growth; and, the metals must be in nanoparticulate form, where the high surface area creates a good template for CNT growth.[79] Furthermore, the larger the nanoparticles of metal, the larger the diameter of the nanotubes. Thus, the support for the metal catalyst is important, so as to allow the metal nanoparticles to develop. Silica has been found to be one of the most effective supports allowing for CNT growth.[88] However, Iron/silica catalysts do not produce the most consistent or graphitic deposit-free CNTs. Yet, within this preliminary study, simple growth of CNT's was more desirable than specific varieties. Thus, an iron catalyst with a silica substrate was chosen for CVD CNT growth.

As CVD of CNT on iron requires temperatures of approximated 700˚C, and crown glass will start to deform at these temperatures, a fused silica substrate was used. This was then coated in titanium and, as required for iron catalysis growth, a thin ~5 nm silica surface was evaporated onto the surface with EBE. A final layer of iron ~1nm thick was then deposited via EBE, which, when heated to the CVD growth conditions, forms iron nanoparticles.

However, it was found that during CVD growth the Ti would become translucent to visible light, as seen in Figure 6-1. This is because the silicon within the quartz leaches into the titanium lattice, forming

titanium silicon complexes when heated to temperatures ranging from 400-800 °C.[89] This would disallow LIFT, as the donor film needs to absorb all the laser radiation, lest the surface particles become damaged or a blister does not form. The titanium was therefore replaced with a nickel film ~200nm in thickness. However, the nickel did not have a strong enough adhesion to the fused silica surface, and therefore peeled away. Thus, a thin layer of titanium ~10nm in thickness was placed upon the fused silica, to act as an adhesion layer between the nickel and fused silica. This allowed for successful growth of MWCNT upon the surface, as verified via Raman and SEM in Figure 5-13 and **Error! Reference source not found.**. However, the thin titanium layer will have changed to a titanium silicide during the CVD growth. This adds a layer of light absorbing material between the laser pulse and the nickel which is the intended target of energy absorption. From Allesandro et al.[90] it's known that $TiSi_2$ is 14% more reflective than titanium at 800 nm (reflectivity of $TiSi_2$ = 0.56). From its extinction coefficient of 3 $LMol^{-1}cm^{-1}$ and the distance of ~10 nm, we can determine that absorption will be negligible. However, the reflectivity means the fluence used must be ~1.8 times higher than for a single layered film.

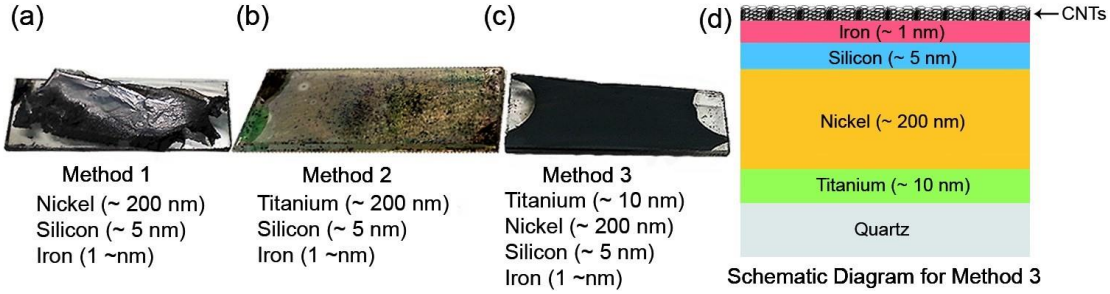

FIGURE 6-1: MULTI-LAYERED SUBSTRATES AFTER CVD GROWTH WAS ATTEMPTED. (A) DEMONSTRATES THAT NICKEL DOESN'T HAVE A STRONG ENOUGH ADSORPTION TO THE GLASS SUBSTRATES, LEADING TO PEELING. (B) DEMONSTRATES THAT TI CHEMICALLY ALTERS BECOMING TRANSLUCENT. (C) SUCCESSFULLY GROWS MWCNT UPON THE SURFACE. (D) SHOWS A SCHEMATIC FOR THE MULTI-LAYERED SYSTEM (C).

The growth was performed within a CVD chamber described by Nerushev et al.[54] The chamber was flushed with Ar (99.996% purity, 600 sccm) and H_2 (99.96% purity, 100 sccm), at atmospheric pressure. It was then heated to 700˚C and C_2H_2 (technical quality, 8sccm) was introduced for 15 minutes. The C_2H_2 flow was stopped, yet the chamber was kept at 700˚C for a further 10 minutes, to flush out excess C_2H_2 and reduce the amount of amorphous carbon deposits. The chamber was then slowly allowed to cool to room temperature, thus following the previous CVD CNT growth protocol trialled by Nerushev et al.[79]

6.2 Results and analysis

From optical and SEM images of the blisters, as shown in **Error! Reference source not found.**, it can be s een that the CNT are successfully desorbed from the blister location. This desorption is not quite as clean in relation to a simple metal film. This is likely due to the different velocities of expansion likely to occur because of the multi-layered system. A small crack can also be observed in **Error! Reference s ource not found.**(c) where the silica iron support layer has fractured due to the expansion. Further complexities in the desorption pattern are also likely, due to inhomogeneous, amorphous carbon deposits, or varying levels of iron catalyst silica surface interaction.

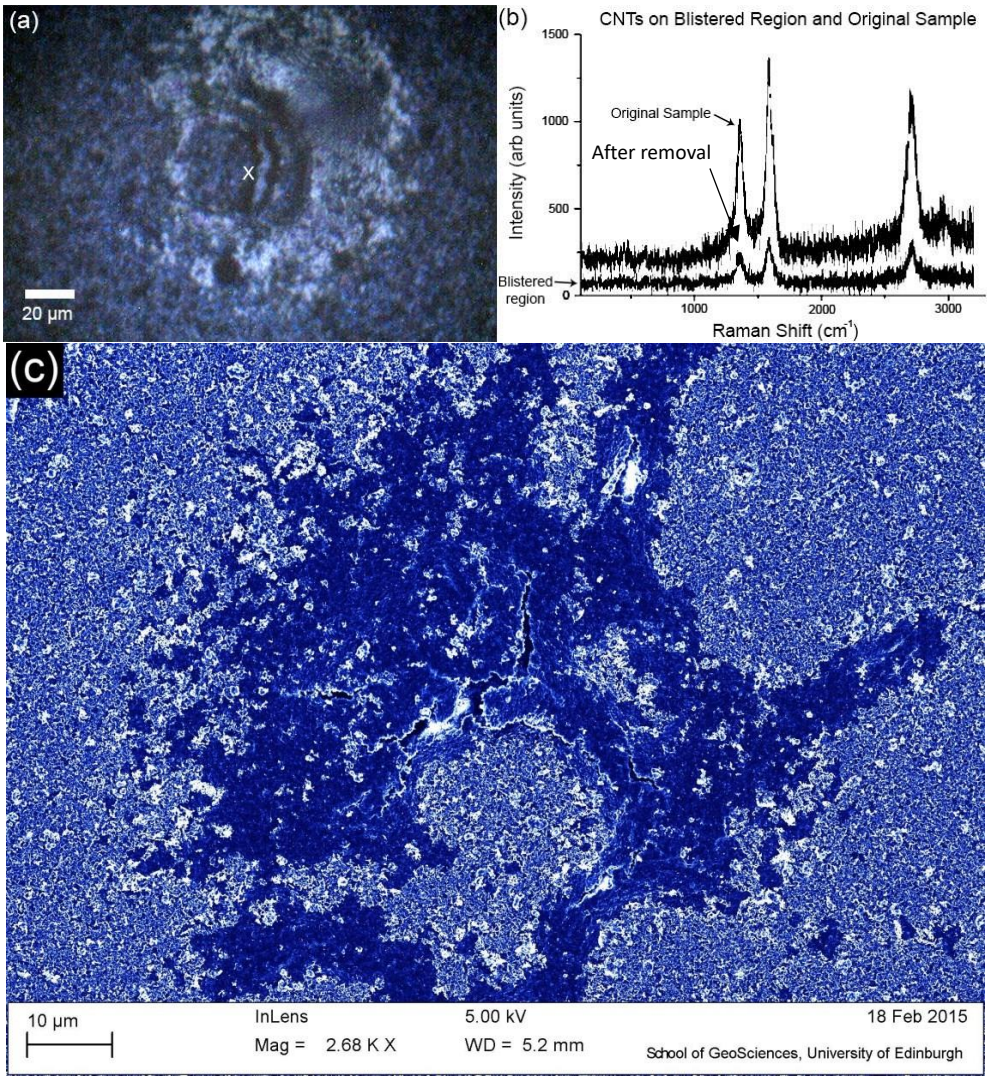

FIGURE 6-2: (A) OPTICAL IMAGE OF FS BLISTER, WITH X SIGNIFYING LOCATION OF RAMAN SPECTRA (B). (C) FALSE COLOURED SEM IMAGE OF THE SAME BLISTER, CLEARLY SHOWING A DESPORPTION OF NANOTUBES. THE BLISTER WAS MADE WITH AN FS LASER PULSE WITH A FLUENCE OF 600 MJCM^{-2}.

From a position marking blister (very high fluence), shown in Figure 6-3, some insight into the mechanisms of the interaction between the silica and nickel film can be observed. The silica film appears to have peeled away from the surface to a greater angle than that to which the film itself expanded. This is likely due to partial recontraction of the blister once the ablated material has resolidified. However, from the exposed surface on the left side of the blister in Figure 6-3(a), and the closer magnification in (c), the silica itself appears to have bent backwards. Thus the momentum from the blister propelled it beyond the films full expansion.

Figure 6-3(b) shows what appear to be silica deposits which have melted into rounded objects upon the nickel surface. In comparison, (d) shows pointed and stretched silica on the underside of the silica film. This demonstrates that the silica on the nickel surface was heated potentially by the confined plasma within the blister. Yet, the silica on the peeled silica film appears to have cooled more rapidly or, potentially, never reached the temperature which was placed upon the silica remaining on the nickel surface. This indicates that the silica nickel adhesion is relatively strong yet the layers can still be separated by the force of the blister expansion at this fluence. From the lack of change in the Raman spectra, shown in **Error! Reference source not found.**, it can be assumed that the MWCNT do not u ndergo significant damage, despite remaining upon the silica surface. Thus, rather little internal energy is maintained within the silica surface layer. This is corroborated by Figure 6-3(d) as discussed earlier. It must also be noted that this blister would have been formed using the full fluence available from a laser pulse; and this heating of the surface will have been greater than normal.

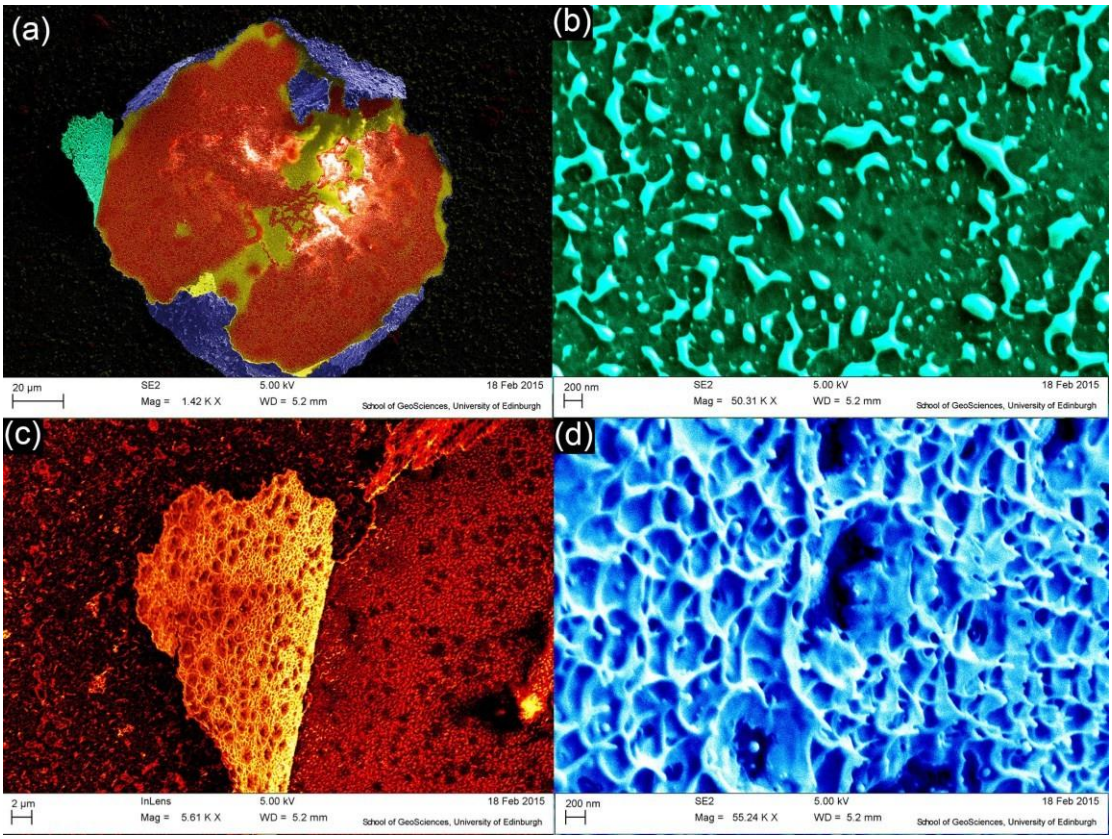

FIGURE 6-3: (A) SHOWS A BLISTER WHICH WAS FORMED VIA A HIGH FLUENCE FS LASER PULSE TO MARK THE POSITION ON THE FILM.(B) IS AND ENLARGED VIEW OF THE EXPOSED NICKEL LAYER WHICH IS LITTERED WITH WHAT APPEARS TO BE MELTED SILICA DEPOSITS. (C) SHOWS A PEELED AWAY EDGE OF THE SILICA LAYERS, WHILST (D) IS A MAGNIFIED IMAGE OF THIS SURFACE STRUCTURE

6.3 Conclusion

From this work, it has been demonstrated that the BB-LIFT technique can be used for complex multilayer systems, allowing the direct deposition of CVD grown nanomaterials without exposing them to direct radiation or any chemical impurities.

7. Conclusion

7.1 Research summary

BB LIFT has been successfully tested and developed into a powerful technique for molecular and nanostructure transfer to the gas phase or for printing. This thesis discusses the fundamental principles behind BB LIFT and investigates the mechanism through experimentation and study of the blisters in relation to the laser pulse duration. The understanding of the fundamental mechanisms and how they influence blister formation has then been expanded to the investigation of the impact they have on the spatial and velocity distributions of the emitted materials. Analysis of materials before and after transfer have also shown BB LIFT to be gentle, and capable of transferring a wide range of materials each existing in a variety of physical complexes, from molecules and nanoparticles to crystalline 1D and 2D structures. Proof of principle experiments have even demonstrated the ability to grow 1D nanostructures on a BB LIFT substrate ready for transfer, thus avoiding the time consuming and potentially damaging transfer mechanisms which currently exist.

The underlying mechanism of BB LIFT was explored through experimentation with fs and ns laser pulse durations alongside theoretical modeling. For ns laser pulses it was shown, by comparing experimental results with a one-dimensional heat transfer model, that blister formation occurs through laser- induced heating of a region of titanium film to >1700 °C within 10 ns, causing its expansion normal to the plane of the film. Comparative studies utilising a fs laser pulse showed that, in this case, blister formation occurred through confined gas expansion at the film and substrate interface. The velocity of the desorbed particles was found to depend strongly on the metal layer thickness but only weakly on the laser fluence. A simple model, described in Chapter 4, could qualitatively explain the observations.

The spatial distribution of the desorbed particles was studied by using a radial distribution analysis of the deposit. It was shown that the beam has a shallow gradient for particle spread within the radius of the blister and expands with a spread of ~7-15° beyond this region. This has a potential, yet untested, dependence upon the particles being desorbed, as well as the pulse duration. The desorbed material thus tends to travel in a fairly confined spatial pulse, thus maintaining a high concentration. The understanding of the spatial distribution in Chapter 4 corroborates with Chapter 3 which discusses how, due to the laser pulse impacting an area rather than a point position, the film expands in such a way as to linearly project the material.

The velocity distribution of the desorbed particles was studied by photoionisation time-of-flight mass spectrometry, using C_{60} and auroshells as representative systems. From these experiments it was found that for ns BB LIFT from a titanium film the desorbed fullerenes travel at ~100 ms^{-1} irrespective of the film thickness. However, due to the heating of the film to 1700-2200 $^{\circ}C$, some C_{60} is evaporated with velocities corresponding to the Ti surface temperature. The auroshells travel at ~50 ms^{-1}. For fs BB LIFT the fullerene's velocity is dependent upon the thickness of the titanium film. Due to the difficulty in stretching a thicker material compared to a thinner one, it is therefore possible to control the velocity distribution of the desorbed particles within the range of 5- 60 ms^{-1}. This experimentally discovered trend also agrees qualitatively with a simplified mathematical model of the effect discussed in Chapter 4.

BB LIFT has also shown potential to be used for a wide variety of fundamental or applied research due to its ability to gently transfer a wide array of materials, whilst maintaining their internal structure. The transfer of molecules and nanoparticles such as C_{60} and PCBM was successful, demonstrating this could aid in basic research of molecules, such as PCBM, which were previously too difficult to study whilst in the gas phase. Furthermore, transfer of deposited MW/SWCNTs, $MoSe_2$ and MoS_2 through BB LIFT opens up a means of cleanly transferring fragile nanoparticles without exposing them to impurities that may adversely affect their electronic and optical properties.

BB LIFT was developed further by introducing multiple substrate layers and thus allowing CVD growth of MWCNT directly to the surface before transferring them without altering them in any way after growth. This process involves creating films with a catalytic top layer, (iron deposited upon a silicon buffer layer), which rests upon a donor film and substrate, capable of withstanding the CVD growth phase, (nickel deposited upon titanium upon quartz). This technique was developed for CNTs, however, the potential for directly combining BB-LIFT with a wide variety of other CVD grown materials such as the 2D crystals successfully transferred, as discussed in chapter 5, is very promising for nanodevice fabrication.

7.2 Future work

Whilst the work within this thesis is expansive, there are still many avenues of advancement for development of BB LIFT from a fundamental perspective as-well as potential applications for its future usage.

7.2.1 Alteration of laser characteristics

Chapter 3 deals with understanding of the mechanism in relation to fs and ns laser pulses, however the bridging pulse duration on the ps timescale has yet to be studied, and may provide insights or applications through the combination of both mechanisms.
The beam shape of the lasers used was Gaussian and whilst this does provide effective blisters, adjustment of the beam to a top-hat profile could give a better understanding and control of the technique since the same fluence would be applied across the whole irradiated surface. There is potential for more varied beam profiles such as Bessel functions which could provide more topographically interesting blister profiles.
Adjustment of the irradiation spot size should also be attempted, so as to define how small and precise the resolution of particle transfer can be, whilst expansion of the irradiation zone could allow larger structures to be transferred. This experimentation could also aid in a fundamental understanding of the dynamic topography of the blister formation as well as the spatial distribution of the desorbed particles.

7.2.2 Donor film material

Whilst some research was conducted into copper, nickel, titanium and PMMA donor films, there was no time to carry out systematic studies. As described within Chapter 3 and 4 the blister mechanisms will be strongly affected by the donor film material. The temperatures which it may reach before melting in relation to its expansion coefficient could allow control over the velocity of the ns desorbed materials, whilst the elastic properties will affect the blister formation for fs BB LIFT.

As discussed within Chapter 6, multi-layered films were tested as a proof of principle for CVD growth of material and transfer. However, a fundamental understanding of the multilayer interactions has yet to be accomplished and an understanding of these interactions from a basic level would help in developing this technique further, allowing a variety of other multilayer systems.

7.2.3 Material to be desorbed

A wide variety of particles have been successfully desorbed, which may lead to further study or applications of these materials. There are a great many more similar material systems which should be tested so as to confirm that this technique is effective for other fragile or difficult to transfer materials. Another interesting aspect would be the experimentation into the effects of surface concentration upon transferred material. It can be observed within the figures of blisters that the majority of the particles

are desorbed, however, there is no conclusive evidence of the effects upon spatial and velocity profile which an altered surface concentration might have.

7.2.4 Application to spectroscopy and 2D crystal studies.

The basis of this thesis has been to understand the mechanisms of BB LIFT and to apply it to a wide variety of difficult to study or transfer systems. This work has proven to be successful, therefore, it is believed that BB LIFT is at a stage in which it can be applied as a common and characterised technique, thus enabling its usage in studies related directly to the transferred materials.

8. Bibliography

1. El-Aneed, A., Cohen, A. & Banoub, J. Mass Spectrometry, Review of the Basics: Electrospray, MALDI, and Commonly Used Mass Analyzers. *Appl. Spectrosc. Rev.* **44,** 210–230 (2009).

2. Fenn, J. B., Mann, M., Meng, C. K. A. I., Wong, S. F. & Whitehouse, C. M. Electrospray Ionization for Mass Spectrometry of Large Biomolecules. *Science (80-.).* **246,** 64–71 (1989).

3. Wilm, M. Principles of electrospray ionization. *Mol. Cell. Proteomics* **10,** M111.009407 (2011).

4. Clark, A. E., Kaleta, E. J., Arora, A. & Wolk, D. M. Matrix-Assisted laser desorption ionization-time of flight mass spectrometry: A fundamental shift in the routine practice of clinical microbiology. *Clin. Microbiol. Rev.* **26,** 547–603 (2013).

5. Lindner, B. & Seydel, U. Laser Desorption Mass Spectrometry of Nonvolatlles under Shock Wave Conditions. *Anal. Chem.* **57,** 895–899 (1985).

6. Shea, R. C. *et al.* Characterization of laser-induced acoustic desorption coupled with a Fourier transform ion cyclotron resonance mass spectrometer. *Anal. Chem.* **78,** 6133–6139 (2006).

7. Gerlach, W. & Stern, O. Der experimentelle Nachweis der Richtungsquantelung im Magnetfeld. *Zeitschrift f{ü}r Phys.* **9,** 349–352 (1922).

8. Meng, C. K., Mann, M. & Fenn, J. B. Of protons or proteins. *Zeitschrift fÜr Phys. D Atoms, Mol. Clust.* **10,** 361–368 (1988).

9. Hillenkamp, F. & Karas, M. Matrix-assisted laser desorption/ionization mass spectrometry of biopolymers. *Analytical chemistry* **63,** 1193–2001 (1991).

10. Calvert, C. R. *et al.* LIAD-fs scheme for studies of ultrafast laser interactions with gas phase biomolecules. *Phys. Chem. Chem. Phys.* **14,** 6289–97 (2012).

11. Calegari, F. *et al.* Charge migration induced by attosecond pulses in bio-relevant molecules. *J. Phys. B At. Mol. Opt. Phys.* **49,** 1–25 (2016).

12. Zinovev, A. V, Veryovkin, I. V, Moore, J. F. & Pellin, M. J. Laser-driven acoustic desorption of organic molecules from back-irradiated solid foils. *Anal. Chem.* **79,** 8232–41 (2007).

13. Golovlev, V. V, Chen, C. H., Allman, S. L., Garrett, W. R. & Taranenko, N. I. Laser-induced acoustic desorption. *Int. J. Mass Spectrom.* **70,** 69–78 (1997).

14. Sezer, U. *et al.* Laser-induced acoustic desorption of natural and functionalized biochromophores. *Anal. Chem.* **87,** 5614–5619 (2015).

15. Lee, D., Miller, A., Kittelson, D. & Zachariah, M. R. Characterization of metal-bearing diesel nanoparticles using single-particle mass spectrometry. *J. Aerosol Sci.* **37,** 88–110 (2006).

16. Lee, K. S., Cho, S. W. & Lee, D. Development and experimental evaluation of aerodynamic lens as an aerosol inlet of single particle mass spectrometry. *J. Aerosol Sci.* **39,** 287–304 (2008).

17. Lee, D., Park, K. & Zachariah, M. R. Determination of the Size Distribution of Polydisperse Nanoparticles with Single-Particle Mass Spectrometry: The Role of Ion Kinetic Energy. *Aerosol Sci. Technol.* **39,** 162–169 (2005).

18. Venkataraman, C. & Raymond, J. Estimating the Lung Deposition of Particulate Polycyclic

Aromatic Hydrocarbons Associated With Multimodal Urban Aerosols. *Inhal. Toxicol.* **10,** 183–204 (1998).

19. Larson, B. W. *et al.* Thermal [6,6] → [6,6] Isomerization and Decomposition of PCBM (Phenyl-C61-butyric Acid Methyl Ester). *Chem. Mater.* **26,** 2361–2367 (2014).

20. Lloyd, M. T., Anthony, J. E. & Malliaras, G. G. Photovoltaics from soluble small molecules. *Mater. Today* **10,** 34–41 (2007).

21. Geim, A. K. & Novoselov, K. S. The rise of graphene. *Nat. Mater.* **6,** 183–191 (2007).

22. Tasis, D. *et al.* Chemistry of Carbon Nanotubes Chemistry of Carbon Nanotubes. *Chem. Rev.* **106,** 1105–1136 (2006).

23. Gourmelon, E. *et al.* MS2 (M = W, Mo) photosensitive thin films for solar cells. *Sol. Energy Mater. Sol. Cells* **46,** 115–121 (1997).

24. Desai, S. B. *et al.* MoS 2 transistors with 1-nanometer gate lengths. *Science (80-.).* **354,** 99–102 (2016).

25. Schalkwijk, W. Van & Scrosati, B. *Advances in lithium-ion batteries*. *Seventeenth Annual Battery Conference on Applications and Advances Proceedings of Conference Cat No02TH8576* (2002). doi:10.1007/b113788

26. Stephenson, T., Li, Z., Olsen, B. & Mitlin, D. Lithium ion battery applications of molybdenum disulfide (MoS 2) nanocomposites. *Energy Environ. Sci.* **7,** 209–231 (2014).

27. Xu, K. *et al.* The positive piezoconductive effect in graphene. *Nat. Commun.* **6,** 8119 (2015).

28. Desai, S. B. *et al.* MoS2 transistors with 1-nanometer gate lengths. *Science (80-.).* **354,** 99–102 (2016).

29. Kuznetsov, a I., Kiyan, R. & Chichkov, B. N. Laser fabrication of 2D and 3D metal nanoparticle structures and arrays. *Opt. Express* **18,** 21198–203 (2010).

30. Kuznetsov, A. I., Koch, J., Chichkov, B. N. & Phipps, C. Laser-Induced Transfer of Metal Nanoparticles. *Am. Inst. Phys.* **832,** 832–837 (2010).

31. Willis, D. a. & Grosu, V. Microdroplet deposition by laser-induced forward transfer. *Appl. Phys. Lett.* **86,** 244103 (2005).

32. Banks, D. P., Grivas, C., Mills, J. D., Eason, R. W. & Zergioti, I. Nanodroplets deposited in microarrays by femtosecond Ti:sapphire laser-induced forward transfer. *Appl. Phys. Lett.* **89,** 193107 (2006).

33. Yang, L. *et al.* Microdroplet deposition of copper film by femtosecond laser-induced forward transfer. *Appl. Phys. Lett.* **89,** 161110 (2006).

34. Narazaki, A., Sato, T., Kurosaki, R., Kawaguchi, Y. & Niino, H. Nano- and Microdot Array Formation of FeSi 2 by Nanosecond Excimer Laser-Induced Forward Transfer. *Appl. Phys. Express* **1,** 57001 (2008).

35. Sanchez-Aniorte, M. I., Mouhamadou, B., Alloncle, A. P., Sarnet, T. & Delaporte, P. Laser-induced forward transfer for improving fine-line metallization in photovoltaic applications. *Appl. Phys. A Mater. Sci. Process.* **122,** 1–5 (2016).

36. Rapp, L. *et al.* Pulsed-laser printing of organic thin-film transistors. *Appl. Phys. Lett.* **95,** 1–4 (2009).

37. Fardel, R., Nagel, M., Nüesch, F., Lippert, T. & Wokaun, A. Laser forward transfer using a sacrificial layer: Influence of the material properties. *Appl. Surf. Sci.* **254,** 1322–1326 (2007).

38. Boutopoulos, C., Tsouti, V., Goustouridis, D., Chatzandroulis, S. & Zergioti, I. Liquid phase direct laser printing of polymers for chemical sensing applications. *Appl. Phys. Lett.* **93,** (2008).

39. Boutopoulos, C., Pandis, C., Giannakopoulos, K., Pissis, P. & Zergioti, I. Polymer/carbon nanotube composite patterns via laser induced forward transfer. *Appl. Phys. Lett.* **96,** 1–4 (2010).

40. Palla-Papavlu, A., Dinescu, M., Wokaun, A. & Lippert, T. Laser-induced forward transfer of single-walled carbon nanotubes. *Appl. Phys. A Mater. Sci. Process.* **117,** 371–376 (2014).

41. Kononenko, T. V., Alloncle, P., Konov, V. I. & Sentis, M. Laser transfer of diamond nanopowder induced by metal film blistering. *Appl. Phys. A* **94,** 531–536 (2008).

42. Brown, M. S., Kattamis, N. T. & Arnold, C. B. Time-resolved dynamics of laser-induced micro-jets from thin liquid films. *Microfluid. Nanofluidics* **11,** 199–207 (2011).

43. Rapp, L. *et al.* Comparative time resolved shadowgraphic imaging studies of nanosecond and picosecond laser transfer of organic materials. *Proc. SPIE* **33,** 71311L–71311L–7 (2008).

44. Jarrell, T. M. *et al.* Laser-Induced Acoustic Desorption/Electron Ionization of Amino Acids and Small Peptides. *J. Am. Soc. Mass Spectrom.* **28,** 1091–1098 (2017).

45. Zinovev, A., Veryovkin, I. & Pellin, M. *Molecular Desorption by Laser-Driven Acoustic Waves: Analytical Applications and Physical Mechanisms*. (2011).

46. Staniforth, M. & Stavros, V. G. Recent advances in experimental techniques to probe fast excited-state dynamics in biological molecules in the gas phase: dynamics in nucleotides, amino acids and beyond. *Proc. Math. Phys. Eng. Sci.* **469,** 20130458 (2013).

47. Sezer, U. *et al.* Laser-induced acoustic desorption of natural and functionalized biochromophores. *Anal. Chem.* (2015). doi:10.1021/acs.analchem.5b00601

48. Kononenko, T. V., Sinyavsky, M. N., Konov, V. I. & Sentis, M. Laser-driven high-frequency vibrations of metal blister surface. *Appl. Phys. A* **112,** 583–589 (2013).

49. Kattamis, N. T., McDaniel, N. D., Bernhard, S. & Arnold, C. B. Laser direct write printing of sensitive and robust light emitting organic molecules. *Appl. Phys. Lett.* **94,** 103306 (2009).

50. Brown, M. S., Kattamis, N. T. & Arnold, C. B. Time-resolved study of polyimide absorption layers for blister-actuated laser-induced forward transfer. *J. Appl. Phys.* **107,** 83103 (2010).

51. Kattamis, N. T., Brown, M. S. & Arnold, C. B. Finite element analysis of blister formation in laser-induced forward transfer. *J. Mater. Res.* **26,** 2438–2449 (2011).

52. Kononenko, T. V., Nagovitsyn, I. a., Chudinova, G. K. & Mihailescu, I. N. Clean, cold, and liquid-free laser transfer of biomaterials. *Laser Phys.* **21,** 823–829 (2011).

53. Bulgakov, A. V. *et al.* Laser-induced transfer of nanoparticles for gas-phase analysis. *J. Opt. Soc. Am. B* **31,** C15 (2014).

54. Nerushev, O. A., Sveningsson, M., Falk, L. K. L. & Rohmund, F. Carbon nanotube films obtained by thermal chemical vapour deposition. *J. Mater. Chem.* **11,** 1122–1132 (2001).

55. Kopova, I., Bacakova, L., Lavrentiev, V. & Vacik, J. Growth and potential damage of human bone-derived cells on fresh and aged fullerene C-60 films. *Int. J. Mol. Sci.* **14,** 9182–9204 (2013).

56. Kitaura, R. *et al.* Chemical vapor deposition growth of graphene and related materials. *J. Phys. Soc. Japan* **84,** 1–13 (2015).

57. Tonndorf, P. *et al.* Photoluminescence emission and Raman. **21,** 4908–4916 (2013).

58. Bäuerle, D. *Laser Processing and Chemistry*. **53,** (2011).

59. Chichkov, B. N., Momma, C., Nolte, S., von Alvensleben, F. & Tünnermann, A. Femtosecond, picosecond and nanosecond laser ablation of solids. *Appl. Phys. A Mater. Sci. Process.* **63,** 109–115 (1996).

60. Lide, D. R. *CRC Handbook of Chemistry and Physics, 96th Edition, 2015-2016*. *Handbook of Chemistry and Physics* (2014). doi:10.1136/oem.53.7.504

61. Meshcheryakov, Y. P., Shugaev, M. V, Mattle, T., Lippert, T. & Bulgakova, N. M. Role of thermal stresses on pulsed laser irradiation of thin films under conditions of microbump formation and nonvaporization forward transfer. 521–529 (2013). doi:10.1007/s00339-013-7563-0

62. Kononenko, T. V., Alloncle, P., Konov, V. I. & Sentis, M. Shadowgraphic imaging of laser transfer driven by metal film blistering. *Appl. Phys. A* **102,** 49–54 (2010).

63. Bulgakova, N. M., Evtushenko, A. B., Shukhov, Y. G., Kudryashov, S. I. & Bulgakov, A. V. Role of laser-induced plasma in ultradeep drilling of materials by nanosecond laser pulses. *Appl. Surf. Sci.* **257,** 10876–10882 (2011).

64. Bulgakova, N. M., Bulgakov, A. V. & Babich, L. P. Energy balance of pulsed laser ablation: thermal model revised. *Appl. Phys. A* **79,** 1323–1326 (2004).

65. Kaschnitz, E. & Reiter, P. Enthalpy and Temperature of the Titanium Alpha-Beta Phase Transformation. *Int. J. Thermophys.* **23,** 1339–1345 (2002).

66. Fang, W. & Lo, C.-Y. On the thermal expansion coefficients of thin films. *Sensors Actuators A Phys.* **84,** 310–314 (2000).

67. Shan, Z. & Sitaraman, S. K. Elastic-plastic characterization of thin films using nanoindentation technique. *Thin Solid Films* **437,** 176–181 (2003).

68. Palik, E. *Handbook of Optical Constants of Solids: Index*. *Handbook of optical constants of solids* (1998).

69. Zhu, X., Villeneuve, D. M., Naumov, A. Y., Nikumb, S. & Corkum, P. B. Experimental study of drilling sub-10 um holes in thin metal foils with femtosecond laser pulses. *Appl. Surf. Sci.* **152,** 138–148 (1999).

70. Levy, Y., Derrien, T. J. Y., Bulgakova, N. M., Gurevich, E. L. & Mocek, T. Relaxation dynamics of femtosecond-laser-induced temperature modulation on the surfaces of metals and semiconductors. *Appl. Surf. Sci.* **374,** 157–164 (2016).

71. Lin, Z., Zhigilei, L. V. & Celli, V. Electron-phonon coupling and electron heat capacity of metals

under conditions of strong electron-phonon nonequilibrium. *Phys. Rev. B - Condens. Matter Mater. Phys.* **77,** 1–17 (2008).

72. Wu, C. & Zhigilei, L. V. Microscopic mechanisms of laser spallation and ablation of metal targets from large-scale molecular dynamics simulations. *Appl. Phys. A Mater. Sci. Process.* **114,** 11–32 (2014).

73. Lei, S., Grojo, D., Ma, J., Yu, X. & Wu, H. Femtosecond Laser Backside Ablation of Gold Film on Silicon Substrate. *Procedia Manuf.* **5,** 594–608 (2016).

74. Meshcheryakov, Y. P., Shugaev, M. V., Mattle, T., Lippert, T. & Bulgakova, N. M. Role of thermal stresses on pulsed laser irradiation of thin films under conditions of microbump formation and nonvaporization forward transfer. *Appl. Phys. A Mater. Sci. Process.* **113,** 521–529 (2013).

75. Demaske, B. J., Zhakhovsky, V. V., Inogamov, N. A. & Oleynik, I. I. Ablation and spallation of gold films irradiated by ultrashort laser pulses. *Phys. Rev. B - Condens. Matter Mater. Phys.* **82,** 1–5 (2010).

76. Gan, Y. & Chen, J. K. An atomic-level study of material ablation and spallation in ultrafast laser processing of gold films. *J. Appl. Phys.* **108,** (2010).

77. Akaike, K. *et al.* Ultraviolet photoelectron spectroscopy and inverse photoemission spectroscopy of [6,6]-phenyl-C61-butyric acid methyl ester in gas and solid phases. *J. Appl. Phys.* **104,** (2008).

78. Szweda, P. & Szweda, P. Laser Patterning of Carbon-Nanotubes Thin Films and Their Applications. *Intech* 528–548 doi:10.1111/j.1740-8784.2012.00295.x

79. Nerushev, O. A. *et al.* The temperature dependence of Fe-catalysed growth of carbon nanotubes on silicon substrates. *Phys. B Condens. Matter* **323,** 51–59 (2002).

80. Choi, S. H., Liman, C. D., Kramer, S., Chabinyc, M. L. & Kramer, E. J. Crystalline Polymorphs of 6,6 - Phenyl-C-61-butyric Acid n-Butyl Ester (PCBNB). *J. Phys. Chem. B* **116,** 13568–13574 (2012).

81. Heising, J. *et al.* Exfoliated and Restacked MoS 2 and WS 2 : Ionic or Neutral Species ? Encapsulation and Ordering of Hard Electropositive Cations. *Am. chem* **121,** 11720–11732 (1999).

82. Wang, S. *et al.* Shape evolution of monolayer MoS2 crystals grown by chemical vapor deposition. *Chem. Mater.* **26,** 6371–6379 (2014).

83. Sheng, Y. *et al.* Mixed multilayered vertical heterostructures utilizing strained monolayer WS 2. *Nanoscale* **8,** 2639–2647 (2016).

84. Lee, C. *et al.* Anomalous lattice vibrations of single-and few-layer MoS2. *ACS Nano* **4,** 2695–700 (2010).

85. Li, H. *et al.* From bulk to monolayer MoS 2: Evolution of Raman scattering. *Adv. Funct. Mater.* **22,** 1385–1390 (2012).

86. Zaharieva, K., Vissokov, G. & Grabis, J. Chemical Vapour Deposition. *phys.technol* **10,** 153–161 (2008).

87. Kumar, M. & Ando, Y. Chemical Vapor Deposition of Carbon Nanotubes: A Review on Growth Mechanism and Mass Production. *J. Nanosci. Nanotechnol.* **10,** 3739–3758 (2010).

88. Hernadi, K., Fonseca, A., Nagy, J. B., Bernaerts, D. & Lucas, A. A. Fe-catalyzed carbon nanotube

formation. *Carbon N. Y.* **34,** 1249–1257 (1996).

89. Jauberteau, I. *et al.* Silicides and Nitrides Formation in Ti Films Coated on Si and Exposed to (Ar-N 2 -H 2) Expanding Plasma. *Coatings* **7,** 2–14 (2017).

90. Alessandro, F. & Levy, F. Optical properties. *Phys. Rev.* **40,** 1611–1615 (1989).

9. Appendix A

code Which controls the motor system

```
#include <AccelStepper.h>
// Define two steppers and the pins they will use
AccelStepper stepper2(AccelStepper::DRIVER, 13, 12);
AccelStepper stepper1(AccelStepper::DRIVER, 3, 2);



// defines the motor speed in steps per second
int horizontal_speed = 200;
int vertical_speed = 200;

int current_y = 0;
int height_increment = 100;
int height = 400;

int current_x = 0;
// width = how far to spin x axis motor
int width = 400;
int width_increment = 100;

//defines the analog pin to measure the laser pulse.
int detectorPin = A1;
// Threshold is from 1-1000 it defines the amount of
//signal required to trigger
int threshold = 320 ;

void setup()
```

```
{
  pinMode(detectorPin, INPUT);
  stepper1.setMaxSpeed(1000);
  stepper2.setMaxSpeed(1000);
}
//defines controls to start and stop motors moving
bool is_x_moving = false;
bool is_y_moving = false;
bool is_not_started = true;
int line_number = 0;

void loop()
{
  // wait for input
  //reads from the detector pin
  if(!is_x_moving && !is_y_moving && analogRead(detectorPin) > threshold){
     // if odd line
     if(current_y == height && current_x == width){
       // do nothing
       // this brace represents the end of the program
     } else if (line_number % 2 && current_x == 0){
       stepper2.moveTo(current_y + height_increment);
       stepper2.setSpeed(vertical_speed);
       is_y_moving = true;
     } else if ((line_number % 2) == 0 && current_x == width) {
       stepper2.moveTo(current_y + height_increment);
       stepper2.setSpeed(vertical_speed);
       is_y_moving = true;
     } else if(line_number % 2){
```

```
      stepper1.moveTo(current_x - width_increment);
      stepper1.setSpeed(-horizontal_speed);
      is_x_moving = true;
    } else if((line_number % 2) == 0){
      stepper1.moveTo(current_x + width_increment);
      stepper1.setSpeed(horizontal_speed);
      is_x_moving = true;
    }
  } else if (is_x_moving && stepper1.distanceToGo() == 0) {
   is_x_moving = false;
   stepper1.setSpeed(0);
   if(line_number % 2){
    current_x = current_x - width_increment;
   } else {
    current_x = current_x + width_increment;
   }
  } else if(is_y_moving && stepper2.distanceToGo() == 0){
   is_y_moving = false;
   stepper2.setSpeed(0);
   current_y += height_increment;
   line_number++;
  }
  stepper1.runSpeed();
  stepper2.runSpeed();
}
```

Appendix B

Experimental section on Lab in Novosibirsk as described by Dr. Alexander Bulgakov

Experimental

Sample: C_{60} molecules deposited by *spin coating* onto a 3-□m-thick polyimide film on glass. There is a small triangle-shaped area in the sample where C_{60} was deposited directly on glass, i.e., without the intermediate polyimide layer (see a map sent previously).

LIFT Laser: ArF excimer laser (193 nm wavelength, 5 ns pulse duration, 3 mJ maximum pulse energy, 3% pulse-to-pulse stability).

The sample was placed on a computer-controlled X-Y stage inside a vacuum chamber (base pressure 10^{-7} mbar). The stage was synchronized with the LIFT laser and translated the sample after every laser pulse (0.7 mm typical translation step). The laser beam was focused by a 30-mm focal-length lens on the back side of the polyimide layer (through the glass) onto a spot of ~0.7 mm in diameter. A circular aperture (2 or 1.2 mm in diameter) was installed in front of the lens in order to sample the central part of the laser beam (its original size at the lens position is about 8 x 8 mm^2) and thus to have a fairly uniform energy distribution within the spot. The laser fluence at the sample was kept at ~30 mJ/cm^2 (for both 2 and 1.4-mm apertures), that was considerably lower than the threshold for breaking the polyimide layer (around 45-50 mJ/cm^2) and resulted in reproducible blisters as was checked in preliminary calibration experiments. The pulse energy was monitored by a pyroelectric energy meter Ophir-PE25BB (20 □J resolution) and adjusted by an attenuator (based on a rotatable dielectrically coated plate).

The LIFT-produced neutral particles traveled **37 mm** (minimal possible distance until the ionization point for our system) and then were pulse-ionized with a ribbon-like electron beam crossing the particle beam (1 □s pulse duration, 90 eV electron energy) at a time delay □ after the laser pulse. The produced ions were sampled in a perpendicular direction by a 500 V repeller pulse following the ionization pulse and analyzed by a reflectron TOF mass spectrometer. Most of the data were obtained by averaging the MS signal over 5 LIFT pulses at a fixed time delay □ (i.e., by producing 5 individual spots on the polyimide film). In some cases, mass spectrum was collected after a single laser shot. The MS detection efficiency was set almost to its maximum (near-highest voltage over a three-stage MCP detector plus a preamplifier) to be able to detect a single ion produced in the ionization region.

Appendix C

Polyimide C_{60} removal and mass spec detection results as written by Dr. Alexander Bulgakov

Unfortunately these were found to be inconclusive.

When the laser pulse is applied to the polyimide-free triangle-shaped area, a strong C_{60} signal is observed (Fig. 1). I suspect this is due to laser-induced desorption from back irradiated C_{60} film. In any case, these measurements allowed us to prove the ability to efficiency detect C_{60} and demonstrated the fragmentation pattern for our ionization conditions. In further analysis of the LIFT process we ignored signals from this triangle-shaped area.

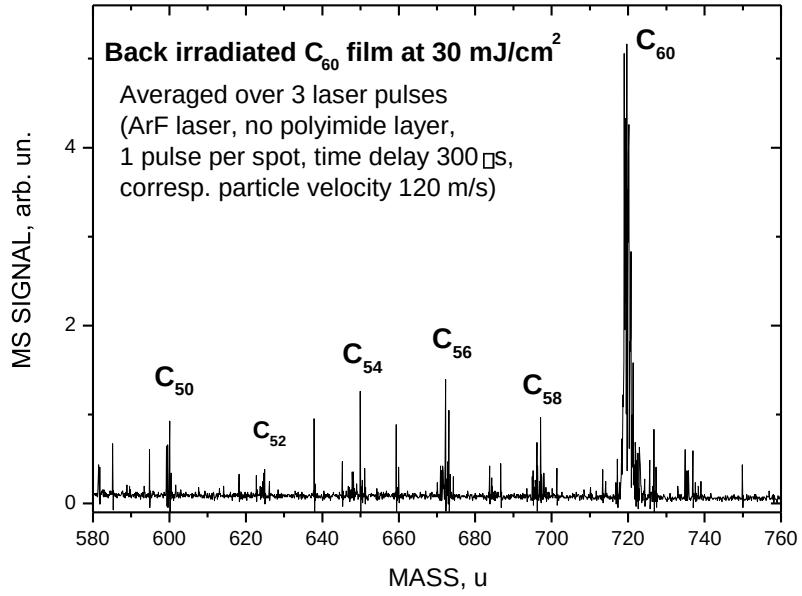

Fig. 1. Mass spectrum of C_{60} and fragments detected at direct ArF-laser irradiation of the C_{60} film – glass interface.

The C_{60} signal under *normal* LIFT conditions (i.e., from polyimide) is found to be, unfortunately, very weak even for optimal time delays (see below) corresponding less that one C_{60} ion pulse (on the average, roughly one detected C_{60} ion per 5-7 pulses). A typical mass spectrum in the 580-760 u mass range obtained by averaging over 50 LIFT pulses (correspondingly, 50 spots were produced to obtain this mass spectrum). The time delay was varied in the range 180-330 □s where the maximum of the C_{60} emission is expected (see below). The C_{60} signal intensity is not enough to quantify it with a reasonable accuracy (for a reasonable averaging number) and thus to obtain the TOF distribution. The low C_{60} signal intensity is possibly due to (a) a long distance L from the sample to the defection point (37 mm) resulting in the low particle density in the detection region (remember that in Edinburgh we detected LIFT-produced C_{60} at L = 4-7 mm while at L = 12 mm the signal almost disappeared) and (b) relatively low ionization efficiency with electron impact.

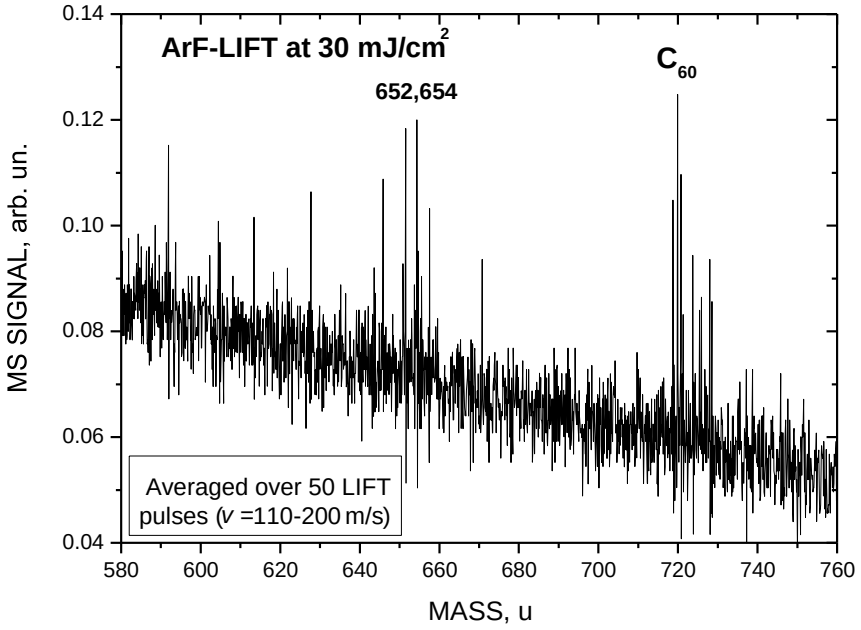

Fig. 2. Mass spectrum in the C_{60} mass region obtained by averaging over 50 LIFT pulses at a time delay in the range 180-330 □s (50 individual spots produced). The peaks at masses 652 and 654 u are from background.

Fortunately, we found that the LIFT pulses resulted in fairly high C_2 and C_2H peaks, considerably higher than the corresponding background peaks (Fig. 3). Most probably, these species are produced due to fragmentation of the LIFT-ejected particles upon electron impact ionization. It is reasonable to expect that not only C_{60} molecules are ejected from the film during the LIFT process but also larger fullerene clusters and even C_{60} nanocrystallites. They are probably partly hydrogenated duet to contact of the C_{60} film with polyimide. Interaction of such species with 90-eV electrons results in efficient production of C_2 and C_2H ions since the C_2 loss is the main channel of fullerene fragmentation. A source of hydrogen for the C_2H ion can be also our vacuum chamber which is not perfectly clean of hydrocarbons.

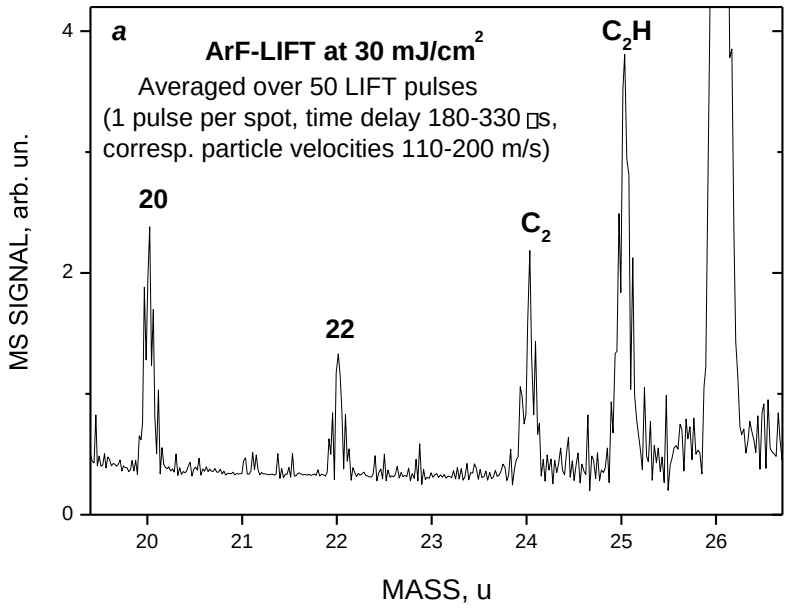

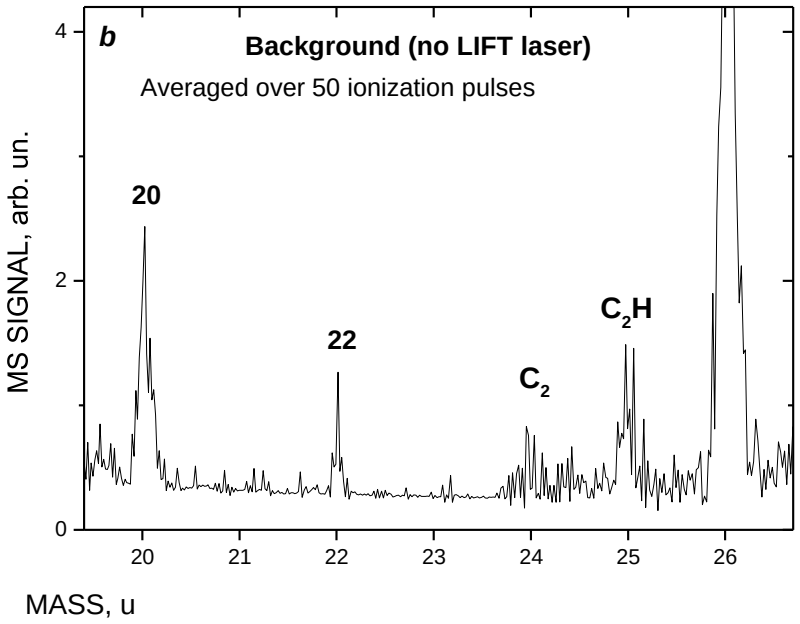

Fig. 3. Mass spectra in the 20-26 u mass region with the LIFT laser applied (*a*) and blocked (*b*). Both spectra are averaged over 50 pulses. With the LIFT pulses, the background peaks at masses 20 and 22 u remain unchanged while the C_2 and C_2H peaks increase strongly. The time delays for the LIFT conditions (180-330 □s) corresponds to the maximum yields of the C_2 and C_2H ions.

The C_2 and C_2H peaks are strong enough to be quantified for a reasonably small averaging number (and even for an individual LIFT pulse) and so it is possible to plot a TOF distribution of the particles emitted from the same sample by collecting the mass spectra at different time delays. The obtained TOF distribution is shown in Fig. 4. Every point was obtained by averaging over 5 laser pulses at a fixed time delay (and thus 5 individual spots were produced). The value "Signal" means the integral of the corresponding averaged peak (i.e., an area under the peak). The signal for C_2 ions was about 2 times smaller than that of C_2H^+ in the same mass spectrum, so it was multiplied by a factor of 2 to normalize it. Figure 5 shows the same data replotted as a velocity distribution (the time-velocity Jacobian transformation factor is taken into account).

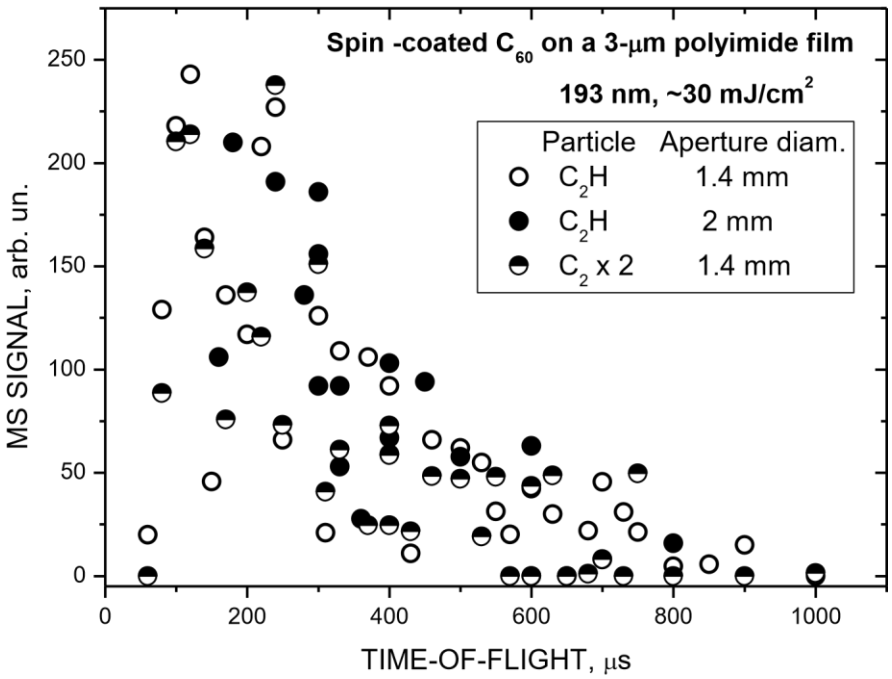

Fig. 4. Time-of-flight distributions of the LIFT-emitted particles from a C_{60} film deposited by spin coating on a 3-□m polyimide layer on glass. The data are presented for C_2 and C_2H species which are assumed to be fragments of larger emitted $(C_{60})_n$ particle produced by electron-impact ionization. Every point is averaged over 5 ArF-laser pulses at a fixed time delay.

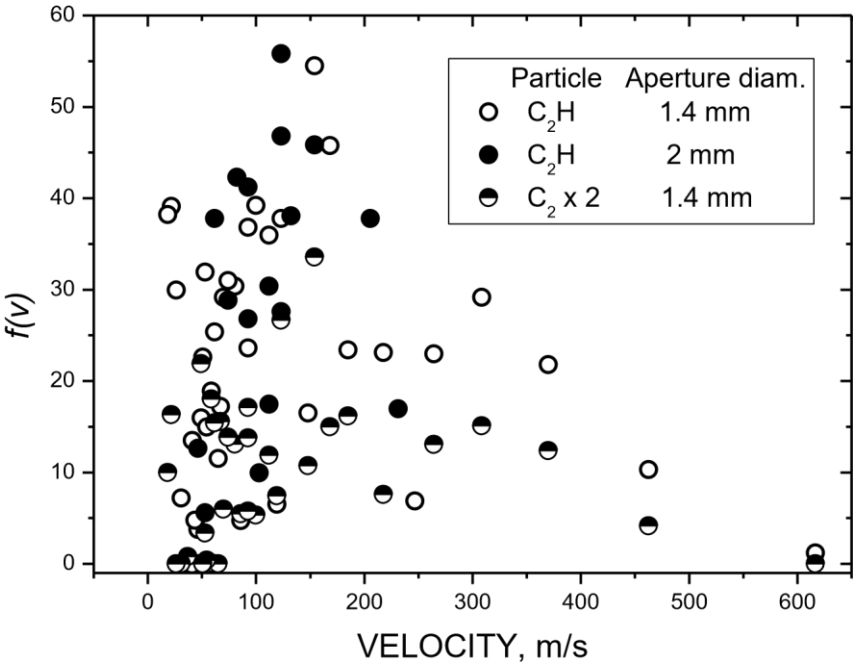

Fig. 5. Same data as in Fig. 4 replotted as velocity distribution.

The data in Figs 4 and 5 are rather scattered. The main reason for this is probably the non-uniformity of the sample. Also, the statistics is quite poor yet. However, the general trends are quite obvious. The TOF distribution is single-peaked and maximized in the range 100-250 □s. The most probable velocity of the emitted particles is around 100-150 m/s. The fast thermal population of the particles (which was observed previously at LIFT from ~300-nm-thick titanium films) is not found here. Since the detected C_2 and C_2H species are assumed to be fragments of larger emitted particles (C_{60} molecules, clusters and nanoparticles) upon their electron impact ionization, the measured TOF and velocity distributions correspond to those of these large particles.

Appendix D

Laser-induced transfer of nanoparticles for gas-phase analysis

Alexander V. Bulgakov,[1,2,*] Nathan Goodfriend,[1] Oleg Nerushev,[1] Nadezhda M. Bulgakova,[2,3] Sergei V. Starinskiy,[2] Yuri G. Shukhov,[2] and Eleanor E. B. Campbell[1,4]

[1]EaStCHEM, School of Chemistry, University of Edinburgh, Edinburgh EH9 3JJ, UK
[2]Institute of Thermophysics, Siberian Branch, Russian Academy of Sciences, Lavrentyev Ave. 1, 630090 Novosibirsk, Russia
[3]HiLASE Centre, Institute of Physics ASCR, Za Radnicí 828, 25241 Dolní Břežany, Czech Republic
[4]Department of Physics, Konkuk University, 143-701 Seoul, South Korea
*Corresponding author: bulgakov@itp.nsc.ru

Received June 2, 2014; revised August 13, 2014; accepted August 25, 2014; posted August 25, 2014 (Doc. ID 212813); published September 24, 2014

An experimental study of laser-induced forward transfer of nanoparticles from a metal-coated glass substrate is presented. Nanoparticles are efficiently removed from the substrates due to transient blister formation. A combination of mass spectrometry, atomic force microscopy studies of the irradiated substrates, and theoretical considerations of temperature distributions and stress in the films during irradiation serves to provide insight into the mechanisms involved. © 2014 Optical Society of America

OCIS codes: (310.6845) Thin film devices and applications; (320.2250) Femtosecond phenomena; (320.4240) Nanosecond phenomena; (350.1820) Damage; (350.3390) Laser materials processing.
http://dx.doi.org/10.1364/JOSAB.31.000C15

1. INTRODUCTION

The detection and characterization of isolated nanoparticles in the gas phase is an extremely challenging problem but of considerable importance for situations ranging from environmental monitoring to experiments that probe the foundations of physics [1,2]. A number of important analytical techniques for isolated particles, such as mass spectrometry and electron spectroscopy, require intact particles to be introduced into a region of high vacuum. One of the frequently used solutions is an aerodynamic lens system capable of delivering nanoparticles in a narrow beam into high vacuum [3,4]. However, the efficiency of this method drops dramatically for small particles (the critical size is ~30 nm), and the method also requires the initial aerosol formation. An alternative method for transferring nanoparticles into vacuum is matrix-assisted pulsed laser evaporation (MAPLE), which is based on the use of a highly absorbing, easily vaporized matrix (usually a polymer) that serves as a solvent for the analyte particles and, being vaporized, carries the analyte toward a detector [5,6]. Another laser-based method, laser-induced forward transfer (LIFT), is a non-contact, single-step, direct-write technique which employs pulsed laser radiation penetrating a transparent substrate to heat and vaporize a donor film deposited on it [7–11]. The transferred material is either spread on the film [9] or introduced into a matrix [10,11]. Both MAPLE and LIFT techniques can provide efficient and "mild" transfer of particles but also have drawbacks. First, the nanoparticles are transferred together with the absorbing matter, which is often unacceptable for analytical purposes. Another evident problem is the selection of an appropriate absorbing matrix. For studying large organic molecules, the matrix-assisted laser desorption/ionization technique has been developed, which is also based on the use of an absorbing matrix [12]. Direct laser desorption is a simple and efficient method for delivering particles for gas-phase analysis [13], but it usually results in heating, ionization, and fragmentation of the desorbed species.

Recently, a new matrix-free modification of the LIFT technique for nanoparticle transfer without destruction of the supporting film was proposed [14,15]. In this method, the nanoparticles are spread over a metal film deposited on a transparent substrate, and the interaction of a laser pulse with the metal–substrate interface causes, under certain conditions, transient blistering of the film, resulting in gentle transfer of nanoparticles without their heating. A variation of the blister-based LIFT method is acoustic wave-induced desorption, in which a thin metal foil is used instead of a coated transparent substrate [16,17]. The efficiency of these contamination-free techniques has been demonstrated for nanoparticle printing on a receiver substrate under standard air conditions [14,17–19] and for mass spectrometry of biomolecules [17]. We believe that this method can be very useful for transferring nanoparticles into analytical instruments for gas-phase analysis.

In this work, we have performed a study of blister-based laser-induced transfer under high-vacuum conditions for mass spectrometric analysis of gold-coated silica particles deposited on a thin titanium film. The gold nanoshells were detected at relatively large distances from the film, and their ejection velocities were measured. Based on an analysis of the laser-produced spots on the film using atomic force microscopy (AFM), we revealed two different regimes of blister formation and particle removal. Finally, we have performed a theoretical analysis of temperatures and mechanical stress realized in the irradiated titanium film under conditions of blister formation.

0740-3224/14/110C15-07$15.00/0

Appendix E

Appl. Phys. A (2016) 122:154
DOI 10.1007/s00339-016-9666-x

Applied Physics A
Materials Science & Processing

Laser pulse duration dependence of blister formation on back-radiated Ti thin films for BB-LIFT

N. T. Goodfriend[1] · S. V. Starinskiy[2] · O. A. Nerushev[1] · N. M. Bulgakova[2,3] · A. V. Bulgakov[1,2] · E. E. B. Campbell[1,4]

Received: 21 January 2016 / Accepted: 24 January 2016 / Published online: 17 February 2016

Abstract The influence of the laser pulse duration on the mechanism of blister formation in the particle transfer technique, blister-based laser-induced forward transfer, was investigated. Pulses from a fs Ti:Sapphire laser (120 fs, 800 nm) and from a ns Nd:YAG laser (7 ns, 532 nm) were used to directly compare blister formation on thin titanium films of ca. 300 nm thickness, deposited on glass. The different blister morphologies were compared and contrasted by using optical microscopy and atomic force microscopy. The results provide evidence for different blister formation mechanisms: for fs pulses the mechanism is predominantly ablation at the metal–glass interface accompanied by confined plasma expansion and deformation of the remaining metal film; for ns pulses it is heating accompanied by thermal expansion of the metal film.

1 Introduction

The transfer of intact nanoparticles and large molecules from the solid to the gas phase is of considerable interest for mass spectrometry [1] and gas phase spectroscopy techniques such as photoelectron spectroscopy [2] as well as for environmental monitoring applications [3] and more exotic studies related to fundamental quantum mechanics [4]. Multiple techniques have been developed to enable the gentle transfer, such as matrix-assisted laser desorption/ionisation (MALDI), electrospray, and laser-induced acoustic desorption (LIAD) [5] being some of the most common. MALDI utilises the direct vaporisation of a matrix that contains the particles of interest. LIAD is similar to MALDI; however, the laser pulse impacts the back of a thin metal foil on which the molecules have been deposited. Electrospray involves spraying a solution of the particles of interest from a charged nozzle, where the charged droplets undergo evaporation and coulomb explosions until individual multiply charged particles remain. Whilst MALDI and electrospray methods are effective for producing beams of charged molecules and have revolutionised the mass spectrometry of large biomolecules, they harbour some significant drawbacks, such as difficulties in quantification, or the need to find an appropriate solution or matrix material that may also then be present in the produced beam, and neither of them are particularly suitable for preparing well-defined beams of neutral species. LIAD can be applied to any molecule that can be deposited on the metal foil and is thus more general; however, there is some controversy concerning the desorption mechanism and the extent to which molecules may be heated and fragment during the desorption process [6].

A technique known as blister-based-laser-induced forward transfer (BB-LIFT), closely related to LIAD, has been introduced and used mainly for depositing nanoparticles or organic molecules in well-defined microscale patterns on substrates [7–10]. More recently, it has been used to produce beams of nanoparticles for gas phase analysis [6]. This technique has the same advantages as LIAD but

✉ E. E. B. Campbell
eleanor.campbell@ed.ac.uk

[1] EaStCHEM and School of Chemistry, University of Edinburgh, David Brewster Road, Edinburgh EH9 3FJ, Scotland, UK

[2] Kutateladze Institute of Thermophysics, Siberian Branch, Russian Academy of Sciences, Lavrentyev Ave. 1, Novosibirsk 630090, Russia

[3] HiLASE Centre, Institute of Physics, ASCR, Za Radnicí 828, 25241 Dolní Břežany, Czech Republic

[4] Division of Quantum Phases and Devices, School of Physics, Konkuk University, Seoul 143701, Korea